Mechanical properties of *Bombyx mori* silkworm silk:

viscoelasticity, structural and molecular origin

Dissertation
zur Erlangung des Doktorgrades
der Mathematisch-Naturwissenschaftlichen Fakultät
der Christian-Albrechts-Universität zu Kiel

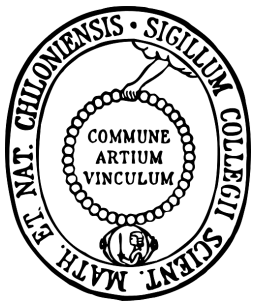

vorgelegt von

Igor Krasnov

Kiel, 2013

Erster Gutachter:	Prof. Dr. M. Müller
Zweiter Gutachter:	Prof. Dr. M. Tolan
Tag der mündlichen Prüfung:	22.11.2013
Zum Druck genehmigt:	Kiel den 22.11.2013

gez. Prof. Dr. rer. nat. Wolfgang J. Duschl, Dekan

Kurzfassung

Die vorgelegte Arbeit ist eine komparative theoretische und experimentelle Untersuchung der mechanischen Eigenschaften von *Bombyx mori* Seide auf makroskopischer und auf molekularer Ebene. Die Reaktion der Seide auf mechanische Einwirkungen wurde erforscht mittels der Beobachtung der Variationen der mikroskopischen Struktur der kristallinen Regionen und der Molekulardynamik der amorphen Phase. Zu diesem Zweck wurden *in situ* Streuungsexperimente durchgeführt, bei denen die Struktur mittels Synchrotronstrahlung erkundet wurde. Hingegen wurden die molekulardynamischen Eigenschaften der amorphen Phase mittels Neutronenstreuung untersucht.

Besonderes viel Aufmerksamkeit widmeten wir den noch wenig erforschten Aspekten der zeitlichen Entwicklung der vorliegenden Phänomene. Dementsprechend wurden unsere Dehnungsexperimente auf mehreren Zeitskalen durchgeführt, mit Dauern von einigen Sekunden bis zu einigen Tagen. Auch wurden unsere Experimente in einer streng kontrollierten Umgebung durchgeführt, da die Temperatur und die Feuchtigkeit der Umgebung die mechanischen Eigenschaften der Seide stark beeinflussen. Um den Einfluß des Wassergehaltes auf die mechanischen Eigenschaften der Seide genauer zu untersuchen wurden die Messungen bei verschiedenen Feuchtigkeiten wiederholt.

Aus der theoretischen Analyse unserer experimentalen Ergebnisse resultierte eine Reihe von zusammenhängenden, viskoelastischen, strukturellen und dynamischen Modellen. Dies erlaubte uns das Verhalten von gedehnten Seidenfasern in den untersuchten Kraft-Dehnungs-Bereichen effektiv zu beschreiben. Insbesonders ermöglichte es uns sowohl die Grundprinzipien des linearen und nicht linearen viskoelastischen Verhaltens von Seide als auch die geometrischen und strukturellen Aspekte der Dehnung der kristallinen Bereiche zu klären. Generell konnte der Zusammenhang zwischen dem makroskopisch-viskoelastischen Verhalten und den Wirkungsmechanismen auf der molekularen Ebene etabliert werden. Mittels unserer experimentellen Techniken und unserer theoretischen Analyse waren wir in der Lage die mechanischen Eigenschaften der kristallinen Bereiche von den Eigenschaften der amorphen Regionen zu trennen und ihre Wechselwirkung zu zeigen. Unserer Meinung nach verdienen einige unserer neuen Ergebnisse aus dem Bereich der langzeit-viskoelastischen-Relaxation und der molekularen Diffusionsprozesse besondere Aufmerksamkeit. Beide Phänomene zeigen einen Memory-Effekt und sind beschreibbar mit Modellen der differential-fraktionellen Analyse. Trotz der Tatsache, dass beide Phänomene zu verschiedenen zeitlichen und räumlichen Ebenen gehören, zeigen ihre fraktionellen Charakteristika große Ähnlichkeiten.

Abstract

This thesis is a comparative experimental and theoretical work focused on the mechanical properties of *Bombyx mori* silk on macroscopic and molecular levels. We did study the response of silk to a mechanical perturbation by monitoring changes of the microscopic structure in the crystalline regions as well as the molecular dynamics of the amorphous phase. In order to achieve this goal *in situ* scattering experiments were performed: synchrotron X-ray radiation and cold neutrons were used as probes of the structure and dynamics, respectively.

Much attention was devoted to the less studied temporal evolution of the surveyed phenomena. Accordingly our stretching experiments covered several time intervals, ranging from fractions of a second up to several days. Because such environmental parameters as temperature and humidity strongly influence the thermo-mechanical properties of silk the measurements were done at controlled environmental conditions and were repeated at several humidities.

The theoretical analysis of our experimental data resulted in the development of a set of interrelated viscoelastic, structural and dynamical models. These models allow to describe the behaviour of stretched silk in the examined range of forces and elongations over almost the whole range of humidity. Particularly, they help to clarify the basic principles of the viscoelastic linear and non-linear behaviour of silk as well as the geometrical and structural aspects of the elongation in the crystalline regions. Generally, a link between the macroscopic viscoelastic behaviour and the mechanism at the molecular length scales has been established. With our experimental techniques and analyses we could separate the mechanical properties of the crystalline region of silk from those of the amorphous part, as well as show their interplay. In our opinion, interesting novel results were also obtained concerning the long-time mechanical relaxation of silk and molecular diffusion processes. Both phenomena exhibit definitive memory effects and can be well described by the models based on fractional calculus. Despite the fact that these phenomena belong to very different temporal and spacial levels the fractional characteristics of these phenomena are very similar.

Contents

Introduction

The interplay of biochemistry, biology and physics has created exciting opportunities for the discovery, invention and application of new and old natural materials. Materials usually used in engineering are hard, while nature builds on the basis of soft materials. What renders softness so successful in nature?
Research on soft materials has brought applications of mechanics and thermodynamics to the forefront of human creativity and contributes to further development of these disciplines. Related chemical and biological phenomena and the investigation of their physical aspects and engineering applications, have motivated the development of theories for diverse soft materials. The experimental and theoretical studies of soft composite matter attempt to answer commonly asked questions, such as: How do thermodynamic, mechanic and dynamic properties and the hierarchical structure of materials work together to produce an effective response to external forces or to allow a large deformation without failure? Which features and characteristics of a material optimize its function? What is the relation between the molecular processes and their effect on the macroscopic behaviour? How effectively can one form of energy be converted into another one within soft materials? Answers have to be defined in an operative form and implemented in the form of software, so that they can be broadly useful in the design of new materials and machines or in the more effective application of well-known materials.

The objective of the presented research is the study of the mechanical response of *Bombyx mori* silk. Being allegiant to the above mentioned general tendency we will probe the subject of our study on both the macroscopic and the microscopic level.
Silk is a soft fibrous material composed of polypeptides, i.e. polymers made of amino acids [24]. It belongs to a large class of polymeric nano-composite materials which are currently of both fundamental and technical interest. Silk is one of the most successful materials "constructed" by nature and has been in human use for at least 4000 years. This is, because it exhibits outstanding mechanical properties [157], combining high elasticity and tensile strength. It is a light-weight material, but its tensile strength is comparable to that of steel and of synthetic high-tenacity fibres such as Kevlar, while its elasticity

is 4-7 times higher than that of Kevlar. Additionally, it is inherently bio-compatible and its production is inexpensive and ecological. It does not only find applications in textiles, but, due to its biocompatibility and slow degradability it is increasingly studied and used in biomedical applications. Silk can play the role of a model in the design of new soft materials. This is not owed to a simple structure, which is in fact rather complex, but in the sense of principles underlying its properties. Once understood, these principals can be used in the design and controlled production of new, light-weight materials with properties adapted for specific use.

In our work, we approach the mechanical properties of silk at several levels. It is intended as a comparative experimental and theoretical study covering a large range of spatial and temporal scales. At the time of starting this work the mechanical response of silk was studied mostly statically (see e.g. [141, 166]) and little was known about its evolution in time [171]. Hence we attempt to step forward in this direction. The macroscopic response is measured and analysed at several time scales: from the moderate time scale of several seconds up to the scale of many hours. We also aim at investigating the connection between the microscopic structure and the dynamics. This is performed with particular interest in the macroscopic response of silk to mechanical excitations. X-rays and neutrons are used as probes of the molecular structure and dynamics on the microscopical level. We combine scattering experiments with *in situ* stretching. Considerable interest is paid to the influence of environmental conditions, e.g. a variation in humidity, which causes the mechanical properties of silk to change in a distinct and reversible fashion.

Such a study requires a sophisticated experimental setup as well as refined methods for the analysis of the measured data. To achieve sufficient resolution in *in situ* X-ray scattering experiments on a single silk fibre, whose diameter is about of 10 μm, we use a micro beam facility of the $ID13$ measurement station at ESRF (Grenoble). A specialized stretching cell with controlled humidity environment is designed, built and used in these experiments. The sample cell fulfills the requirements for a high temporal and spatial resolution as well as high resolution in force sensing for exact monitoring and control. We elaborate a procedure of the analysis of the diffraction images from silk fibres. This provides access to detailed information on the structure of the elongated crystallites in the crystalline regions of silk fibre as well as the distributional characteristics, e.g. the orientation of the crystallites in the stretched fibre.

Because a quantitative analysis of the influence of the applied force and environmental conditions is possible only within a chosen model we will adapt some existing models and construct our own one. For this purpose we use the principles of thermodynamics whose laws are insensitive to the very details of a material. The mechanical as well as the mi-

croscopic structural and dynamical properties which we can measure are the sum of the contributions of a huge amount of mesoscopically sized interconnected subsystems of silk fibre. The author sets out to pick out the main properties of these subsystems to replace them (in a simulation of the behaviour) by a set of simple subsystems. The cumulative contribution from such simplified sub-systems to the average response of the system as a whole will be described by viscoelastic-like dash-pots and springs. Such an approach (in case of success) will result in simple models with few parameters. They will help to classify the results of the measurements and also to understand the behaviour of silk on an averaged level.

This thesis is organized as follows:
In the first chapter generally known aspects of the structure of *Bombyx mori* silk as well as its building blocks are presented. In the second chapter we give a short introduction into the linear viscoelastic theory which we shall use later. This is followed by a presentation of the models of the fractional viscoelastic theory together with the minimal background of the calculus of the differential operators of fractional order. The fractional linear viscoelasticity is used to describe the behaviour of silk on long time scales. The last part of this chapter is devoted to the non-linear treatment of the viscoelastic phenomena. Here we discuss the models based on the Transition State Theory which we apply to the behaviour of silk on the "intermediate" time scales. In chapter 3 a short introduction into scattering methods and their basic theory is given.
The experimental setups is introduced in the chapter 4. Here we present our sample cells, their constructions and driving programs as well as the calibration of sensors and actuators. This chapter ends with a short overview of the instruments at DESY (Hamburg), ESRF and ILL (Grenoble) where our scattering experiments where performed.
Chapter 5 starts with the reduction of the data from our measurements. Then the analysis of the measurements and the results together with the models used are given. The chapter ends with a detailed presentation of our model describing the X-ray scattering from the crystalline region of stretched silk fibre followed by its applications to measured diffraction images. An extensive discussion of the results and the conclusions are given in the chapters 6 and 7, respectively.

1. Silk: structure and properties

1.1. Silk

Silks are naturally occurring materials, consist of protein polymers and are produced by a wide variety of insects and spiders [25, 176]. In nature silks exhibit diverse structures and functions which are evolutionary tailored to the conditions of the environment inhabited by silk-producing species. The diverse functions of silk range from web construction and prey capture (spider webs), safety lines (draglines) and constructions of nests to reproduction (cocoons) and housing [3, 40, 174, 181].

Silkworm silk is the best known type of natural protein fiber, which can be woven into textiles and has been in use for about 4000 years. It is obtained from cocoons produced by the larvae of the mulberry silkworm *Bombyx mori* reared in captivity (sericulture).

The scientific interest in this material is due to its remarkable mechanical properties: it provides an excellent combination of lightweight, an extra toughness and elasticity. E.g., its tensile strength is comparable to that of steel and of synthetic high-tenacity fibers as Kevlar, its elasticity is 4-7 times higher then that of Kevlar. Additionally, silk is increasingly studied in biomedical applications due to is biocompatibility and slow degradability.

Together with the spider *Nephila clavipes*, *Bombyx mori* is the most widely studied silk [25,55,84,95,175]. In its natural form silk is composed of a filament core protein, silk fibroin, and a glue-like coating consisting of a family of sericin proteins [176, 181]. Structurally, silk fibroins are characterized as natural block copolymers composed of hydrophobic blocks with highly preserved repetitive sequence consisting of short side-chain amino acids such as glycine and alanine, and hydrophilic blocks with more complex sequences that consist of larger side-chain amino acids as well as charged amino acids. The hydrophobic blocks tend to form (β-sheet) crystallites by hydrogen bonding and hydrophobic interactions, forming the basis for the tensile strength of silk fibroins. These ordered hydrophobic blocks combined with the less ordered hydrophilic blocks give rise to the elasticity and toughness of silk fibroins.

1.2. The biology and structure of silk

Silk of *Bombyx mori* silkworm is produced by the larvae of insects that complete their metamorphosis by producing a cocoon in which the pupa has to be embedded. The cocoon is formed from a single silk-fiber (thread) with a length of about 1 kilometer. It is synthesized in the posterior silk gland cells of silkworm and secreted into the lumen of the posterior silk gland. By building the cocoon around itself, the worm pulls the silk thread from its spinneret (spinning nozzle), which is situated close to its mouth. During the spinning, the solvated random-coil fibroin protein, which is stored in the silk gland in a liquid crystalline phase [101–104] [180], is transformed into a semi-crystalline silk thread (bave) composed of two brins within a sericin coating [101] (see Fig. 1.1). The bave is responsible for the cocoon's toughness and the seritine coating acts like a glue.

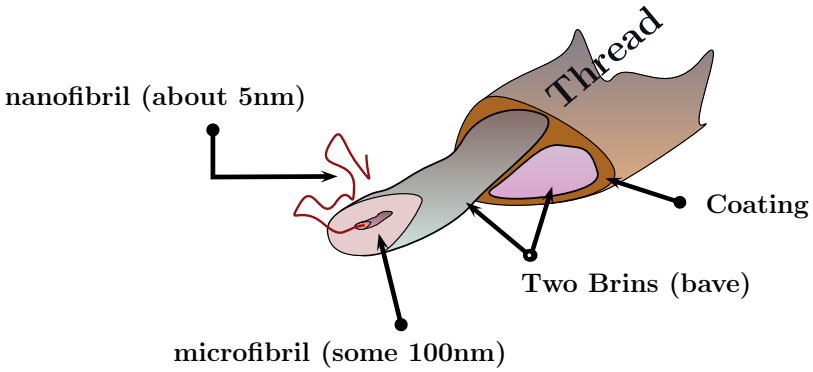

Figure 1.1.: **Sketch of the hierarchical structure of silk**
Schematic diagram of a hierarchical composite structure of a silk thread from nano- up to macro-scale, (drawn after [62]).

Symbolically we can describe the structural peculiarities of silk (fig. 1.1) on the following hierarchical levels:

macroscopic level
structure of thread with its coating and bave, ranges over the length scale of some μm

micro-/mesoscopic level
comprises of nano- and micro-fibrils and ranges over the scale about some 100 nm

nanoscopic level
organisation of semi-crystalline structure of the bave at the nanoscopic scale. Using the

common classification of proteins structures, this level contains: secondary, tertiary and quaternary structures of the fibroin molecular chain.

molecular level

is defined by the chemical structure, i.e. the amino acid sequence of the fibroin subunits and rules of their composition. It is a primary and secondary structure of fibroin. The scale is about 1 nm.

Biocomposite materials, such as a silk, show a strong interplay between different spatial scales. Additionally, silk demonstrates a complex interplay of two types of scaling: chemical-binding topology scaling and 3D-space scaling. Chemically, silk fibroin is composed of highly repeated six-pack units, each of them is a composition of a six polypeptide dimers connected to one glucoprotein chain (called P25 protein) through non-covalent binding [61]. Each of such polypeptide dimers is a disulfide bounded pack of two polypeptide chains, one of which is much larger then the other (they are called heavy and light chains, respectively) [17,78,79,165]. Each of these chains is a covalently bonded combination of the simpler motives constructed as chain combinations of the almost elemental peptide units, amino acid molecules. Every subsequence of them has a possibility to build a H-bonds at the inter- or intra-chain level. This raises a spatial configuration topology [173]. One can say, that the properties of silk are coded at the molecular level, but they are manifesting at the very supper-molecular scale.
Subunits of every chain can undergo a *reversible* disorder $\rightleftarrows$ order transition called *protein folding*. The typical time of folding lays in the microseconds to milliseconds range [121]. Under suitable conditions, all of the information needed to realize the ordered form of most sub-chains is encoded in their linear sequences; no auxiliary components are necessary to guide the disordered chain to its unique, native three-dimensional structure. In fact, fibroin self-assembles spontaneously and iteratively, from a top-down structural hierarchy that terminates with protein monomers, which assemble themselves.
In the following paragraphs we will discuss some aspects of characteristics for a particular length scale, starting from the molecular level.

1.2.1. Molecular level

Amino Acide Units

The most basic subunits of the silk fibroin structure are amino acids. Amino acids are molecules containing four different groups bonded to a central carbon in their structure (see diagram in fig. 1.2): a *hydrogen*, an *amino* group, a *carboxylic acid* group and a

Name (Residue)	3-letter code	Single code	Charged, Polar, Hydro-phobic
Alanine	ALA	A	H
Arginine	ARG	R	C+
Asparagine	ASN	N	P
Aspartate	ASP	D	C-
Cysteine	CYS	C	P
Glutamate	GLU	E	C-
Glutamine	GLN	Q	P
Glycine	GLY	G	-
Histidine	HIS	H	P,C+
Isoleucine	ILE	I	H
Leucine	LEU	L	H
Lysine	LYS	K	C+
Methionine	MET	M	H
Phenylalanine	PHE	F	H
Proline	PRO	P	H
Serine	SER	S	P
Threonine	THR	T	P
Tryptophan	TRP	W	P
Tyrosine	TYR	Y	P
Valine	VAL	V	H

Table 1.1.: **One and three letter symbols for amino acids**

side chain (called residual or R) that varies between different amino acids. In the alpha amino acids, the amino and carboxylate groups are attached to the same carbon atom, which is called the α–carbon. The various alpha amino acids differ in which side chain (R

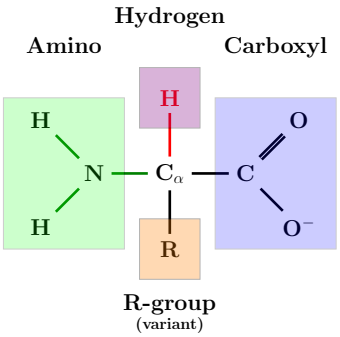

Figure 1.2.: **Amino acid structure**

Here, R is an organic substituent (side chain). In the amino acids, the amino and carboxylate groups are attached to the same carbon atom, which is called the α–carbon. The figure is taken from [179].

group) is attached to their alpha carbon. These side chains can vary in size from just a hydrogen atom in glycine, to a methyl group in alanine, through to a large heterocyclic group in tryptophan. Table 1.1 shows a list of 20 relevant for us amino acids, together with a three-/single- term name convention and some physical properties.

Primary structure

In silk, as in every protein, the amino acids are joined together by the *peptide bonds* between the carboxyl and amino groups of adjacent amino acid residues. The representation of such a binding as a chemical reaction (called condensation) is shown in fig. 1.3. By repeating

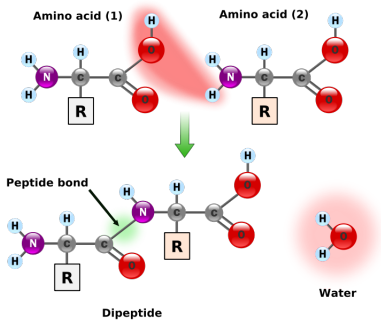

Figure 1.3.: **Condensation of two amino acids**
The figure shows an illustration for the chemical reaction (called condensation) of two amino acids forming a peptide bond. The figure is taken from [179].

this reaction, long chains of residues (amino acids in a peptide bond) can be generated. This reaction is catalysed by the ribosome in a process known as translation. In the resulting sequence, the chain of $[\text{-N-C}(\alpha)\text{-C-}]_n$ is called the *backbone* and *R-atoms* form the so-called side groups. The chain of amino acids is also known as a *polypeptide*. A protein can contain one or more polypeptide chains.
Because the covalent bonds C–C and C–N are both strong and directional, the geometry of such chains will be defined, in principal, by the three dihedral angles (see Fig.1.4):

- Ω – the bond between C and N (the peptide bond)
- Φ – the bond between N and C_α
- Ψ – (the bond between C_α and C (of the Carboxyl group)

The peptide bond is in fact planar due to the delocalization of the electrons from the double bond [129]. This causes, that the rigid peptide dihedral angle, Ω is always close to 180 degrees. But the angles Φ and Ψ can have a certain range of possible values. These angles are the degrees of freedom of a protein, they control the protein's three dimensional structure. They are restrained by geometry and the interactions of side groups to allowed ranges typical for particular secondary structure elements, and represented in a

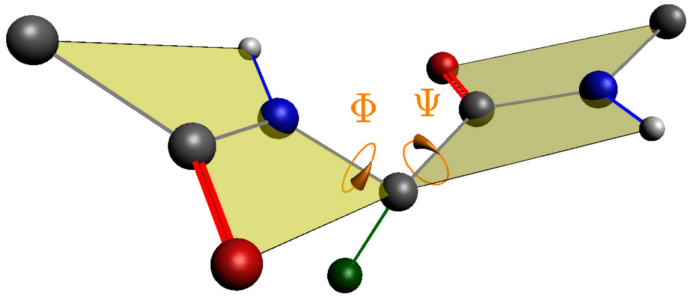

Figure 1.4.: **Dihedral angles**
A peptidic bond has two degree of freedom, the dihedral angles named Φ and Ψ by Ramachandran. Each atom type is represented by its usual in the literature colour: *H* - white ○, *C* - grey ●, *N* - blue ●, *O* - red ●. The first atom of the residual is an exeption, it is represented by green color ●.

Ramachandran plot (i.e. plot of population vs. Φ and Ψ). The sequence of the different amino acids is called the *primary structure* of the peptide or protein.

Secondary structure

In 1951 Pauling and coworkers [129] established two fundamental structural principles in arriving at the most probable configurations of polypeptide chains in proteins:

- the coplanarity of the atoms comprising the aminde group
- the formation of close to the maximum possible number of N−H · · · O=C hydrogen bonds

On their basis the two first elements of secondary structure, the alpha helix and the beta sheet (β-sheet), were suggested in 1951 by Linus Pauling and coworkers [128–132]. Each of these two secondary structure elements have a regular geometry, meaning they are constrained to specific values of the dihedral angles Φ and Ψ. Thus they can be found in a specific region of the Ramachandran plot. Both the alpha helix and the beta sheet represent a way of saturating all the hydrogen bond donors and acceptors in the peptide backbone. These secondary structure elements only depend on properties of the polypeptide main chain, explaining why they occur in all proteins. The part of the protein that is not in a regular secondary structure is said to be a "**non-regular structure**".

Silk fibroin on the macro-molecular level

The coating is made of several serine enriched proteins named sericin. The brins are made up of fibroin, which is comprised of natural block copolymers composed of hydrophobic blocks with a highly preserved repetitive sequence consisting of a short side-chain amino acids such as glycine and alanine, and a hydrophilic block with a more complex sequences that consist of a larger side-chain amino acids as well as charged amino acids. The hydrophobic blocks tend to form β-sheets or crystals held together by hydrogen bonding and hydrophobic interactions, forming the basis for the high tensile strength of silk fibroins. These ordered hydrophobic blocks combined with the less ordered hydrophilic blocks give rise to the elasticity and toughness of silk fibroins. [61, 62, 101]

The fibroin of *Bombyx mori* can be viewed as a sequence of two types of polypeptide chains, the light (Fib-l or L-fibroin) and heavy (Fib-h of H-fibroin) chain, additionally a small amount of glucoprotein P25 is connected to six (Fib-l,Fib-h)-units. Fib-l and Fib-h are linked together by disulfide bridges [61] (see sketch on Fig. 1.5), and P25 associates with disulphide-linked heavy and light chains by non-covalent interactions. P25 plays an important role in maintaining the integrity of the complex and causes solubility of the Fib-H during the transport through the middle silk gland, where heterogeneous molecules of sericin are added, and further towards the anterior part of the silk gland, where the silk fiber is formed and spun [61, 78, 79, 165].

These three components are appearing in the silk fiber with the molar ratio equal 6:6:1. The molecular weights are 26 kDa of L-fibroin, about 390 kDa of H-fibroin and about 30 kDa of P25. Their sequences contain 262 **amino acids** (sometimes abbreviated **aa**) in Fib-L, 5263 amino acids in Fib-H and 220 amino acids in P25 [17, 78, 79, 165]. The core sequence of the fibroin chain, corresponding to a motif (pattern) of the form: –[GAGAGX]– (where X is S, Y, A or V) forms domains of crystalline, anti-parallel β-sheets of the regenerated silk structure. It is often assumed, that during the process of spinning the fibroin transforms from the Silk I into the Silk II structure. This transformation occurs due to the light tensile stress. The Fib-l possesses a non repetitive structure (see fig 1.6) and is responsible for the disordered part of the silk fiber. [3, 53, 61, 101, 185] The Fib-h has a modular primary structure (shown on fig. 1.7) composed of 12 repetitive regions rich of alanine-glycine *amino acid* (shown in red) with 11 spacer regions (shown in green). The heavy chain starts and ends with Amino- and Carboxyl-terminals (blue), respectively. Spacer regions have irregular compositions and play a major role in the overall conformation adopted by the silk fibroin molecules [61]. This modular structure is essential for building the β-pleated-sheet crystalline part of the silk structure.

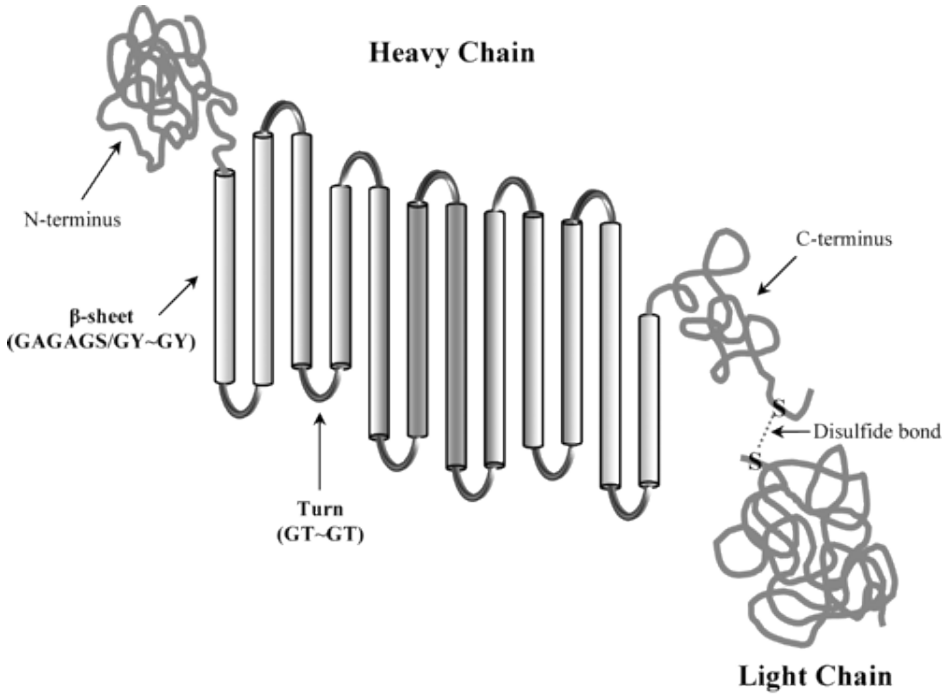

Figure 1.5.: **Symbolical representation of the Fibroin peptide unit**
Here N- and C-terminus mean Amino- and Carboxyl-terminals of the Fib-h, β-sheet and Turn mean regular and irregular (spacer) parts of the Fib-h sequence. See figs. 1.7,1.6 for amino acid sequences.The figure was taken from [61].

MKPIFLVLLV ATSAYAAPSV TINQYSDNEI PRDIDDGKAS SVISRAWDYV DDTDKSIAIL
NVQEILKDMA SQGDYASQAS AVAQTAGIIA HLSAGIPGDA CAAANVINSY TDGVRSGNFA
GFRQSLGPFF GHVGQNLNLI NQLVINPGQL RYSVGPALGC AGGGRIYDFE AAWDAILASS
DSSFLNEEYC IVKRLYNSRN SQSNNIAAYI TAHLLPPVAQ VFHQSAGSIT DLLRGVGNGN
DATGLVANAQ RYIAQAASQV HV

Figure 1.6.: **Fib-l polypeptide sequence**
The Fib-l possesses non–repetitive structure and is responsible for the disordered part of the silk fiber.

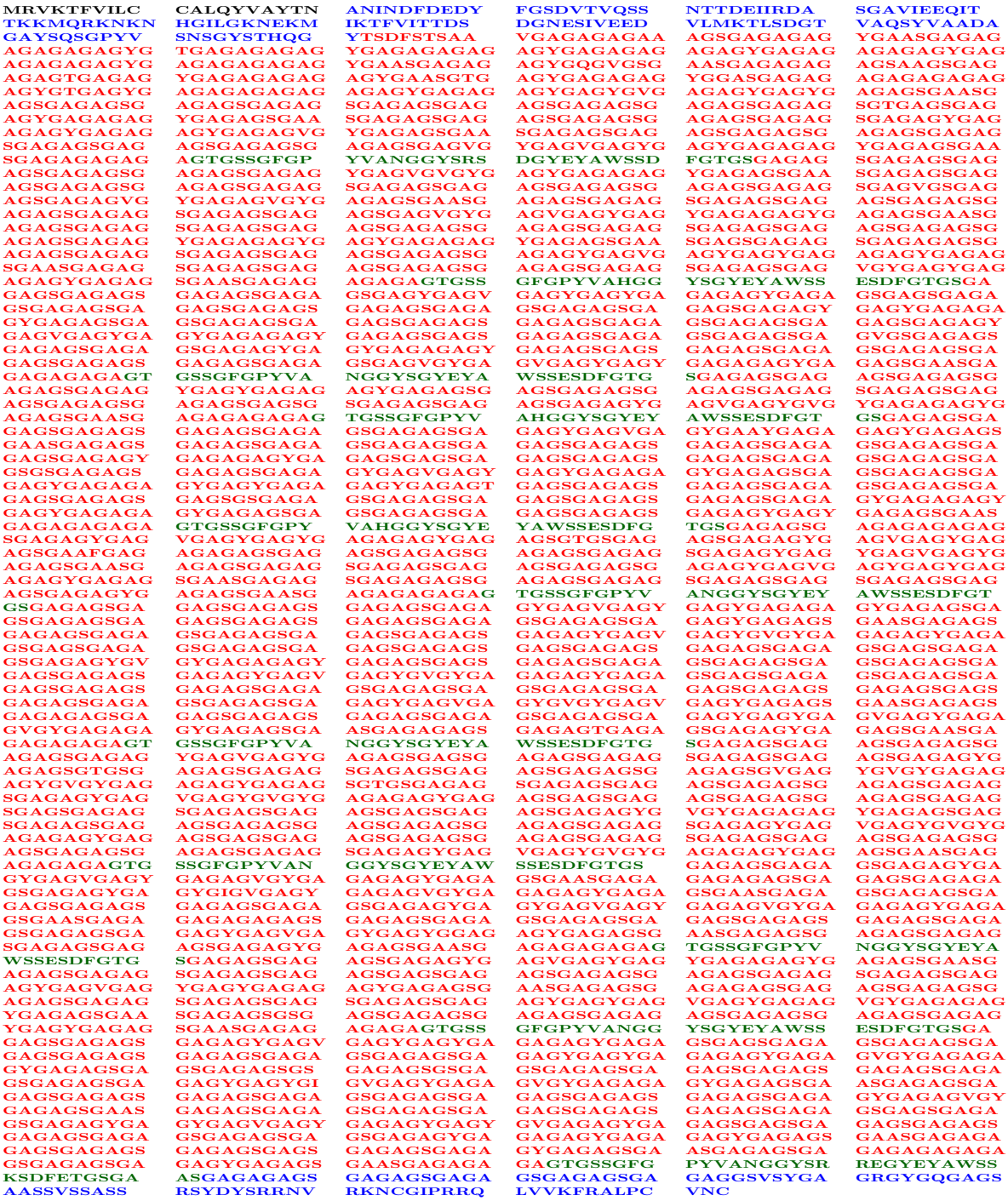

Figure 1.7.: **Fib-h polypeptide sequence**

The Fib-h has a modular primary structure made of 12 repetitive regions rich of alanine-glycine amino acids (shown in red) with 11 spacer regions (shown in green). The heavy chain starts and ends with Amino- and Carboxyl-terminals (blue), respectively.

2. Mechanical and Thermodynamical Properties of Viscoelastic Bodies

In this chapter we give a short summary of the theoretical background for the various kinds of viscoelasticity as well as the description of the mechanical models used in this thesis. The aspects of numerical computations are given mostly as hints with exception of the Block Pulse Functions (BPF). The latter we introduce in section 2.2, where our application of them to the fractional differential equation is described.
The chapter is organized as follows: The classical viscoelastic theory is discussed in section 2.1. A presentation of the linear fractional viscoelasticity and a summary of the basic elements of fractional calculus are given in section 2.2. In section 2.3, the description of several non-linear viscoelastic models based on the Transition State Theory is given. The latter section shows the theoretical considerations which are adapted to the specific properties of silk. The models are presented in the modified form, so that their application to measurements will need only a minimal modification given in section 5.2.6.

2.1. Introductory notes on the linear theory of viscoelasticity

Here some basic concepts of the linear viscoelastic theory [35, 168] are given, which are used in the modelling of the mechanical properties of silk. We will describe: (i) the basic model units of the phenomenological representation of the mechanical response, (ii) the main principles of the model building and (iii) the modified Standard Linear Viscoelastic Solid Model (SLVSM) we use to describe the response of pre-stretched silk. Using the method of the integral Laplace transform we arrive at the description of the mechanical response in an analytical form, with parameters independent of the shape of the excitation. Further, some limitations and drawbacks of the theory will be discussed. This section ends with the introduction of the Rouse model, which describes a viscoelastic behaviour of a coiled polymer chains immersed in a Newtonian fluid. The classical viscoelastic description

of the Rouse model requires an infinite (or very large number) of viscoelastic units. In the next section 2.2 we show that in the frame of the fractional viscoelasticity the Rouse model can be described with only one viscoelastic element.
There exists a long tradition of the application of the linear viscoelastic theory to the mechanical response of polymers [35,168]. However, this type of representation does not imply that these models reflect molecular mechanisms causing the actual relaxation behaviour of these complex materials. In general, there is a multiplicity of models to represent the same viscoelastic behaviour. The physical meaning of the parameters appearing in the viscoelastic models based on springs and dashpots is far from evidence. Therefore, in the subsection 2.3 we describe the non equilibrium approach to the relaxation phenomena and will clarify the physical meaning of model parameters appearing in the linear theory of viscoelasticity.
Based on the filament-like geometry of the sample structure the quasi one-dimensional assumption is applied. This means that the tensorial character of stress $[\sigma_{ij}]$ and strain $[\epsilon_{ij}]$ will be disregarded. All relations as they apply to a time-dependent shear stress, say $\sigma_{12}(t)$, will be simply called stress and will be represented by $\sigma(t)$. Similar, the corresponding time-dependent amount of shear, e.g. $\epsilon_{12}(t)$, will be simply called strain and denoted by $\epsilon(t)$.

2.1.1. Basic principles

If stress or strain is imposed upon a body, rearrangements take place inside a material as a response to the imposed excitation. On the atomistic scale, the length and angles of the chemical bonds connecting the atoms may become distorted as the atoms may be moved to new positions of greater internal energy. This is a small amount of motion and occurs very quickly, requiring only about some picoseconds.
If the material is a polymer and has sufficient molecular mobility, larger-scale rearrangements of the atoms may also be possible. Depending on the mobility, a polymer molecule can extend itself in the direction of the applied stress, which decreases its conformational entropy. Elastomers respond almost entirely by this entropic mechanism, with little distortion of their covalent bonds or change in their internal energy.
So, from a thermodynamical point of view the amount of mechanical work fdx (force $\times$ path) done on the system at the temperature T can produce an increase of the internal energy dE or/and decrease the entropy dS:

$$fdx = dE - TdS$$

With an increment of the temperature the role of the entropic force will increase, while the role of the potential response (energy storage) will decrease. The entropic and dissipative parts of the response depend strongly on the molecular mobility, which is a function of the many physical and chemical factors such as temperature, humidity, presence of other fluids or stress/strain applied to the system.
In any real material the response rearrangements require a finite time. This rearrangement (or response) time has to be compared to the time spent for measurement and/or time-scale of a measurement.

When the changes take place so rapidly, i.e. the time is negligible compared to the time scale of the experiment, we regard the material as **purely viscous**. In a purely viscous materials, all the energy required to produce the deformation is dissipated as heat.
When the material rearrangements take a virtually infinite time, we speak of a **purely elastic** material. In purely elastic materials the energy of deformation is stored and may be recovered completely upon release of the forces acting on it (infinite long memory).
In principle, however, all real materials are **viscoelastic**. Some energy may always be stored during the deformation of a material under appropriate conditions, and energy storage is always accompanied by dissipation of some portion of energy.
In a typical viscoelastic material the time necessary for the material rearrangements to take place is comparable to the time scale of the experiment. The relation between the two time scales can be conveniently expressed by a dimensionless number, called *Deborah Number*, introduced by Reiner [149]

$$N_D = \frac{\tau_{mat}}{\tau_{exp}} \tag{2.1}$$

where τ_{mat} is the time scale of material rearrangements and τ_{exp} is the time scale of experiment. This equation express the relativity of the material and experimental time scales.

$$\begin{aligned} N_D \gg 1 : \text{purely elastic} &: \sigma(t) = G\,\epsilon(t) \\ N_D \ll 1 : \text{purely viscous} &: \sigma(t) = \eta\,\frac{d\epsilon}{dt} \\ N_D \approx 1 : \text{viscoelastic} &: \sigma(t) = \text{Functional}[\epsilon(t-\tau)] \end{aligned}$$

where G is elastic modulus of the material and η is materials viscosity. σ, ϵ are stress and strain, correspondingly.
As stated above, usually one has an intermediate situation, where N_D is comparable with unity, i.e. the material rearrangements take place on a time scale comparable to that of the experiment. As a consequence of this, the relations between stress and strain cannot be

expressed by *material constants* as in the case of purely elastic or purely viscous materials. The rheological behaviour of viscoelastic materials is characterized by a time-dependent *material function*. Generally the stress becomes a functional of the strain, i.e. it depends on the strain history. We can denote it by writing:

$$\sigma(t) \;=\; \hat{\Xi}_{\sigma}\big[\epsilon(\tau)\big]_{-\infty}^{t} \tag{2.2}$$

where t is present (current) time, τ is past (historical) time. Here Ξ_{σ} represents (symbolically) a functional relation between the value of stress at the current time and the whole history of applied strain at the all past times τ. The functional relation is a rule by which to every function $\epsilon(t)$ defined on the whole time domain (starting from the current time t up to the past) there can be assigned one and only one value, a value of σ at the current time t. Similarly, the strain may be regarded as a functional of the stress applied to the system. This can be wrote symmetrically as

$$\epsilon(t) \;=\; \hat{\Xi}_{\epsilon}\big[\sigma(\tau)\big]_{-\infty}^{t} \tag{2.3}$$

For a large class of phenomena, e.g. for sufficiently small deformations, those functionals can be expressed by linear differential equations with constant coefficients, or, equivalently, by convolution integrals with difference kernels. Generally, we can regard the response consisting of a combination of the following types:

- **"conservative" response**: small rearrangements causing an increase in the internal energy. By such a situation the major part of deformation work is stored by the material and can be recovered upon release of the force acting on it.
  This kind of rearrangement can be described in the frame of linear theories under constrains of small amount of deformations.

- **dissipative transport processes**: here the main part of deformation-work is dissipated with time to heat and deformation is irreversible.
  The most simple example is the response of the Newtonian fluids, where the energy of deformation is dissipated immediately. Similarly, such laws as Fourier, Fick or Ohm belong to this class of reactions, where corresponding currents are proportional to the conjugated thermodynamical forces (or gradients).

  The linear description of such processes should in principle be appropriate only when the magnitude of gradients is small. In practice, linear relations of the viscoelastic theory (and those proposed by the linearized non equilibrium thermodynamics) have been proven to work well for many transport processes, even in presence of large gradients.

- **entropy based relaxation**: plays an important role in soft condensed matter and biophysics where typical energies are of the order of the thermal energy.
  Under suitable conditions, including small amounts of deviations and gradients together with the condition of sufficiently large temperature, such phenomena can be described in the frame of the linear response theories, e.g. the thermal spring-dashpot models for elastomer.

- **activated processes** [65]: parts of the system have to overcome some kind of barriers of energetic or entropic nature (e.g. many kinds of forced phase transition between stable or metastable states, diffusion limited aggregations, etc.)

  Activated processes are genuinely nonlinear in their basic nature and cannot be analyzed with linear viscoelastic theories (see e.g. [65, 148]).

To describe the mechanical response of a viscoelastic body, the linear theory combines two basic polar units of purely viscous and purely elastic responses together to mimic the behaviour of a material.

2.1.2. Linear time-dependent behaviour

Purely elastic and purely viscous linear behaviour is typically expressed by the constitutive equations of the form

$$\sigma(t) = G\epsilon(t) \tag{2.4}$$

for the elastic case, and

$$\sigma(t) = \eta\frac{d\epsilon}{dt} \tag{2.5}$$

for the viscous case. Generally, it can be shown that the simplest constitutive equation which adequately describes small deformations of a viscoelastic body is a linear differential equation of the first order with constant coefficients (a,b,c) and has following form

$$\sigma(t) + a\,\frac{d\sigma}{dt} = b\,\epsilon(t) + c\,\frac{d\epsilon}{dt} \tag{2.6}$$

An adequate description of the behaviour of real materials generally requires differential equations containing higher derivatives of both stress and strain. Moreover, in a general deformation, the constitutive equation may not be linear or containing constant coefficients. But under the same conditions, e.g. in the case of infinitesimal deformations with the absence of non-linear phenomena (such as activated processes), the viscoelastic behaviour can be described by the linear differential equations with constant coefficients. Such behaviour

is termed **linear viscoelastic behaviour**. In practice, linear viscoelastic behaviour is observed even in finite deformations as long as the strain remains below a certain limit, called the **linear viscoelastic limit**. The value of this limit is a material property.

To describe a linear behaviour, Ξ-functionals, introduced by the equations (2.2, 2.3), have to satisfy two conditions of linearity. The first one, called *stress-strain linearity*, means that increase in the stimulus (excitation) by an arbitrary factor α will increase the response by the same factor, i.e.

$$\hat{\Xi}[\alpha f(\tau)]_{-\infty}^{t} = \alpha \hat{\Xi}[f(\tau)]_{-\infty}^{t} \tag{2.7}$$

where the symbol f is to be understand as σ or ϵ and $\hat{\Xi}[\dots]$ denotes one of the stress or strain based functionals. The second condition, often referred as *time shift invariance*, means that an arbitrary sequence of stimuli must elicit a response, equal to the sum of responses which would have been obtained from independently acting terms of the stimuli sequence.

$$\hat{\Xi}\Big[\sum_{n=1}^{\infty} f(t-\tau_n)\Big]_{-\infty}^{t} = \sum_{n=1}^{\infty} \hat{\Xi}[f(t-\tau_n)]_{-\infty}^{t} \tag{2.8}$$

where $t-\tau$ is the elapsed time. This symbolic notation emphasizes that the stimuli may be imposed at different times and that the shift of the stimulus along the time scale result in a corresponding shift of the response without changing it in any other way. In spite of the fact that with proper interpretation of the stimuli the equation (2.7) follows from (2.8), these two conditions are to be carefully distinguished for the linear viscoelastic behaviour. General differential equations with constant coefficients and convolution-based integral equations satisfy the above conditions of linearity.

Differential representation The most general equation of this type linking the time dependent stress and strain can be written in the form

$$\sum_{n=0}^{\infty} u_n \frac{d^n \sigma}{dt^n} = \sum_{m=0}^{\infty} q_m \frac{d^m \epsilon}{dt^m} \tag{2.9}$$

where u_n and q_m are the constant coefficients, not all of which has to be non-zero and summation has not to be infinite. Together with suitable initial conditions this equation describes the time-dependent (linear viscoelastic) behaviour of a material subjected to an infinitesimally small shear deformation. The set of parameters $\{q_m,u_n\}$ in this equation can be related to a rheological model (will be introduced later in sec. 2.1.5).

To analyse such an equation we need to specify the suitable type of the initial conditions with accordance to the experimental definition of the **reference state** of the material under consideration. Commonly, there are two types of materials:

arrheodictic: Such materials have a preferred configuration, so we can consider the state in which the material is at $t = 0$ to be a reference state. In the reference state the material is free from the effects of any stress or strain history it might have experienced prior to $t = 0$.

rheodictic: Such materials do not have a preferred configuration and it does not make sense to speak of about an undeformed state. Experiments with such material have to be arranged so that the material may be considered to be completely in rest for times before $t = 0$, so that the strain at $t = 0$ can still be taken as the reference state.

Using the Laplace transform After the initial conditions are clarified, one can choose the strain at $t = 0$ to be the reference strain and enjoy the simplicity of analysis of the equation (2.9) in terms of the operator calculus, i.e. it terms of Laplace integral transform (see fig 2.1).
For convenience we give here the definition of the Laplace transform. For a real-valued function $f(t)$ the integral transformation

$$\bar{f}(t) \;=\; \int_0^\infty f(t)\, e^{-st} dt \;=\; \hat{LT}\left[f(t)\right] \tag{2.10}$$

is called Laplace transform of $f(t)$, if the integral in the above expression exists. The Laplace transform variable, s, is in general complex, i.e. $s = q + i\omega$. For inverse Laplace transform $\hat{LT}^{-1}\bar{f}$ is used. Sometimes, we will use expressions like $f(t) \doteq \bar{f}(s)$ to denote the relation between a function and its Laplace image.
Indeed, applying the Laplace transform to the equation (2.9) we get the simple algebraic equation in the complex domain (Laplace plane). This can be manipulated algebraically with the result re-transformed back into the time domain, where the result can be compared with measured values. Indeed, with zeros initial conditions (i.e. function together with its derivations are zero at $t = 0$) the application of the Laplace transform yields the simple relation:

$$\bar{u}(s)\,\bar{\sigma}(s) \;=\; \bar{q}(s)\,\bar{\epsilon}(s) \tag{2.11}$$

where $\bar{\sigma}(s)$ and $\bar{\epsilon}(s)$ are the stress and strain transforms, respectively, and

$$\bar{u}(s) = \sum_n u_n s^n \quad \text{and} \quad \bar{q}(s) = \sum_m q_m s^m \tag{2.12}$$

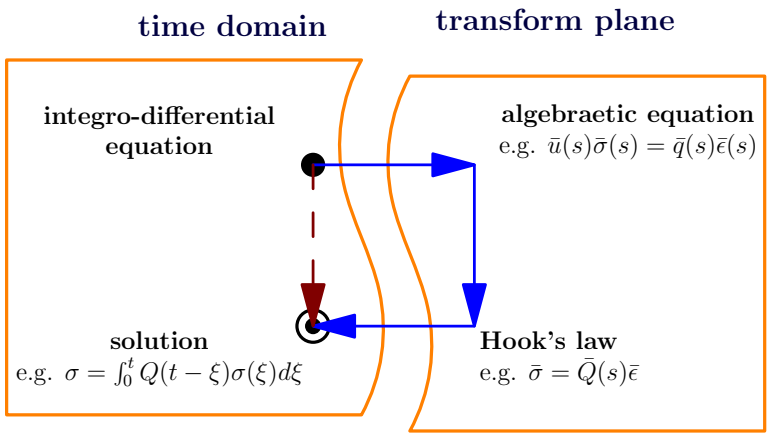

Figure 2.1.: **Diagram representation of the solution route**
A linear integro-differential equation can be solved through the Laplace transform, using transformation rules for differential and integral relations $\hat{LT}\left[\frac{d^n}{dt^n}\right] = s^n$ and $\hat{LT}\left[\int_0^t f(t)dt\right] = 1/s$. The red, dashed arrow represents the direct (difficult) way, the blue arrows represent the way through the transform plane. Instead of this integral in the solution one can often use the tables of the Laplace transform to get the solution in the analytical form.

are polynomials in the transform variable s.
Division of the equation (2.11) by the polynomial $\bar{u}(s)$ or $\bar{q}(s)$ yields:

$$\bar{\sigma}(s) \;=\; \bar{Q}(s)\,\bar{\epsilon}(s) \quad \text{or} \quad \bar{\epsilon}(s) \;=\; \bar{U}(s)\,\bar{\sigma}(s) \tag{2.13}$$

where the rational functions $\bar{Q}(s)$, $\bar{U}(s)$ are defined as

$$\bar{Q}(s) \;=\; \frac{\bar{q}(s)}{\bar{u}(s)} \quad \text{or} \quad \bar{U}(s) \;=\; \frac{\bar{u}(s)}{\bar{q}(s)}. \tag{2.14}$$

The (rational) functions $\bar{Q}(s)$ and $\bar{U}(s)$ are often called *operational relaxance* and *retardance*, respectively. Or, in common, they are termed as *respondances*. It can be shown that they describe a response to the impulse (Dirac δ-function formed) stimulus and, therefore, their time domain images can play the role of the Green's function.

Integral representation The Laplace inverse-transform of the equations (2.13) yields the *Boltzmann superposition principle* stated in terms of *Boltzmann superposition integrals*

$$\sigma(t) \;=\; \int_0^t Q(t-\tau)\,\epsilon(\tau)\,d\tau \quad \text{and} \quad \epsilon(t) \;=\; \int_0^t U(t-\tau)\,\sigma(\tau)\,d\tau \tag{2.15}$$

This can be read as follows: the response (stress or strain) at a current time t to a stimulus (strain or stress) history is a linear superposition of the all the stimuli applied at all previous times τ, multiplied by the weighting function ($Q(t)$ or $U(t)$). The latter represent the material response functions and are termed *(characteristic) material functions*. Sometimes they are called *memory* functions.
The equations (2.13) can be viewed as the viscoelastic forms of Hooke's law in the transform plane. They give rise of the reciprocal relation between respondances:

$$\bar{Q}(s)\,\bar{U}(s) \;=\; 1 \tag{2.16}$$

which in the time domain takes the following form

$$\int_0^t Q(t-\xi)U(\xi)d\xi \;=\; \int_0^t Q(\xi)U(t-\xi)d\xi \;=\; \delta(t) \tag{2.17}$$

2.1.3. Excitation/response in transform plane

Here, we define, for convenience, some conceptual terms (such as relaxation modulus, creep compliance) we will use to analysis our experimental results. Additionally, we describe the form and properties of the excitations used in our stretching experiments.

The behaviour of a viscoelastic material will depend of the kind of the time dependence of the excitation chosen to elicit the response. In an idealized situation the knowledge of the response to an excitation with some form of time dependence over the whole time domain will completely determine the materials behaviour. Hence, at least theoretically, any linear response of the material can be converted into any other. Practically, the choice of the excitation form for the purpose of determining material properties is based on the criterion of the experimental or theoretical simplicity. But, there are some practical criteria, e.g. the time domain coverage possible: the step excitation allows linear viscoelastic behaviour to be determined over about 1.5-4.5 log-decades of time. For larger time spans one can choose a combination of the step and harmonic excitation. The so-called non-standard excitations like slope, tooth or similar are often convenient to use in the *in situ* experiments or to cover a large range of time or frequency domains.

Impulse response: relaxance $Q(t)$ and retardance $U(t)$ Impulse response is defined through the Dirac delta-function and has only analytical importance. Consider the excita-

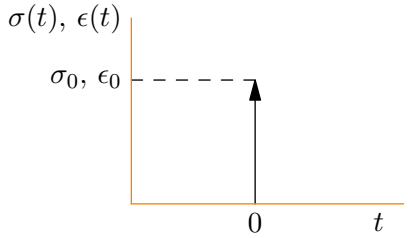

Figure 2.2.: **Impulse excitation**

Shows impulse excitation for stress (of strength σ_0) or strain (of strength ϵ_0). The arrow denotes (symbolically) the impulse.

tion be an impulse strain of strength ϵ_0 applied at $t = 0$ (see fig. 2.2). The strain excitation can be written as

$$\epsilon(t) \;=\; \epsilon_0\, \delta(t)$$

Laplace transform of this function yields constant

$$\bar{\epsilon}(s) \;=\; \epsilon_0$$

and using the equation of the viscoelastic Hooke's law (2.13) we obtain the operational *relaxance*

$$\bar{Q}(s) = \bar{\sigma}(s)/\epsilon_0.$$

Similar manipulations follow us to the operational *retardance*

$$\bar{U}(s) = \bar{\epsilon}(s)/\sigma_0.$$

The meaning of this functions is:

relaxance, $Q(t)$: is the response to the unit impulse of strain,

retardance, $U(t)$: is the response to the unit impulse of stress.

Because any excitation can be represented as superposition of Dirac δ functions

$$\sigma(t) = \int_0^\infty \delta(t-\xi)\sigma(\xi)d\xi \quad \text{or} \quad \epsilon(t) = \int_0^\infty \delta(t-\xi)\epsilon(\xi)d\xi$$

it can be shown that Boltzmann superposition principle can be written in terms of impulse respondances as

$$\epsilon(t) = \int_0^t U(t-\xi)\sigma(\xi)d\xi \quad \text{or} \quad \sigma(t) = \int_0^t Q(t-\xi)\epsilon(\xi)d\xi$$

Step response: relaxation modulus $G(t)$ **and creep compliance** $J(t)$ This is the most widely used form of excitation and can be mathematically described though the unit step (Heaviside) function (see fig. 2.3):

$$h(t) = \begin{cases} 0 & : \quad t \leqslant 0 \\ 1 & : \quad t > 0 \end{cases} \tag{2.18}$$

with properties

$$\frac{d}{dt}h(t) = \delta(t) \quad \text{and} \quad h(t) \doteqdot s^{-1} \tag{2.19}$$

where the symbol $\doteqdot$ denotes the relation of a function to its Laplace image.
So, e.g., the strain step function of strength ϵ_0 can be written as

$$\epsilon(t) = \epsilon_0 h(t). \tag{2.20}$$

Although this is a mathematical abstraction and is not realizable experimentally, one can approximate it very closely with suitable experimental setup.
With respect to a step stimulus one defines following terms:

relaxation modulus, $G(t)$: is a material response to a unit step of strain excitation, i.e. it is a gradual decrease of stress when the material is held at constant strain.

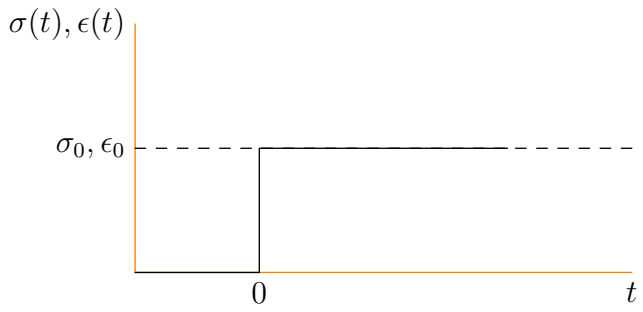

Figure 2.3.: **Step excitation**

Shows step excitation for stress (of strength σ_0) or strain (of strength ϵ_0).

creep compliance, $J(t)$: is a material response to a unit step of stress excitation, i.e. it is a slow, progressive deformation of a material under constant stress.

Substitution of the Laplace transform of (2.20) (i.e. $\epsilon(t) \div \epsilon_0/s$) into the viscoelastic Hooke's law and the inverse transformation into the time domain will give

$$\bar{\sigma}(s) = \epsilon_0 \frac{\bar{Q}(s)}{s} \qquad \Longrightarrow \qquad \sigma(t) = \epsilon_0 \hat{LT}^{-1}\left[\frac{\bar{Q}(s)}{s}\right]. \tag{2.21}$$

Since the inverse transform of the $\bar{Q}(s)/s$ has the dimension of a modulus the transform of the stress response to the unit strain step excitation

$$\bar{G}(s) = \frac{\bar{Q}(s)}{s} \tag{2.22}$$

it is called transformed modulus and its re-transform $G(t)$ is termed as *relaxation modulus*, i.e.

$$G(t) \;=\; \frac{\sigma(t)}{\epsilon_0} \;=\; \hat{LT}^{-1}\left[\frac{\bar{Q}(s)}{s}\right] \;=\; \int_0^t Q(\xi)d\xi. \tag{2.23}$$

Here, $\sigma(t)$ is the material response to the step of strain stimulus (e.g. as it measured in experiment), $Q(t)$ is the relaxance (i.e. response to the unit impulse of strain).
Similarly, we can introduce the *creep compliance* $J(t)$ as the material response to the unit step of stress excitation, which transform is

$$\bar{J}(s) = \frac{\bar{U}(s)}{s} \tag{2.24}$$

and in analogy with (2.23)

$$J(t) \;=\; \frac{\epsilon(t)}{\sigma_0} \;=\; \hat{LT}^{-1}\left[\frac{\bar{U}(s)}{s}\right] \;=\; \int_0^t U(\xi)d\xi \tag{2.25}$$

here $\epsilon(t)$ is the material response to the step of stress stimulus (e.g. as it measured in experiment), $U(t)$ is the retardance (i.e. response to the unit impulse of stress).

The relation to the relaxance and retardance follow from the re-transformation of $\bar{Q}(s) = s\bar{G}(s)$ and $\bar{U}(s) = s\bar{J}(s)$ (cf. (2.22, 2.24))

$$\begin{aligned} Q(t) &= \frac{dG(t)}{dt} + G(0)\delta(t) \\ U(t) &= \frac{dJ(t)}{dt} + J(0)\delta(t). \end{aligned}$$

Here the delta function is due to initial conditions and $G(0), J(0)$ are values of the $G(t), J(t)$ at $t = 0$. In the tradition of the polymer rheology these values are termed as *glassy modulus* and *glassy compliance* and denoted G_g, J_g, respectively.
For an arbitrary excitation form the viscoelastic Hooke's law takes in terms of the step response function the following form

$$\bar{\sigma}(s) = s\bar{G}(s)\bar{\epsilon}(s) \qquad \text{and} \qquad \bar{\epsilon}(s) = s\bar{U}(s)\bar{\sigma}(s), \tag{2.26}$$

which in the time domain can be written as

$$\sigma(t) = \begin{cases} G_g\epsilon(t) + \int_0^t \epsilon(t-\xi)\, d\, G(\xi) \\ \int_0^t G(t-\xi)\, d\, \epsilon(\xi) \end{cases} \tag{2.27}$$

for the response to a strain excitation $\epsilon(t)$ and

$$\epsilon(t) = \begin{cases} J_g\epsilon(t) + \int_0^t \sigma(t-\xi)\, d\, J(\xi) \\ \int_0^t J(t-\xi)\, d\, \sigma(\xi) \end{cases} \tag{2.28}$$

for the response to a stress excitation $\sigma(t)$.

Slope response: generalized viscosity $\eta(t)$ This excitation can be called constant rate of strain (stress) excitation, because it consists in the imposition of a strain or a stress at a constant rate (see fig.2.4). This can be described in terms of unit slope function:

$$p(t) = t\, h(t) \tag{2.29}$$

where $h(t)$ is the unit step function (2.19). The use of the $h(t)$ here is due to the initial conditions. Let us denote a value of a constant rate of stress by $\dot{\sigma}_0$ and a value of a constant rate of strain by $\dot{\sigma}_0$. A constant rate of strain excitation imposed at $t = 0$ can be written as

$$\epsilon(t) = \dot{\epsilon}_0 p(t) = \dot{\epsilon}_0 t, \qquad (t \geqslant 0) \tag{2.30}$$

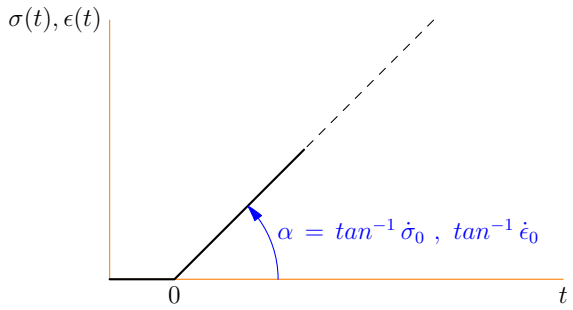

Figure 2.4.: **Slope excitation**

Shows slope excitation for stress (with rate $\dot{\sigma}_0$) or strain (with rate $\dot{\epsilon}_0$).

Following the same scheme as in the paragraphs above, one can introduce the *generalized viscosity* as material response to the stress excitation with unit rate. In the time domain

$$\eta(t) = \frac{\sigma(t)}{\dot{\epsilon}_0} = \int_0^t G(\xi)d\xi = \int_0^t \int_0^{t_1} Q(\xi)d\xi dt_1 \tag{2.31}$$

where $\sigma(t)$ is a response to the strain excitation with constant rate $\dot{\epsilon}_0$ (as it can be measured), $G(t)$ is relaxation modulus and $Q(t)$ is the relaxance.
In the transform plane one get

$$\bar{\eta}(s) \equiv \hat{LT}\left[\eta(t)\right] = \frac{\bar{Q}(s)}{s^2} = \frac{\bar{G}(s)}{s} \tag{2.32}$$

Analogously, one can introduce the response to the unit constant stress rate excitation $\chi(t)$, with similar relations as above.

2.1.4. Stimuli catalogue

For convenience, we will give a short description of strain excitations which are of relevance for our experiments and theoretical considerations.

Table 2.1.: **Stimuli catalogue**

A short description of used strain excitations.

step excitation: The strain is suddenly raised to some height h (ϵ_0), where it is held constant.

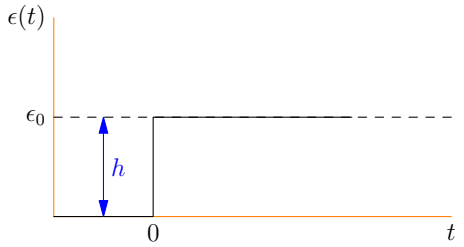

slope excitation: Stretching with a constant rate of strain (velocity) $\dot{\epsilon}_0$.

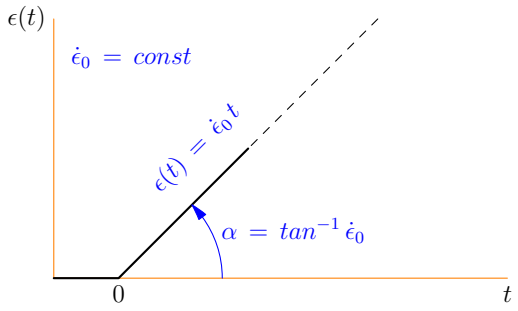

ramp excitation: Applying the slope excitation up to some point t_{turn}. After this the strain is held constant.

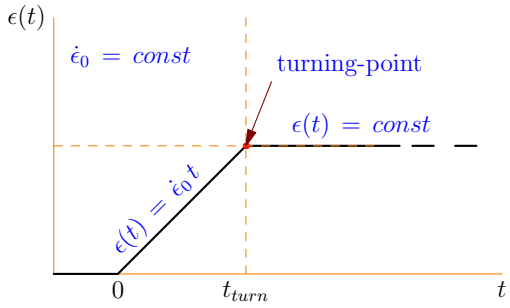

tooth excitation: Consists of two slopes: an increasing one (with positive velocity) and decreasing slope (with negative velocity).

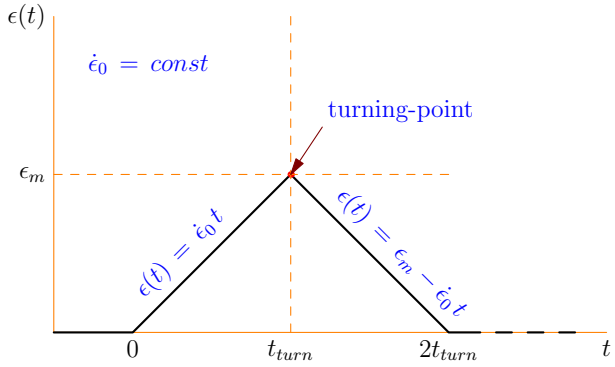

cyclic tooth excitation: Sequential application of a tooth excitation.

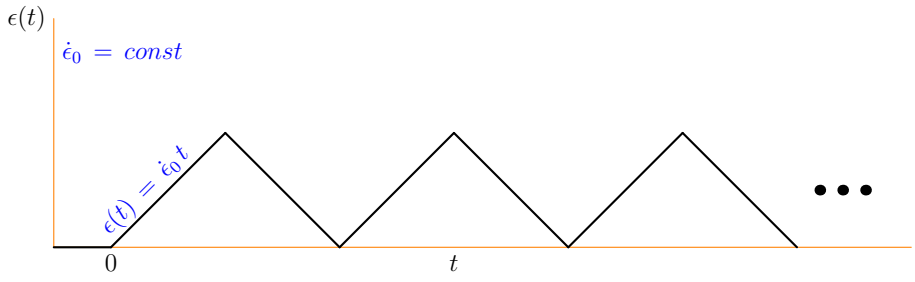

2.1.5. Model representation of linear viscoelastic behaviour

Viscoelastic materials can be modeled in order to determine their stress or strain response to an arbitrary stimulus. In the direct analogy with the electric circuit theory the underlying physical system is replaced by idealized counterparts of its actual constitutive elements. The interconnection of these elements is shown in graphical form to facilitate the analysis of the system. The most familiar examples of such elements are *spring*, where energy is stored potentially, and the *dashpot* (or dumper), in which energy is dissipated as heat. (See fig. 2.5(c,d)). The spring is assumed to be a Hookean spring and dashpot a Newtonian dashpot. The response of the spring is defined to be purely elastic (i.e. no energy is dissipated in it and its mass is zero), similary the response of dashpot is purely viscous (i.e. it is rigid and its mass is again negligible). The stress and strain are also represented as by a two-terminal elements as shown in fig.2.5(a,b). The two-terminal nature of stress (force) is in accord with Newtonian's law of action and reaction. One has to take into account not only the point of application of the force (stress), but also the point of reaction. To represent the relation between stress and strain in a linear system one shell formulate them in the transform plane. For example, denoting the stress transform by $\bar{\sigma}$ and stress transform by

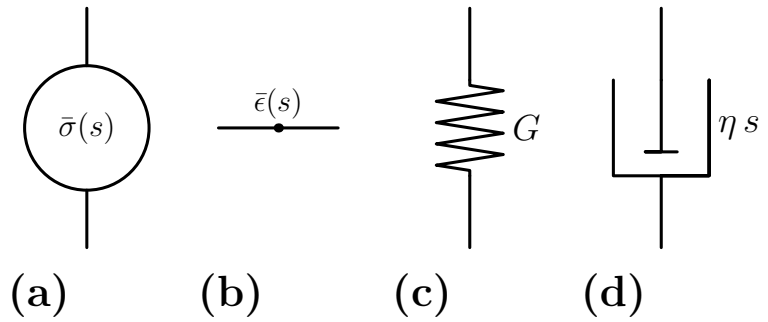

Figure 2.5.: **Usual symbols for viscoelastic model diagrams**
(**a**) stress, (**b**) strain or strain rate, (**c**) spring, (**d**) dashpot

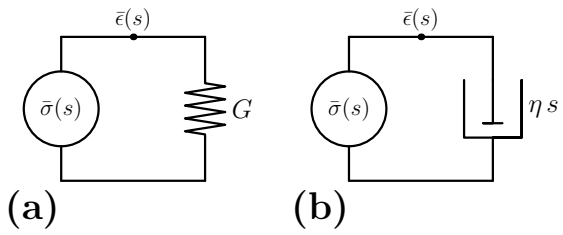

Figure 2.6.: **Systems with purely (a) elastic and (b) viscouse response**

$\bar{\epsilon}$ we can describe the potential energy storage by

$$\bar{\sigma}(s) = G\bar{\epsilon}(s)$$

and energy dissipation by

$$\bar{\sigma}(s) = \eta s\bar{\epsilon}(s) = \eta\dot{\bar{\epsilon}}(s).$$

The graphical representation of this expressions are shown in fig. 2.6.
The connection between a constitutive equation and its diagram representation is based on the generalized d'Alambert's principle and combination rules. The d'Alambert's principle can be formulated as follows: at any node in the diagram the impressed instantaneous stress equals the product of the instantaneous node displacement (strain) and node relaxance. The definition of the node relaxance is govern by the combination rules: relaxances add in parallel, retardances add in series. The combination rules follow from the additivity of forces in a parallel combination of passive elements and from the additivity of the displacements in series combinations.

Elementary respondances In the example above (fig. 2.6) we can identify the relaxance, $\bar{Q}(s)$ for purely elastic system is G (modulus) and ηs for purely viscous. G and η are the parameters of the model. Similarly, one can use J and ϕ. The table 2.2 shows the connection between the model parameters and respondances.

Table 2.2.: **Elementary respondances**

Model parameter	Operational respondance	Harmonic respondance
G	G	G
J	J	J
η	$\eta\, s$	$i\omega\eta$
ϕ	ϕ/s	$\phi/(i\omega)$

Model units

There are two possibilities to combine a spring and a dashpot into a one system unit: parallel and serial combination. The parallel combination is commonly referred to as a Voigt model unit and the serial is referred to as a Maxwell model unit. This combinations does not represent viscoelastic behaviour adequately, but are an important building blocks in other, more complex models.

Voigt unit The fig. 2.7 shows the mechanical representation of the Voigt model unit, which is a parallel combination of the a sprint and a dashpot.

Following the combination rules we obtain the the relaxance of the system in the following

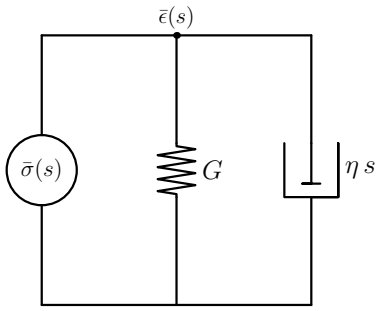

Figure 2.7.: **The Voigt model unit**

form:

$$\bar{Q}(s) \;=\; G \;+\; \eta s \tag{2.33}$$

and hence

$$\bar{\sigma}(s) = (G + \eta s)\ \bar{\epsilon}(s). \tag{2.34}$$

This leads to the differential equation:

$$\sigma(t) = G\epsilon(t) + \eta\dot{\epsilon}(t). \tag{2.35}$$

The retardance takes following form:

$$\bar{U}_V(s) = \frac{J}{1 + \tau_V s} \tag{2.36}$$

where τ_V is the retardation time and is defined through

$$\tau_V = J/\phi = \eta/G \tag{2.37}$$

with $\phi = 1/\eta$.

Maxwell unit This is the second most simple model. It is a serial combination of a spring and dashpot (see fig.2.8) Following combination rules one get a retardance in the form:

$$\bar{U}(s) = J + \phi/s \tag{2.38}$$

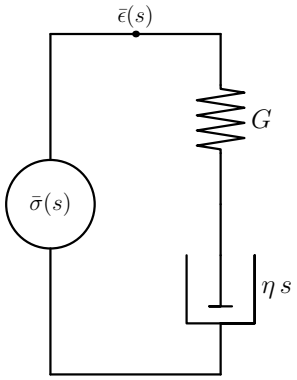

Figure 2.8.: **The Maxwell model unit**

where $J = 1/G$ and $\phi = 1/\eta$. Then for arbitrary stress excitation $\sigma(t)$:

$$\bar{\epsilon}(s) = (J + \phi/s)\ \bar{\sigma}(s) \tag{2.39}$$

which leads to the differential equation

$$\epsilon(s) = J\,\sigma(t) + \phi\,\dot{\sigma}(t) = \frac{1}{\eta}\sigma(t) + \frac{1}{G}\dot{\sigma}(t) \tag{2.40}$$

Writing the relaxation time as

$$\tau_M = \eta/G \tag{2.41}$$

the relaxance of the Maxwell unit become

$$\bar{Q}_M(s) = G\frac{\tau_M s}{1 + \tau_M s}. \tag{2.42}$$

Series-parallel models of viscoelastic body

The Voigt and Maxwell units alone cannot represent viscoelastic behaviour adequately. Because the Maxwell unit does not represent strain retardation and Voigt unit can not represent the stress relaxation. This is the reason that this constructions are called units rather than models [168]. To overcome this drawback the combination of them is used to model of a viscoelastic behaviour. The minimal of such models mast have at least 3-elements to describe the solid-like behaviour and 4-elements to describe the liquid-like behaviour.

The models of the Standard Linear Solid The 3-parameter models are constructed by adding a spring to a Voigt unit in series or to a Maxwell unit in parallel. The diagrams

of them are shown in figure 2.9, and figure 2.10 shows how they respond to a step of stress and strain.
Both models from the diagrams shown in 2.9 can be represented with an differential equation of the form
or more exactly as a tree parameters equation 2.6, which we reproduce here, for convenience:

$$\sigma(t) + a\,\frac{d\sigma}{dt} = b\,\epsilon(t) + c\,\frac{d\epsilon}{dt} \tag{2.43}$$

where parameters a,b,c are defined in terms of G,Ge,η for Maxwell model and in term of Jg,J,ϕ for the Voigt model.
The retardance of the Voigt model is:

$$\bar{U}_{3V}(s) = J_g + \frac{J}{1+\tau s} \tag{2.44}$$

where J_g, J, ϕ are operational retardances, $\tau_v = J/\phi$ is retardation time. This give us the response to a step of strain:

$$\epsilon(t)/\sigma_0 = J_g + J\left(1 - e^{-\frac{t}{\tau}}\right) \tag{2.45}$$

The model describes the response to a constant stress with a sudden strain of magnitude $\epsilon_0 = J_g\sigma_0$ followed by a delayed strain which reaches an equilibrium strain $\epsilon_e = \epsilon_0 + \epsilon = J_e\sigma_0$ at infinity, see figure 2.10. Using the relation $U(s)Q(s) = 1$ one get the relaxance of the Voigt model:

$$\bar{Q}_{3V}(s) = \frac{1+\tau s}{J_e + J_g\tau s} \tag{2.46}$$

and the response to a unit step of strain is:

$$\sigma(t) = \sigma_e + \sigma e^{-\frac{t}{\tau'}} \tag{2.47}$$

where $\tau' = J_g\tau/J_e$, $\sigma_e = \epsilon_0/J_g$ and $\sigma = 1/J_e - 1/J_g$. The models responds to a unit step of strain with an initial stress $\sigma_0 \equiv \sigma(0) = \epsilon_0/J_g$ and relaxes to an equilibrium value σ_e.
The relaxance of the Maxwell model is:

$$\bar{Q}_{3M}(s) = G_e + G\frac{J}{1+\tau s} \tag{2.48}$$

where G_e, G, τ are parameters of the model, with τ defined as η/G.
For a step of strain of height ϵ_0 we find:

$$\sigma(t) = \epsilon_0\left(G_e + Ge^{-\frac{t}{\tau}}\right) = \sigma_e + \sigma e^{-\frac{t}{\tau}} \tag{2.49}$$

The model possesses an instantaneous modulus $G_g = G_e + G$ and shows the same behaviour as Voigt model above.
The retardance of the model is:

$$\bar{U}_{3M}(s) = \frac{1 + \tau s}{G_e + G_g \tau s} \tag{2.50}$$

and its response to a step of stress of height σ_0 takes the form:

$$\epsilon(t) = \sigma_0 \left(\frac{1}{G_g} + \frac{G_g - G_e}{G_g G_e} (1 - e^{-\frac{t}{\tau}}) \right) = \epsilon_0 + \epsilon (1 - e^{-\frac{t}{\tau}}) \tag{2.51}$$

Therefore, the model responds to a step of stress with an initial strain $\epsilon_0 = \sigma_0 / G_g$ and then increases stress up to equilibrium value $\epsilon_e = \sigma_0 / G$.
The both models are conjugate in the sense that Voigt and Maxwell responds identically to the same excitation with a proper choice of values for model parameters. The Voigt model is more suitable to study the response to a excitation in stress and Maxwell model to an excitation in strain.

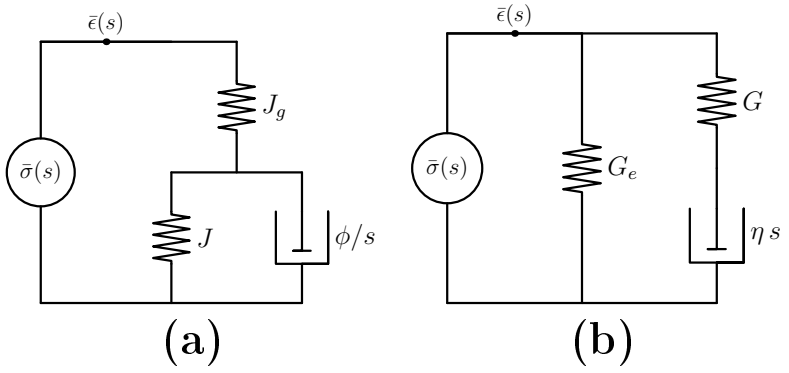

Figure 2.9.: **Models of the Standard Linear Solid**

The figure shows diagram representations of the Standard Linear Solid: Voidg (a) and Maxwell (b) model. These models are conjugate to each other because by the proper choice of their parameters they will show the same respond to the same exitation.

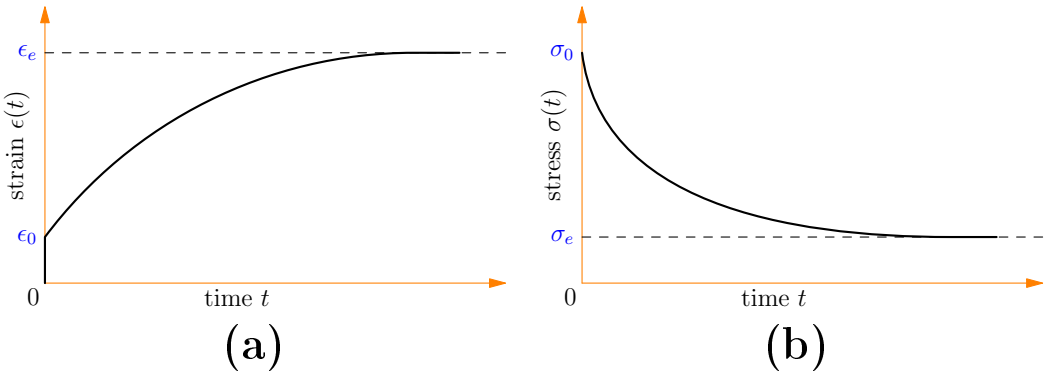

Figure 2.10.: **Responses of Standard 3-elements model to steps exitations**
(a) shows respnse to a step to stress and (b) to a step of strain

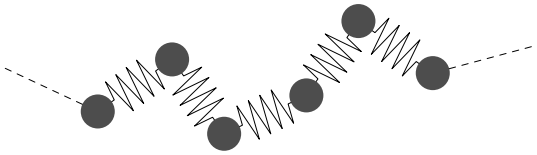

Figure 2.11.: **Bead-and-spring model of a linear polymer**

Rouse model

The Rouse model of linear polymers in fluids and its adaptation to polymer solids are most frequently used models in polymer physics [35]. Materials composed of flexible long-chain polymers usually show a large spectrum of respondance times. The long respondance times are due to cooperative motions required for long-chain moleculues to accomodate after an imposed stress or strain.
The Rouse theory [152] describes the macroscopic viscoelastic behaviour of a dilute solution of coiled polymer molecules immersed into a Newtonian fluid. The model assumes that the molecules are subjected to a random thermal force and a drag force. The ansatz is the same as in the Langevine description of a dynamical system coupled with a thermal bath, e.g. Brownian motion. Ferry and coworkers [36] adapt the Rouse theory to concentrated polymer solutions and polymer solids, composed of linear polymers without static crosslinking or with a low degree of crosslinking.
In the viscoelastic description a polymer molecule is viewed as a linear assembly of massless beads connected by Hookean springs. During deformation or recovery from a deformation the storage of energy is provided by this springs while, energy is dissipating due to the frictional forces caused by the interaction of the moving beads with their environment, see figure 2.11. The diagram representation is shown in figure 2.12. Such arrangements of viscoelastic elements are called ladder models [168]. If all springs and all dashpots are identical the diagramm represents a regular ladder model. For regular ladder models the computation of respondances is much easier. For example, in the Laplace plane the relaxance of the Rouse model takes the form:

$$\bar{Q}(s) = G \sum_{n=1}^{N} \frac{\tau_n \, s}{1 + \tau_n \, s}, \quad \tau_n = \tau_1 / n^2 \tag{2.52}$$

where N is the number of molecular units in the chain, τ_1 is the first relaxation time, which is a function of the model parameters: viscosity τ and elastic modulus G. Figure 2.13 shows the generalized modulus (response to the unit step) and generalized viscosity

(response to the unit slope) computed on the basis of the equation (2.52). With increasing of the number of molecular units N the behaviour convergs very fast to the assimptotic case $N = \infty$. E.g. the relaxation curves are nearly coinside for N $50, 100$ and 1000.
In the Rouse molecular theory τ_1 is expressed as function of steady-flow viscosities of the solution and solvent, temperature and the molecular number density. Also, parameters of the model have a clear physical meaning and are expressible through the measurable values.

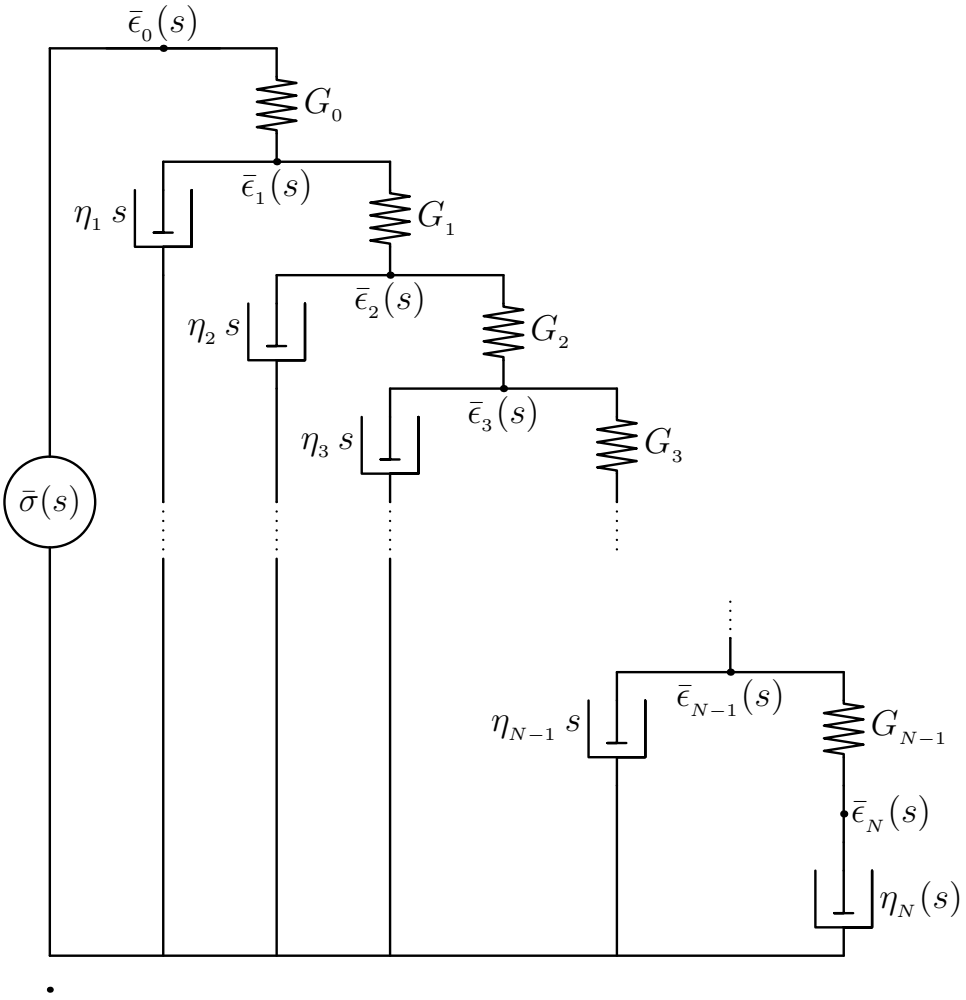

Figure 2.12.: **An example of a standard ladder model** [168]

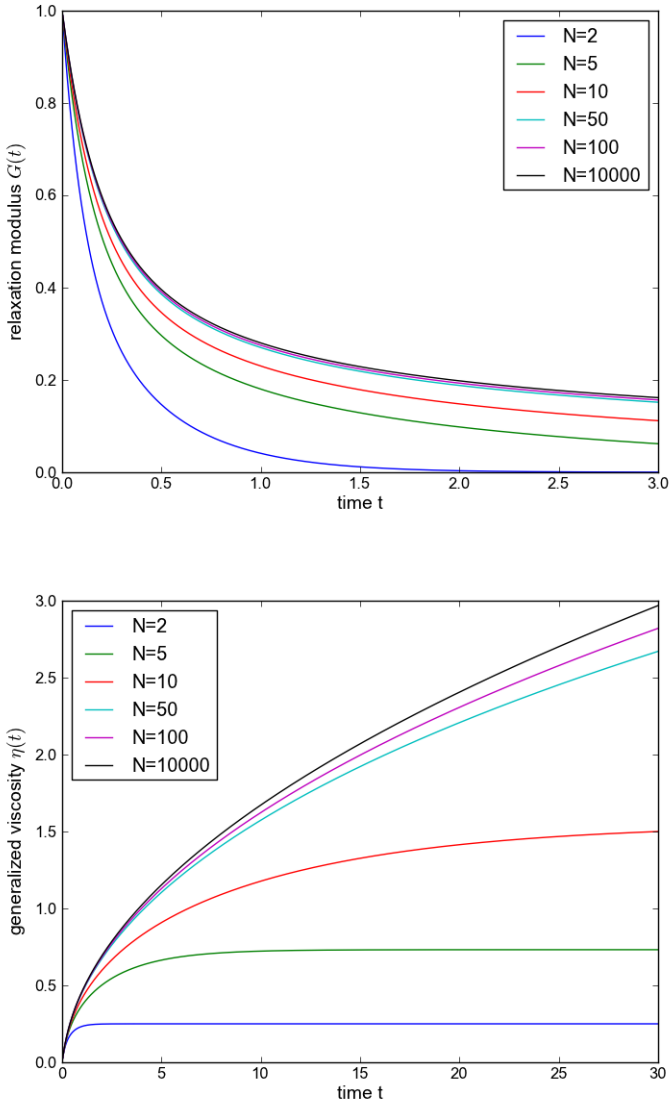

Figure 2.13.: **Responses of the Rouse model to standard excitations**
On the upper pane the relaxation modulus (response to the unit step) is shown and the lower pane shows the response to the unit slope excitation. The response is depicted for several values of relaxation units corresponding to the terms in eq. (2.52).
None the rapid convergence of the curves with respect to increasing of the number of the molecular units (viscoelastic elements) N. Especsially, the relaxation curves (upper pane) are nearly coinside for the $N \geqslant 50$.

2.2. Fractional Models

The linear viscoelastic models, outlined in ch. 2.1, describe a material behaviour in terms of arrangements of lossless elastic springs and lossy viscous dampers, i.e. dashpots. Such models provide a useful description of relaxation and creep for some viscoelastic materials with simple internal structures. However, for many complex materials, such as biological composites, they are not sufficiently accurate. Therefore, an extension of the viscoelastic theory in terms of the calculus of the derivative of fractional order [87] has been developed and successfully applied (see e.g. [105]). In this extension a new viscoelastic element relating stress and a "**fractional order derivative**" of strain is introduced. The models based on this extension allow [28]

- to describe viscoelastic processes over long time intervals by means of a simple relation with only few adjustable parameters.
- to model the experimentally measured non-Debye relaxation phenomena [109, 116]
- a phenomenological quantative description of the memory effects and effects of stochastic molecular motion on both a micro- and a mesoscopic level in viscoelastic processes [109].

In the following we will give a short outline of such models together with numerical methods we did use for fitting the experimental data.

2.2.1. Motivation

We start with a heuristic motivation for the fractional viscoelasticity. Then, after some short historical remarks, the formulation of the basic operators of the fractional calculus and a fractional extension of the standard solid model are provided.
In the following we show an intuitive introduction of a new viscoelastic element which allows to describe non-Debye relaxations and which is neither purely viscous nor elastic in its response but incorporates the property of dashpot and string as its limiting cases. For this purpose we will go through the "solution route", schematically depicted if the figure 2.1. The following relations between the time and Laplace domain will be used:

$$\begin{array}{c|c} \delta(t) \doteq 1 = s^0 & h(t) \doteq 1/s \\ \frac{d^n}{dt^n} f(t) \doteq s^n \bar{f}(s) \quad - \quad \sum_{k=0}^{n-1} f^{(k)}(0)\, s^{n-k-1} & \left(\int dt\right)^n f(t) \doteq 1/s^n \bar{f}(s) \end{array} \tag{2.53}$$

$$\text{convolution Theorem:} \qquad \int_0^t g(t-\xi)\, f(\xi) d\xi \doteq \bar{g}(s) \cdot \bar{f}(s)$$

where $\doteq$ relates an expression in the time domain to its Laplace image, $h(t)$ is the Heaviside step function (2.18), $\delta(t)$ denotes the Dirac delta function. $f(t), g(t)$ denote some functions of time, $f^{(k)}(0)$ denotes the kth derivative of $f(t)$ at $t = 0$ and $\bar{f}(s)$ is the Laplace transform of $f(t)$.

The two building blocks (elements) of linear viscoelastic models are the elastic spring and the viscous dashpot. The former is responsible for energy storage and the latter for energy dissipation. As was discussed in the previous section, both elements exhibit an instantaneous response to a perturbation. Usually, this is expressed as:

$$\begin{aligned} G_e \epsilon(t) &= \sigma(t), \\ \eta \frac{d\epsilon(t)}{dt} &= \sigma(t) \end{aligned} \tag{2.54}$$

where $\sigma(t)$ and $\epsilon(t)$ are time-dependent stress and strain functions, respectively. G_e is Young's modulus and η the coefficient of viscosity (see table 2.2).

A graphical representation of this elements is given in fig. 2.5. It sketches the relations (2.54) in the Laplace (operational) domain, namely:

$$\begin{aligned} G_e \, \bar{\epsilon}(s) &= \bar{\sigma}(s), \\ s \, \eta \, \bar{\epsilon}(s) &= \bar{\sigma}(s) \end{aligned} \tag{2.55}$$

where s is the variable in the operational plane, $\bar{\sigma}(s)$ and $\bar{\epsilon}(s)$ are Laplace images of the stress and the strain functions, respectively. To build a model which describes a material behaviour with more complex structure one usually arranges this elements in series-parallel connections. But such models inherit the drawback, common to these elements. They are inaccurate describing non-Debye relaxation phenomena and they cannot adequately describe a viscoelastic phenomenon with memory effects. To avoid this drawback in the frame of the classical viscoelastic theory one needs to use models with an infinite number of elemental units, e.g. Maxwell units. So, the large spectrum of relaxation times reflects a very large number of the damping mechanisms incorporated into the model. Such models usually require a large number of parameters for their specification.

Our motivation is to find an element which allows to include the whole spectrum of damping mechanisms from above into a model with a single internal variable.

Within linear response theory the behaviour of a system with memory effects is governed by a generalized susceptibility or memory function $\kappa_\alpha(t_1,t_2)$, e.g.:

$$\int_0^t \kappa_\alpha(t,\xi)\epsilon(\xi)d\xi = \sigma(t) \tag{2.56}$$

The response is now governed by the integral equation of the Volterra type with memory function $\kappa_\alpha(t,\xi)$ as kernel. This kernel $\kappa_\alpha(t,\xi)$ connects the response of the new element with its history and for time-shift invariant linear system it is of the convolution type, i.e. $\kappa_\alpha(t,\xi) = \kappa_\alpha(t-\xi)$, i.e. it is a function of only one variable. The subscript α symbolically represents a possible parameters specifying the kernel. The energy now will neither be completely stored nor completely dissipated in one element. For the kernel of the convolution type the relation (2.56) takes a simple form in the Laplace domain:

$$\bar{\kappa}_\alpha(s)\bar{\epsilon}(s) = \bar{\sigma}(s) \tag{2.57}$$

To incorporate the behaviour of the spring and dashpot elements into this terminology we can write:

$$\begin{aligned} G_e \int_0^t \delta(t-\xi)\epsilon(\xi)d\xi &= \sigma(t) \\ \eta \int_0^t \delta^{(1)}(t-\xi)\epsilon(\xi)d\xi &= \sigma(t) \end{aligned} \tag{2.58}$$

where $\delta(t), \delta^{(1)}(t)$ are the Dirac delta function and its first derivative, respectively. The former plays the role of $\kappa_\alpha(t)$ in the case of purely elastic response (spring) and the latter in the case of purely viscous response (dashpot). Of course, the Laplace image of this relations remains unchanged, see equation (2.55).
A comparison of the stress-strain relations (2.55) shows that the simplest response function of our element would take in the Laplace domain the following form:

$$s^\alpha \bar{\epsilon}(s) \sim \bar{\sigma}(s), \qquad \text{i.e.} \quad \bar{\kappa}_\alpha(s) \equiv s^\alpha \tag{2.59}$$

Up to the multiplicity constants G_e, η, this relation reduces to the Hooke's law if $\alpha = 0$ and to the dashpot behaviour if $\alpha = 1$. Generally, for any integer α the relation $s^\alpha\bar{\epsilon}(s)$ takes the form of the usual derivative in the time domain (here we assume zero initial conditions):

$$s^\alpha \bar{\epsilon}(s) \doteq \frac{d^\alpha}{dt^\alpha}\epsilon(t), \quad \alpha \in \mathbb{N} \tag{2.60}$$

where, as before, we use the symbol $\doteq$ to represent the relation between a function in the time domain and its Laplace image.
For a negative power function $\kappa_\alpha(s) = 1/s^\alpha$ (with real $\alpha > 0$) as kernel, we can use the Laplace transform pair:

$$\frac{t^{\alpha-1}}{\Gamma(\alpha)} \doteq \frac{1}{s^\alpha} \tag{2.61}$$

where $\Gamma(t)$ is the Euler gamma function.
Due to the convolution theorem and (2.61), the relation (2.59) will take for the kernel $\kappa_\alpha(s) = 1/s^\alpha$ following form in the time domain:

$$\frac{1}{\Gamma(\alpha)} \int_0^t (t-\xi)^{\alpha-1} \epsilon(\xi) = \sigma(t) \tag{2.62}$$

For the integer α (i.e. $\alpha = n > 0$, $n \in \mathbb{N}$) the left hand expression has the meaning of an n-fold (repeated) integration (see e.g. [26]):

$$\overbrace{\int_a^t dt_1 \int_a^{t_1} dt_2 \ldots \int_a^{t_{n-1}}}^{n-\text{times}} dt_n \, \epsilon(t_n) \quad \doteq \quad \frac{1}{s^n} \quad \doteq \quad \frac{1}{(n-1)!} \int_0^t (t-\xi)^{n-1} \epsilon(\xi) d\xi \tag{2.63}$$

where the relation between the expressions on the left hand side and on the right hand side is the famous Cauchy formula reducing the n-fold integration to a single integration of the convolution type. In the right hand expression we did use the relation $\Gamma(n+1) = n!$ for integer n.

At this stage we can write down the relation (2.59) in the time domain for the new viscoelastic element for two classes of the Laplace image of the elements kernel $\bar{\kappa}_\alpha(s)$: (i) $\bar{\kappa}_\alpha(s) = 1/s^\alpha$ for all real $\alpha > 0$ (see equation (2.62)) and (ii) $\bar{\kappa}_\alpha(s) = s^\alpha$ only for integer $\alpha \in \mathbb{N}$ (see equation (2.60)).
In order to know the form of the relation (2.59) in the time domain (for any real α) it remains to cover the set of strictly non integer positive $\alpha \notin \mathbb{N}, \alpha > 0$. For this purpose we rewrite the equation (2.59) for non-integer α, say $n-1 < \alpha < n$ ($n \in \mathbb{N}$), as

$$s^n \frac{1}{s^\nu} \bar{\epsilon}(s) = \bar{\sigma}(s), \quad \nu = n - \alpha, \quad 0 < \nu < 1 \tag{2.64}$$

Now we can interpret the term s^n as differentiation in the time domain and use the Laplace transform pair for the power function (2.61) for the $1/s^\nu$ term. The result is:

$$\frac{1}{\Gamma(n-\alpha)} \frac{d^n}{dt^n} \int_0^t (t-\xi)^{n-\alpha-1} \epsilon(\xi) = \sigma(t), \alpha > 0 \tag{2.65}$$

This is the stress-strain relation for our new element.
For the range $0 < \alpha < 1$, which is solely of importance for the viscoelastic models, this element obeys the simpler relation:

$$\frac{1}{\Gamma(1-\alpha)} \frac{d}{dt} \int_0^t (t-\xi)^{-\alpha} \epsilon(\xi) = \sigma(t) \tag{2.66}$$

For $\alpha = 0$ equation (2.66) exhibits the Hooke's law and for $\alpha = 1$ its behaviour is equivalent to that of the dashpot.
It can be shown by direct computation that in the intermediate range $0 < \alpha < 1$ the new element exhibits a power relaxation (as response to a step strain excitation):

$$\sigma(t) = \frac{t^{-\alpha}}{\Gamma(1-\alpha)} \tag{2.67}$$

reported for many complex materials [105], e.g. long-chain polymers. Bagley shows [6] that for the $\alpha = 1/2$ the new element describes the behaviour of the Rouse model (see page 38) with a very large number of molecular units, this is demonstrated in figure 2.14.

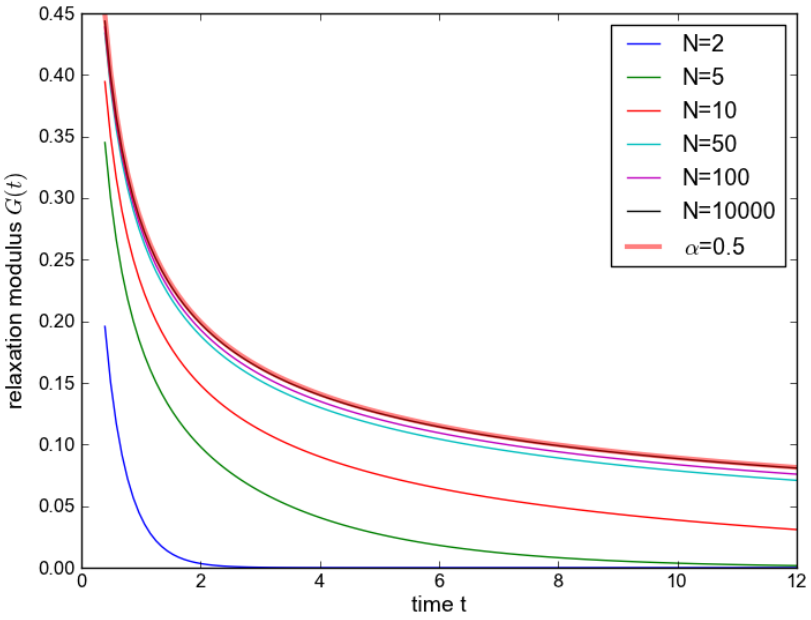

Figure 2.14.: **The fractional 'dashpot' as limiting case of the Rouse model**
A relaxation modulus (response to the unit step) of the Rouse model for several values of the molecular units number N (thin coloured lines) and of the fractional viscoelastic element for the $\alpha = 1/2$ (thick red line) is shown. With increasing of N the response of the Rouse model approaches the behaviour of the fractional element and for $N \sim 100$ and larger the relaxation curves almost coincide. This example shows how a single fractional element describes the whole spectrum of damping mechanisms otherwise modelled by a large number of the 'classical' viscoelastic elements.

The comparison of the equations (2.60, 2.63) for the integer values of the parameter α

in the Laplace images of the forms s^α and $1/s^\alpha$, respectively, with the equations (2.65, 2.62) for the non integer α shows the similarity between the n-fold differentiation and integration to their non integer counterparts (2.65, 2.62). Actually, the right hand parts of the equations (2.65, 2.62) represent the so-called fractional derivative and integration of Riemann-Liouville type. The notion of the operation of a fractional derivative exists since Leibniz (for about 300 years already). Today there is a fully established theory of the calculus of the differential operators of fractional order (or simply "fractional calculus") [108]. Fractional calculus represents a generalization of the ordinary differentiation and integration to non-integer (real and complex) order. In the last few decades it was used to establish new models in many fields of physics, e.g. viscoelastisity, heat conduction, anomalous diffusion, chaos, percolation and fractals (see e.g. [7, 86, 105, 109]).

In the viscoelastic theory the fractional approach goes back to the early observations of Nutting [123]. He found that some material shows a stress relaxation which can be described by fractional inverse power functions of time rather than by the usual decay exponents. Later, Gemant [44] proposed to use the time differentiation of fractional order to model the behaviour of materials shows the relaxation in form of power functions or responses which can be described as fractional powers of frequency.

In the literature the fractional viscoelastic element discussed above is frequently represented as a triangle. Sometimes, the usual dashpot graphical element is used. The element is labelled by ηs^α or (τ^α, s^α), representing its behaviour in the Laplace plane. η represents the viscosity and τ the characteristic time of relaxation. Figure 2.15 shows an example.

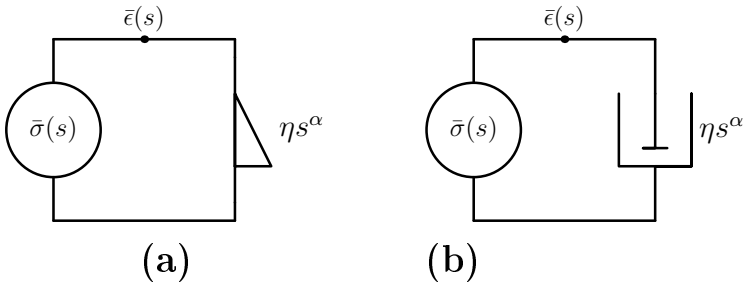

Figure 2.15.: **Viscoelastic element of fractional order** α

The figure shows a graphical representations of the fractional element: (a) by the triangle with label ηs^α, (b) the dashpot of usual form but with label ηs^α instead of ηs connected with elements of stress and strain. The element of fractional order are representation of the response with Laplace transform image of the form s^α. The symbol η denotes the elements respondance.

2.2.2. Definitions and notation

In spite of the fact that the operations of integration and differentiation of fractional order have not well established geometrical interpretation, the notion of fractional operations arrose naturally in the study of the dynamics of systems with self-similar composition of random processes. The exaples are diffusion and polymer dynamics [6, 52, 109, 112, 119]. Below we provide a minimal set of the definitions and noitions of the fractional calculus required for the formulation the basic models of fractional viscoelastisity. We will restrict ouwself to the fractional operations of real order. The rigorous treatise of this subject can be found in [87, 110]. For applications to viscoelasticity see e.g. [105].

Fractional integration

The Riemann-Liouville integration of the order $\alpha > 0$ is defined as a generalisation of the Cauchy n-fold integration:

$$ {}_aI_t^\alpha f(t) \equiv {}_aI_t^\alpha[f](t) = \frac{1}{\Gamma(\alpha)} \int_a^t (t-\xi)^{\alpha-1} f(\xi) d\xi, \qquad \alpha \in \mathbb{R} \quad \alpha > 0 \tag{2.68} $$

Here ${}_aI_t$ denotes the operator of integration from a to t, e.g. the subscripts in I denote the boundary of integration in the given order. $f(t)$ denotes some function of the real variable t. Compare this definition with equations (2.62, 2.63) from the heuristic motivation given in previous paragraph.

For $\alpha = 0$ the operation ${}_aI_t^\alpha$ is the identity operation, i.e. ${}_aI_t^0 f(t) = f(t)$. For integer α (2.68) is becomes the usual n-fold integration.

For sufficiently good functions, e.g. functions which are almost everywhere continuous, the fractional integration is commutative and satisfies the additive semi-group property:

$$ {}_aI_t^\alpha \, {}_aI_t^\beta \, [f] =_a I_t^{\alpha+\beta}[f] \tag{2.69} $$

Fractional differentiation

Like in the usual calculus the operator of fractional integration will not commute with the differentiation operator $D = d/dt$. Hence, the operator of differentiation can be defined either as left or right inverse of the Riemann-Liouville integration operator.

The Riemann-Liouville derivative of order $\alpha > 0$ is defined as

$$ {}_aD_t^\alpha f(t) = {}_aD_t^\alpha[f] = \frac{d^n}{dt^n} \, {}_aI_t^{n-\alpha} f(x) \tag{2.70} $$

where the integer value n is such that $n - 1 < \alpha < n$. For integers $\alpha = n$ ($n \in \mathbb{N}$) the Riemann-Liouville derivative is reduced to the usual derivative, i.e. ${}_aD_t^n \equiv d^n/dt^n$ and for

$\alpha = 0$ it is defined to be the identity operation. This operation has the property of being the left inverse of the Riemann-Liouville integration ${}_aD_t^\alpha \, {}_aI_t^\alpha f(t) = f(t)$. This definition coincides with the right hand expression in the equation (2.65) for $a = 0$.

For $0 < \alpha < 1$ the Riemann-Liouville derivative take the form:

$$ {}_aD_t^\alpha \, f(t) = \frac{1}{\Gamma(1-\alpha)} \frac{d}{dt} \int_a^t \frac{f(\xi) d\xi}{(t-\xi)^\alpha} \tag{2.71} $$

This is the same expression as the 'derived' relation (2.66) between stress and strain for the fractional viscoelastic element, introduced in the previous discussion.

Another form frequently used in the literature is the fractional derivative introduced by Caputo.

Caputo derivative of the order $\beta > 0$ is defined as:

$$ {}_a^C D_t^\beta [y] \equiv {}_aD_t^\beta \left[y(t) - \sum_{k=0}^{n-1} \frac{y^{(k)}(a)}{k!} (t-a)^k \right], \quad \beta > 0 \tag{2.72} $$

where n is the integer value such that $n-1 < \alpha \leqslant n$ and ${}_aD_t^\beta$ is the derivative of Riemann-Liouville type, defined in (2.70). $y(t)$ is a function of the real variable t and $y^{(k)}(a)$ denotes the kth derivative of the function $f(t)$ taken at the point $t = a$.
This operation ${}_a^C D_t^\alpha$ is a left inverse of the Riemann-Liouville integration.

For the special case $0 < \beta < 1$ the Caputo derivative can be represented as:

$$ {}_a^C D_t^\beta [y(x)](t) = \frac{1}{\Gamma(1-\beta)} \int_a^t \frac{y'(\xi) d\xi}{(t-\xi)^\beta} \equiv {}_aI_t^{1-\beta} \left[\frac{d}{d\xi} y(\xi) \right](t) \tag{2.73} $$

where $y'(\xi)$ denotes the first order derivative of the function $y(\xi)$.

Mittag-Lefler function

The Mittag-Lefler function plays a fundamental role in the fractional viscoelastic theory because the response of the basic models can be expressed in terms of this function. It is an entire function of a complex variable and can be defined through its power series expansion:

$$ E_{\alpha,\beta}(z) = \sum_{n=0}^{\infty} \frac{z^n}{\Gamma(\alpha n + \beta)} \tag{2.74} $$

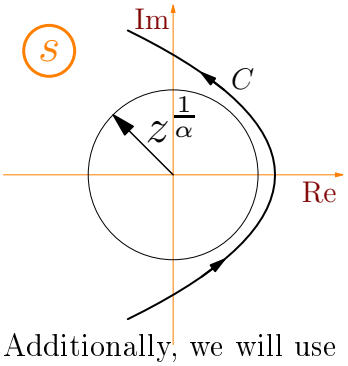

A representation, more suitable for numerical evaluations, is the contour integral in the complex plane $s \in \mathbb{C}$:

$$E_{\alpha,\beta}(z) = \frac{1}{2\pi i} \int_C e^s \frac{s^{\alpha-\beta}}{s^\alpha + z} ds \tag{2.75}$$

where the integration path C starts at $-\infty$ passes around the circle $\|s\| = z^{1/\alpha}$ in the positive sense and finishes at ∞ (see example in sketch on the left).

Additionally, we will use the following Laplace transform:

$$t^{\beta-1} E_{\alpha,\beta}(\lambda t^\alpha) \doteq \frac{s^{\alpha-\beta}}{s^\alpha - \lambda} \quad \lambda \in \mathbb{R}, \alpha > 0, \beta \in \mathbb{R} \tag{2.76}$$

2.2.3. Models

In the last few decades the fractional calculus was successfully applied to describe relaxation and transport phenomena in complex materials. In the context of linear viscoelastic behaviour of polymers and composite materials the progress was reported in the application of the generalized viscoelastic models based on the fractional relaxation relations [6, 28, 42, 48, 48, 105, 108, 118, 119, 122]. Such models provide a relationship between stress and strain of viscoelastic media in terms of a simple constitutive equation which, in contrast to 'classical' viscoelastic theory yields non-Debye relaxations observed in many experiments [109, 116]. Like in the 'classical' viscoelastic theory the fractional description based on the equation which can be applied to various types of experimental setups, i.e. the same relations describe the response to a step, slope, sinusoidal or non-standard excitations.

Relaxation equation The 'classical' viscoelastic description is closely related to the 'classical' relaxation equation whose homogeneous version can be written either in the differential form

$$\begin{cases} D\,\phi(t) & \equiv & \frac{d}{dt}\,\phi(t) & = & -\frac{1}{\tau}\,\phi(t) \\ \phi(0) & = & \phi_0 & \leftarrow & \text{initial condition} \end{cases} \tag{2.77}$$

or in the integral form

$$\phi(t) - \phi_0 = -\frac{1}{\tau}\, I\phi(t) \equiv -\frac{1}{\tau} \int_0^t \phi(\xi) d\xi \tag{2.78}$$

with the exponent $exp(-t/\tau)$ as its Green function. For the purpose of a convenient comparison, the shorthand notation of the operators for usual integration $I \equiv {}_0I_t^1$ and

differentiation $D \equiv d/dt$ is additionally used.
Similar to the 'classical' theory the fractional viscoelastic models relate (implicitly or explicitly) to the fractional extension/generalization of the usual relaxation equation [51,122]. In the integral form the latter can be directly derived from (2.78), replacing the operator of integration I by a fractional Riemann-Liouville integration operator

$$\phi(t) - \phi_0 = -\frac{1}{\tau^q} I^q \phi(t), \quad 0 < q < 1 \tag{2.79}$$

The equation (2.79) is regarded as **the standard version of the fractional relaxation equation** [51]. The differential form is readily obtained from the above equation by applying the operation of fractional differentiation:

$$^C D^q \, \phi(t) = -\frac{1}{\tau^q} \phi(t) \tag{2.80}$$

$$D^q \left[\phi(t) - \phi_0\right] \equiv D^q \, \phi(t) - \phi_0 \frac{t^{-q}}{\Gamma(1-q)} = -\frac{1}{\tau^q} \phi(t) \tag{2.81}$$

The second line is obtained from the first one by rewriting the Caputo type derivative $^C D^q = {}_0^C D_t^q$ in terms of the Riemann-Liouville derivation using its definition and expansion of the domain brackets of the D^q.
The solution of this equation (or its inhomogeneous version) appears in all fractional viscoelastic models, It is remarkable that the fractional relaxation equation is closely connected to anomalous continuous random walks [109] (e.g. random walks of the trapping type). This leads to the identification of the parameter q in (2.79) with the Lévy index of the waiting time distribution function of the hopping process (see e.g. [49–51]). The models of the trapped random walks are frequently used to describe glassy or dynamically constrained/frustrated systems. Hence the fractional relaxation equation together with fractional models of viscoelastity the based on it are related to the stochastic behaviour on a more microscopic (often molecular) level.
The solution can be found using e.g. the power series method or the method of Laplace/Melin transforms [67,86,137]. In the Laplace plane the integral equation (2.79) takes the form:

$$(1 + \frac{1}{(s\tau)^q}) \bar{\phi}(s) = \phi_0 / s \tag{2.82}$$

where we rearranged the terms. Then the Laplace image of the solution is obtained by division of the right hand expression by the pre-factor of the $\bar{\phi}(s)$ of the left hand expression:

$$\bar{\phi}(s) = \phi_0 \, \frac{s^{q-1}}{s^q + 1/\tau^q} \tag{2.83}$$

The comparison with equation (2.76) shows that the solution can be expressed in terms of the Mittag-Leffler function, taking $\alpha = q$, $\beta = 1$ and $\lambda = -1/\tau^q$. This means, that in the time domain the solution has the form:

$$\phi(t) = \phi_0 E_{q,1}\left(-\left[\frac{t}{\tau}\right]^q\right), \qquad t > 0, \tau > 0 \tag{2.84}$$

The solution of the fractional relaxation equation is shown with a log-log plot in figure

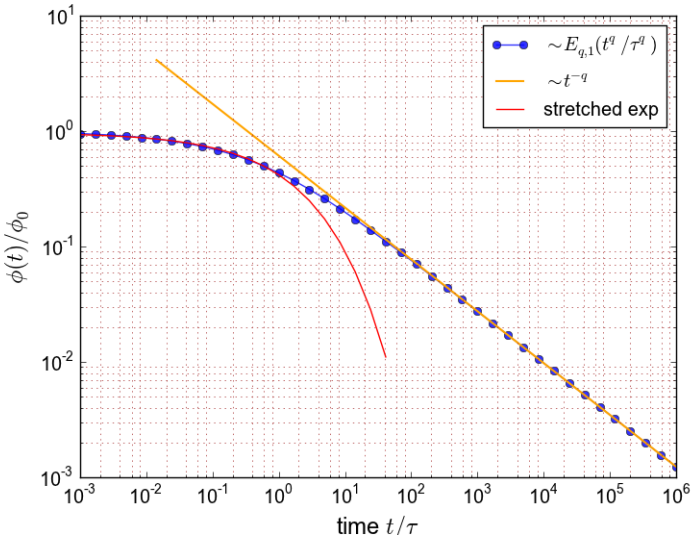

Figure 2.16.: **Fractional relaxation function** (2.84)
The figure shows the solution (2.84) of the fractional relaxation equation (2.79) (blue line and circles) in comparison with the stretched exponent law $\sim exp(-at^q)$ (red line) and the power function $\sim t^{-q}$ (orange line), with $q = 0.45$. This figure reproduces the famous demonstration of the ability of the fractional relaxation to interpolates between the stretched exponent (at small t) and power function (at large t) (plotted after [48]).

2.16. For $0 < q < 1$ this function interpolates between a stretched exponential law for small t and inverse power law for large t. In figure 2.17 the solution of the fractional relaxation equation is plotted for several values of q. For $0 < q < 1$ the function shows a monotone decrease and for $1 < q < 2$ it exhibits the behaviour of a damped oscillator. For the integer value $q = 1$ it becomes the usual exponent and for $q = 2$ the cosine function.
The function (2.84) can be considered as the response to a step excitation.
The Greens function (impulse response) can be obtained by the same method applied to an inhomogeneous version of the equation (2.80). Here the initial value is $\phi_0 = 0$ and the

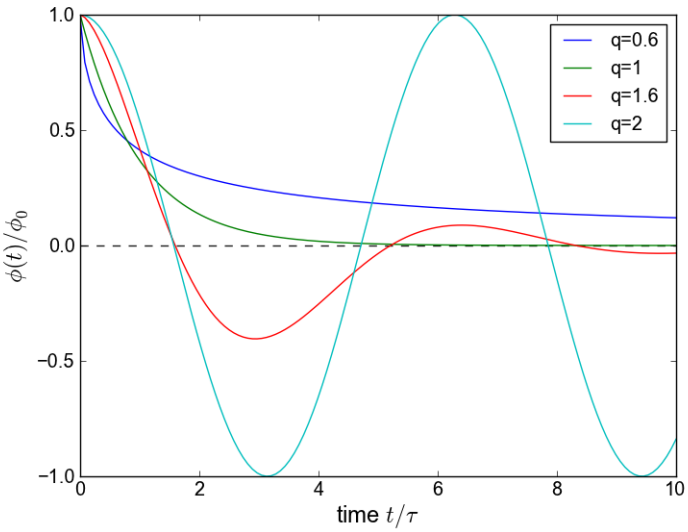

Figure 2.17.: **Fractional relaxation function for several values of q**
The solution of the fractional relaxation equation is plotted for several values of q. The initial conditions were chosen to be: (i) $\phi(0) = \phi_0$ for $q \leqslant 1$ and (ii) $\phi(0) = \phi_0, \dot{\phi}(0) = 0$ for $1 < q \leqslant 2$.

Dirac delta impulse function function is used as perturbation. The result is:

$$\bar{\phi}(s) = \frac{1}{s^q + 1/\tau^q} \tag{2.85}$$

In the time domain the comparison with equation (2.76) yields:

$$\phi(t) = t^{q-1} E_{q,q}\left(-\left[\frac{t}{\tau}\right]^q\right), \qquad t > 0, \tau > 0 \tag{2.86}$$

The partial solution of the forced (inhomogeneous) relaxation equation can be constructed as convolution with the impulse response function 2.86; see details in e.g. [139].

Fractional Maxwell unit Figure 2.18 shows the classical Maxwell element and its possible counterpart in the fractional viscoelastic theory, where the dashpot is replaced by the fractional viscoelastic element. To derive the constitutive equation we can follow the

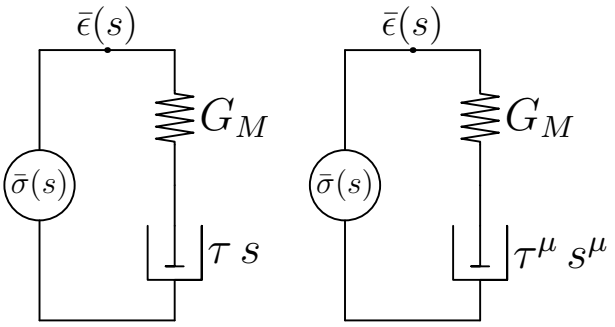

Figure 2.18.: **Viscoelastic Maxwell Units**

The classical (left pane) and fractional (right pane) Maxwell units are shown. In the classical viscoelastic theory the relaxation time τ is related to the viscosity as $\tau = \eta/G_M$, where G_M is elastic modulus.

same procedure as in the classical viscoelastic theory. In the Laplace plane the relation between stress and strain images takes the form

$$\left(\frac{1}{G_M} + \frac{1}{G_M \tau^\mu\, s^\mu}\right) \bar{\sigma} = \bar{\epsilon}(s) \tag{2.87}$$

where the classical rule was used: retardances adds in series and rlaxances in parallel. In the time domain, we can write this relation either as fractional integral- or differential equations:

$$(1 + \frac{1}{\tau^\mu} I^\mu)\, \sigma(t) - \sigma_0 = G_M\, (\epsilon(t) - \epsilon_0) \tag{2.88}$$

$$\sigma(t) + \tau^\mu D^\mu\, (\sigma(t) - \sigma_0) = G_M \tau^\mu D^\mu\, (\epsilon(t) - \epsilon_0) \tag{2.89}$$

In [42, 48] a slightly extended version of the above equations was suggested:

$$\boxed{\sigma(t) + \tau^\alpha D^\alpha(\sigma(t) - \sigma_0) = G_M \tau^\mu D^\mu(\epsilon(t) - \epsilon_0), \quad 0 < \alpha \leqslant \mu \leqslant 1, \quad t > 0} \tag{2.90}$$

The model fulfils the thermodynamic conditions of non-negative dissipation of energy if $\alpha \leqslant \mu$. In the limiting cases (1) $\alpha = \mu = 0$ we get a Hookean element, and (2) $\alpha = \mu = 1$ the classical Maxwell Unit.

In the time domain the relaxation modulus $G(t)$ (response to a unit stress) can be represented in terms of the Mittag-Leffler function as [42]:

$$G(t) = \left(\frac{t}{\tau}\right)^{\beta-1} E_{\alpha,\beta}\left(\frac{t^\alpha}{\tau^\alpha}\right) \tag{2.91}$$

where $\beta = \alpha - \mu + 1$. Both in the long-range asymptotic and in the range of small t function $G(t)$ is of the power law type. For $\alpha = \mu = 1$ we get the well-known exponential relaxation law of the classical Maxwell Unit.

Fractional Standard Solid model As with the Maxwell Unit above we can directly write the stress-strain operational relation for the Standard Solid model from its graphical representation, given in figure 2.19.

In the Laplace domain this relation is:

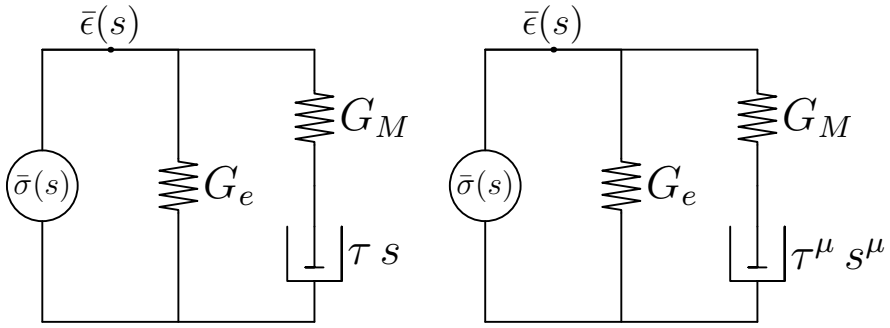

Figure 2.19.: **Viscoelastic Standard Solid Model**

The classical (left pane) and fractional (right pane) Standard Solid Models are shown. G_e,G_M are elastic moduli of the single spring and the spring in the Maxwell unit. In the classical viscoelastic theory the relaxation time τ is related with the viscosity by $\tau = \eta/G_M$.

$$\left(1 + \frac{1}{(\tau s)^\mu}\right) \bar{\sigma}(s) = \left(G_g + G_e \frac{1}{(\tau s)^\mu}\right) \bar{\epsilon}(s) \tag{2.92}$$

In the time domain this relation take the form:

$$\frac{1}{\tau^\mu} I^\mu\, \sigma(t) + (\sigma(t) - \sigma_0) = G_g(\epsilon(t) - \epsilon_0) + G_e \frac{1}{\tau^\mu} I^\mu\, \epsilon(t) \tag{2.93}$$

where , as in the classical Standard Solid model, $G_g = G_e + G_M$ is glassy (instantaneous) modulus. Above, we used the shorthand notation $I =_0 I_t$ for integration operator. σ_0, ϵ_0 are initial stress and strain, respectively.

In [48] the generalized version of this model was derived with the following stress-strain relation:

$$\boxed{\frac{1}{\tau^q} I^q\, \sigma(t) + (\sigma(t) - \sigma_0) = G_g(\epsilon(t) - \epsilon_0) + G_e \frac{1}{\tau^\mu} I^\mu\, \epsilon(t), \quad 0 < \mu \leqslant q \leqslant 1} \tag{2.94}$$

The equivalent representation in terms of fractional differential equation reads:

$$(1 + \tau^q\, {}^C\!D^q)\sigma(t) = (G_g\, \tau^q\, {}^C\!D^q + G_e\, \tau^\nu D^\nu)\epsilon(t), \qquad \nu = q - \mu \tag{2.95}$$

The solution of this equations for a given excitation can be read from their Laplace image, e.g. the image of equation (2.94) is:

$$\left(\frac{1}{(\tau s)^q} + 1\right) \bar{\sigma}(s) - \frac{\sigma_0}{s} = \left(\frac{G_e}{(\tau s)^\mu} + G_g\right) \bar{\epsilon}(s) - \frac{G_g \epsilon_0}{s} \tag{2.96}$$

Using the technique of Block Pulse Functions (BPF)

The Block pulse functions (BPF) are a set of orthogonal functions with piecewise constant values. The sketch in figure 2.20 shows an expample (blue lines) of such functions. A set of M block pulse function ϕ_m ($m = (0,1,2,\ldots,M-1)$ can be defined in the interval $t \in [0,T)$ as

$$\phi_m(t) = \begin{cases} 1 & \text{for} \quad (m-1)\,h \leqslant t < m\,h, \quad h \equiv \frac{T}{M} \\ 0 & \text{otherwise} \end{cases} \tag{2.97}$$

where h is the length of the subintervals, $T > 0$ is a predefined length of the interval of interest, M is the number of subintervals in $[0,T)$.

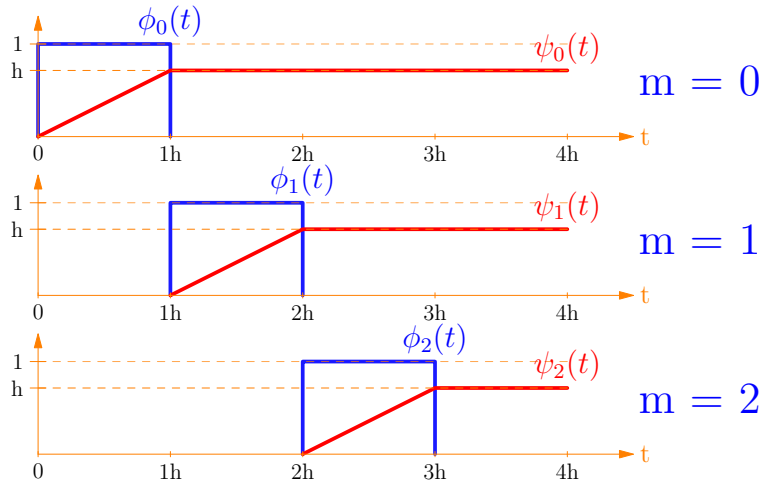

Figure 2.20.: **Block pulse functions and their integrals**
The first three block pulse functions $\phi_m(t)$ (blue lines) and their integration $\psi(t) = \int_0^t \phi_m(t)dt$ (red lines) are shown. The m is the function number, in the sketch $m \in (0,1,3)$. h is the length of the subintervals partitioning the axis t; for each such subinterval there is only one block pulse function which takes non-zeros values in it.

The technique outlined here is frequently used to reduce the complexity of numerical problems [83]. Generally, it is applicable utilizing an any complete set of orthogonal functions, but the BPF offer the most simple relations. The main idea of this technique is rather simple, see figure 2.20. The original functions are first exanded into the BPF series, then the operations of the BPF series are applied to obtain the piecewise constant approximation of the solution. The extreme simplicity of the operations in the BPF space leads to the solution procedures with drastically reduced complexity.

The method was introduced by Chen et.al. in [19], particularly for the pupose of the numerical solution of the problems within the Fractional Calculus. In this article the solution technique was transferred from the domain of the Walsh functions [19, 177] into the domain of BPF. One may say that it was rediscovered several times, e.g. in [97, 138].

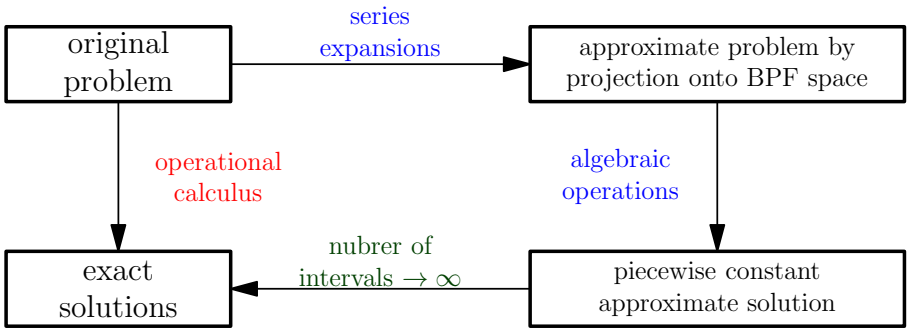

Figure 2.21.: **Basic idea of block pulse function technique**

Drawn after [83].

The set of BPF is complete in the sense that any piecewise continuous function $f(t)$ can be expanded uniquely (for a given M and T) into block pulse functions by minimizing the mean-square difference between $f(t)$ and its approximation [83], i.e.

$$f(t) \simeq \sum_{m=0}^{M-1} f_m \phi_m(t), \qquad 0 \leqslant t < T \tag{2.98}$$

where the expansion coefficients are

$$f_m = \frac{1}{h} \int_0^T f(t)\phi_m(t)dt = \frac{1}{h} \int_{m\,h}^{(m+1)h} f(t)dt \tag{2.99}$$

Or, in Dirac's notation:

$$f(t) \equiv \langle f \,|\, t \rangle \simeq \langle f \,|\, m \rangle \langle m | t \rangle \equiv \sum_{m=0}^{M-1} f_m \phi_m(x) \tag{2.100}$$

$$f_m \equiv \langle f \,|\, m \rangle = \langle f \,|\, x \rangle \langle x \,|\, m \rangle \equiv \frac{1}{h} \int_0^T f(t)\phi(t)dt \tag{2.101}$$

In this notation the integration operator in terms of the BPF is a matrix with elements:

$$\mathbf{H}_{mn} \equiv \langle m \,|\, I \,|\, n \rangle = \frac{1}{h} \int_0^T \phi_m dt \int_0^t \phi_n(\xi) d\xi \tag{2.102}$$

where, as before, we denote the operator of integration by I, i.e. $I{=}_0 I_t^1$. This means, that we integrate each nth basis function $\phi_n(t)$ $(0 \leqslant n < M)$ from 0 to t and then expand the result of integration into the same basis set. Figure 2.20 shows the integrated functions (red curves). The resultant matrix of the expansion coefficients is called operational integration matrix $\mathbf{H}$. The elements of $\mathbf{H}$ are:

$$\mathbf{H}_{mn} = \langle m \,|\, I \,|\, n \rangle = \begin{cases} 0, & m < n \\ h/2, & m = n \\ h, & m > n \end{cases} \tag{2.103}$$

In terms of the integration matrix we can approximate the result of multiple integration of a piecewise continuous function $f(t)$:

$$I^\alpha \,|f\rangle \simeq \sum_m (H^\alpha)_{mn} \,|m\rangle \langle m \,|\, f \rangle \tag{2.104}$$

I.e., the result of the integration of the BPF series representation of a function $f(t)$ is expressed as a BPF series.

The matrix $\mathbf{H}$ is the upper triangular matrix of the Teuplitz type; the operations of addition, multiplication, power will result in the matrix of the same type. Additionally, we can represent matrices of this type as series of the so-called delay matirces Q_k (k = 0,1,2,..$M{-}1$) with ones on the k-diagonal above the the main diagonal and zeros elsewhere. We note that Q_0 is the identity matrix. Delay matrices can be represented as powers of the matrix $Q \equiv Q_1$:

$$Q_k = Q^k, \quad \text{with} \quad Q \equiv Q_1 \tag{2.105}$$

Additionally, we have $Q^k = 0$ for any $k \geqslant M$.

Now, we can represent the operational integration matrix as:

$$\mathbf{H} = h \left(\frac{1}{2} Q_0 + \sum_{k \geqslant 1} Q_1^k \right) = \frac{h}{2} \cdot \frac{1+Q}{1-Q} \tag{2.106}$$

In this representation the integration matrix can be inverted to get the operational differentiation matrix:

$$\mathbf{B} = H^{-1} = \frac{2}{h}(1-Q)\left(\frac{1}{2} + \sum_{k=1}^{\infty}(-1)^k Q^k\right) = \frac{2}{h}\cdot\frac{1-Q}{1+Q} \tag{2.107}$$

For α real we can express the power function of integration matrix (using the binomial theorem) as a sum of integer powers of Q:

$$\mathbf{H}^{\alpha} = \left(\frac{h}{2}\right)^{\alpha}(1+Q)^{\alpha}(1-Q)^{-\alpha} = \left(\frac{h}{2}\right)^{\alpha}\sum_{n}\binom{\alpha}{n}Q^n\sum_{k}\binom{-\alpha}{k}Q^k \tag{2.108}$$

This allows to approximate the fractional integration and differentiation and to reduce integro-differential equations to the algebraetic relations. More over, if a function $F((1-q)/(1+q))$ can be represented by a Tailor series of the variable q, then the functional matrix $F(H)$ can be easily computed by the method discussed above. The last property offers a posibility of computing the inversion of the Laplace tranform. This is based on the direct relation between the integration matrix $\mathbf{H}$ and the expression $1/s$, where s is the complex variable of the Laplace transform.
The method can be outlined as follows: assume that a function $f(t)$ of the real variable $t \geqslant 0$ has its Laplace transform $f(t) \doteq \bar{f}(s)$. Then we can represent $\bar{f}(s)$ as

$$\bar{f}(s) = \frac{1}{s}\bar{f}_1(\frac{1}{s}) \tag{2.109}$$

Now, the method of inversion of Laplace transform associates the function $\bar{f}_1(1/s)$ with the Taylor series expansion of

$$\bar{f}_1\left(\frac{h}{2}\frac{1-q}{1+q}\right) \tag{2.110}$$

in terms of the variable q. Then each power of q, say q^k, is associated with the kth power of the matrix Q to give the operational upper triangular marix F. The applicaton of this matrix to a BPF series with all coeficients equals 1 (this is the expansion of the unit step) gives the desiered Laplace inverse of the $\bar{f}(s)$.

The procedure of the inversion of Laplace transform discussed above provides the suitable method for solving the equations of the classical and the fractional viscoelastic theories. The algorithm can be outlined as following (compare fig. 2.1):

- transfer the equation at hand into the Laplace domain and solve this algebraetically. The result will be a function $\bar{f}(s)$ representing the Laplace transform of the desired solution, say $f(t)$.

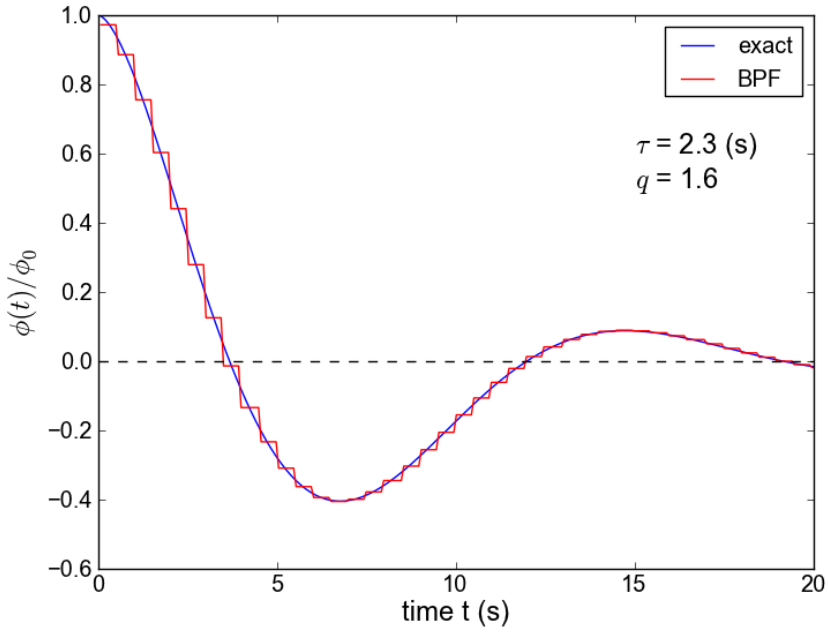

Figure 2.22.: **BPF solution of the fractional relaxation equation**
The solution of the relaxation equation (2.79) for a characteristic time $\tau = 2.3$ (s) and fractional order $q = 1.5$ is shown. The blue curve represents the solution computed by the algorithm from [72] with tolerance $\epsilon = 10^{-9}$. The red line shows the BPF piecewise approximation with $M = 42$ basis functions. A relatively small number M of basis functions is chosen to show the nature of the approximation, which will be closer to the exact solution when M increases. The analytical solution is given in equation (2.84) and its Laplace transform used in BPF solution is given in (2.83).

- apply the above method to compute the approximation of the inverse Laplace transform of the function $f(s)$. The result is a piecewise approximation of the desired solution $f(t)$.

An example of the application of the BPF approach to solve the fractional relaxation equation (2.79) is shown in figure 2.22.

2.3. Specifics of high polymeric materials and simplistic description of non linear viscoelastic behaviour

The specific aspects of behaviour of materials made of high polymers is discussed. The classification of response of such materials to an elongation is considered and non linear character of the behaviour is shown. Then the connection to protein folding mechanisms with the mechanical response of protein based materials is shortly discussed and two kind of simplistic models based on the State Transition Theory of activated process are introduced.

2.3.1. Stress-Strain behaviour of materials consisting of high polymers

The mechanical properties of high weighted polymers can vary widely with the environmental conditions and the characteristic scale (or frequency) of measurements. The composition, structure, physical and chemical configuration on a wide range of spacial scales play a very important role. At low temperatures or, equivalently, a short time scales a polymer material is in a glass-like state with an elastic (Young's) modulus of the order $10-12$ GPa and it will start to flow at strains of about 4-6% [35,77] . But at high temperatures or longer time scales a rubber-like behaviour is observed and the modulus is lowering some orders of magnitude (down to about $1-10$ MPa). In the glass-transition region, i.e. intermediate temperature/frequency range, the polymer is neither glassy nor rubber-like. Additionally, the stress/strain behaviour can strongly depend on the pre-stretching history. In general the stress/strain behaviour of polymeric materials can be grouped [77] into several categories (see sketch on fig. 2.23):

brittle-like behaviour (curve A) is characterized by the absence of a yield point and sudden failure.

yield behaviour (curve B,C) is characterized by a maximum amount of stress (strain) after which a yielding deformation occurs. This is manifested by a some flow phenomena usually associated with a crazing or shear. This, however, does not always mean a completely irreversible deformation of the structure of the polymer sample.

rubber-like (curve D) is characterized by a spread out yield behaviour with a plateau in the stress-strain curve. This is often accomplished by a final increase in the stress before the failure.

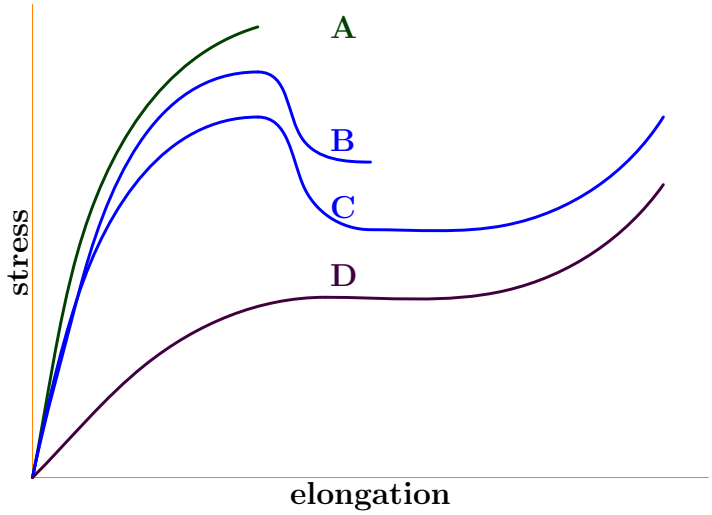

Figure 2.23.: **Sketch of stress-elongation curves at different temperatures** Shows a common types of stress-strain behaviour: curve A – brittle-like behaviour, B and C – yield behaviour, D – rubber-like behaviour. This figure is sketched after [77].

Some or all of these categories occure for the same polymer structure at various environmental conditions or various time scales of measurement. The time-scale dependence of the mechanical properties of polymers can be demonstrated by an example: in the literature the stiffness of silk fibres is often compared with the stiffness of steel, if the measurements are done on the time scale of several seconds. But, one can easily break them, applying a relatively weak force over time intervals of some hundreds of hours.
The relation between the time scale of the experiment and the temperature is known in the literature as the 'time-temperature equivalence principle' (see e.g. [35, 77]).
The amorphous high polymers usually show four characteristic regions which are clearly separated, they are: glassy, transition, rubbery and flow. For the application to silk we should note, that for a polycrystalline polymeric material this four regions are not so clearly defined. E.g. the Young's modulus changes less dramatically with temperature than in the case of amorphous polymers. At high temperatures crystallites can act as cross-links and, hence, prevent the irreversible molecular flow, so there is no more well defined rubber-like state.

Regimes of the stretching process The stages, which a polymeric material under load undergoes, are usually described by means of tensile tests with constant rate of strain. With

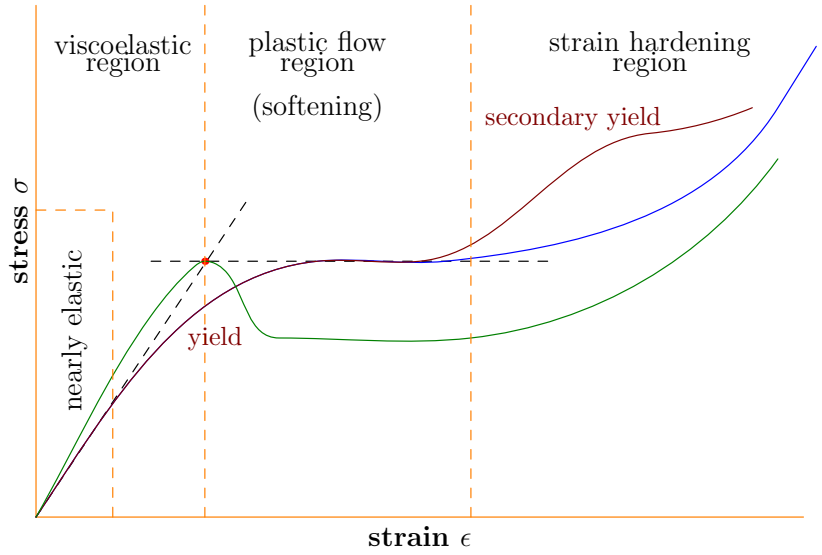

Figure 2.24.: **Symbolical classification of ranges on the stress-strain curves** The figure shows specific ranges of stress-strain curves, describing the response to an excitation with a constant rate of strain. The red point, together with two dashed lines, shows of the geometrical definition of the yield point, by example. The declination of the second dashed curve can be positive, zero or negative. In case it is negative the yield point will be defined as the local maximum of the stretching curve in the yielding range (see the green curve). Some material types exhibit more then one yield point. This fact is symbolically shown by the brown curve.

the help of the sketch on the figure 2.24 we can describe this regimes as follows:

viscoelastic region

At a very small deformation the system is in the vicinity of the equilibrium state and exhibits nearly elastic response (Hooke's law). With increasing deformation the system changes to a (time dependent) linear viscoelastic behaviour. By approaching the yield point the response of the system becomes more and more non-linear.

softening (plastic flow)

At the yield point stress-induced plastic flow processes is activated and the deformation becomes irreducible (at least at moderately short time scales). Some systems exhibit a phase transition over a sequence of metastable states and only return to the initial state after heating over the temperature of the glass transition or through a special physico-chemical processing [85, 114].

Because of strong interdependence of strain-rate, temperature and humidity there are no simple yield criteria similar to the classical criteria known for simple materials.

strain hardening

With further increasing deformation the stiffness response is progressively increasing.

Additionally, in figure 2.24 the determination of the yield point is sketched. The yield point is defined either as maximal stress in the yielding region or as intersection of the two asymptotic lines (dashed lines on the figure), one before and one after the yield region. In the figure the green line represents the former case and the blue and brown colored curves represent the latter case.

Many attempts were performed to explain such non-linear phenomena as softening, strain hardening and yield phenomena. Most explanations are based on the transit state theories [33, 147, 167], including the theories with direct application of the metal-flow theories. Others are based on computer simulations [111] or on the viscoelastic theory of internal time [9]. But most of the existing theories borrow the mechanism of thermally activated molecular flow from models similar to the given by Eyring and Tobolsky [167].

2.3.2. Molecular theory of viscoelastic behaviour

Relation between theories of linear viscoelasticity and reaction rates [32, 33, 140].

The linear viscoelastic theory is based on the spring-dashpot mechanical analogies and can be derived from the linear theory of irreversible thermodynamics (see e.g. [11, 12]). The

latter has its origin in the formulation of the "reciprocal relation" by Onsager [125]. The theory works only in the vicinity of equilibrium for the systems under study and it does not use the information on the molecular level directly. In this theory the state of a system is specified in terms of its equilibrium parameters and their expansion coefficients for small deviations from their equilibrium values.

On the other hand, in the treatment of irreversible processes based on the theory of the "absolute reaction rates" [32, 182] one adapts the idea that in any transport process or reaction the molecules occupy successive equilibrium (micro-) states and pass from one to the next through a region of relatively high potential energy, potential barriers. The properties of the virtual (intermediate) state of the highest potential energy determine (mostly) the probabilities of the transitions from one equilibrium position to the next. In such a view, the properties of the 'activated state' and the driving forces determine the rate of the transport flow. This theory is applicable to systems far outside thermodynamical equilibrium. But close to the equilibrium state it provides exactly the same information as that from the linearized theory of irreversible processes [127]. The interplay between these theories will be used later.

The idea of molecular transitions (reactions) can be extended to the transitions on the level of 'molecular units' which either can be (inter-molecular) conglomerations or (intra-molecular) parts of larger molecules or a small thermodynamical subsystems in the sense of Hill [74].

This theory was successfully applied to describe such phenomena as diffusion, plasticity and viscosity of simple materials and polymer melts [33, 34, 146, 147].

Eyring's reaction rate theory

Eyring [32, 182] [1] has proposed the general equation for the rate of any process in which matter rearranges by surmounting a potential energy barrier in the following form [34]:

$$k = \kappa \frac{k_B T}{h} \frac{Q^{\ddagger}}{Q_A} e^{-\frac{E_a}{k_B T}} \tag{2.111}$$

where k is the rate of the process (reaction), T is the absolute temperature, h is the Planck's constant. Q_A is a partition function of the initial state (reactants) of the process, $Q^{\ddagger}$ is a partition function of the transition state (activation complex, see below), without taking into account the degree of freedom associated with the reaction coordinate. E_a is

[1] independently, this theory was proposed by [43]; additionally, it must be noted, that a somewhat later theory of Kramers [92] has the same general structure and its multidimensional extension (see e.g. [65, 140]) is applicable in the same manner as Eyring's expression.

the energy difference between the initial and transition states. The meaning of the energy barier will be discussed later, and a sketch of the situation is present in figure 2.25.
κ is a correction factor (transmissions coefficient) introduced *ad hoc* by Eyring to correct for those situations when the system has reached the transition state but then returns to the initial state, without contributing to the reaction product. Frequently, this factor is considered to be unity and the resulting value of k in (2.111) is called the `transition theory rate` $k \equiv k_{TST}$.
The coefficient $\frac{k_B T}{h}$ is known as the `universal rate constant for a transition state`. It is the averaged frequency of the vibrational mode responsible for converting the activated complex to the product of reaction. At room temperatures its value is about $6.2 \cdot 10^{12} s^{-1}$. Not every vibration leads to the formation of the product, so a proportionality constant κ, as mentioned above, is introduced to account for this fact.
The equation (2.111) can be rewritten as:

$$k = \kappa \frac{k_B T}{h} e^{-\frac{\Delta G^{\ddagger}}{k_B T}} \tag{2.112}$$

where $\Delta G^{\ddagger}$ is the Gibbs free energy of activation, typically $\Delta G^{\ddagger}$ is of the order of $20 - 30$ kcal/mol.
A process (reaction) is assumed to cross an intermediate (transition) state, denoted as AB^* on the sketch in figure 2.25. The `energy barrier` is defined as the minimum of energy (work) required to start the reaction. The intermediate state, called `activated complex`, is formed on the top of the activation barrier. Once the energy barrier is surmounted, the reaction proceeds downhill to the reaction product with the probability κ.
The theory is very general and based on the following postulates:

- the reactants and the transition state are in thermodynamic equilibrium
- the rate of reaction is proportional to the concentration of the particles in the higher energy transition state (denoted by AB^* on the figure).

The Gibbs energy $\Delta G^{\ddagger}$ can be represented through

$$\Delta G^{\ddagger} = \Delta H^{\ddagger} - T \Delta S^{\ddagger} \tag{2.113}$$

where $\Delta H^{\ddagger}$ is the activation enthalpy and $\Delta S^{\ddagger}$ is the activation entropy. The presence of entropy in the equation (2.113) shows that increasing an entropy by the formation of the activated complex can compensate the amount of potential energy of the barrier.
The reaction rate theory is very similar to that of Arrhenius, also known as van 't Hoff-Arrhenius law:

$$k = \nu e^{-\frac{E}{k_B T}} \tag{2.114}$$

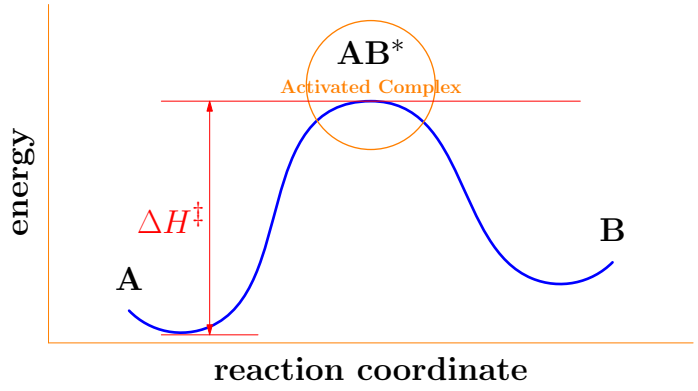

Figure 2.25.: **Barrier of reaction**

Sketch for a process (reaction) $A \rightarrow B$, where A represents an initial state (reactants) and B a final state (products) of the process. AB^* represents the 'activated complex'. The 'reaction coordinate' measures the progress of the reaction. $\Delta H\ddagger$ represents the non-entropical part of the work of formation of the activated complex.

with E denoting the threshold energy for activation and ν is a prefactor.
Both theories describe the reaction rate as a function of temperature and energy of activation. Strictly speaking, the Arrhenius equation was derived for reactions in the gas phase using the collision theory, while Eyring equation is based on more common principles, and was derived to be applicable to reactions in all the known phases. But it must be noted [65], that in his original article Arrhenius introduced a 'hypothetical body' (known now as activated complex) and proposed the existence of equilibrium between molecules in the initial and activated states. So, the further investigations of the problem, including those of Eyring and Kramers, were concentrated around the prefactor ν in the equation (2.114), e.g. compare with (2.111).

Applicability of the reaction rate theory to strain/stress behaviour of polymeric materials

The deformation of polymer materials at any level of stress involved has its origin in their ability to adjust the conformation of chains on the molecular level. This is realized by rotation around covalent bonds [35, 77]. This rotation is constrained by the intra-molecular and inter-molecular interactions, which define the energy barriers which have to be overcome during the conformational changes. The rate of these changes is defined by the thermal energy available to the polymer and the forces applied to it.

On the other hand, the folding process, i.e. the transitions between the native (folded) and denatured (unfolded) states (see ch. 1), is very important for the deformation of the materials consisting of proteins. There is no detailed description of the folding mechanisms, but novel theoretical and experimental approaches have recently confirmed [37, 46, 81] the earlier suggestions, that the folding process is a barrier-limited process [2]. Proteins seem to fold via a limited number of accumulated intermediates. Several proteins display a simple two-state behaviour. Thus, a key role in protein folding studies has been played by the description of folding transition states (activated complexes) [81].
The are two mainstream folding scenarios (see fig. 2.26):

Diffusion-collision (DC): the folding happens in a step-wise manner. The rapid formation of micro-domains with secondary structure, followed by their collision and consolidation into the ternary structure.

Nucleation-condensation (NT): the folding is a transition between two states: folded-unfolded. The nucleation-condensation model describes the folding process as concurrent (simultaneous) formation of secondary and ternary structures around the weakly-structured preformed nucleus.

In [47] it is suggested that the DC and NT are different manifestations of an underlying common mechanism. Generally, the folding mechanism can vary with environmental parameters and applied stress [57].

[2] An exception is the downhill folding mechanism, which is not established yet.

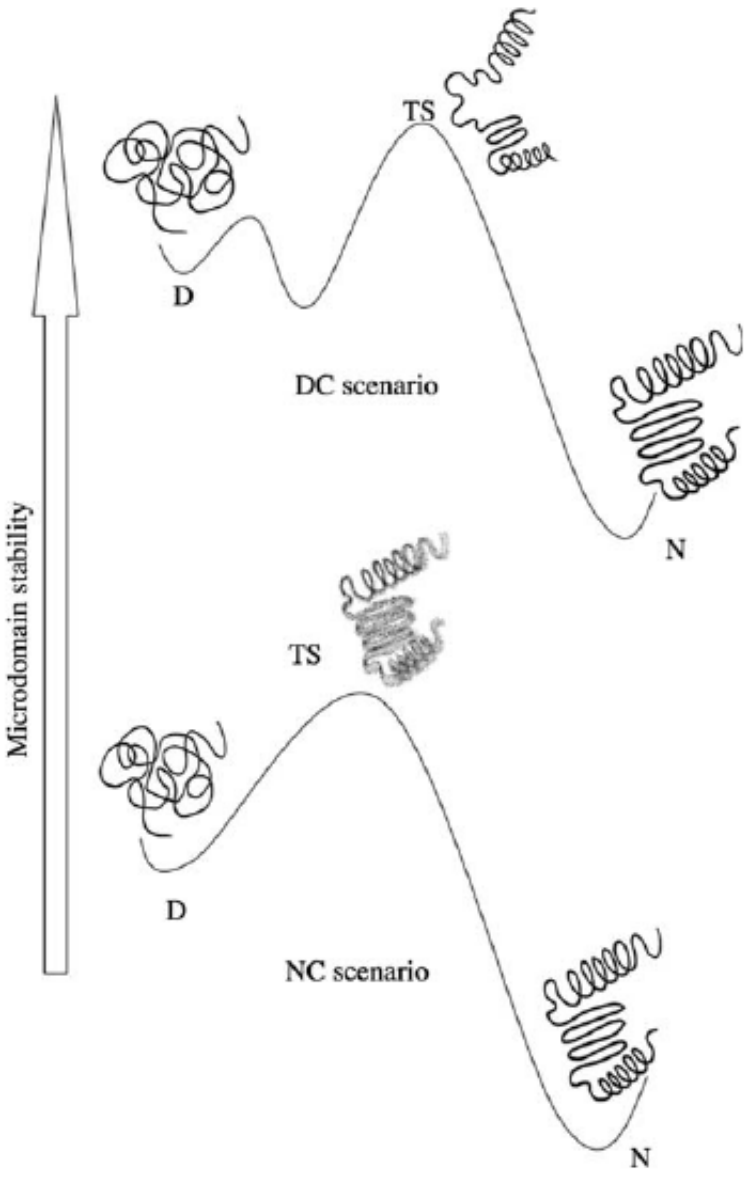

Figure 2.26.: **Sketch of the classical mechanisms for protein folding**
D,TS,N denote the denatured, transition, natural (folded) state, respectively.
Figure shows a schematic representation of the classical mechanisms for protein folding described in the text. The diffusion–collision (DC) model (top panel) is based on the existence of micro-domains, involving segments of secondary structure, whose productive collision represents the rate-limiting step of folding. On the other hand, according to the nucleation–condensation (NC) model (bottom panel), the main folding TS is a distorted version of the native state and folding occurs via simultaneous formation of secondary and tertiary structure, around a weakly-structured folding nucleus.
Reprinted from [81].

Models for strain-stress behaviour of polymeric materials

In the section 2.1 the 3-elements model for the standard linear solid was shown, it provides the first linear approximation to the behaviour of a viscoelastic body. Eyring with coworkers [63, 146, 147, 167] adapted the idea that the deformation of a polymer is a thermally activated process involving the motion of *molecular units* (segments of a chain molecules) over potential barriers. They modify the standard linear solid model so that the dynamics of its `dashpot element` is not more a linear functional but is governed by the law of activated process. The resulting model is a simplistic representation of a non-linear viscoelastic behaviour with a non-Newtonian viscosity. Burte and Halsey [14] applied this strategy to the situation where molecular units (in the averaged sense) are spatially extended due to a thermally activated molecular phase transition process. The elongation then is described as function of population of the molecular units in the longer state. These models are useful, at least, for a qualitative understanding of the underlying molecular mechanisms of deformation because their parameters include the activation energy and activation volume of the molecular movements.

Also, two polar types of behaviour for polymer material under load were proposed:

Eyring's Non-Newtonian Model [63, 146, 147, 167]

The movement of polymer chains is realized by the translation of a 'molecular unit', which exchanges of the 'old neighbours for the new one' [63]. This can be compared with the moving art of a centipede. It walks by stepping only one or few legs at a time, but not all of them simultaneously. Because the flow from one position to another involves the breaking of bonds quite similar for the each position the situation similar to hopping in a statistically periodic potential consolidated with reversible energy storage (spring) mounted in parallel. This spring represents the accumulation of the potential energy of deformation by non-broken bonds. The rate of elongation is then proportional to the rate of translations of the 'molecular unit' times the mean distance between the stacking positions. A molecular system of this type is schematically sketched in fig. 2.27.

'Chemical model of flow' (two-state model)

The movement is realized by a transition of molecular segments form initial configuration (state) A to a new configuration B and thereby becomes unmovable. Neglecting an elastic deformation of molecules in either state, the elongation is proportional to the fraction of the segments which is in the state B. The states `A` and `B` are separated by an energy barrier, hence the rate of the transition can be computed in the frame of the reaction rate theory. This type of viscous behaviour was introduced

in [14, 15], where the model was extended to three states to include such phenomena as secondary yield. This kind of models is inspired by protein folding, see sketch in figure 2.26.

Both models are able to describe such phenomena as yield point as well as softening and hardening. The second model seems to be closer to the modern point of view of the behaviour of materials consisting of protein chains.

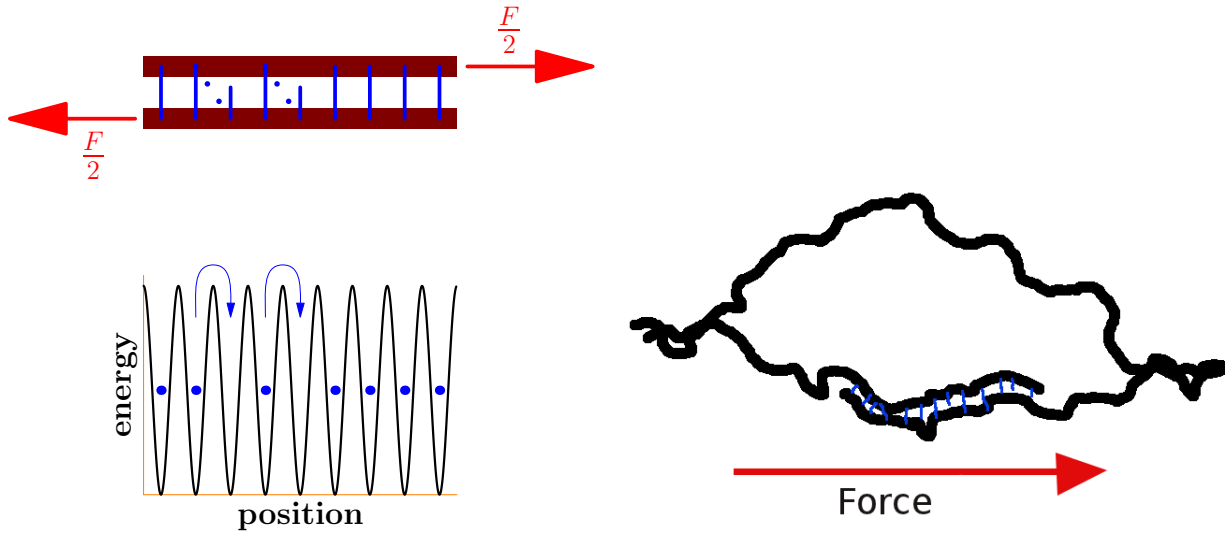

Figure 2.27.: **Molecular system exhibiting the 'exchange of old neighbours for new ones'**

Panel on the left symbolically sketches a representation for a of breaking and rebuilding of a bond as a process of surmounting an energy barrier. Panel on the right is a figure from a classroom lecture at Princeton University wroten by H. Eyrng. It sketches a situation with molecular chain under shear flow. Drawn after [14]

In what follows, we give a short description of the constitutive equations governing these models. For graphical representation of such processes we will use the Eyring graphical (dashpot) element $\eta(\sigma)$ as shown in figure 2.28.

Modeling of non-Newtonian flow

Eyring's model

In a general sense Eyring's model assumes that a macroscopic deformation is the result of basic (thermally activated) processes whose rate depends on the ease at which the

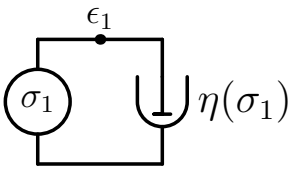

Figure 2.28.: **Eyring dashpot element representing non-linear viscoelasticity**

molecular flow unit (chain segment) can overcome a potential barrier. Such processes can be either inter-molecular (chain-sliding) or intra-molecular (changes in the conformation of the chain). Even when no stress is applied the same processes are going on. In this case a dynamical equilibrium exists, so that an equal number of flow units moves in each direction over the potential barrier with a rate given by

$$k_{eq} = \nu_0 \exp(-\frac{\Delta G^{\ddagger}}{k_B T}) \tag{2.115}$$

with the same meaning of the parameters $\Delta G^{\ddagger}, k_B, T$ as in (2.111, 2.112) and ν_0 equals to the universal rate constant for a transition state, i.e. $\nu_0 = \frac{k_B T}{h}$.

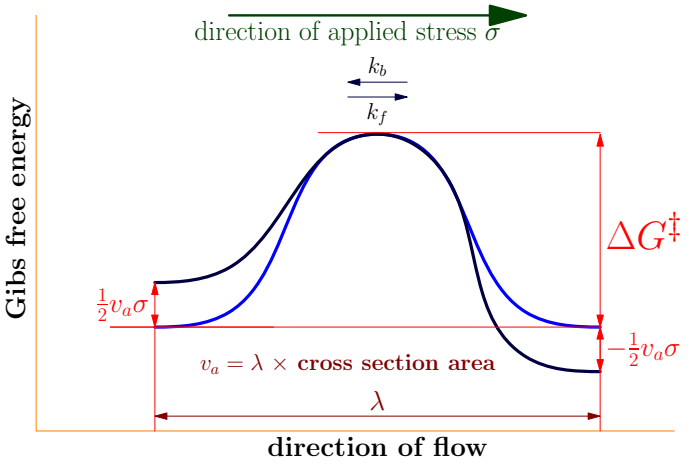

Figure 2.29.: **An energy barrier in the model on non-Newtonian flow**
Shows an energy barrier separating two successive minima in the Eyring's model of non-Newtonian flow. k_f, f_b are forward and backward rates. λ is a averaged distance between two minima of free energy. The 'activation volume' is $v_a = \lambda \times$ *effective cross section area*, it is a volume covered by the molecular unit throw the transition. σ denotes an applied stress.

Under an applied stress σ these processes are unbalanced and accelerated into the direction

of stress. I.e. the applied stress produces a symmetrical linear shift $v_a\sigma$ of the energy barriers, where v_a has the dimensions of a volume and is called activation volume. It is a volume covered by the molecular unit by overcoming the potential barrier, so that $\frac{1}{2}v_a\sigma$ measures the work needed to surmount the barrier, see figure 2.29. Now the forward rate k_f and the backward rate k_b are described by:

$$k_f = k_{eq}\exp\left(+\frac{v_a\sigma}{2k_BT}\right) \tag{2.116}$$

$$k_b = k_{eq}\exp\left(-\frac{v_a\sigma}{2k_BT}\right) \tag{2.117}$$

where k_{eq} is defined by (2.115). The net rate then is the difference $k = k_f - k_b$. Assuming the average distance between the potential minima to be λ the velocity of flow will be proportional to $\lambda \times k \times n$, where n is the number of flow units per unit length. With assumption, that the net flow is directly proportional to the rate of strain $\dot{\epsilon}$ we get

$$\dot{\epsilon} = n\lambda k = \lambda n k_{eq}\left(e^{\alpha\sigma} - e^{-\alpha\sigma}\right) = K\sinh\alpha\sigma \tag{2.118}$$

here we have introduced the shorthand notation $\alpha = \frac{v_a}{2k_BT}$ and the thermal rate $K = 2\lambda n k_{eq}$, K/n is the velocity of flow units at equilibrium in both directions without stress. The equation (2.118) defines the viscosity due to activated processes [3], which can be incorporated into the dashpot of the linear viscoelastic models, e.g. standard linear solid as shown in figure 2.30. Such models were tested against experimental data for several fibres [63] and gave a good fit over four decades of time.
For sufficiently small stress such that $v_a\sigma \ll k_BT$ the equation (2.118) will give a constant viscosity

$$\eta \equiv \dot{\epsilon}/\sigma \approx \alpha K \tag{2.119}$$

and the behaviour of the material will reduce to 'linear viscoelastic'.

Application of the Eyring's model to relaxation experiments [63, 167] In an idealized relaxation experiments the response to a strain excitation with a form of the Heaviside step-function is measured. Because the rate of strain is zero it is enough to consider the response of the element shown on the figure 2.30 (a). The rate of strain $\dot{\epsilon}$ is given by

$$\dot{\epsilon} = 0 = \dot{\sigma}/G + K\sinh(\alpha\sigma) \tag{2.120}$$

[3] if the value ϵ is measured in relative units, then λ in the equation (2.118) has to be replaced by λ divided by the length of sample at rest.

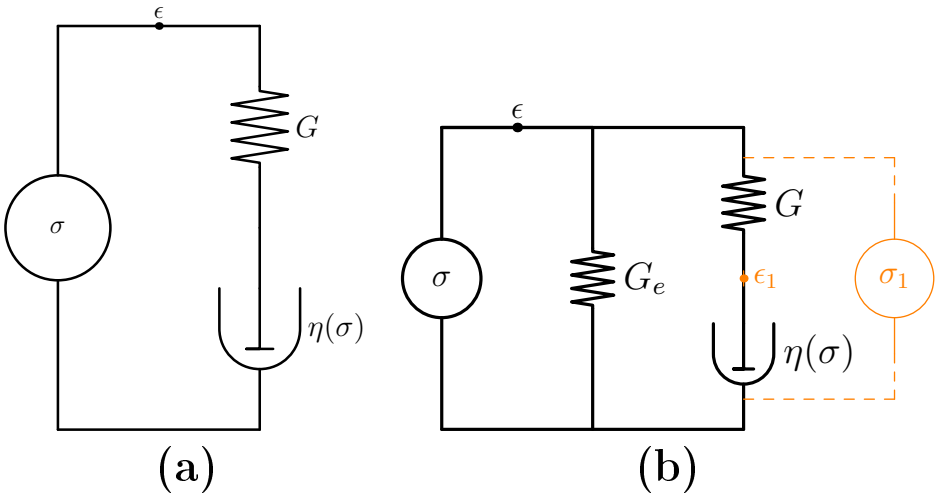

Figure 2.30.: **Eyring model for viscoelastic processes**
Diagram representation of a purely viscous process (a) and of the solid viscoelastic body model (b) with non-Newtonian dashpot $\eta(\sigma)$ described by equation (2.118). Springs G and Ge represent purely elastic components, which store the energy according to the Hook's law $\sigma(t) = G\epsilon(t)$.

where $\dot{\epsilon}$ is the rate of strain and $\dot{\sigma}$ is the rate of stress, G is the elastic modulus of the spring. Introducing the substitutions

$$\tau \equiv -(K\alpha G)t, \quad \phi \equiv \alpha\sigma \tag{2.121}$$

we arrive at the equation

$$\frac{d\phi}{d\tau} = \sinh(\phi) \tag{2.122}$$

which can be integrated using the standard integral (e.g. Gradstain, Rishik [56]):

$$\int \frac{dx}{\sinh x} = \ln \operatorname{th}\frac{x}{2} = \frac{1}{2}\ln\frac{\cosh x - 1}{\cosh x + 1} \tag{2.123}$$

this leads to

$$\ln \operatorname{th}\frac{\phi}{2} = \tau + const \tag{2.124}$$

With the initial conditions $\sigma(t = 0) = \sigma_0$ the above equation reads

$$\operatorname{th}\frac{\alpha\sigma}{2} = \operatorname{th}\frac{\alpha\sigma_0}{2}\ \exp(-ct) \tag{2.125}$$

where $\equiv c = \alpha KG$ defines the time-scale of the relaxation process as $\tau_0 = 1/c$. Figure 2.31 shows a plot of stress $\sigma(t)$ against $\log_{10} ct$ according to equation (2.125) for several values

of the parameter $\alpha\sigma_0$. If the value of $\alpha\sigma$ is larger than unity and $\sigma_0 > \sigma > 1/(2\alpha)$, the behaviour of $\sigma(t)$ can be approximated [167] as:

$$\sigma(t) = -\frac{1}{\alpha}\left(\ln(c/2) + \ln(t)\right) = -\frac{1}{\alpha}\ln\frac{t}{2\tau_0} \tag{2.126}$$

which is the expression of the type: $b - a\ln(t)$, where a,b are constants. Such a behaviour was reported for rubber.

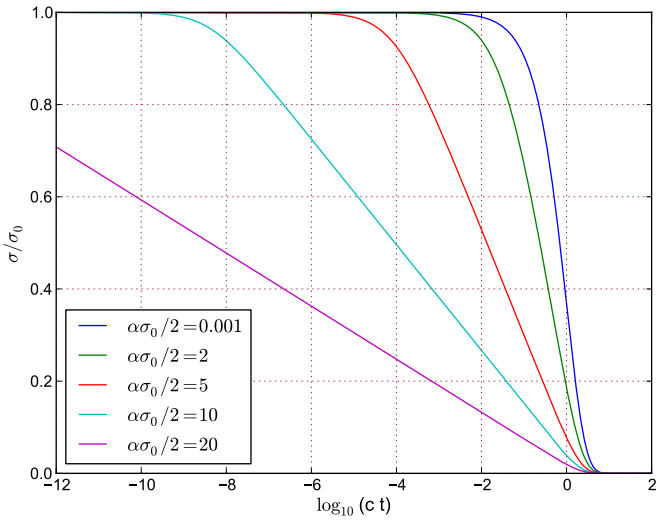

Figure 2.31.: **Relaxation of stress**

Figure shows a plot of the stress $\sigma(t)$ against $\log_{10} ct$ according to equation (2.125) for several values of the parameter $\alpha\sigma_0$.

Another, very similar, approximation for large values of α can be made [77] using the asymptotic of the sinh function, i.e. $\sinh x \approx \exp(x)$ for $x \gg 1$..
Equation (2.122) then reads

$$\frac{d\phi}{d\tau} = \exp(\phi) \tag{2.127}$$

and the approximated behaviour is

$$\sigma(t) = \sigma_0 - \frac{2}{\alpha}\ln(1 + bt) \tag{2.128}$$

with b equals to $KG\alpha\exp(\alpha\sigma_0/2)$.

Application of Eyring's model to experiments with constant rate of strain [63, 167]

Similar considerations apply to the case when the rate of strain is constant but non-zero. The constitutive equation for the viscous element with a spring in series (see Figure 2.30(a)) becomes:

$$\dot{\epsilon} = \dot{\sigma}_1/G + K\sinh(\alpha\sigma_1) \tag{2.129}$$

Where ϵ is strain, α,K are defined in the previous paragraph and σ_1 relates to a total response stress σ as

$$\sigma = \sigma_1 + G_e\epsilon \tag{2.130}$$

G_e is the equilibrium modulus of elasticity. The meaning of the parameters is shown in Figure 2.30 (b).
Using a substitution similar to (2.121), i.e.

$$\begin{aligned} \tau &\equiv (K\alpha G)t = t/\tau_0 \\ \phi &\equiv \alpha\sigma_1(t) \\ \beta &\equiv \frac{\dot{\epsilon}_0}{K} \end{aligned} \tag{2.131}$$

we can reduce the differential equation (2.129) to the following form:

$$\frac{d\phi}{d\tau} = \beta - \sinh\phi \tag{2.132}$$

The parameters α, K, G have the same meaning as in (2.121). $\beta = \dot{\epsilon}/K$ is the quotient of the rate of strain to the velocity of the thermally activated of flow K forward or backward in the case in equilibrium and $\sigma = 0$.
The authors of [63] give the integration of the reduced equation above in the form which is not suitable for our further purposes. Hence we derive here an alternative solution of the equation (2.132). This is done using the integral from (Gradstain and Rishik [56]):

$$\int \frac{d\phi}{\beta - \sinh\phi} = \frac{2}{\sqrt{\beta^2+1}}\mathrm{th}^{-1}\frac{\beta\mathrm{th}(\phi/2)+1}{\sqrt{\beta^2+1}} = \tau - c \tag{2.133}$$

Resolving this with respect to ϕ (which is $\alpha\sigma$) we arrive at:

$$\phi(\tau) = 2\mathrm{th}^{-1}\frac{\sqrt{\beta^2+1}\mathrm{th}\left[\frac{\sqrt{\beta^2+1}}{2}(\tau-c)\right]-1}{\beta} \tag{2.134}$$

The value of the constant c is defined by the initial condition $\phi_0 = \phi(0)$ resulting in

$$c = -\frac{2}{\sqrt{\beta^2+1}}\mathrm{th}^{-1}\frac{\beta\mathrm{th}(\phi_0/2)+1}{\sqrt{\beta^2+1}} \tag{2.135}$$

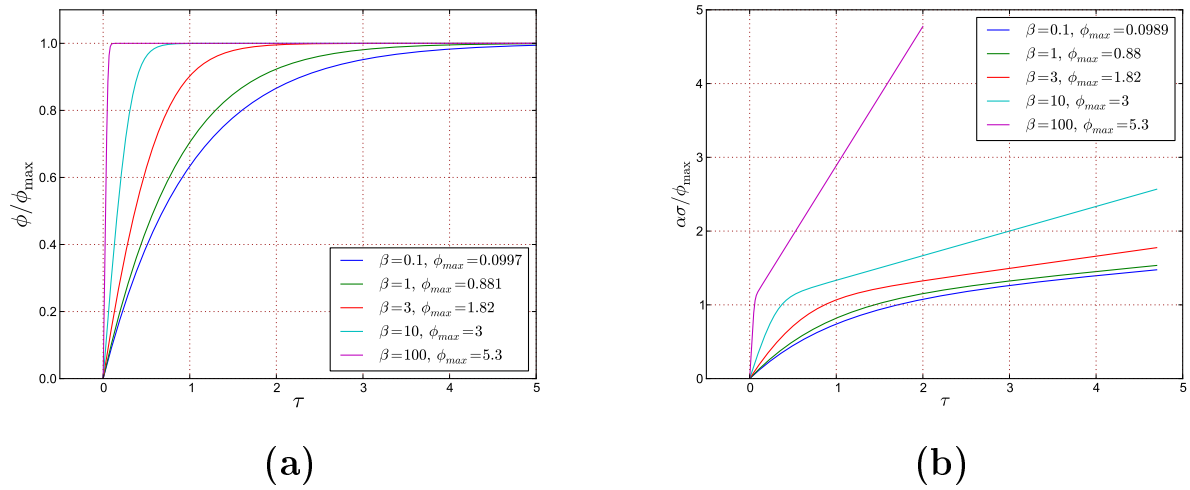

Figure 2.32.: **A response to a slope excitation for various values of** β
Panel (a) shows a plot of $\phi(\tau)/\max(\phi)$ for several values of β. The value of $\max\phi$ is defined in equation (2.136). Panel (b) shows the response of a 3-element-model to a constant rate of strain for the same values of β as in panel (a) and $G_e/G = 0.1$, (see eq. (2.137)).

Figure 2.32 shows a plot of $\phi(\tau)/\max(\phi)$ for several values of β. The function $\phi(\tau)$ reaches its maximum value at $\tau = \infty$:

$$\phi_{\max} = \lim_{\tau=\infty} \phi(\tau) = 2 * \text{th}^{-1} \frac{\sqrt{\beta^2 + 1} - 1}{\beta} \tag{2.136}$$

The over-all response shown by the 3-elements-model to an excitation with constant rate of strain will be a sum of the stress due to the Maxwell unit (i.e. dashpot η and spring G in series) $\sigma_1 = \phi/\alpha$ and stress caused by the spring element $G_e\dot{\epsilon}t$ as in (2.130). I.e. in reduced units (2.131) the total response stress is defined as

$$\sigma = \frac{\phi(\tau) + \frac{Ge}{G}\beta\tau}{\alpha} \tag{2.137}$$

Yield point as function of the rate of strain The yield point for the 3-element-model, as shown in figure 2.31(b) can be specified as follows (see fig. 2.33):

The yield point is defined as the intersection of two asymptotic lines: one is the asymptote

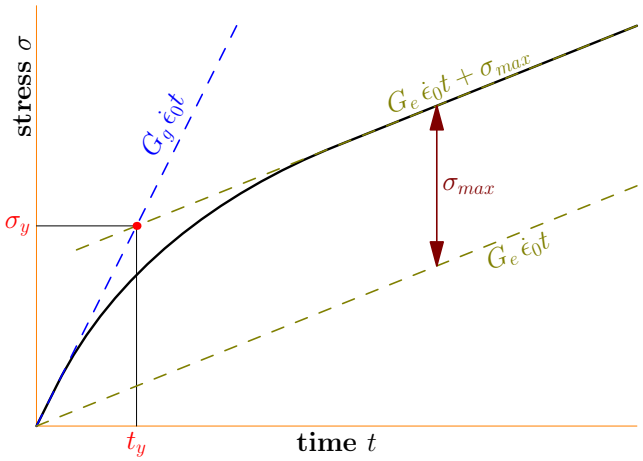

Figure 2.33.: **Determination of the yield point for 3 element model**

at small times $G_g\dot{\epsilon}_0 t$ and the other for large times $G_e\dot{\epsilon}_0 t + \sigma_{max}$. Here $\sigma_{max} = \phi_{max}/\alpha$ and ϕ_{max} are given in (2.136) and means the stress at which the steady flow is reached. This leads to expression for coordinates of the yield point (t_y, σ_y):

$$t_y = \frac{\sigma_{max}}{G\dot{\epsilon}} = \frac{\phi_{max}}{(\alpha G K)\beta} = \tau_0 \frac{\phi_{max}}{\beta} \tag{2.138}$$

$$\sigma_y = G_g\dot{\epsilon}_0 t_y = \frac{G_g}{G}\frac{\phi_{max}}{\alpha} \tag{2.139}$$

In the space of reduced variables τ, ϕ this takes the form:

$$\tau_y = \frac{\phi_{max}}{\beta} \tag{2.140}$$

$$\phi_y = \frac{G_g}{G}\phi_{max} \tag{2.141}$$

$$\tag{2.142}$$

Functions $\phi_{max}(\beta)$ and $\tau_y(\beta)$ are shown in figure 2.34. The equations (2.142) have to be compared for the yield point coordinates, derived for the 3-elements-model of the linear viscoelastic theory:

$$t_y = \tau = \eta/G \tag{2.143}$$

$$\sigma_y = G_g \tau \dot{\epsilon}_0 \tag{2.144}$$

this shows a linear dependence of the yield stress σ_y from the rate of strain $\dot{\epsilon}_0$ and yield time is constant, equals to the relaxation time τ.
Frequently, somewhat different definition of the yield point is used in the literature [77]: a yield point is defined as the point at which $\dot{\sigma} = 0$. This definition is less practical, because it can be difficult to derive the position of this point from the experimental data. Together with the constitutive equation (2.132) this definition yields:

$$\phi_y = \alpha\sigma_y = \sinh^{-1}\beta \approx \ln(\beta) \tag{2.145}$$

where the last approximation assumes $\alpha\sigma \gg 1$. This means that the dependence of the yield point on the rate of strain is a straight line in the plots of stress versus logarithm of rate of strain.

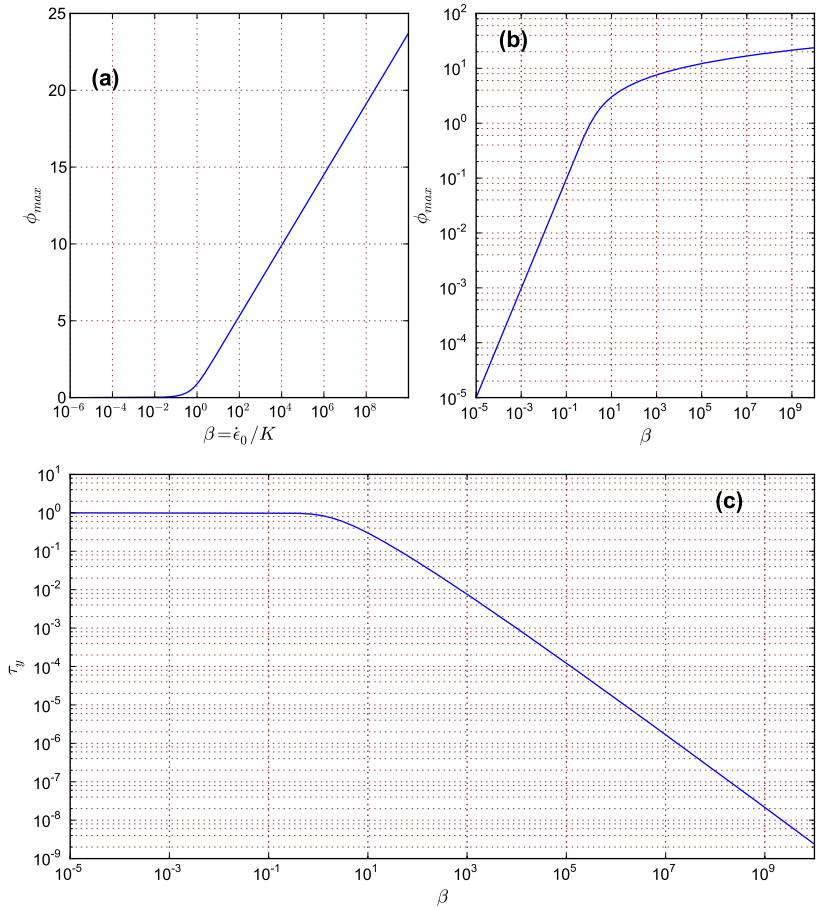

Figure 2.34.: **functions $\phi_{\mathbf{max}}(\beta)$ and $\tau_{\mathbf{y}}(\beta)$**

The functions ϕ_{max} and τ_y directly relate to the coordinates of the yield point, see equation (2.142). From figure it is visible, that time position of the yield point is nearly constant for small rate of strain $\beta \leqslant 1$ and is logarithmically decreasing if the range of large rate of strain. Similar, the behaviour of $\phi_{max}(\beta)$ exhibit a two types of behaviour. In the range of large strain of rate it is nearly linear dependent from $\log(\beta)$ and in the range of small β it is nearly linear function of β. This demonstrate that in the range of small β the Eyring's 3-element-model behaviour is very close to the linear viscoelastic one.

Two-state model

The model, discussed here, is introduced in [14, 15] in order to describe mechanical properties of fibrous polymeric materials. It was inspired by the folding kinetic of proteins such as the $\alpha \to \beta$ transition in keratin. Our interest in this model is based on the modern perception in the protein physics, i.e. that the folded and unfolded (denatured) protein structures are separated by the all-or-nothing phase transition. See the short discussion on p. 66. A theoretical justification of the two-state kinetic model of protein folding has recently been given by R. Zwanzig [186] in terms of rate constants and folding thermodynamics.

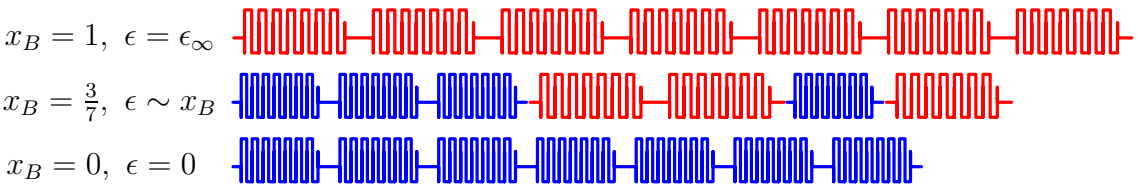

Figure 2.35.: **Elongation due to an $A \to B$ transition**
The sketch demonstrates an elongation due to the molecular transition from the state A (represented by blue coloured units) to the state B (represented by red coloured units). x_A and x_B are fractions of the A and B species, respectively. The conservation rule $x_A + x_B = 1$ applies. Neglecting the elastic deformation of the molecular units in the A and B states, the strain is proportional to the populations of B species.

We will introduce the model with the help of figures 2.35 and 2.36.

- `binary (solid) solution:` The material is assumed to contain a molecular units (in a very averaged sense) which can be in a one of the two-states, let us call them A,B. Molecular units in the state B are longer than those in the A state.
- `species` A,B `are purely elastic:` In each state the molecular units respond only elastically to an external excitation.
- `elongation as phase transition in binary system` The inelastic part of elongation of the material is postulated to be due to the transition $A \leftrightharpoons B$ and qualitatively is proportional to the population of the B species. See sketch in figure 2.35
- `rates of reaction` In the phase space the states of molecular units are separated by a barrier as shown in figure 2.36. Hence, the rates of reaction $A \leftrightarrow B$ can be described in the manner of the Eyring's theory of reaction rates, described earlier on page 64.

Remark 1 *The two states A,B should not be thought as a separate states (discrete entities), but rather as an averaging points for a spectrum of states. The main assumption is that there is a well defined boundary separating spectra at the low end of elongation from that of the high end of elongation. The conditions of applicability of the two-state dynamics are similar to that, suggested for emulation of protein folding dynamics by two-state kinetics in [186].*

`Purely viscous element (dash-pot):`

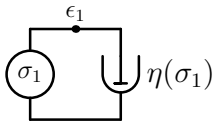

We will, firstly, neglect the elastic deformation of the two structures, an elastic correction will be done later. If elastic deformations are neglected, the elongation becomes a conformational nature and is proportional to the fraction (population) of molecular units in the state B. Because the material consists of a solid solution of the molecular units in the states A and B we will find the rate of the elongation to be proportional to the relative abundance of the transformed species. If ϵ_∞ is the relative elongation (strain) when all of the molecular units are in the state B, then some intermediate strain ϵ relates to the population x_B of the molecular segments in the state B responsible for this elongation as

$$x_B = \frac{\epsilon}{\epsilon_\infty} \tag{2.146}$$

Without applied stress, the forward rate k_f^o and backwards rate k_b^o of reaction $A \underset{k_f}{\overset{k_b}{\rightleftharpoons}} B$ are

$$k_f^o = \frac{k_B T}{h} e^{-\frac{\Delta G_A^\ddagger}{k_B T}} \tag{2.147}$$

$$k_b^o = \frac{k_B T}{h} e^{-\frac{\Delta G_B^\ddagger}{k_B T}} \tag{2.148}$$

where k_B is the Boltzmann and h is the Planck's constants,respectively. T is the temperature, and $\Delta G_A^\ddagger, \Delta G_B^\ddagger$ are heights of the barrier to be surmounted in the transitions $A \rightarrow B$ and $A \leftarrow B$ respectively; see sketch on figure 2.36.
When a stress σ is applied the reaction coefficients are modified and:

$$k_f = \frac{k_B T}{h} e^{-\frac{\Delta G_A^\ddagger - v_a \sigma/2}{k_B T}} = k_f^o e^{\frac{v_a \sigma}{2 k_B T}} \tag{2.149}$$

$$k_b = \frac{k_B T}{h} e^{-\frac{\Delta G_B^\ddagger + v_a \sigma/2}{k_B T}} = k_b^o e^{-\frac{v_a \sigma}{2 k_B T}} \tag{2.150}$$

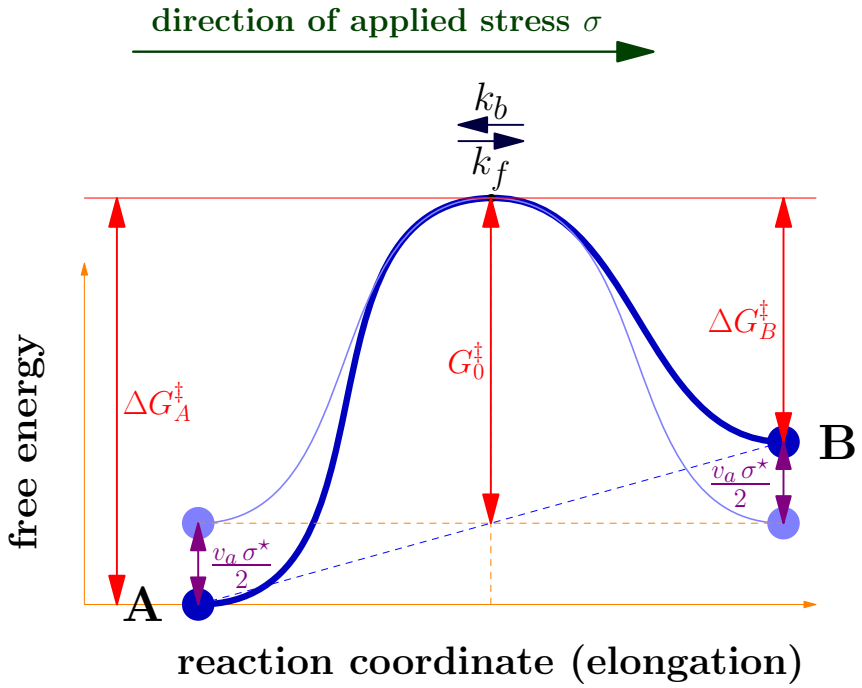

Figure 2.36.: **Potential barrier separating states A and B**
A free energy barrier separating the two states A and B is shown. The thick blue line represents a real barrier. $\Delta G_A^\ddagger$ is the barrier height to be surmounted by the reaction $A \rightarrow B$ and $\Delta G_B^\ddagger$ is the barrier height to be surmounted by the reaction $B \rightarrow A$. The forward coefficient of reaction is denoted by k_f and backwards coefficient by k_b. The thin light-blue line represents a hypothetical symmetric potential used to simplify calculations, see equations (2.151 - 2.160) The symmetric potential is transformed to the (asymmetrical) real potential by application of the 'internal stress' $\sigma^\star$. It is defined in (2.151, 2.152). $\Delta G_0^\ddagger$ is the height of the symmetrical potential and v_a is the activation volume of the reaction.

where v_a is an activation volume, i.e. the volume covered by the molecular unit through the $A \rightarrow B$ reaction or its inverse. Introducing the mean barrier height $\Delta G_0^{\ddagger}$ and the *internal stress* $\sigma^{\star}$

$$\Delta G_0^{\ddagger} = \frac{\Delta G_A^{\ddagger} + \Delta G_B^{\ddagger}}{2} \tag{2.151}$$

$$v_a \sigma^{\star} = \Delta G_A^{\ddagger} - \Delta G_B^{\ddagger} \tag{2.152}$$

we can write these coefficients in a symmetrical way:

$$k_f = K e^{\alpha(\sigma - \sigma^{\star})} \tag{2.153}$$

$$k_b = K e^{-\alpha(\sigma - \sigma^{\star})} \tag{2.154}$$

$$\tag{2.155}$$

where the following substitutions are used:

$$K = \frac{k_B T}{h} e^{-\frac{\Delta G_0^{\ddagger}}{k_B T}} \tag{2.156}$$

$$\alpha = \frac{v_a}{2 k_B T} \tag{2.157}$$

The net rate of reaction then takes the form:

$$\dot{x}_B = k_f - (k_f + k_b) x_B = k_f - k x_B = k(\frac{k_f}{k} - x_B) = -k(x_B - x_B^{eq}) \tag{2.158}$$

where $\Delta\sigma = \sigma - \sigma^{\star}$ and the 'equilibrium' population x_B^{eq} of molecular units in the B state is introduced as:

$$x_B^{eq} = \frac{k_f}{k_f + k_b} = \frac{1}{1 + e^{-2\alpha(\sigma - \sigma^{\star})}} = \frac{1}{2}\left(1 + \mathrm{th}\left(\alpha(\sigma - \sigma^{\star})\right)\right) \tag{2.159}$$

The 'equilibrium population' x_B^{eq} means the population x_B at which the system would be in equilibrium with the stress σ, i.e. it is defined by the condition $\dot{x}_B(\sigma = const) = 0$. The curve drawn through the points (σ, x_B^{eq}) is called '`spring line`'.
The value k denotes the sum of the reaction coefficients $k_f + k_b$ and can be rewritten as:

$$k \equiv k_f + k_b = 2K \cosh\left(\alpha(\sigma - \sigma^{\star})\right) \tag{2.160}$$

with K defined in (2.156).
From the above consideration it is obvious that at equilibrium and in absence of stress some (usually small) amount of the molecular units (x_B^o) will be in the state B, corresponding to the equilibration of the transition $A \leftrightharpoons B$ at given environmental conditions. This leads

to a usually small (but non-zero) initial elongation, already present without any stress applied:

$$\epsilon^o = \epsilon_\infty x_B^o = \frac{\epsilon_\infty}{1 + e^{2\alpha\sigma^\star}} \tag{2.161}$$

The rate of strain corresponding to $\dot{x}_B$ in (2.158) becomes:

$$\dot{\epsilon} = \epsilon_\infty \dot{x}_B = -2K\epsilon_\infty \cosh(\alpha\Delta\sigma)(x_B - x_B^{eq}) \tag{2.162}$$

Or, introducing the reduced units:

$$\beta = \frac{\dot{\epsilon}}{\epsilon_\infty K} \tag{2.163}$$

$$\phi = \alpha\sigma\,, \quad \phi^\star = \alpha\sigma^\star \tag{2.164}$$

$$\Delta\phi = \alpha\Delta\sigma = \phi - \phi^\star \tag{2.165}$$

(2.162) transforms to the reduced equation for the rate of strain:

$$\beta = e^{\Delta\phi} - 2x_B \cosh(\Delta\phi), \quad \texttt{or} \quad \Delta\phi = \ln\left(\frac{\beta + \sqrt{\beta^2 + 4x(1-x)}}{2(1-x)}\right) \tag{2.166}$$

Three limiting cases can be distinguished:

1. `fast elongation` $\beta >> 1$
   a large value of the rate of strain leads to a large amount of stress, which can be approximated as
   $$\Delta\phi = \ln\frac{\beta}{1 - x_B}$$
2. `slow deformation` $\beta \approx 0$
   by small values of β the material will be nearly relaxed and the value of $x_B \approx x_B^{eq}$. The approximated relation for the stress becomes
   $$\Delta\phi = \frac{1}{2}\ln\frac{x_B}{1 - x_B}$$
3. `contraction`
   Because no contraction (negative) stress can be applied to a fibrous material, the maximal value of $-\beta$ on the contraction path can not exceed the value $x_B e^{\phi^\star}$.

Figure 2.37 shows a plot of $\phi(x_B)$ for several values of β computed using equation (2.166) with the internal stress $\phi^\star = 2.0$.

`correction for elastic deformation:`

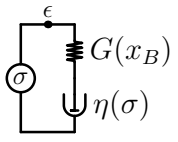

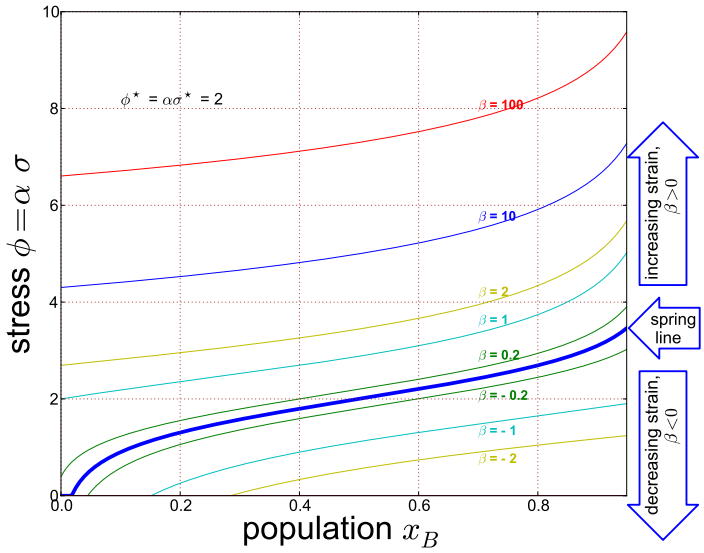

Figure 2.37.: **Model behaviour without elastic correction (β=const)** The thick blue line shows the equilibrium or 'spring' line. The area above the spring line corresponds to an elongation, i.e. positive velocities $\beta > 0$. The area under this line corresponds to a contraction, $\beta < 0$.

Let us introduce the elasticities of the molecular units. We allow molecular units to respond elastically with elastic moduli G_A in the state A and G_B in the state B. Then the constitutive equation of the model becomes:

$$\dot{\epsilon} = \frac{\dot{\sigma}}{G(x_B)} + \epsilon_\infty \dot{x}_B(\sigma) \tag{2.167}$$

$$\dot{x}_B = -2K\cosh(\alpha\Delta\sigma)(x_B - x_B^{eq}) \tag{2.168}$$

where $G(x_B)$ is a combined elastic modulus, which will be a function of the population x_B. The form of this function will depend on the way we arrange the elastic moduli of the molecular units in the state A and B, see figure 2.38 (a). Two possible combination of the pure elastic elements for A and B states are shown in panels (a,b) of figure 2.38. With such arrangements of the elastic elements the combined relaxance $G(x_B)$ becomes:

$$G(x_B) = G_A(1 - x_B) + G_B x_B, \quad \texttt{in parallel}, \texttt{fig. 2.38(b)} \tag{2.169}$$

$$\frac{1}{G(x_B)} = \frac{(1 - x_B)}{G_A} + \frac{x_B}{G_B}, \quad \texttt{in series}, \texttt{fig. 2.38(c)} \tag{2.170}$$

If $G_A = G_B$, then $G(x_B)$ will be constant, independent from the population x_B.
The equation (2.167) was suggested in [14] to connect strain, stress and population x_B of the B species. We must note here that another ansatz for such a relation is possible, namely:

$$\epsilon(t) = \frac{\sigma}{G(x_B)} + \epsilon_\infty x_B(t) \tag{2.171}$$

The differentiation of 2.171 with respect to time will lead to additionally the term $-\sigma\frac{\dot{G}(x_B)}{G^2(x_B)}$ because x_B is a function of time. This term is zero in the case of an equality of the elastic moduli in the A and B states.
For demonstration purposes we show an example of the model behaviour for a tooth-like strain excitation in figure 2.39 and a step strain excitation in figure 2.40. The model constants where chosen as follows:

> Elastic moduli $\alpha \cdot G_A = \alpha \cdot G_B = 350$, max strain due to $A \rightarrow B$ transition $\epsilon_\infty = \frac{1}{10}$, transition frequency constant $K = 0.001\frac{1}{s}$ and 'internal stress' $\phi^\star = 2$.

From this example is it clearly visible that the model shows a similar relaxation behaviour as compared with that discussed previously, that is Eyring's model of shear flow (compare with fig. 2.31). From the response to a constant rate of strain excitation it can be concluded that model can simulate the rubbery behaviour, i.e. a yield point followed by a plateau which transits to the strain hardening regime, see figure 2.39.

Generally, to be applicable to specific behaviour of a material, the following two condition must be satisfied:

1. The locus points, i.e. the spring line, must be a single-valued function of the elongation. This criterion is common to all 3-elements-models.
2. The response of the material to a cyclic tooth-like excitation must be reproducible on each successive loop.

The model reproduces many viscoelastic properties of the wool-nylon-rubber type quite well [14].

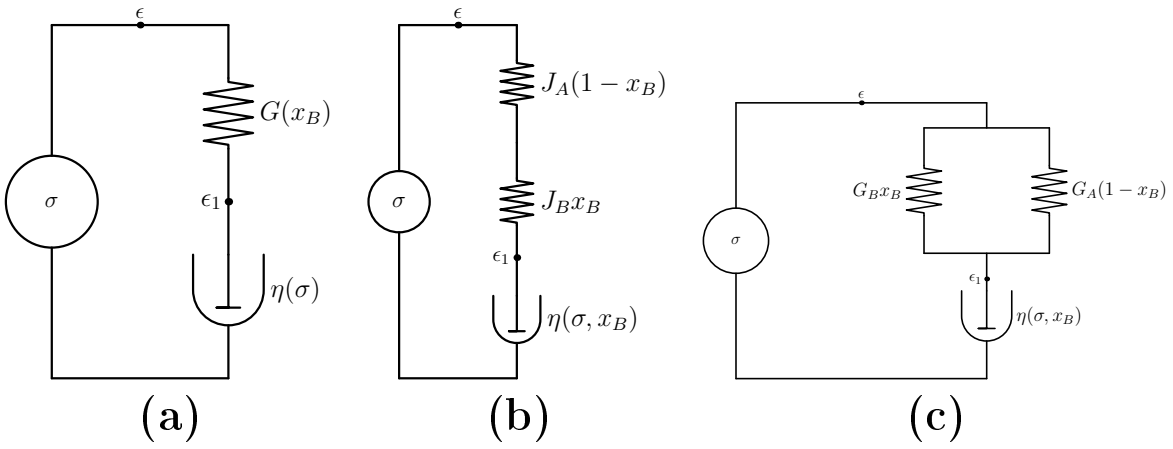

Figure 2.38.: **Dash-pot/spring representation of the two-state model**
A dash-pot/spring representation of the two-state model element is shown. Panel (a) shows a reduced representation, where $G(x_B)$ represents a combination of the Hooke's elements of a molecular unit in the state A and B as function of the population x_B. Panel (b) shows a situation with the Hooke's elements are combined in series. The combined retardance becomes $J(x_B) = 1/G(x_B) = J_A(1 - x_B) + J_B x_B$. Panel (c) shows a parallel combination of the elastic elements. The combined relaxance becomes $G(x_B) = G_A(1 - x_B) + G_B x_B$.
The model retardances are $J_A = 1/G_A, J_B = 1/G_B$, where G_A,G_B are the molecular unit moduli in the states A and B, respectively. The non-Newtonian dash-pot element denoted as $\eta(\sigma)$ represents the response at the $A \leftrightarrow B$ transition.

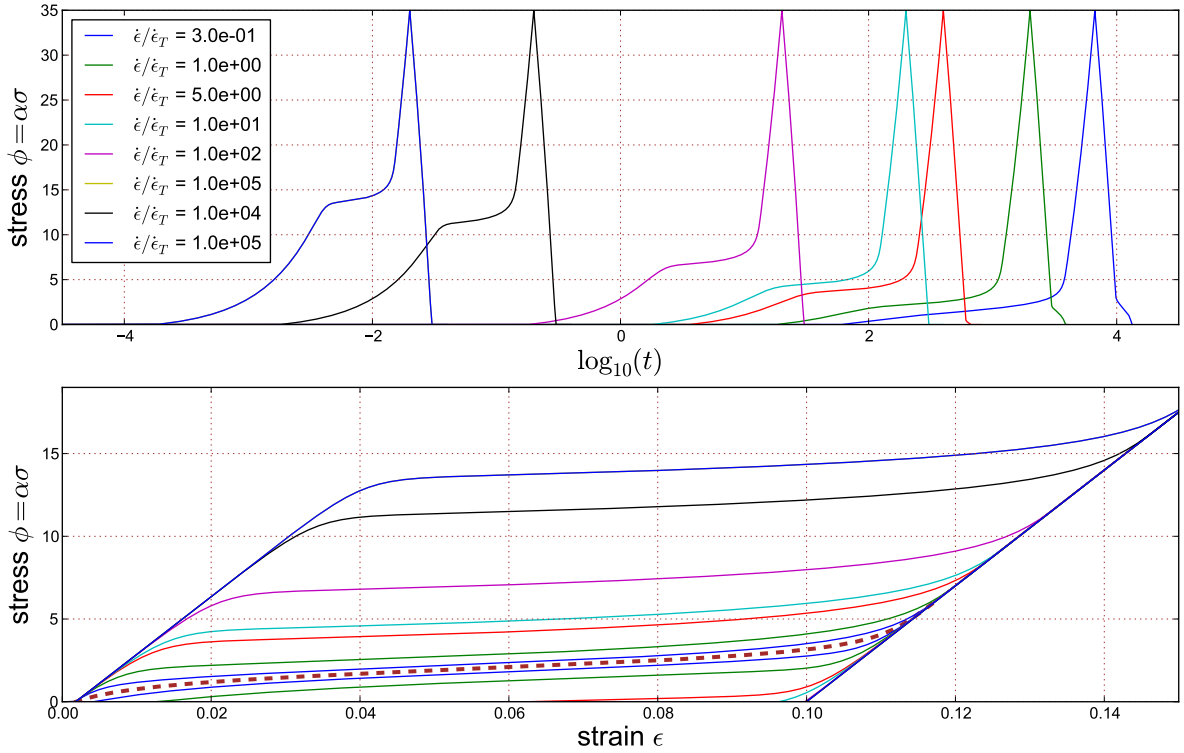

Figure 2.39.: **Model behaviour with elastic correction**

The figure shows a model response to an excitation of tooth form for several values of the rate of strain $\dot{\epsilon}$. The dashed brown line represents a spring (relaxed) line. The area above the spring line corresponds to the elongations, i.e. positive rate of strain $\dot{\epsilon} > 0$. The area below this line corresponds to contractions, i.e. $\dot{\epsilon} < 0$. The `'rate of thermal strain'` is defined as $\epsilon_T = K\epsilon_\infty$.

The model parameters used for the computation are:

$\alpha \cdot G_A = G_B = 350$, $\epsilon_\infty = \frac{1}{10}$, $K = 0.001\frac{1}{s}$, $\phi^\star = 2$

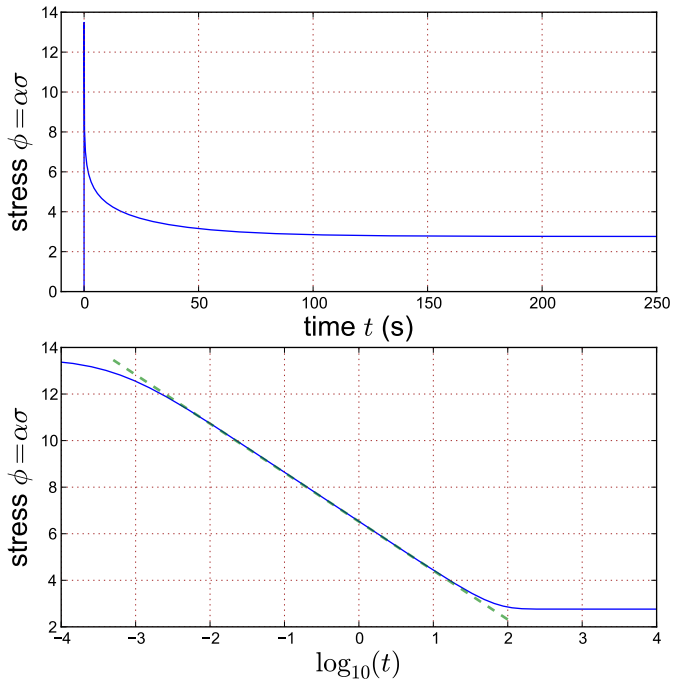

Figure 2.40.: **Model relaxation behaviour**

An example of the relaxation behaviour for the two-state model is shown. The model parameters used for the computation are:

$\alpha \cdot G_A = G_B = 350$, $\epsilon_\infty = \frac{1}{10}$, $K = 0.001\frac{1}{s}$, $\phi^\star = 2$.

The green line on the bottom panel demonstrates the similarity with Eyring model of shear flow, i.e. there is a wide linear range in the $\alpha\sigma(\log t)$ plot.

Three-state model As was discussed above the two-state model can describe a material with a simple response which is reproducible for a cyclic excitation. Consider, for example, a response to a cyclic loop excitation, shown on the figure 2.41.

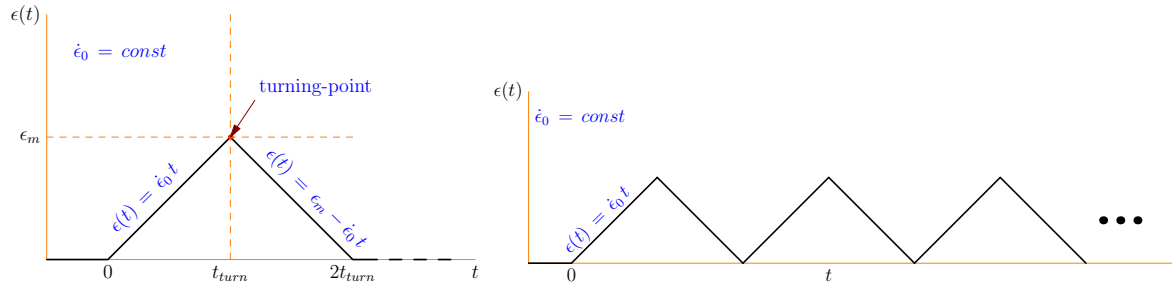

Figure 2.41.: **The form of a cyclic tooth excitation in strain**
The diagram on the left shows a parametrisation of a tooth-like strain excitation. The sketch on the right shows an example of the cyclic tooth excitation, it is realized by a repeated application of the excitation defined on the left panel.

A typical response to a such excitation which can be modeled by the two-state model is shown in the figure 2.42 (*a*). The response curve is reproduced during each successive 'tooth' (loop). On the other hand, silk belongs to a class of so called '`thixotropic`' materials [29]. Such materials show a response to a cyclic tooth excitation which is schematically represented in figure 2.42 (*b*). More details about these two types of response are given in the figure caption.
The main characteristics of a such response are:

- the response to the first elongation (olive curve in the figure) deviates from the response to the elongation in later loops.
- frequently there are one or more secondary yield regions.
- the response on the contraction path is nearly the same on each excitation loop.
- the responses in successive loops are very similar to each other. Frequently they are coincide.

A simple extension of the two-state model, introduced in [14, 15], allows to incorporate the phenomena listed above into a single model, which remain rather simple. This extension is the most simple from the rich set of similar models, which recently attained much attention in the studies of competitive trapping in the complex state space. This type of models is used to study of the interplay between the `energetic`, `entropic` and `kinetic` futures of the underlying molecular processes (see e.g. [38] and reference therein).

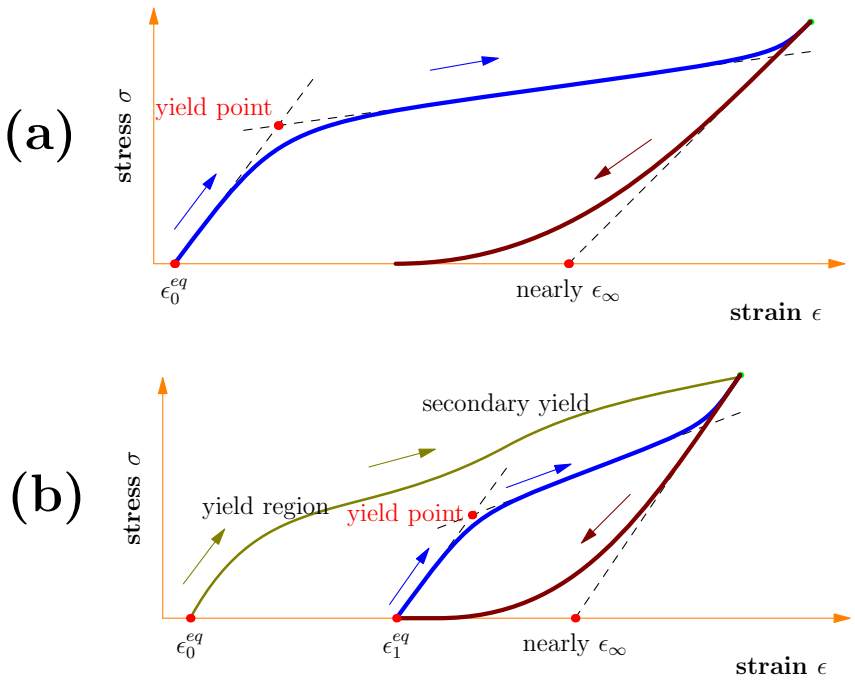

Figure 2.42.: **Two kinds of responses to a cyclic tooth excitation**
Two different types of response to a cyclic tooth excitation are sketched. The arrows indicate the direction of the strain-change (whether elongation or contraction).
Panel (a) shows a response which can be modeled by the two-state model. The behaviour is governed by the population of species in the state B. Here the response to an elongation is shown by the blue curve and the response to a contraction is shown by the brown curve. The response starts at the initial elongation, whose strain is denoted by ϵ_0^{eq} on the figure. The second point, denoted by the '`nearly` ϵ_∞' is defined by the value of elongation when all molecular units are in the state B. The response curve is fully enclosed by the 'elastic boundary', shown by the dashed black lines (on the left and right of the curve).
Panel (b) shows a response to a cyclic tooth excitation of a 'thixotropical' material: the response to a first elongation (olive curve) deviates from the repeated response due to the successive elongations (blue curve). The contraction path (brown curve) is the same on the each loop. The point ϵ_1^{eq} denotes the point where the response to an excitation is started on the each successive elongation. The second type of response frequently exhibits a `secondary yield` region.

Additionally to the two-states (i.e. folded A and extended B) in the previously considered model a third state C is introduced. This state is a pre-folded (or a 'pre-molten') state with the same average spatial elongation as the folded one but possessing a number of not established bonds and/or an unclosed ternary configuration. Hence the energy level of the C state has to be higher than that of the A state. The rate of transitions between the states A and C does not depend on the applied stress, because both states have the same spatial extension. The situation is represented by a diagram in figure 2.43.

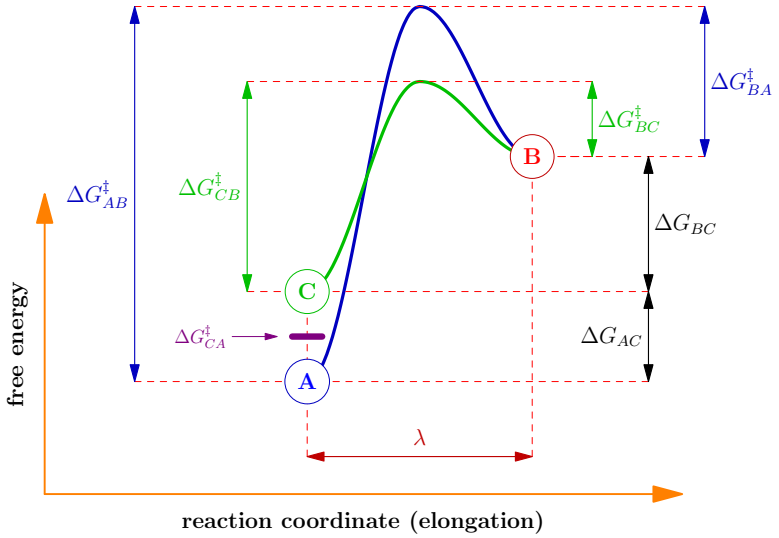

Figure 2.43.: **Energy barriers separating the states A, B, C**
Energy barriers for the three-state model are sketched. The blue curve is the barrier separating A and B states and the green curve that separating C and B. A represents the contracted (folded) state, B represents the elongated (denatured or unfolded) state. C is the pre-folded (or 'pre-molten') state with the same average elongation as the folded one but possessing a number of not established bonds and/or unclosed ternary configuration. Hence the energy of the C state is larger than that of the A state. The barrier separating A and C states is symbolically represented by a magenta thick line between the A and C circular knots.
Additionally, the figure gives a graphical definition of the values of activation energies $\Delta G^{\ddagger}_{\alpha\beta}$ and energy level differences $\Delta G_{\alpha\beta}$, where α, β can be any of A, B and C. The model can be specified by four energy parameters, e.g. $\Delta G^{\ddagger}_{BA}, \Delta G^{\ddagger}_{BC}, \Delta G_{AC}, \Delta G_{BC}$ shown on the right and the activation energy $\Delta G^{\ddagger}_{CA}$ for $C \to A$ transition. λ is the elongation of the molecular unit due to the transition either from the A or the C state to the state B.

The assumptions of the new model can be shortly summarized as follows (see figure 2.43):

- the molecular units in the states A and C are of the same size.
- the energy barrier for the reaction $B \leftrightarrow C$ is lover than that for the reaction $B \leftrightarrow A$, hence the former reaction is faster than latter.
- the rate of the transitions $C \leftrightarrow A$ is defined by the free energy barrier, but it is not a function of the elongation or stress. The transitions between the states A and C are considered to be much slower than the other transitions $A \leftrightarrow B$ and $C \leftrightarrow B$.
- similar to the two-state model, the strain of the material is governed by the population of the species in the state B, i.e. $\epsilon = \epsilon_{elastic} + \epsilon_{\infty} x_B$.

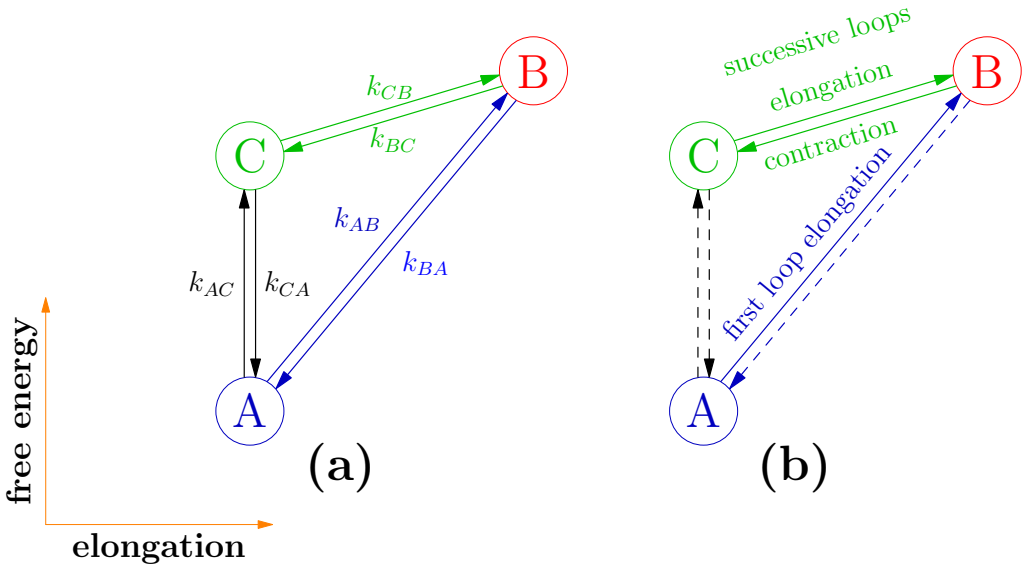

Figure 2.44.: **Transitions chart in the energy-elongation plane**
The transitions in the three-state model are sketched. Panel (a) shows the notation used for reaction coefficients of the transitions. The transition coefficients are related to activation energies as $k_{\alpha\beta} \sim \exp\left(-\frac{\Delta G^{\ddagger}_{\alpha\beta}}{k_B T}\right)$. Panel ($b$) shows a 'mainstream' transition of the model as they occur in a repeated stretching experiments. The 'mainstream' (most probable) transitions are represented by solid lines. The blue solid line shows the 'mainstream' transition during the first elongation, the green solid line $B \rightarrow C$ represents a 'mainstream' transition by the contraction in the each stretching loop, the line $C \rightarrow B$ represents the most probable transition by elongation in all successive loops. Dashed lines denote the other, slower processes.

To demonstrate the effects due to the presence of the third state C in the system let us consider an application of a cyclic tooth excitation, see sketch in figures 2.43, 2.44(b), 2.42(b) and numericaly computed examples shown in figures 2.46 and 2.47.
Let us first consider an idealized situation, where the material is initially prepared so that all its molecular units in the A state:

- `on the first loop`:
  The first elongation will cause a migration from the state A to the state B. This is represented by the blue arrow in figure 2.44(b).
  On retraction, the condition $\Delta G^{\ddagger}_{BA} > \Delta G^{\ddagger}_{BC}$ causes that a larger portion of B-species will transit into the state C, green down-left arrow on the figure.
- `on the successive cycles`
  At the beginning of each new loop the sample will be effectively longer than at the beginning of the first one. This loops initial elongation is due to a distribution of species over the states A, C and B, i.e. due to the presence of B-species in the system.
  Since $\Delta G^{\ddagger}_{AB} > \Delta G^{\ddagger}_{CB}$, the elongation will require less stress than necessary during the first stage, i.e. the richer the population of the C species is the less stress is required for the same elongation.
  During the retraction the system follows the same path as on the first loop.

More generally, the material can be prepared so that initially there is a distribution over the states A, B and C. In equilibrium the distribution is well defined and determines by the energy levels. Since the rate of transitions between the A and C states is assumed to be much lower than rates of $A \leftrightarrow B$ and $C \leftrightarrow B$ transitions, at the experimental time-scale the population of C species will define the 'length of the sample at rest'.
The rule of the thumb is as followed:

> any migration of the species from the A state to the C state will cause the redistribution of species between the C and B states, with increasing the population of B state. This means an effective elongation of the sample.

Now consider a sample in the initially equilibrated state. Its initial strain ϵ_0^{eq} is shown in figure 2.42(b); it is proportional to the equilibrated population x_B^{eq} of B species, i.e. $\epsilon_0^{eq} = \epsilon_\infty x_B^{eq}$.

- `on the first loop`:
  transition $C \to B$ will dominate until the population of C species is exhausted. On this stage the system will show a `first yielding` behaviour. Then the domination

of the transition $A \rightarrow B$ will cause an increase of the responding stress followed by the `secondary yielding` regime. See olive curves in figure 2.42(b) and in figures 2.46, 2.47.

On retraction, the $B \rightarrow C$ transition will dominate and at the end of the first cycle the elongation of the sample is defined mostly by the destribution over the C and B states. See brown curves in figures 2.42(b), 2.46 and 2.47.

- `on the successive cycles`
  as before, the dominat transition is $C \leftrightarrow B$ (blue curve in the mentioned figures) and the 'length at rest' is defined by a steady (or equilibrated) distribution at the end of the each successive loop. The initial strain at the beginning of each successive loop is denoted as ϵ_1^{eq} in figure 2.42(b).
- `after the last cycle`
  If the system will stay at rest, the dissipation of the B and C states will take place until equilibrium is reached. This dissipation is driven by the slowly transition $C \rightarrow A$ and the equilibration process can take a very long time, e.g. a few days or some decades of ohrs.
  This process can be called '`thixotropic recovery`'.

Mathematically the Maxwell element, shown in the figure 2.38(a), is described by the viscoelastic relation:

$$\dot{\epsilon} = \frac{\dot{\sigma}}{G} - \epsilon_\infty \dot{x}_B \qquad \texttt{or} \qquad \epsilon = \frac{\sigma}{G} - \epsilon_\infty x_B \tag{2.172}$$

where the meaning of symbols is the same as in the two-state model. The exception is G which represents here the combination of the three elastic elements. For purpose of simplification we will assume that the molecular units possess the same elastic modulus G in the each of their three states.

The time evolution of species population is described by a master equation for transitions between the states. It is based on the reaction coefficients $k_{\alpha\beta}$ for $\alpha \rightarrow \beta$ transition, where α, β can be one of A, B or C. As before, the value of the coefficients is defined by the activation energies:

$$k_{\alpha\beta} = \frac{k_B T}{h} e^{\frac{-\Delta G^{\ddagger}_{\alpha\beta}}{k_B T}} \tag{2.173}$$

The reaction rates can be specified as:

$$\begin{array}{lllllllll} r_{BA} & = & k_{BA}\, e^{-\alpha\,\sigma}\, x_B & r_{AB} & = & k_{AB}\, e^{\alpha\,\sigma}\, x_A & = & k_{BA}\, e^{\frac{\Delta G_{AB}}{k_B T}}\, e^{\alpha\,\sigma}\, x_A \\ r_{CA} & = & k_{CA}\, x_C & r_{AC} & = & k_{AC}\, x_A & = & k_{BA}\, e^{\frac{\Delta G_{AC}}{k_B T}}\, x_A \\ r_{BC} & = & k_{BC}\, e^{-\alpha\,\sigma}\, x_B & r_{CB} & = & k_{CB}\, e^{\alpha\,\sigma}\, x_C & = & k_{BA}\, e^{\frac{\Delta G_{BC}}{k_B T}}\, e^{\alpha\,\sigma}\, x_C \end{array} \tag{2.174}$$

the meaning of the coefficients $k_{\alpha,\beta}$ is sketched in figure 2.44, the activation free energies $\Delta G_{\alpha\beta}$ and the differences between energy levels $\Delta G\alpha\beta^{\ddagger}$ are defined as in figure 2.43. As before $\alpha = v_a/2k_BT$ and v_a is the activation volume, which we for convenience put to have the same value for each transition.
Introducing the following shorthands:

$$\begin{array}{ll} K_1 = k_{BA} & D_1 = e^{\frac{\Delta G_{AB}}{k_B T}} = D_2 D_3 \\ K_2 = k_{BC} & D_2 = e^{\frac{\Delta G_{BC}}{k_B T}} \\ K_3 = k_{CA} & D_3 = e^{\frac{\Delta G_{AC}}{k_B T}} \end{array} \tag{2.175}$$

the reaction rates from (2.174) will read:

$$\begin{array}{ll} r_{BA} = K_1\, e^{-\alpha\,\sigma}\, x_B & r_{AB} = K_1\, D_2 D_3\, e^{\alpha\sigma}\, x_A \\ r_{CA} = K_3\, x_C & r_{AC} = K_3\, D_3\, x_A \\ r_{BC} = K_2\, e^{-\alpha\,\sigma}\, x_B & r_{CB} = K_2\, D_2\, e^{\alpha\sigma}\, x_C \end{array} \tag{2.176}$$

The master equations for the evolution of the species populations is defined in terms of the reaction rates (2.176) as following:

$$\left\{ \begin{array}{lcl} \dot{x}_B & = & (r_{AB} - r_{BA}) + (r_{CB} - r_{BC}) \\ \dot{x}_C & = & (r_{BC} - r_{CB}) + (r_{CA} - r_{AC}) \end{array} \right. \tag{2.177}$$

which together with the viscoelastic relation (2.172) and the conservation law

$$x_A + x_B + x_C = 1$$

builds the simultaneus system of the equations describing the viscoelastic evolution of the system.
To demonstrate the behaviour of the model the responses to the strain excitations in the form of a slope (emulation of relaxation experiment) and a cyclic tooth is computed. Figure 2.45 shows an example of a relaxcation behaviour of the model and figures 2.46 and 2.47 show the response to a cyclic tooth excitation. It is clearly visible that the model resembles the main property of some real thixotropic materials (e.g. wet silk), i.e. the first and second yield, softening (rubbery plateau) and hardening.

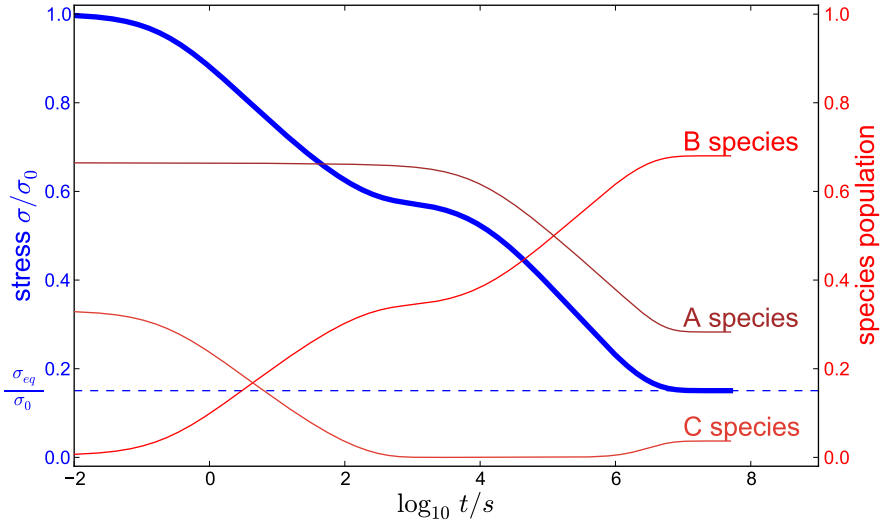

Figure 2.45.: **Relaxation behaviour of the three-state model**
Shows an example of a relaxation behaviour of the tree-state model. The axis on the left shows the stress and the axis on the right shows the populations of the states. The thick blue line represents the relaxation stress curve. The blue dashed line represents the equilibrated stress $\sigma_{eq} = G\left(\epsilon_0 - \epsilon_\infty x_B^{eq}\right)$. The initial values of strain ϵ_0 and force $\alpha\sigma_0$ were 0.08 and 11.93, respectively. The system relaxed in two stages: first the relaxation is mostly due to the dissipation of the C state, then due to the dissipation of A. The parameters of the model were chosen as follows: $\alpha G = 150.0$, $\epsilon_\infty = 0.1$, $\epsilon_\infty K_1 = 2 \cdot 10^{-7}\ 1/s$, $\epsilon_\infty K_2 = 10^{-6}\ 1/s$, $D_2 = 0.5$, $D_3 = 0.1$, $K_3 = 5 \cdot 10^{-7}\ Hz$.

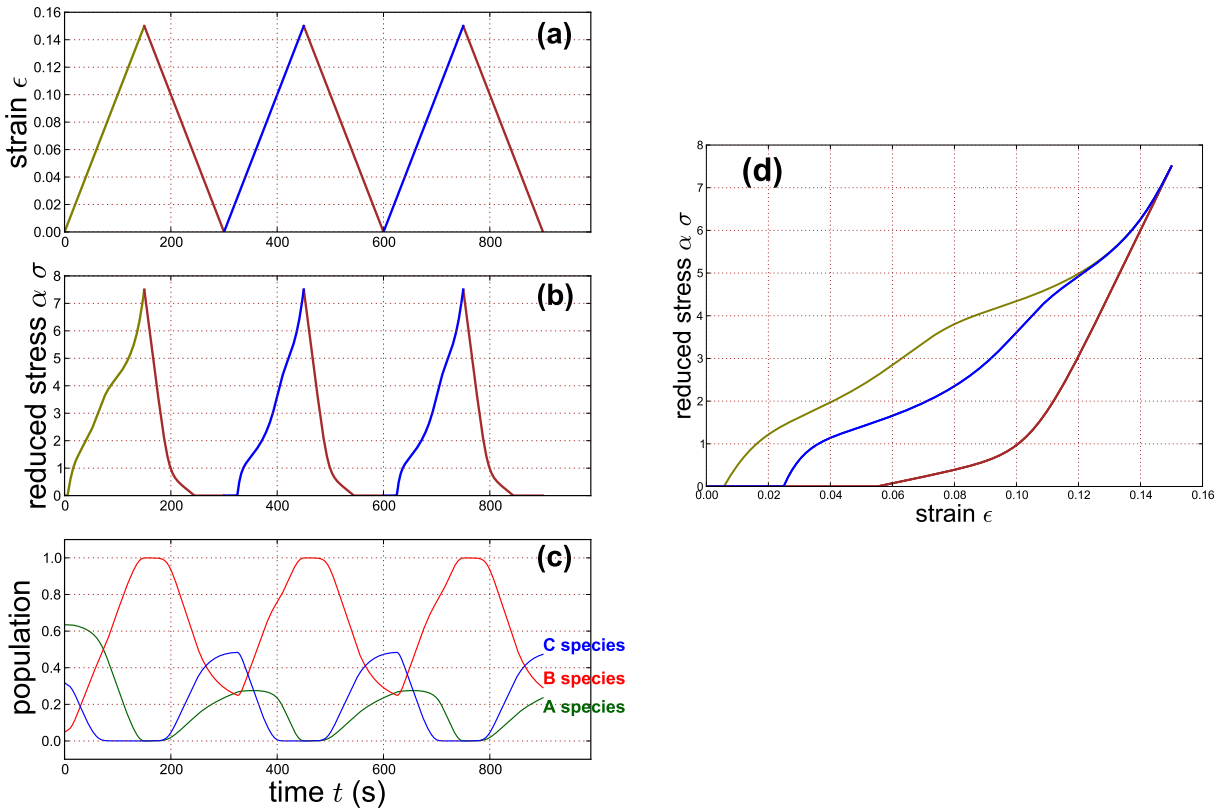

Figure 2.46.: **Response to a tooth excitation**

A response to a cyclic tooth excitation is shown. Panel (a) shows the strain excitation vs. time. Panel (b) shows the responded stress vs. time. Panel (c) shows the time evolution of populations of the A,B,C states. Panel (d) shows the plot of the stress-strain curve, this can be compared with figure 2.42. Three phenomena are visible: yielding, strain softening and strain hardening. The model exhibits a two yielding ranges on the first elongation, the second yielding region is visibly reduced on the successive stretching. The computation are done with the assumption that K_3 is small enough to be neglected. The parameters of the model were chosen as follows: αG=150, ϵ_∞=0.100, $K_1\epsilon_\infty$=0.0005 $(1/s)$, $K_2\epsilon_\infty$=0.00155 $(1/s)$, D_2=0.5, D_3=0.15, rates of strain ϵ=2 $K_1\epsilon_\infty$

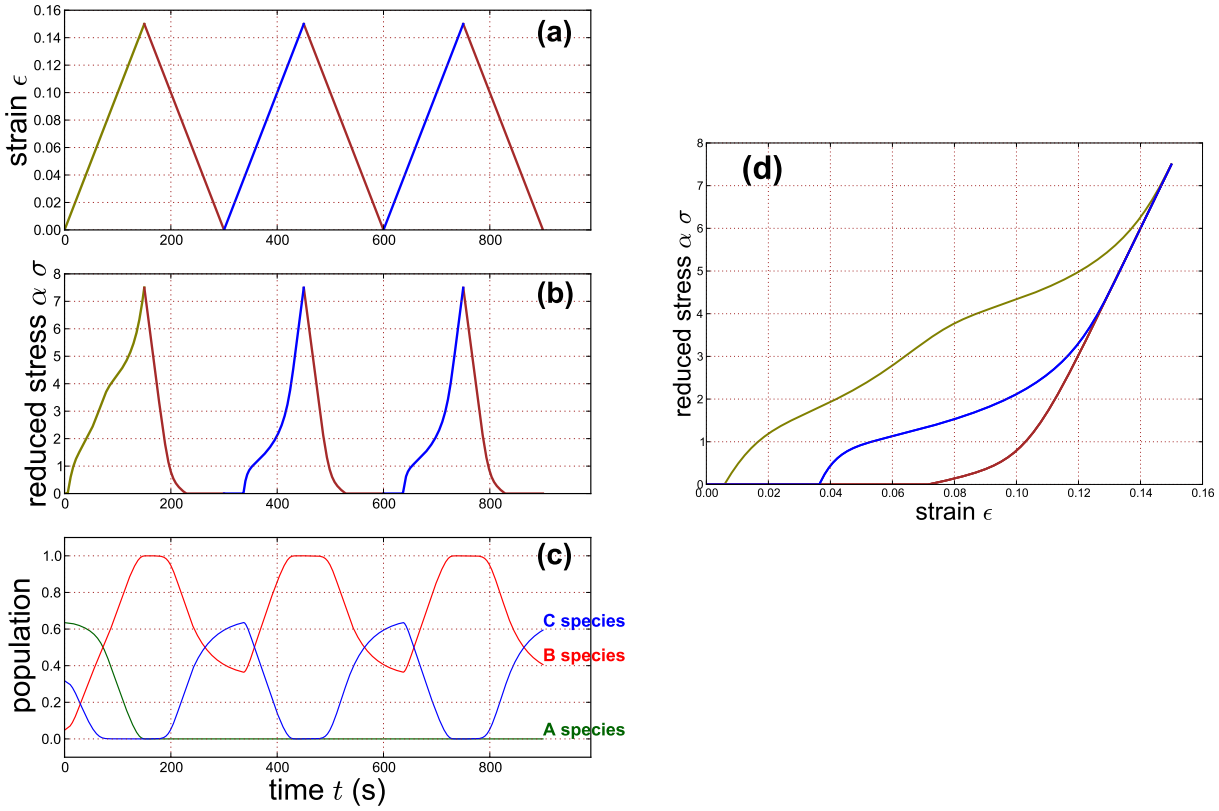

Figure 2.47.: **Response to a tooth excitation with a forbidden $A \leftarrow B$ transition**
A response to a cyclic tooth excitation is shown. The model parameters are the same as in figure 2.46, but the returning path is going exclusive over the $C \leftarrow B$ transition. With this regime the model shows no secondary yield point in successive loops.
Panel (a) shows the strain excitation as function of time. Panel (b) shows the responded stress as function of time. Panel (c) shows the time evolution of populations of the A,B,C states. Panel (d) show the plot of the stress-strain curve.

3. X-ray and neutron scattering

Neutron and X-ray scattering experiments belong to the best methods for studying the structural properties of matter on the molecular (atomic) level. A great deal of our knowledge about the structure and dynamics of condensed matter stems from such scattering experiments. In our *in situ* experiments we exploited cold neutrons and X-rays as probes to study the structure and the dynamics of stretched silk fibres as a function of the applied strain. In this chapter we summarize basic aspects and notations of the elementary scattering theory which are relevant to our work. For this brief presentation we mostly relied on: textbooks on X-ray diffraction [2, 60, 178] and neutron scattering [8, 162] as well as a review on diffraction [39] and lecture notes [4] about scattering methods. For more details about general scattering theory we refer to [96, 100].

3.1. Scattering problem

In a scattering experiment a beam of quanta[1] is allowed to strike a sample (i.e. scattering target) while quanta emerging from the sample area are observed. A sketch of a typical scattering experimental situation is shown in fig. 3.1. There are, at least, three elements of

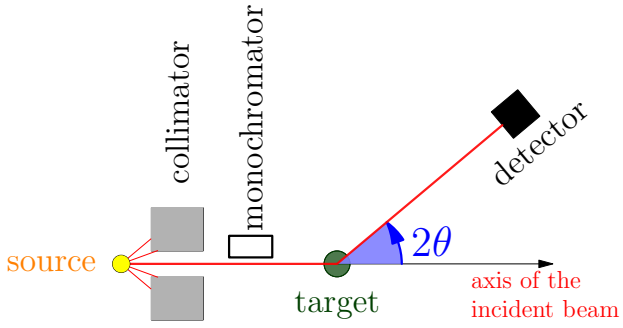

Figure 3.1.: **A typical set-up of a scattering experiment consisting of a source of quanta, a target (sample) and a detector**

[1] in our case the notion quanta denotes either neutrons or X-rays

a scattering experiment: a source of the incident beam, a target and a detector. As source we understand a device producing quanta; usually it is equipped with a collimator and a monochromator. The role of a collimator is to narrow the beam of particles or waves, i.e. it either causes the direction of motion to become more aligned in a chosen direction or it causes the spatial cross section of the beam to become smaller. A monochromator is a device which transmits a narrow band of energies (wavelengths) of radiation chosen from a wider range of wavelength available at the input. The role of the detector is to count (and record) the number of the scattered quanta as a function of direction and distance from the target. The recorded signal (counts) is usually called intensity. Scattering theory provides a convenient framework for an analysis/study of the properties of a target system in terms of the output of scattering experiments. The branch of the scattering theory, which is relevant for us, is based on a set of approximations and concepts, which will be shortly outlined in the following sections.

Specification of scattering experiments

In condensed matter science the so-called Fraunhofer or far-field approximation is usually valid. In this approximation the incident and scattered quanta can be described as plane waves with wavelengths λ_i and λ_f, propagating in the directions $\hat{k}_i$ and $\hat{k}_f$[2], respectively. The geometry of this process is illustrated in Figure 3.2.

The above-mentioned approximation implies [13] that in a scattering experiment the wave packet of the incident quantum is characterized by the (initial) state $(\vec{k}_i, E_i, \vec{e}_i)$ and the scattered quantum by the (final) state $(\vec{k}_f, E_f, \vec{e}_f)$:

$$(\vec{k}_i, E_i, \vec{e}_i) \xrightarrow{\text{scattering}} (\vec{k}_f, E_f, \vec{e}_f) \tag{3.1}$$

where $\vec{k}$ denotes the wave vector, E is the energy (eigenvalue) and $\vec{e}$ denotes the internal degree of freedom of quanta (for X-ray it is the polarization vector and for neutrons the spin). If the energy of the scattered quanta is unchanged in a scattering experiment one called it elastic scattering or diffraction, otherwise inelastic scattering. The analysis of the scattered intensity and of the energy of the scattered quanta with respect to the incident energy is called spectroscopy.

According to de Broglie, the momentum $\vec{p}$ of a quantum is related to the wave vector $\vec{k}$ and the wavelength λ as:

$$\hbar\vec{k} = \vec{p} \tag{3.2}$$

$$\lambda = \frac{2\pi}{|\vec{k}|} \tag{3.3}$$

[2] unit vectors are marked by a circumflex ˆ

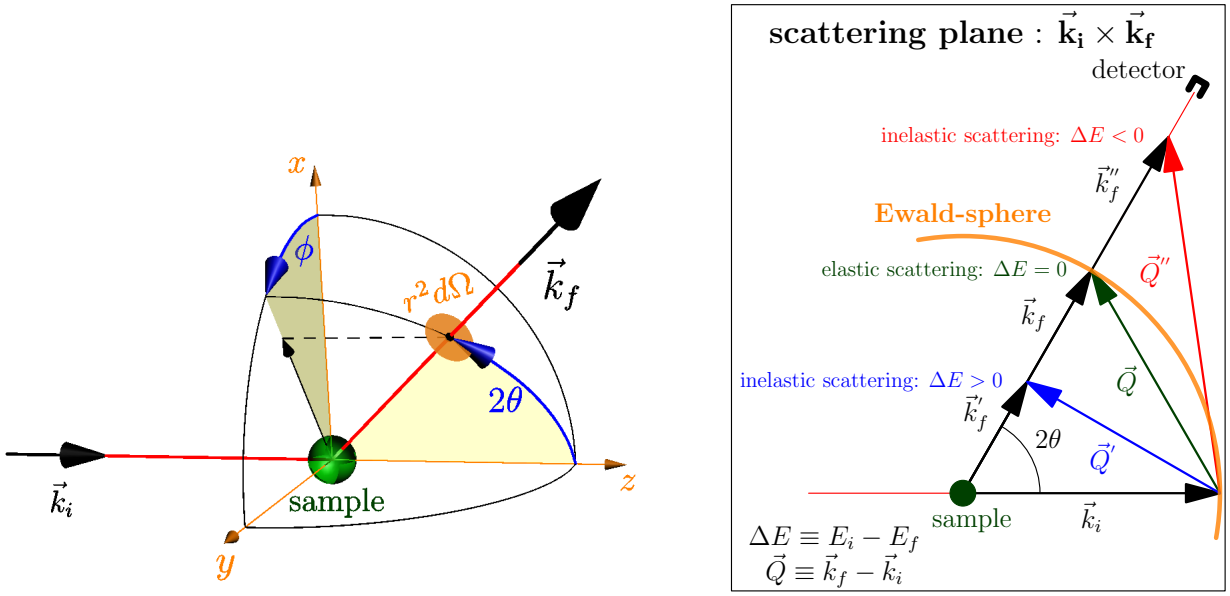

Figure 3.2.: **Geometry of a scattering experiment**
The left pane shows a 3D sketch of a scattering process. It illustrates the meaning of the scattering direction $(2\theta,\phi)$ and the solid angle $d\Omega$ where the scattered quantum is recorded. The right pane shows the geometry in the scattering plane defined by the vectors $\vec{k}_i$ and $\vec{k}_f$. The sketch illustrates the momentum transfer $\vec{Q}$ and the energy transfer ΔE. $\vec{k}_i$ is the incident wave vector; $\vec{k}_f$ denotes the wave vector of elastically scattered quanta; $\vec{k}'_f$ and $\vec{k}''_f$ are the wave vectors of the inelastically scattered quanta.

while the energy E and wavelength λ are related as:

$$E = \begin{cases} \frac{\hbar^2|\vec{k}|^2}{2m_n} = \frac{h^2}{2m_n\lambda^2} & \text{for neutrons with the mass } m_n \\ \frac{h\,c}{\lambda} & \text{for photons (X-rays), massless} \end{cases} \tag{3.4}$$

A scattering event is characterized by two quantities: the `scattering vector` $\vec{Q}$ and the `energy transfer` $\Delta E \equiv \hbar\omega$, see fig. 3.2. They are defined as:

$$\vec{Q} = \vec{k}_f - \vec{k}_i \tag{3.5}$$

$$\Delta E \equiv \hbar\omega = E_i - E_f \tag{3.6}$$

The given definition of the energy transfer is related to the sample. $\Delta E > 0$ means an energy increase of the sample, this implies an energy decrease of the scattered quantum. The vector $\hbar\vec{Q}$ describes the momentum transfer during the scattering process. The scattered quantum is assumed to be recorded in the direction $\hat{k}_f$ with spherical coordinates $(2\theta,\phi)$ on the detector surface corresponding to the solid angle $d\Omega = 2\sin 2\theta d\theta d\phi$. The magnitude Q

of the scattering vector can be expressed as:

$$Q = \sqrt{k_i^2 + k_f^2 - 2k_i k_f \cos 2\theta}. \tag{3.7}$$

In the special case of elastic scattering the relations $E_i = E_f$ and $|\vec{k}_i| = |\vec{k}_f|$ are valid and all possible scattering vectors are located on a sphere, called `Ewald sphere`, see fig. 3.2 (right pane). In the case of elastic scattering the magnitude Q of the scattering vector is related to the wavelength λ and the scattering angle 2θ as:

$$Q = k_i\sqrt{2(1 - \cos 2\theta)} = \frac{4\pi}{\lambda}\sin\theta \tag{3.8}$$

Scattering cross section σ

Operationally, a scattering experiment consists of measurements of the 'scattered intensity' distribution as a function of the scattering vector and energy. Usually, a notion of the cross section σ is introduced. The cross section is proportional to the scattered intensity, where the proportionality factor is a geometrical property of the scattering experiment. We give the definition of the cross section with the help of the sketch on the left pane in figure 3.2. Consider a number n of quanta scattered per second and per energy interval $[E_f, E_f + dE_f]$ into the solid angle $d\Omega$ seen by the detector in the direction $(2\theta, \phi)$.
The `double differential cross section` is defined as:

$$\frac{\partial^2\sigma}{\partial\Omega\partial E_f} = \frac{n}{\Phi d\Omega dE_f} \tag{3.9}$$

where Φ denotes the incident beam flux expressed in the number of quanta per area and time. This value describes the probability density that a quantum is scattered into a solid angle element $d\Omega$ with an energy $E_f \in [E_f, E_f + dE_f]$.
The `differential cross section` is defined through the integration over the accessible energy range:

$$\frac{d\sigma}{d\Omega} = \int_0^\infty \frac{d^2\sigma}{d\Omega dE_f} dE_f \tag{3.10}$$

It is the probability that a quantum is scattered into a solid angle element $d\Omega$.
The `scattering cross section` is defined as the total scattering probability independent of the energy transfer and scattering angle:

$$\sigma = \int \frac{d\sigma}{d\Omega} d\Omega \tag{3.11}$$

Notion of form factor and elementary scattering

Usually, in condensed matter science, the relationship between the scattered intensity and the related properties of the sample is derived in the so-called `Born approximation` (or `kinematic scattering approximation`). This implies that refraction, multiple scattering events and extinction of the primary beam due to the scattering within the sample are neglected. In this approximation a scattering event is a transition (3.1) which probability is computed by the application of Fermi's golden rules. The general observation [100] is as follows: by scattering at a particle, bounded in a (larger) complex system, the probability of this transition can be factorized into the product of (i) the corresponding transition probability for a free scatterer and (ii) a `form factor`, i.e. it is proportional to:

$$\left|g(\vec{Q})\right|^2 \quad \left|\langle\alpha_f|e^{i\vec{Q}\cdot\vec{r}}|\alpha_i\rangle\right|^2 \tag{3.12}$$

where $g(\vec{Q})$ represents the strength of the interaction causing the scattering, $e^{i\vec{Q}\cdot\vec{r}}$ denotes the operator of the momentum transfer and α_i, α_f describe the initial and final state of the (sub) system (consisting of the target + quanta), respectively. The first factor in (3.12) occurs due to `elementary scattering processes` (radiation process) and depends on the interaction of the scattered quanta with the material (content) of the sample. The latter depends only on the momentum and energy transfer ($\vec{Q}$, $\hbar\omega$) and the properties of the bound system and is independent from the details of the radiation process. This independence of the form factor from the details of elementary scattering processes allows to achieve a unifying description of sample's properties. Depending on the experimental situation the above-mentioned form factor sometimes is called differently, e.g. structure factor, scattering function or Debye-Waller factor. Due to the duality and complementarity principles of quantum mechanics it is often possible to express the form factor in terms of classical physics.

3.2. Elementary scattering processes

The above-mentioned interaction of the scattered quanta with matter is related to elementary scattering processes which are specific for the radiation used as probe. An elementary scattering process is usually described in terms of the scattering length b_X which measures the 'scattering power' of the elementary scatterer 'X' and, as such, it is a fundamental value in the computation of the scattered intensity. Below we summarize the relevant descriptions for neutrons and X-rays.

3.2.1. Neutrons

A neutron interacts with matter in two ways: 1) the strong nuclear force causes a significant scattering cross section from each nucleus in the sample; 2) due to its magnetic moment the neutron interacts with magnetic scatterers in the target. For us, only the first interaction type is relevant. In spite of the complexity of the neutron-kernel strong interaction, the description of scattering of thermal neutrons is relatively simple. This arises from the fact that, at thermal energies, the de Broglie wavelength of the neutron (about 1 Å) is very large compared to the range of the strong interaction (about 10^{-5} Å). Thus the neutron-nucleus interaction is represented by the Fermi pseudo-potential, i.e. the Dirac delta function:

$$V(\vec{r}) = \frac{2\pi\hbar^2}{m_n}\, b\, \delta(\vec{r}) \tag{3.13}$$

where m_n is the neutron mass and b is the s-wave scattering length, which is a function of the neutron spin $\vec{s}$ and the vector of the nuclear angular momentum $\vec{I}$:

$$b = b_c + 2b_i\, \vec{s} \cdot \vec{I} \tag{3.14}$$

For historical reasons, the two parameters b_c and b_i are called the `coherent` and the `incoherent scattering length`, respectively, because they are closely related to the coherent σ_{coh} and incoherent σ_{inc} cross sections. Indeed, both of them describe well coherent phenomena but, usually, through a scattering experiment, there is no control over the spin state of the nucleus in the sample. Thus, usually, the nuclear spin state is considered to be random, causing the resulting scattering to be `incoherent`. The isotope distribution in samples is usually random as well, which again contributes to the incoherent scattering.
Generally, b can be a function of energy and has a real and an imaginary part. The latter describes the absorption of the neutrons, due to the nuclear reactions. All parameters required to specify a concrete value of b are accurately measured and tabulated for all isotopes of the periodic table of elements [8].
Usually, neutron scattering is described in terms of the (differential) cross section of the elementary scattering events. Since the nucleus is 'visible' by thermal neutrons as a point like object (3.13) the differential cross section (3.10) for nuclear scattering is constant and is given by:

$$\frac{d\sigma}{d\Omega} = |b|^2 \tag{3.15}$$

The (total) scattering cross section (3.11), has a coherent and an incoherent term:

$$\sigma = \sigma_{coh} + \sigma_{inc} = 4\pi \left(|b_c|^2 + |b_i|^2\right). \tag{3.16}$$

The coherent part is responsible for the (dynamical) interference phenomena in a scattering process and relates to the collective properties of the system under study while the incoherent part relates to the single particle behaviour. The imaginary part of b results in the absorption cross section σ_{abs}.

3.2.2. X-rays

The elementary scattering unit of X-rays, which is relevant for our purpose, is the Thomson scattering on a single electron. The differential cross section (3.9) becomes in this case is given by [2]:

$$\frac{d\sigma}{d\Omega} = r_0^2 P. \tag{3.17}$$

Here $r_0 = 2.8210^{-5}$ Å is the Thomson scattering length[3] and P denotes the polarisation factor which depends on the X-ray source and geometry of the experimental set-up.
In contrast to the Thomson scattering and to the above-mentioned neutron scattering, the scattering of X-rays by an atom is defined by the spatial distribution of its electrons and cannot be considered as a point scatterer. Hence, the scattering function (intensity) becomes a function of the momentum transfer[4]. More generally, the scattering from an atom with Z electrons is described by the atomic form factor (scattering amplitude) [2]:

$$f(\vec{Q}, \hbar\omega) = f(|\vec{Q}|) + f'(\hbar\omega) + if''(\hbar\omega) \tag{3.18}$$

where f' and f'' are known as the dispersion corrections to f. The values of $f(Q)$ are tabulated in the *International Tables of Crystallography* [80].

3.3. Diffraction

Generally, diffraction phenomena do not only occur in elastic scattering but also in the so-called static approximation (see e.g. [39]). In the static approximation the energy transfer $\Delta E = \hbar\omega$ is considered to be very small compared to the incident energy. There is a difference between the static approximation and the picture of the purely elastic scattering, where $\hbar\omega = 0$. Due to the uncertainty principle $\omega\Delta t \sim 1$, the elastic scattering corresponds to scattering form the time-averaged atomic positions in the sample; indeed, equating the

[3] sometimes, following the tradition of the neutron scattering, we will use the symbol b for this scattering length.

[4] i.e., in the classical approach, it relates to the distribution of the atomic electrons by means of the spatial Fourier transform.

ω to zero will require an infinite time for the scattering event. As a consequence there is no strongly elastic scattering from samples without well defined thermal averaged structure, e.g. liquids. Hence, the diffraction patterns from such samples correspond to an additive average of the instantaneous snapshots taken in a diffraction experiment [39, 60, 162]. The characteristic time of a diffraction 'snapshot' can be defined as [39, 162]:

$$\tau_{snapshot} = (a/\lambda_i)(\hbar/E_i), \tag{3.19}$$

where a denotes an inter-atomic distance; λ_i, E_i are incident wavelength and energy, respectively. In other words: the static approximation corresponds to a situation when the structure of the sample is relatively static during the time required by a scattered quantum to travel the mean distance between two atomic positions ($t \to 0$) while the elastic scattering corresponds to a relatively long-time average of the positions of the scatterers through a scattering event ($t \to \infty$). The above-discussed takes no influence on the operational aspects of the diffraction experiment but can be important for the analysis and interpretation of its results.

3.3.1. Structure factor and correlation function

A system with N slowly varying positions of the scatterers can be represented (at least for a time of the snap-short (3.19)) either by the positions of points $\vec{r}_j$ or by a time-independent density $\rho(\vec{r})$. The former case can be incorporated into the latter as:

$$\rho(\vec{r}) = \sum_j \delta(\vec{r} - \vec{r}_j). \tag{3.20}$$

The differential cross section (3.9) has the form[5]:

$$\frac{d\sigma}{d\Omega} = \left\langle \left| \sum_{j=1}^{N} b_j e^{i\vec{Q}\cdot\vec{r}_j} \right|^2 \right\rangle \tag{3.21}$$

where b_j is the scattering length of the scatterer j. The angular brackets $< \ldots >$ denote the average, the reason for this average is two-fold: (i) For the systems with slow dynamics (not causing a visible inelasticity) the averaging brackets express a temporal average over the experimental time, because the scatterers will rearrange over the time of the experiment (see page 107). (ii) If the radiation used is not highly coherent, the sum over the amplitudes in (3.21) must be restricted to the coherence volume which can be smaller than

[5] it has the form of the squared magnitude of the Fourier transformed distribution density of scattering lengths.

the illuminated volume of the sample. The results from different regions have to be added after squared magnitudes are computed (incoherent superposition of intensities).
For a system consisting of identical scatterers it is possible to factorize the material-specific properties, i.e. number of scatterers N and their scattering length b:

$$\frac{d\sigma}{d\Omega} = |b|^2 \, N \, S(\vec{Q}) \tag{3.22}$$

where we introduced the structure factor[6] $S(\vec{Q})$:

$$S(\vec{Q}) = \frac{1}{N} \left\langle \left| \sum_{j=1}^{N} e^{i\vec{Q}\cdot\vec{r}_j} \right|^2 \right\rangle \equiv \left| F(\vec{Q}) \right|^2 \tag{3.23}$$

where $F(\vec{Q})$ means the amplitude of the structure factor. This quantities depend only on the statistic of the positions of the scatterers in the sample. The pair-correlation function can be defined as:

$$< \rho(\vec{r}_1)\rho(\vec{r}_2) > \;=\; < \rho(0)\rho(\vec{r}_2 - \vec{r}_1) >= \rho_0 \left\langle \sum_{j,k=1}^{N} \delta(r_j - r_k + r_2 - r_1) \right\rangle \tag{3.24}$$

$$\rho_0^2 \;=\; \langle \rho(\vec{r}_1) \rangle \, \langle \rho(\vec{r}_2) \rangle \tag{3.25}$$

In terms of this function the structure factor then can be written as:

$$S(\vec{Q}) = \frac{1}{\rho_0} \int_{V_{dis}} < \rho(0)\rho(\vec{r}) > e^{i\vec{Q}\cdot\vec{r}} d^3r \tag{3.26}$$

where V_{dis} means the 'volume' of all distances in the sample. The last expression can offer a computational simplification, e.g. by evaluation of the rotational average of the scattering intensity.

Generally, there are two alternative routes to compute the structure factor $S(\vec{Q})$ (or scattering intensity) from the known microscopic distribution density $\rho(\vec{r})$. This is illustrated in the sketch shown on the right. The first way (upper route) is represented by (3.21) and (3.23). It starts with computing the scattering amplitude $F(\vec{Q})$ by means of Fourier transform. The squared magnitude of $F(\vec{Q})$ give the structure factor $S(\vec{Q})$. The second (lower route) starts with computing the correlation function $\langle \rho(0)\rho(\vec{r}) \rangle$, which Fourier transform results in the required structure factor, see equation (3.26).

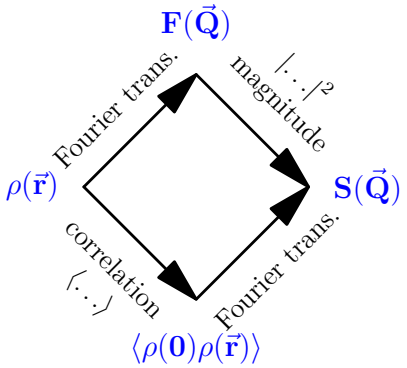

[6] it has the form of the squared magnitude of the Fourier transformed distribution density of scatterers.

3.3.2. Diffraction from a periodic structure

A periodic structure, usually a crystal structure, consists of a group of atoms (molecules) which is identically repeated at points (knots) of a periodical lattice. Such a lattice can be represented by a density function like:

$$\rho(\vec{r}) = \sum_{i_1,i_2,i_3} \delta(\vec{r} - \vec{r}_{i_1 i_2 i_3}) \tag{3.27}$$

where $\vec{r}_{i_1 i_2 i_3} = i_1\vec{a}_1 + i_2\vec{a}_2 + i_3\vec{a}_3$ is the vector pointing to the lattice knots, indexed by $\{i_1,i_2,i_3\}$ and the summation runs over all knots of the lattice. Above, we introduced three basis (Bravais) vectors $\{\vec{a}_1, \vec{a}_2, \vec{a}_3\}$ defining the lattice in the real space.
The structure factor of such a system can be factorized as:

$$S(\vec{Q}) = \left|F_{lat}(\vec{Q})\right|^2 \ \left|F_{uc}(\vec{Q})\right|^2 \tag{3.28}$$

where the amplitude of the `form factor` $F_{lat}(\vec{Q})$ is the Fourier transform of the lattice density function (3.27). The amplitude of the `structure factor` $F_{uc}(\vec{Q})$ is the scattering amplitude of the repeated group, usually called unit cell; it can be computed by means of (3.23) or (3.26).
The `Laue condition` for the observation of constructive interference (diffraction) from a periodic lattice can be formulated as follows. $F_{lat}(\vec{Q})$ is not vanishing if and only if $\vec{Q}$ coincides with a reciprocal lattice vector $\vec{G}$, i.e.

$$\vec{Q} = \vec{G} \tag{3.29}$$

The reciprocal lattice vector $\vec{G}$ is defined as:

$$\vec{G} = h\vec{\tau}_1 + k\vec{\tau}_2 + l\vec{\tau}_3 \tag{3.30}$$

where (h,k,l) are integers; the `reciprocal lattice basis vectors` $\{\vec{\tau}_1, \vec{\tau}_2, \vec{\tau}_3\}$ are solutions of the system of linear equations: $\vec{a}_i \cdot \vec{\tau}_j = 2\pi\delta_{ij}$ (δ_{ij} is the Kronecker delta symbol):

$$\begin{cases} \tau_1 &= 2\pi\frac{\vec{a}_2\times\vec{a}_3}{v_{uc}} \\ \tau_2 &= 2\pi\frac{\vec{a}_3\times\vec{a}_1}{v_{uc}} \\ \tau_3 &= 2\pi\frac{\vec{a}_1\times\vec{a}_2}{v_{uc}} \end{cases} \tag{3.31}$$

where $v_{uc} = \vec{a}_1 \cdot [\vec{a}_2 \times \vec{a}_3]$ is the volume of the unit cell.
The Laue condition (3.29) coincides with the Bragg's law, which is formulated for a diffraction of waves (of wavelength λ) with an incident angle θ to a set of lattice planes separated

by a distance d[7]:

$$m\lambda = 2\,d\,\sin\theta \tag{3.32}$$

where m is an integer.

Scattering from a large (infinite) crystal is characterized by distinct points (sharp Bragg peaks) in reciprocal space. The intensities of the Bragg peaks are the intensities of the lattice scattering factor (form factor) $|F_{lat}|^2$ modulated by the structure factor $|F_{uc}(Q)|^2$ of the unit cell. Their positions are defined by the Laue condition and are independent of the content of the unit cell.

In real crystals, the shape of the Bragg peaks is influenced by such factors as dynamics of the system, thermal motions and imperfection of the structure. The influence of the dynamics can be described in terms of the `Debye-Waller` factor. The latter has the meaning [99] of the ratio of the scattering cross section of quanta scattered by a particle bound to a complex system to the value for the same process on the free particle. An intensity reduction occurs e.g. due to the variation of the bond lengths and angles. To describe the resulting diffraction one has to take into account the modulation by a Gaussian-like function with width of the form $\vec{G}^2_{hkl}\langle|\vec{u}|^2\rangle$, where $\langle|\vec{u}|^2\rangle$ is the mean square fluctuation in the position of the atom. E.g. the approximation by a harmonic oscillator results in the peak form $\exp(-Q^2\langle\vec{|}u|^2\rangle)$, corresponding to its quantum mechanical state of minimal energy.

The finiteness of the crystal's size, describes by its shape results in the broadening (Bragg's) peaks, which is described by a convolution in the reciprocal space. A shape of a crystal can be described by a characteristic function $\xi(\vec{r})$:

$$\xi(\vec{r}) = \begin{cases} 1, & \vec{r}\text{ is in crystal} \\ 0, & \text{otherwise} \end{cases} \tag{3.33}$$

The lattice scattering amplitude is given by a convolution of the spatial Fourier transform $\Xi(\vec{Q})$ of the characteristic function $\xi(\vec{r})$ and the scattering amplitude from the infinite lattice:

$$F_{lat}(\vec{Q}) \rightarrow F_{lat}(\vec{Q}) \star \Xi(Q) \tag{3.34}$$

The most prominent example of such a broadening is given by Laue, who introduced the function $L(Q) = \sin(NaQ)/\sin(aQ)$, describing a scattering amplitude of an 1D crystal consisting of N knots separated by the distance a. In a 3D system it becomes:

$$F_{lat}(\vec{Q}) = \prod_{i=1}^{3} \frac{\sin(N_i\vec{a}_i \cdot \vec{Q})}{\sin(\vec{a}_i \cdot \vec{Q})} \tag{3.35}$$

[7] Note, that θ is the angle between the incident beam and lattice planes

where N_i denotes the number of cells in the direction of the lattice vector $\vec{a}_i$.
By nano-sized crystallites the size effect and the effect of their thermal motion[8] will dominate, while the Debye-Waller factor only plays a minor role.
In the present work the above discussed diffraction theory is applied to the analysis of the *in situ* X-ray scattering at the polycrystalline regions of silk fibres. Some of our computation are based on the expression (3.35). The results and models are presented in chapter 5 and, additionally, discussed in the chapter 6.

3.4. Quasi-elastic neutrons scattering (QENS)

QENS is a long time approach [9] in the dynamical neutron scattering. Because the our QENS measurements were performed at room temperature, we will restrict ourself to an overview of the classical approach. The latter is based on the theory of van Hove (pair) correlation functions [8, 162, 170]. We proceed as follows: First, we introduce the basic concepts of the dynamical neutron scattering and then the QENS will be described.

Scattering and (pair) correlation functions

Generally, by scattering from a dynamical system the energy may be transferred to or from the scattered quanta. Thus an `energy transfer` $\Delta E = \hbar\omega$ occurs and the scattering process becomes `inelastic`. As illustrated in fig. 3.2 $|\vec{k}_f| \neq |\vec{k}_i|$ and, hence the momentum transfer $\vec{Q}$ and the scattered intensity become functions of the energy transfer. This implies that the scattering experiment must be described in terms of the `double differential cross-section`, see equation (3.9). In the far-field approach using the Born approximation the double differential cross section is given by the Fermi's second Golden Rule, which reads:

$$\frac{\partial^2\sigma}{\partial E \partial\Omega} \quad \propto \quad \frac{k_f}{k_i} \sum_{\alpha_i,\alpha_f} P_\alpha \left| \langle \alpha_f | \langle \vec{k}_f \left| \hat{V} \right| \vec{k}_i \rangle | \alpha_i \rangle \right|^2 \delta\left(\hbar\omega + E_{\alpha_i} - E_{\alpha_f}\right) \tag{3.36}$$

where the set of variables α_i, α_f describes the quantum mechanical state of the sample before and after the scattering event, respectively. $|\vec{k}_i\rangle, |\vec{k}_f\rangle$ denote plane waves of the incident and scattered neutron, respectively. P_{α_i} is the probability of the initial state α_i of the sample. The Dirac delta function guaranties energy conservation. $\hat{V}$ is the operator of interaction between the scattered neutron and a nucleus of the sample. Due to (3.13) the

[8] which have to be averaged in terms of the static approximation, discussed in sec. 3.3, page 107.
[9] here is the origin of the term "quasi-elastic", because with the limit $t \to \infty$ in the time domain one approaches the elastic component of the spectra, i.e. $\omega \to 0$.

latter is simply:

$$\hat{V} \propto \sum_j b_j \delta(\vec{r} - \hat{\vec{r}_j})$$

where $\{b_j\}$ are the scattering lengths. The simplicity of the interaction potential above allows a description of the scattering processes in terms of the spatial and temporal Fourier transforms.

The description is based on three key notions:

- the `scattering function` $S(\vec{Q},\omega)$
- the `intermediate scattering function` $I(\vec{Q},t)$ and
- the van Hove's `correlation function` $G(\vec{r},t)$,

which are interrelated by means of the Fourier transform.

The scattering function is related to the double differential cross section as[10]:

$$\frac{\partial\sigma}{\partial\Omega\partial E} = \frac{k_f}{k_i} S(\vec{Q},\omega) \tag{3.37}$$

Due to observations given on the page 106, the scattering function can be decomposed into two parts: coherent and incoherent. Thus, the double differential cross section becomes:

$$\frac{\partial\sigma}{\partial\Omega\partial E} = \frac{k_f}{k_i}\frac{N}{4\pi}\left(\sigma_{coh} S_{coh}(\vec{Q},\omega) + \sigma_{inc} S_{inc}(\vec{Q},\omega)\right) \tag{3.38}$$

where the N is the number of scatterers.

Further, this separation into coherent and incoherent terms leads to a corresponding separation of the intermediate scattering function and correlation function. E.g. the incoherent scattering function $S_{inc}(\vec{Q},\omega)$ is the temporal Fourier transform of the incoherent intermediate scattering function $I_{inc}(\vec{Q},t)$ and the latter is the spatial Fourier transform of the self correlation function $G_s(\vec{r},t)$. The latter describes the probability of a scatterer to be found at time t in the location $\vec{r}$, if it was initially ($t = 0$) at the origin.

In the classical approximation this becomes:

$$G_s^{cl}(\vec{r},t) = \frac{1}{N}\sum_j \delta(\vec{r} - r_j(t) + r_j(0)) \tag{3.39}$$

Then, the intermediate incoherent scattering function reads:

$$I_{inc}^{cl} = \frac{1}{N}\sum_j \langle e^{i\vec{Q}\cdot\vec{r}_j(0)} e^{-i\vec{Q}\cdot\vec{r}_j(t)}\rangle = \frac{1}{N}\sum_j \langle e^{-i\vec{Q}\cdot\Delta\vec{r}_j(t)}\rangle \tag{3.40}$$

[10] In following we assume, without loss of generality, mono-isotope scattering.

where $\Delta\vec{r}_j(t) = \vec{r}_j(t) - \vec{r}_j(0)$ is a particle displacement during the time interval t. And, finally, the (classical) incoherent scattering function can be written as:

$$S^{cl}_{inc}(\vec{Q},\omega) = \frac{1}{2\pi}\int_{-\infty}^{\infty} I^{cl}_{inc}(\vec{Q},t)\, e^{-i\omega t} \tag{3.41}$$

The scattering function, calculated in the classical limit, violates the principle of the detailed balance and has to be corrected as [8]:

$$S_{inc}(\vec{Q},\omega) = \exp\left(-\frac{\hbar\omega}{2k_BT}\right) S^{cl}_{icn}(\vec{Q},\omega) \tag{3.42}$$

QENS

In the long time limit the self correlation function will asymptotically approach a constant value[11] $G(\vec{r},\infty)$, which corresponds to the incoherent intermediate scattering function $I(\vec{Q},\infty)$ [8]:

$$I_{inc}(\vec{Q},\infty) = \frac{1}{N}\sum_j \left|\left\langle e^{i\vec{Q}\cdot\vec{r}_j}\right\rangle\right|^2 \tag{3.43}$$

meaning the Fourier transform of the $3D$ area, which is accessible for the scatterers. I.e. it is the Fourier transform of the final (equilibrated) distribution of all positions of the scatterers averaged over all their possible initial positions. Hence, the incoherent intermediate scattering function can be represented by two terms, the independent and the dependent of time:

$$I_{inc}(\vec{Q},t) = I_{inc}(\vec{Q},\infty) + I^q_{inc}(\vec{Q},t) \tag{3.44}$$

The related incoherent scattering function consists of two terms:

$$S_{inc}(\vec{Q},\omega) = I_{inc}(Q,\infty)\delta(\omega) + S^q_{inc}(\vec{Q},\omega) \tag{3.45}$$

where the first one, containing the Dirac delta function $\delta(\omega)$, is purely elastic while the second exhibits a non vanishing broadening and is called `quasielastic`. The shape and, especially, the width of the latter provides information concerning the characteristic times of the system-dynamics in the long time regime. The first term has the meaning of a structure factor, hence it is called 'elastic incoherent structure factor'. From the above it is clear, that the presence of a non-vanishing elastic component in the scattered intensity is an indicator for spatial constraints in the motion of some scatterers in the system.
The theory of QENS as well as the main relation of the neutron scattering theory, presented in this section, were used in this work for the analysis of *in situ* neutron scattering experiments of silk fibres. The results are presented in chapter 6 on page 246.

[11] this vanishes if the scatterers are not spatially constrained in their movements.

4. Experimental

In this chapter the experimental techniques are described. We start with the common principles underlying our stretching experiments and common aspects of the construction of the sample cells we used. Then a short description of the monitoring and control of the mechanical engines and the environment of our sample cells is given, which is followed by the specification of the components of the sample cells and a discussion of the calibration procedures. Then we describe the sample preparation. At the end of this chapter we describe our sample cells and the instruments at large-scale facilities, where the *in situ* scattering experiments were performed.

4.1. Common principles

In our stretching experiments the samples are stretched by a motor/actuator and the response to this stretching is measured as function of time. Simultaneous a series of scattering measurements was accomplished through the progress of the stretching. Figure 4.1 (a) shows a common (schematic) layout of *in situ* stretching experiments.
The components of the *in situ* stretching experiments setup are:

- Control and monitoring (storing) of the sample-environment parameters such as relative humidity, temperature (RHT).
- Driving the excitation (force or strain), in our case it was strain.
- Monitoring (storing) the sample-response (stress) as a function of time.
- Synchronisation of the record of scattered intensity with the stretching regime. This was achieved by storing the TTL (transistor-transistor logic standard) signal from each recording event.
- In the case of micro-beam scattering experiments (ID13, ESRF), we have to control the position of the sample relative to the beam and to illuminate different locations of the sample. We did scans: positioning of the sample at several spacial points relative to the beam. See a representation of such a scan on the figure 4.1.

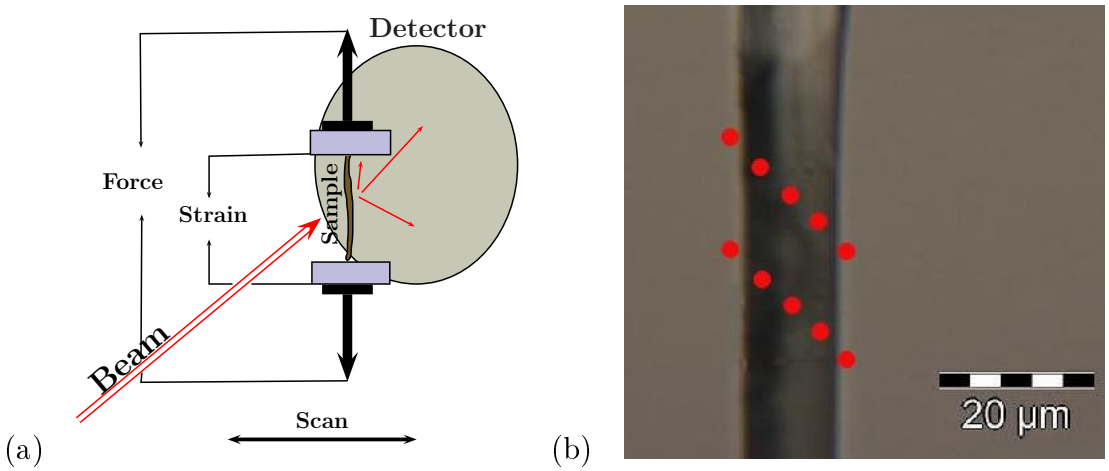

Figure 4.1.: **Stretching experiment**
On the pane (a) a diagram of a stretching experiment setup is shown; (b) shows a microscope photograph of a single silk fibre with an example of a scan path drawn as red circles, representing the position and size of the beam.

Thus, the experimental equipment has to include environment sensors (for temperature and humidity), force and strain sensors and an actuator/motor to stretch the sample. In the case of micro diffraction, the control software has to include the possibility to use the interface offered by a beamline support to control motors used for scanning.

The driving of the strain-motor/actuator was done using the hardware built-in controller connected with a computer through the RS232 interface. If more accurate time dependence was needed the controlling was done using an Analog Digital Converting (ADC) board card with built-in high frequency timer.

The measurements of the force, strain and TTL signal were carried out using the ADC board card (National Instrument [117]) with a suitable converter frequency to achieving the required time resolution.

A centralized access to all this hardware is realized through an especially for this purpose developed software. The software based on the server-client architecture and allows a remote control of an experiment with the possibility of automated script-based experiments performing in a batch mode. The controller client can run on a remote PC with full featured control-terminal and GUI based monitoring (see example screen-shot of this controller in fig.4.7).

In following sections the acquisition scheme used and sensors are described separately. Then three stretching sample cells for stretching of a single fibre `SPLC` (4.3.1,132), a median

sized fibre bundle HUSTEN (4.3.2, page 136) and a large bundle LLC (4.3.3, page 137) are discussed. But before, we will specify components and building schema which are common for all our cells.

4.1.1. Common aspects of stretching sample cells

All our sample cells (with exception of some cells for neutron scattering experiments) have the same building principle to fulfill about the same principal requirements for *in situ* stretching experiments:

- Controllable and stable sample environment, at least values of relative humidity (RH) need to be stable.
- Possibility to do a scattering experiments, i.e. beam entry window, minimum perturbation of the scattered radiation, etc.
- Equipped with driving/acquisition facility for stretching process and synchronisation with scattering events.
- Positioning of the sample relative to a radiation beam and, eventually, a facility to perform scans (illuminations of a set of different parts of the sample with a micro-sized beam).

The difference between them are due to the size of the sample (single fibre, medium or large fibre bundles) and the type of radiation used for scattering (see table 4.1). The main

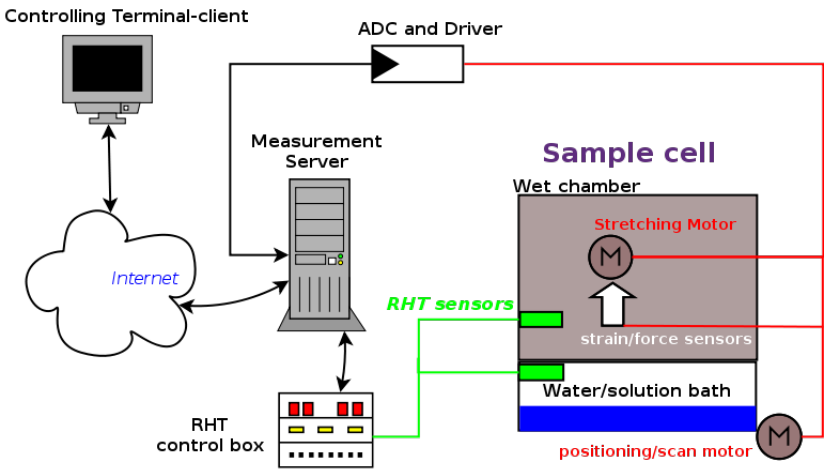

Figure 4.2.: **Sketch of principal setup for *in situ* stretching experiments**

components of such an environmental cell are (see fig. 4.2):

- wet chamber for samples, with a beam window and a stretching engine and sample holding frame;
- water/solution bath connected with the wet chamber;
- stretching motor with controller;
- force/stretching sensors;
- RHT sensors;
- control/monitor (acquisition) software;
- synchronisation with scattering events software; (synchronisation is usually done through a TTL signal).

sample cell	**type of sample**	**maximal load (N)**	**maximal path**	**readout speed (sps)**	**relative humidity range (%)**	**radiation**
SPLC	single fibre or small fibre bundle	0.5	190 μm	$\leqslant 16\times10^6$	2-100	X-ray
HUSTEN	median bundle	5	$\geqslant$ 10 (cm)	about 100	19-100	X-ray
LLC	large bundle	256	$\geqslant$ 10 (cm)	about 100	vacuum to 100	neutrons or X-ray

Table 4.1.: **Sample cells used in this work**
These sample cells were developed and constructed by the working group of Prof. Dr. Müller, university Kiel (Germany).
"sps" means samples per second

4.2. Acquisition and calibration

4.2.1. Aspects of data acquisition and control

In the following the term **acquisition** is used as synonym for reading information from the hardware (analog to digital conversion) or driving the hardware by writing information (digital to analog conversion) in the opposite direction.
For the purpose of computer-aided monitoring and driving the multifunctional/multichannel analog-digital converter board cards (from National Instruments Corporation [117]) were used. Such cards allow the acquisition at a frequency of some megasamples per second.
Three principal regimes of acquisition are possible:

1. **request-response:** one measurement per request;
2. **instruction**: a set of measurement per request;
3. **command**: a sequential acquisition, controlled by the built-in board clock.

The first type of acquisition regime was used in the control system of the HUSTEN sample cell based on the Labview environment running under the MS Windows. Our experience shows that because of the high latency of standard operation systems (Window, Linux) this regime does not satisfy our requirements. The synchronisation was very bad and measured data must be reinterpolated to get the values at the same time from the different channels. The errors were very large and the Labview-based system was not stable enouph and required a lot of computer resources.
The second generation of the driving software used the "command" (see above) regime. It is based on the low level open-source library "comedi" [21]. Under this regime the acquisition process is running as a periodical sequence of the set of channels conversions (AD or DA) called scans (see fig. 4.3) with the specified frequency. This allows one to realize a so-called soft real-time process, because the command uses the timer which is built into the board card and is independed from the rest of the computer or operation system. The acquisition frequency can be up to some megasamples per second, but for our purpose it was sufficient to use one kilo-sample per second (1 kHz).
To run such a command one has to specifiy (see fig. 4.3):

- Start and end events for the whole acquisition sequence.
- Start and end events of the each acquisition scan.
- Numbers and order of channels in the scan.
- Each channel in the scan (conversion type, connection type etc.).

This type of acquisition and control is very flexible and allows to save a lot of computer resources. Once the command is specified and started the permanent readable data stream is accessible to the system and one has only: read it, transfer it into the physical values, save the data on a storage device and, possibly, print the data on the monitor terminal-window or plot them on the screen.

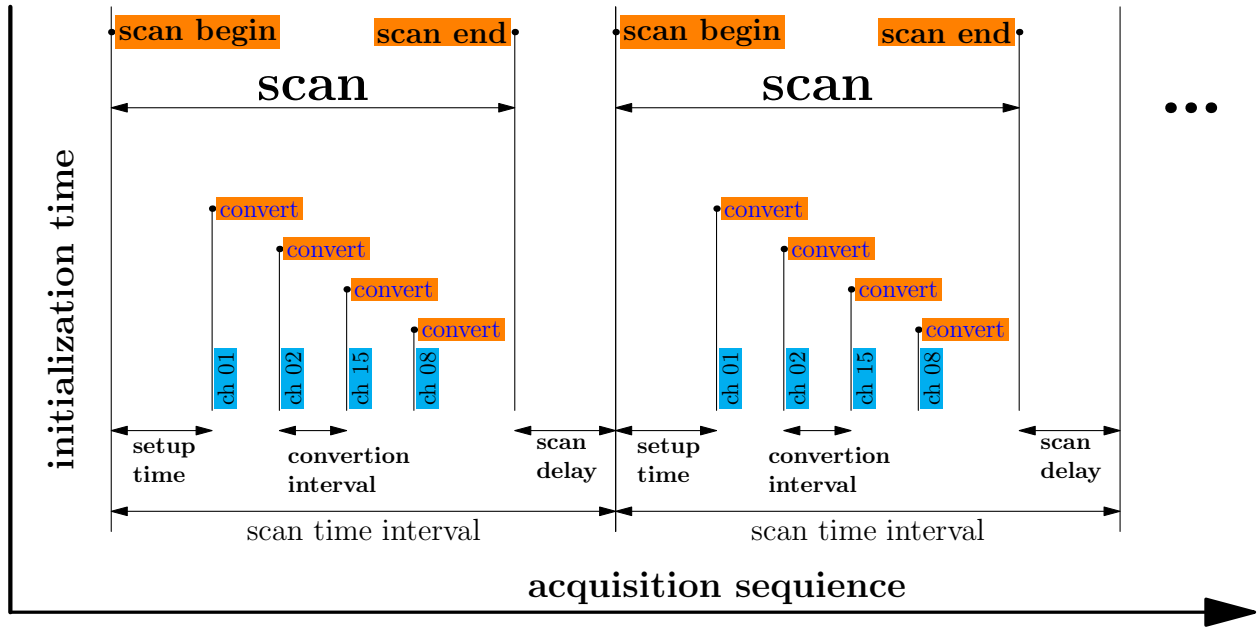

Figure 4.3.: **Chart of the acquisition process under the "command" regime**
The orange labels denote the events to start or to stop an operation, blue labels shows, symbolically, the contents of a scan.

4.2.2. Environmental control and sensoric

Cell environment. The mechanical properties of silk strongly depend on its environment, especially they depend very strongly on water content in the surrounding air.
The dependence on the temperature is twofold: silk thermodynamical properties depends directly on the temperature, while there is an implicit dependence through the water content of the air, which is a function of the temperature. Our target temperature regime was ambient (about 20-25° C), hence for our purpose it was sufficient to use the room temperature in the experimental hall.
To achieve a stable controllable sample environment stabilization media were used as humidity reservoir, i.e. saturated solution or silica gel powder. The sample was put into a closed cell which was in direct connection with a bath, where the stabilization media was placed (see fig. 4.6).
Now, for convenience, we give a simple physical description of the phenomenon we use. Consider an closed system with an water-air interface (see fig. 4.4). After the system reaches its equilibrium state the mean number of evaporated water molecules per (macroscopic) time interval is statistically equal to the mean number of condensed water molecules. Quantitatively, this is described through the fact that under equilibrium conditions in a multi-phase/multi-component thermodynamic system the chemical potentials of all components in all present phases have to be equal. The partial pressure of the water vapour in the air is called the `saturated vapour pressure` $p_{w,g}$, this value governs/characterizes the water content in the gas phase. The (equilibrium) saturation pressure is described by the Clausius-Clapeyron relation:

$$\frac{dP}{dT} = \frac{L_v}{T\Delta V}$$

where L_v is the `latent heat` or `molar enthalpy` of the vaporisation, T the absolute temperature (Kelvin), ΔV is the (molar) volume change of the phase transition (vaporisation). The presence of a solute in water will cause some changes to the value of the chemical potential of the water molecules in the liquid phase with respective changes in the conditions on the saturation pressure of the water in the gas phase. The salt content in the solution strongly influences value of the partial pressure of the saturation vapour under the water-air interface. Similar consideration are valid with respect to the waters saturation partial pressure in the air in contact with large amount of silica gel. Here, the equilibrium conditions are defined by the geometry and topology (e.g. curvature, connectivity) of mesopores (cavities) in silica gel material. Each deviation from the equilibrium state causes irreversible processes which drive the system back into the equilibrium state.
The term `relative humidity (RH)` is a mostly used term to describe quantitatively the

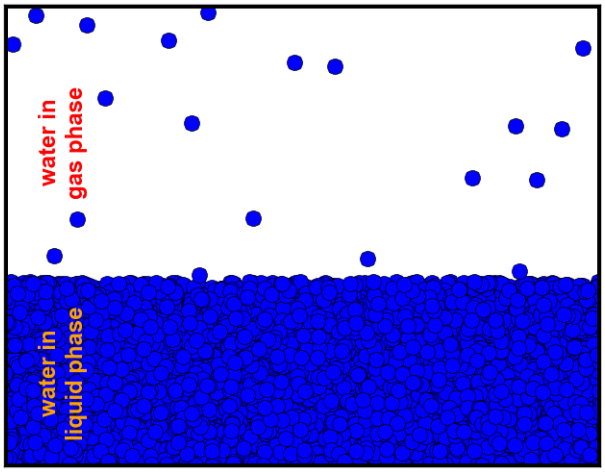

Figure 4.4.: **Equilibrium between liquid and vapour in a closed system**

Salt	Rel. humidity of the air [%] at the temperature ...°C				Solubility at 20°C [g/100g H_2O]
	15	**20**	**25**	**30**	
Natriumhydroxid	6	6	6	6	108,3
Magnesiumchlorid	33	33	33	33	54,4
Kaliumcarbonat	43	43	43	–	110,6
Natriumbromid	60	59	58	57	90,6
Natriumchlorid	75	75	75	75	36,0

Table 4.2.: **Relative humidity over a saturated salt solutions and solubility in water for some salts** [98]

content of water molecules in the air. It is introduced as a relative relation of the pressure P in the system under consideration to the saturation pressure under water-air interface $P_{w,g}(T)$ at the same temperature T:

$$RH = \frac{P}{P_{w,g}(T)} \times 100\%$$

Therefore, the RH value in the system, described above (fig. 4.4), of the water-air interface in the closed volume is exactly 100% in the equilibrium state at each temperature.
For each target humidity a suitable type of salt was used. Table 4.2 shows relative humidity at various temperatures for some salts we used in our experiments. One can see that RH values remain essentially unchanged over wide range of temperatures.
Saturated salt solutions were used for the range 30-85% of RH. For about 90-98% RH we used pure water and for a very dry environment (up to 2-4%) silica gel was used as stabilization medium.

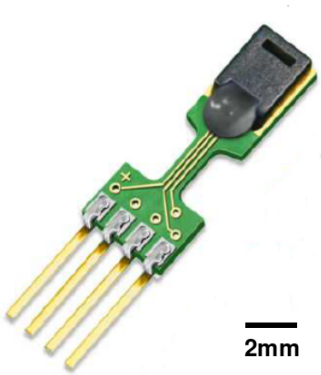

Figure 4.5.: **Humidity-Temperature combined sensor, SHT7x Sensirion [153]**

Sensors for relative humidity and temperature (RHT sensors) The combined sensor element SHT7x (Sensirion [153]) was used in our experiments to monitor the temperature and relative humidity. The small size of the element allows us to place some of them in the vicinity of our sample without disturbing the stretching engine or the scattered beam. Figure 4.5 shows such a sensor-element and figure 4.6 shows a principal connection and placement chart of such sensors in a sample cell. SHT7x is a combination of two elements: one is for temperature- and other for relative humidity measurement.
The temperature measurement is based on the band-gap principal and the relative humidity measurement on the capacity measurement of a polymer-element. Both measurements are

done nearly simultaneously and spatially very close to each other. The simultaneity of the measurement of temperature at the sampe location allows for the "on the fly" correction of the measured relative humidity values, with a resulting relative error of about 1.8% (see data sheet in [153]).
For the acquisition of more than one sensor per time the sensors were connected with a computer system through an acquisition box (build by Mathias Greve, CAU Kiel). The box allows a simultaneous acquisition of up to four sensors and can be driven by a "Labview" program, written by M. Greve for Windows or by a python program, written by the author for Linux or Window OS. The python program allows to drive the measurement process remotely using a protocol based on a client-server architecture, this was very handy for experiments with X-ray scattering. The principal connection and placing scheme for RHT sensors is shown in the sketch 4.6.

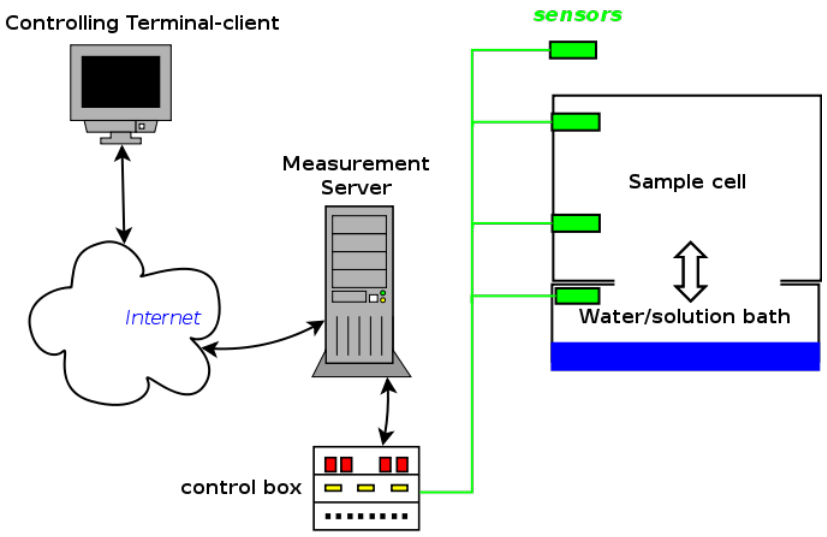

Figure 4.6.: **Connection and placing of RHT sensors**
Two sensors are placed direct in the sample-cell: one is above the sample and other is under the sample. One sensor is placed on top of the bath and the last sensor is used to monitor the outside surrounding state.

In fig. 4.7 one can see a screen shot of the working client controller user interface embedded into the acquisition environment, developed for our measurements. At high humidity (about 95-98%) the measured values can be perturbed by the process of drop formation in the sample cell. To reduce this effect the program allows to heat the sensors for a short time to free the sensors from water saturation.

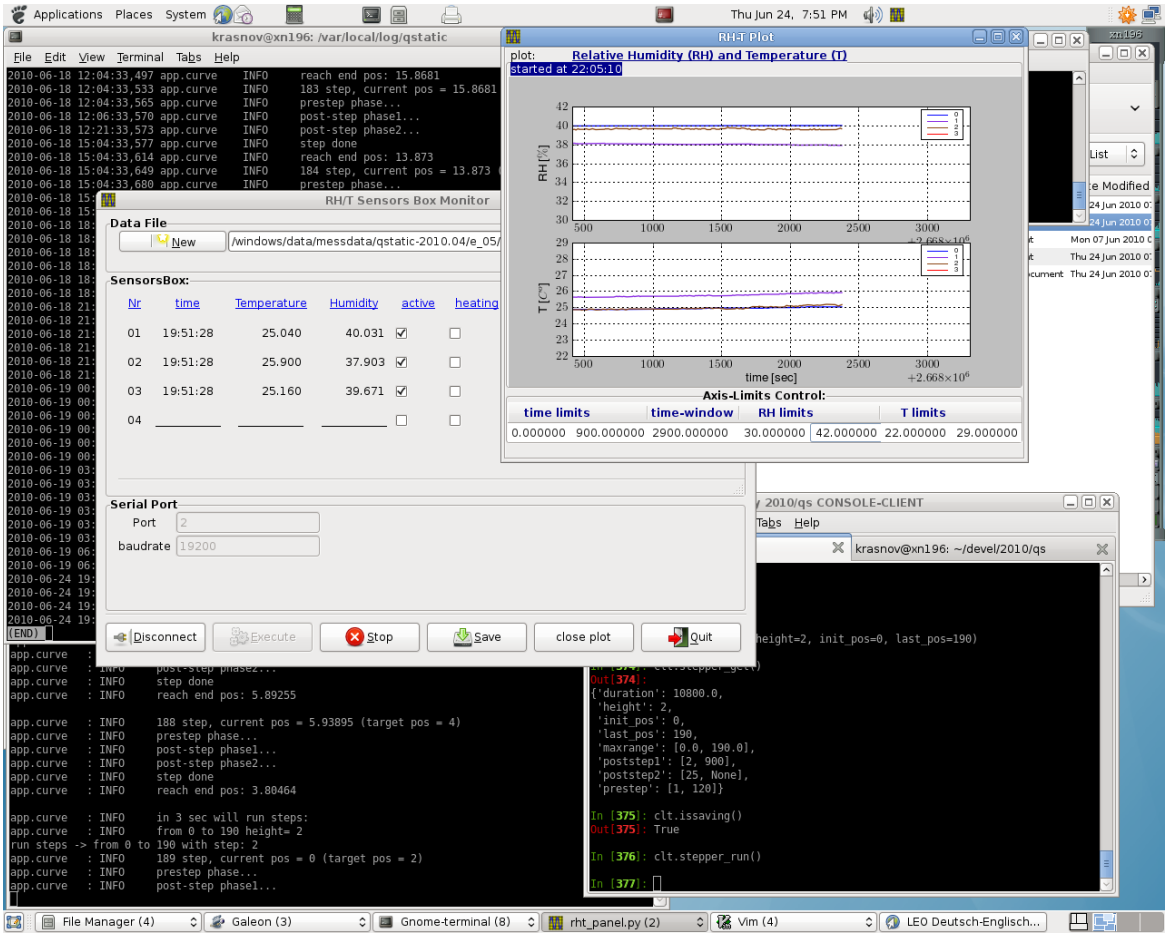

Figure 4.7.: **Python acquisition program, client part GUI**
Shows the GUI user interface to the temperature and relative humidity measurement system together with control terminal and measuring state monitor.

Control measurements To test the stability of the sample environment and control the error range of the sensors we have measured the RHT values for a relative long times (some tens of hours) with different saturated salt solutions. This measurements shows that after some relaxation time (about 20-40 min) the saturated salt solutions stabilize the sample cell atmosphere. The sensors shows the error range about 1.7-2.0%, with the same value of deviation from the theoretical table values of the relative humidity under saturated solutions.

The tests with very dry environment (achieved using silicagel in the place of salt solutions) show the same stability and the same error range as in the measurements with saturated salt. However, we cannot achieve some satisfactory low humidity in the HUSTEN cell (see.

4.3.2), the minimal value was about 20%. The reason was the construction of this cell, a relative large volume with non-separated electronics with many possibilities for water to condense. The piezo-cell SPLC (see.4.3.1) shows much better results, about 2-4% RH.

4.2.3. Calibration of stretching mechanics and sensors

For the study of the viscoelastic properties of *Bombyx mori* silk *in situ* stretching experiments on a single silk fibre, medium-sized (few fibres) and large (hundreds) fibre bundles were carried out. For a single fibre experiment a sample cell SPLC (see 4.3.1, on page 132) based on the piezo actuator with a spatial resolution about 0.3 μm was used, for middle bundles a sample cell HUSTEN (see 4.3.2) was used. Each sample cell has a different spatial measurement devices but the same building principal, and force sensors were of the same construction and same manufacture (Entran). Here the positioning and force sensors are described together with calibration procedures. And later some technical details of our sample cells are shortly described.

4.2.4. Force sensors

In all our experiments we used the same art of flat force sensors (from Entran GbmH) with force ranges from (0.5, 1.5, 5.0, 250) [N]. Figure 4.8 shows an example of such a sensor mounted on the piezo actuator head. The force signal was amplified and filtered with a 1 kHz filter to remove the aliasing effects and acquired using an ADC board card (National Instruments) mentioned early.
The calibration is carried out using a set of calibration weights. Each weight is hung on the sensor and sets of measurements of ADC channels are done. Then the operation is repeated with the next calibration weight. The resulting data were fitted with a linear function: ADC channel $\rightarrow$ force $[\mu N]$. Figure 4.9 shows an example of such calibration. fitted parameter are used to convert the ADC channels into the physical units.

4.2.5. Position sensors

Two types of position sensors were used to measure the stretching path. One is a strain foil gauge sensor (jena GmbH), used in the piezo based sample cell SPLC for a single fibre experiment. The other one is a position linear enconder (HEIDENHEIN GbmH [69]) is used in the HUSTEN sample cell [59]. The calibration of the gauge sensor will be described here and for details about the position line encoder see [59].

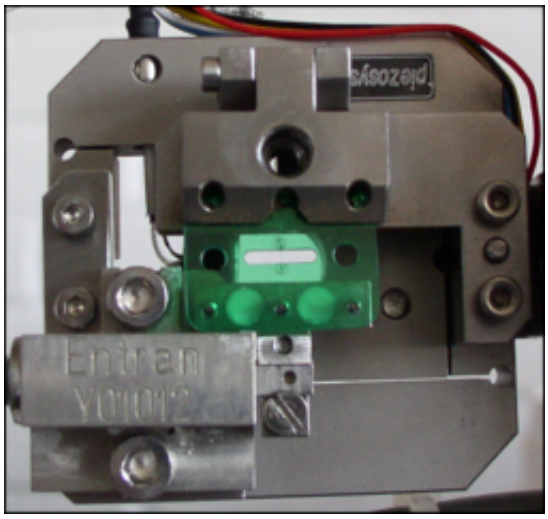

Figure 4.8.: **Force sensor (Entran) on the piezo actuator head**

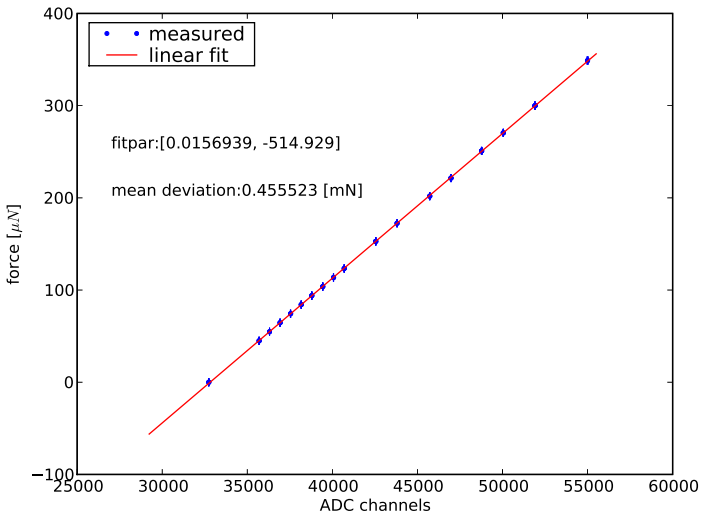

Figure 4.9.: **Calibration of the force sensor**

The calibration was done using sample weights which was hung on the force-sensor and the channel numbers was measured through a suitable time interval.

Optical calibration

To drive and monitor the strain the "resistance strain gauge sensor" has to be calibrated and the mapping from the Analog Digital Converter channels to physical distance has to be determined.
The following calibration procedure was used:

- The piezo cell actuator was equipment with two jaws with sharp edges.
- A microscope photographs with a suitable zooming was taken for a set of positions of the piezo actuator. Fig. 4.10 shows an example of such photographs (zooming 12x).
- Simultaneously a series of measurements of AD channels was done for each picture and the mean channel value and its standard deviation was computed.

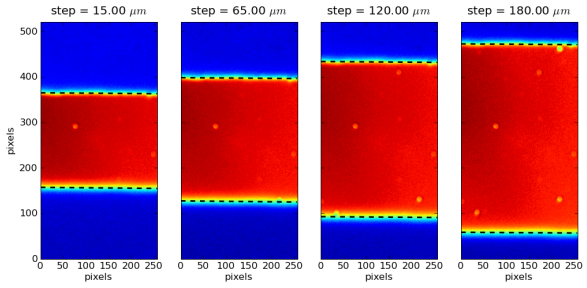

Figure 4.10.: **Microscope-photographs (zoom = 12x) of the piezo cell at four positions**

The blue ranges are the image of piezo jaws, the red range is the gap between the jaws and the dashed lines are computed edges boundary (front) of jaws. Each photograph is rotated, so that the mean-gradients of edge-fronts of jaws is parallel to the y-axis. The mean-gradient orientation is defined by a procedure based on Prewitt filter [144].

- For each photograph the position (measured in pixel numbers) of the jaw edges was computed. For this purpose the prewitt filter method of edge determination was used. This is a smoothing variant of differentiation filter. Fig. 4.11 shows an exaple of such computations: the photograph, the filtered image and an intensity profiles of the image and filtered image along the mean edge gradient, shown as arrow.
- For the chosen zoom the effective pixel size was defined. I.e. the photograph of a calibration micrometer sample scale (μm-scale) was taken with the corresponding

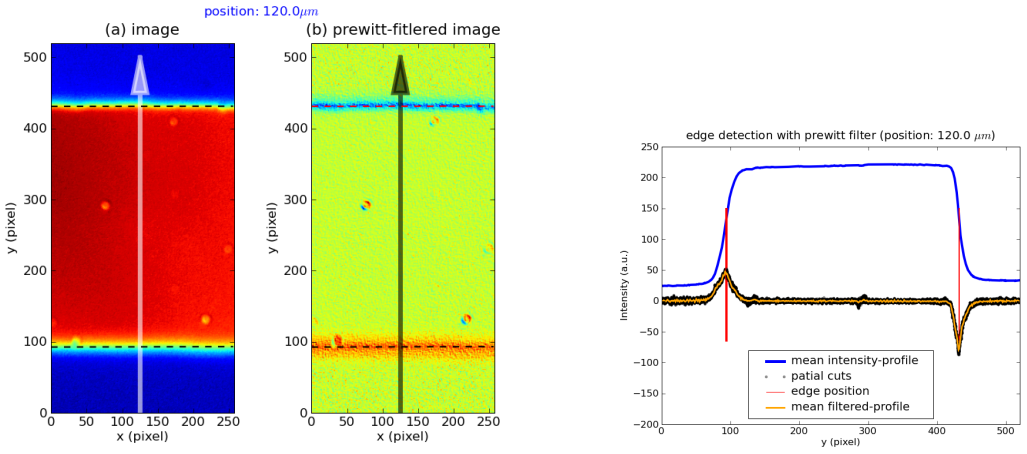

(a) **(b)**

Figure 4.11.: **Edge-positions definition for piezo cell jaws**

- **(a)** shows an image and filtered image for strain position 120.0 μm. The arrows pointing in the direction of the mean gradient of edge fronts. The dashed lines show the position of determined edges. The image is rotated so that the gradient of edge fronts is parallel to y-axis.
- **(b)** Intensity profiles. The blue curve shows the mean intensity along the direction of the mean gradient (defined by the edge detection procedure). The orange curve is the mean intensity profile of the filtered image in the same direction. The maxima/minima of the curve pointing to the position of the edges. The black points are the deviations of this curve at several ranges of the x-axis. Due to the usual random deviations of the intensity, a procedure based on the naive difference differentiation would not be able to find a correct direction of the edge-front, hence is not suitable for the edge determination. The red lines poin at the position of the edge for several ranges of x-axis.

zooming and the mean number of pixel ticks were counted. The effective mean pixel size is defined as $N_{ticks} * l_{tick}/N_{pixel}$, where N_{ticks} is number of ticks on a choosen range of the calibration mass scall, l_{tick} is the tick's length, N_{pixel} is the number of the pixels alongth the same range of the mass scale. Fig. 4.11 shows the photograph of the calibration micrometer scale used and the intensity curve used to count the mean number of pixel per tick.

- The optically measured position of the jaws is converted from pixel units into the physical distance and the straight line is fitted as function mapping ADC channels onto the physical distance. See fig. 4.13.

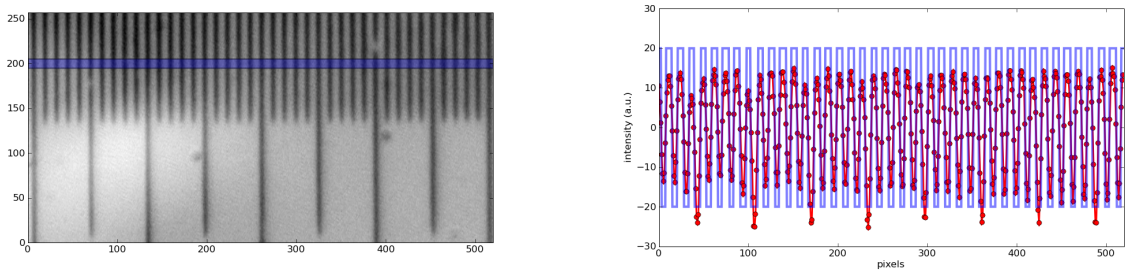

(a) **(b)**

Figure 4.12.: **Calibration μm-scale used to compute the effective pixel size** (a) a microscope photograph of the calibration scale at zoom 12x, the smallest tick corresponds to 10 μm. (b) the intensity profile curve alone the blue span shown on (a) the red curve is the intensity measured and blue one is the boundary curve used to count the ticks.

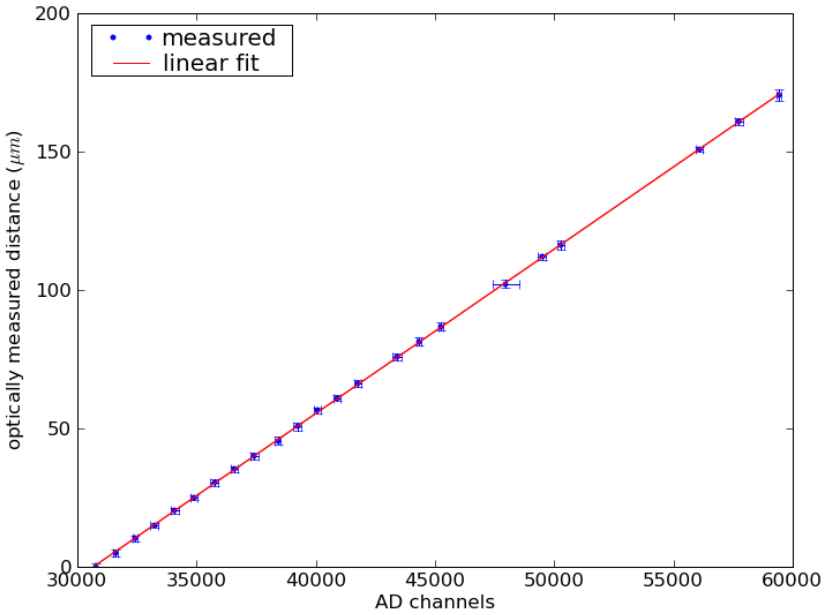

Figure 4.13.: **Strain calibration curve**
The abscissa shows the mean value of Analog-Digital Converter (ADC) channels, the ordinate shows optically measured distance in micrometer. The straight line is a linear fit, which has to be used in the conversion from ADC channels to distance measured in micrometer.

4.3. Environmental sample cells

4.3.1. Piezo-Electric Load Cell with controlled environment (SPLC)

Figures 4.14 and 4.15 show the setup of the Piezo-Electric sample cell called SLPC. This setup is used for stretching experiments with *in situ* X-ray scattering on a single fibre, which is about of 10 micrometer diameter. It was mainly employed for our measurements at ID13 (ERSF, Grenoble).
The sample fibre is glued on the holding plastic frames, shown on the figure 4.14 (c) and (d). The frame is placed on the actuator head (see figure 4.14 (c)), so that the bottom side of the frame is connected with the force sensor and the upper side is fixed to the actuators holder. Then the actuator head is placed into the wet-chamber with a suitable humidity atmosphere. The chamber is connected with the bath containing a humidity stabilization media (see 4.2.2). The tilting mechanics[1] allows an exact orientation of the fibre relative to the incoming X-ray beam (see figure 4.14 (b)). The incoming X-ray beam and scattered radiation pass through the Kapton-film windows.
The downside of this construction is the requirement to open/detach the top part of the wet chamber to change a sample. This means that on each sample change operation the humidity state is lost for a short time and needs, after the sample change, some time (about 20-40 min) to restore its stable state. The top part of the wet chamber can be removed by screwing of three bolts, holding this part.
The stretching engine consists of a piezo actuator, which is a modification[1] of the piezo slit/shutter system PSZ 1 from the "piezosystem jena GmbH" [82] manufacture. PSZ 1 is equipped with a strain gage measurement system with a measurement accuracy of about 0.2% and suitable driving system (see tab. 4.3). Maximal opening (strain path) is about 230 μm without controller and about 190 μm with using the linearized controller. The second regime is running without hysteresis and hence is more suitable for stretching experiments. The system can be driven/monitored through the RS232 or GPIB interfaces (with response time about 10 μs). Alternatively, the system offers a control/monitoring through the voltage signal. The last possibility was used for reading the value of the strain path synchronously with the force values and the TTL signal. The signals were read using the ACD board card NI-PCI-6221 (National Instruments), the principle of its use was discussed in 4.2.1. This card allows resolution of 16 bits in one digital value, so, e.g. the measurement of strain has a channel resolution of about 3 nm per ADC channel. More

[1] the tilting device and the last adaptation of the piezo head were designed by Mathias Greve (CAU Kiel).

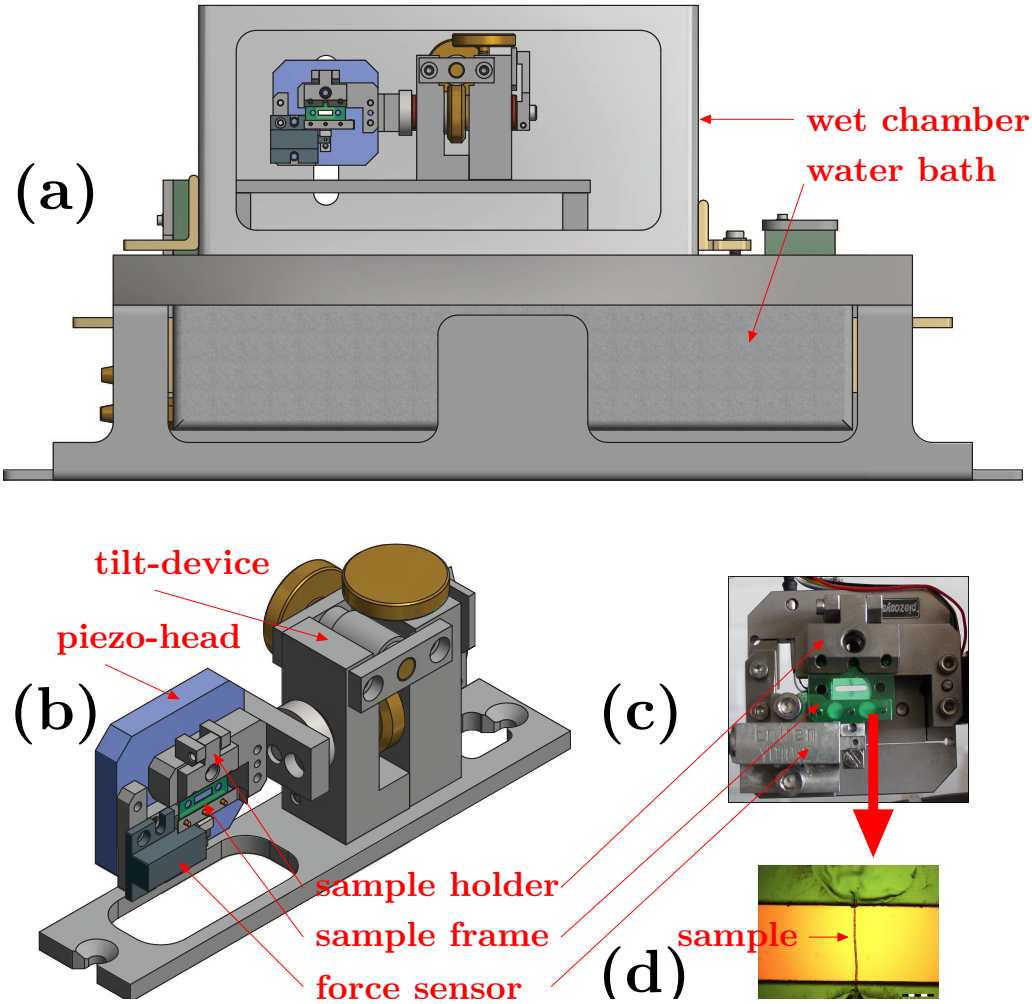

Figure 4.14.: **Piezo sample cell for stretching experiments with single fibres** (a) a sketch of the SPLC is shown; (b) the detachable mechanical part of the SPLC consisting of sample stretching and tilt devices. The latter is used for optimized orientation of the fibre relative to the X-ray beam. (c) the piezo actuator head, equipped with a sample frame holder and a force sensor. (d) a sample frame with a glued-in sample fibre.

detailed description of the driving software is given on page 134.

The maximal load of the force sensor is equal to 0.5 mN, with allowed overloading up to 5N. The card resolution is about of 15 μN per ADC channel. Because the cell has a flat form and a very compact built it is very suitable for the measurements on measurement stations similar to ID13 in ERSF (see below). The sample can be placed very close to the optical component of the synchrotron measurement station and the cell allowed to record

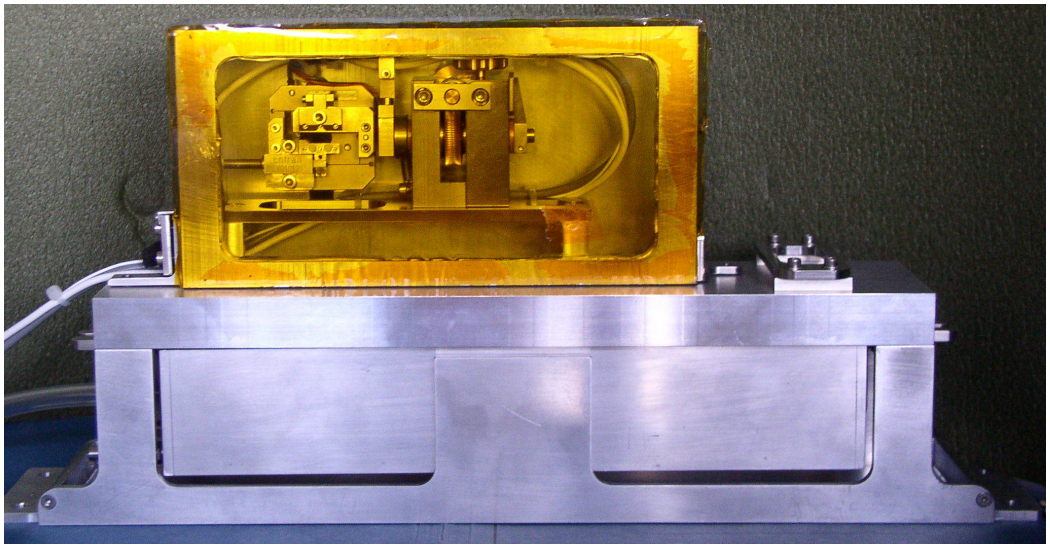

Figure 4.15.: **A photograph of the Piezo sample cell (SPLC)**

engine	piezo actuator with strain sensor	force sensor
firma	piezojena	Entran
components	actuator head PZS 1 power supply unit ENT 150/200 voltage amplifier module ENV 40 controller/interface ER 1 AD/DA converter EDA 3	Sensor ELG-H-0.5N

Table 4.3.: **Components of the piezo-electric stretching cell**

a shadowing/perturbation free diffractogramm.

Software

A software package has been designed and implemented which controls all the hardware integrated in the sample cell. Its server-client architecture allows a remote access to the stretching process. The software offers a possibility to communicate with a software of large-scale facility instruments with a goal to drive a scattering experiment synchronously with a chosen stretching protocol. E.g. it can connect to a SPEC server and take a control over a set of beamline motors, detectors and a shutter. The integration with a TANGO server is possible too.

As mentioned above, the driving software is based on the server-client architecture (see fig.4.16) and is running on the Linux OS (Debian). The server is implemented as a xml [183]/yaml [184] based remote procedure call system. Where a client connects the server and calls some functional procedures or acquires the status by forming and sending the request (command) and receiving the response in the form of data, which it can then represent to the user in the form of graphical or text information. The client part can run on the same or a separate PC (e.g. laptop) and is responsible for communication with an operator. A screen shot of the running client interface is shown on the fig. 4.7 on the page 125.

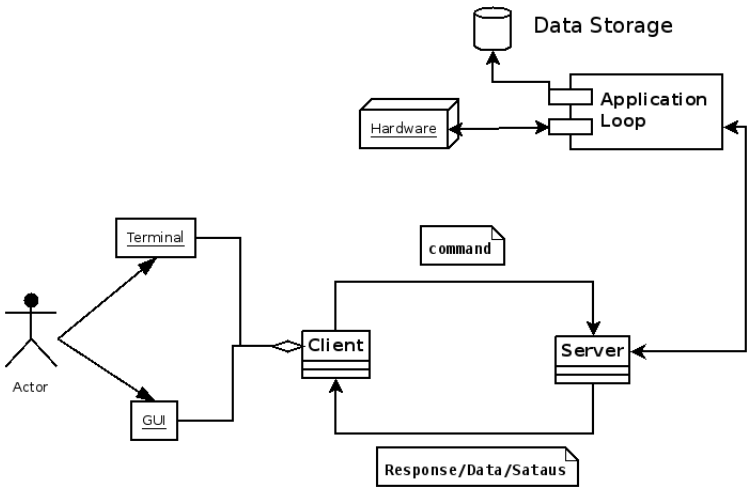

Figure 4.16.: **Sketch diagram for organization of the driver software for the piezo cell**

The server is running on the measurement PC, which was usually placed in the experimental hutch to reduce of the length of the connecting wires. The application loop is responsible for control/acquiring the hardware (motors, electrical controllers, sensors, TTL signals) and for the streaming of the data, especially for saving of the measured data to the hard disk. The loop is implemented as a set of communicating sub processes to achieve the optimal use of the resources and to assure that no data will be lost. The communication of the operator (user) with the hardware can be done ether in the single command regime (request-response) or in a batch mode, where a prepared script (python based) is sent to the server and loaded into the application loop, where it is running to drive the experiment. Additionally, there is a possibility to run python scripts as separate clients on a remote PC with a similar functionality as a batch macros, mentioned above.

The principle of low level data acquisition is described in 4.2.1, on page 118. The processing of the incoming data stream is organized as a chain of repositories and based on the Producer-Consumer Pattern (for design patterns see [172]), where a single Producer is responsible for the read the data-stream from the hardware and distribute it to several registered consumers (e.g. saving consumer, monitor, safety filter, etc.). For purpose of flexibility this part of the system is built as an extensible plug-in system, where it is possible to install for example a new safety filter or a TTL based pausing filter as synchronisation with some other subprocesses.
Some attention was payed to organisation of logging and configuration of the system. The configuration system allowed to change (on the fly) parameters such as IP addresses, conversion constants of the measured data stream, order of the channels etc. without needing to change the source code. Indeed, one can change the whole board card AD converter and, after adapting of configuration files to the parameters of the new card, immediately start to measure.

4.3.2. HUSTEN

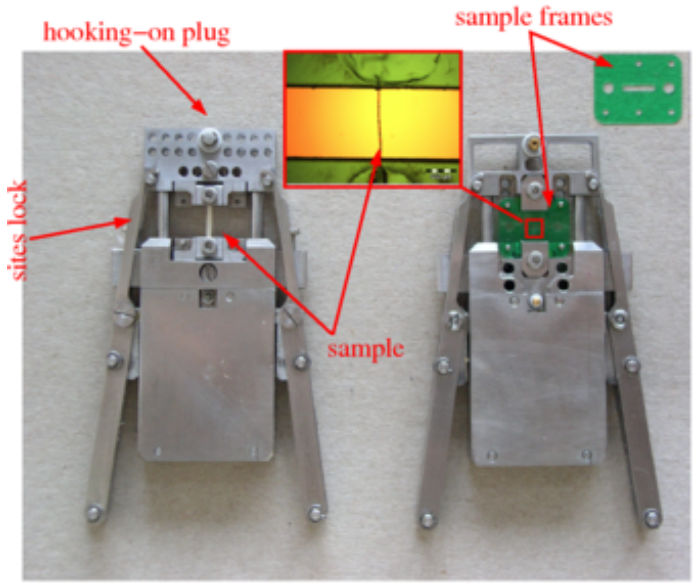

Figure 4.17.: **Sample holding system for use with HUSTEN**

HUSTEN is a measurement system for *in situ* X-ray scattering experiments on fibre bundles

of medium size. It was developed by Ingo Grotkopp and is in detail described in his PhD Thesis [59]. As shown on the figure 4.18 the main building principal remains be the same as for the piezo-electric cell SPLC. The stretching engine is based on a step-servo motor and the strain is measured using a position sensing device (linear encoder from HEIDENHAIN CORPORATION [69]) This cell possesses a mechanical engine to change the samples with minimal perturbation of the atmosphere in the wet chamber. The sample is glued on the same plastic frame as mentioned above, then this plastic frame is mechanically fixed on the larger steel frame, see figure 4.17. The last frame can be put in to the wet chamber through the pre-chamber, which is a some kind of sewer port or lock (see fig. 4.18). From there with help of a mechanical engine the sample is driven to the stretching hooks, where it is locked. This mechanical system is build up similarly to a cigarette automat ☺.
Force measurements are done with a force sensor (from Entran) with maximal load of 5N, an ADC board card is used for recording the force and TTL signals.
The driving program was developed on the basis of the LabView program environment and is running on the XP Windows OS. It offers a graphical user interface with a command terminal and possesses a very moderate batch mode facility. The motor is driven through the RS232 interface to the motor controller, with possesses a very rich command system. The measured data are incoming through two channels, one from the force sensor through a ADC board card (National Instruments) and the other from the linear encoder (strain) through its own board card (Heidenhain). Accordingly, the measured data are saved into two ASCII files: one for force and TTL signal and other for strain. Because data are measured not simultaneously they need to be post-processed, i.e. the re-sampling through the interpolation is required to get the values of force and strain at the same time. The nominal acquisition speed is about 50-100 samples per second (sps) and is based on the clock of the operation system (Windows), which has very large latency.
The complexity of mechanics causes a reduction of the resolution. A recalibration of sensors can not be done without change the source code and recompilation. Any changes in the channels ordering or AD card will require reprogramming effort.

4.3.3. Cell for large bundle stretching experiments (LLC)

The cell for large bundle stretching experiments was developed first by Klaas Kölln (see description in [91]) and modified through the diploma work of Wiebke Knoll [90]. Additionally to the above mentioned requirements this system has to fulfill following exigences:

- It must be possible to adapt the system to experiments with neutron scattering with different instrument boundary constraints.

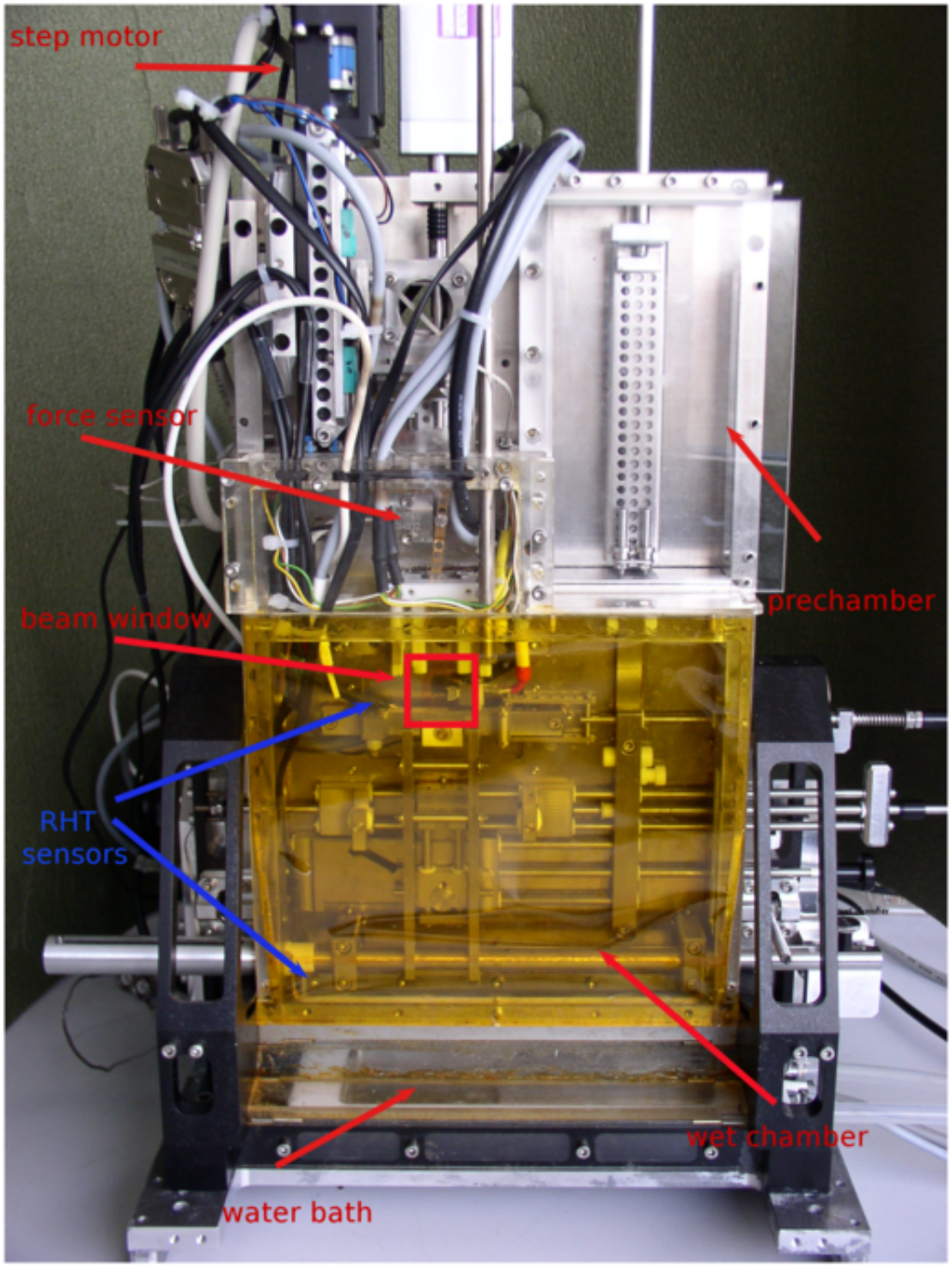

Figure 4.18.: **Sample environment cell HUSTEN**

- Loading force in the range from some N up to 200 N. This value is a result of requirements on the mass of the sample to achieve a suitable level of scattered intensity.
- The system must be vacuum sealed. To reduce the parasitic air scattering signal the neutron path has to be evacuated.

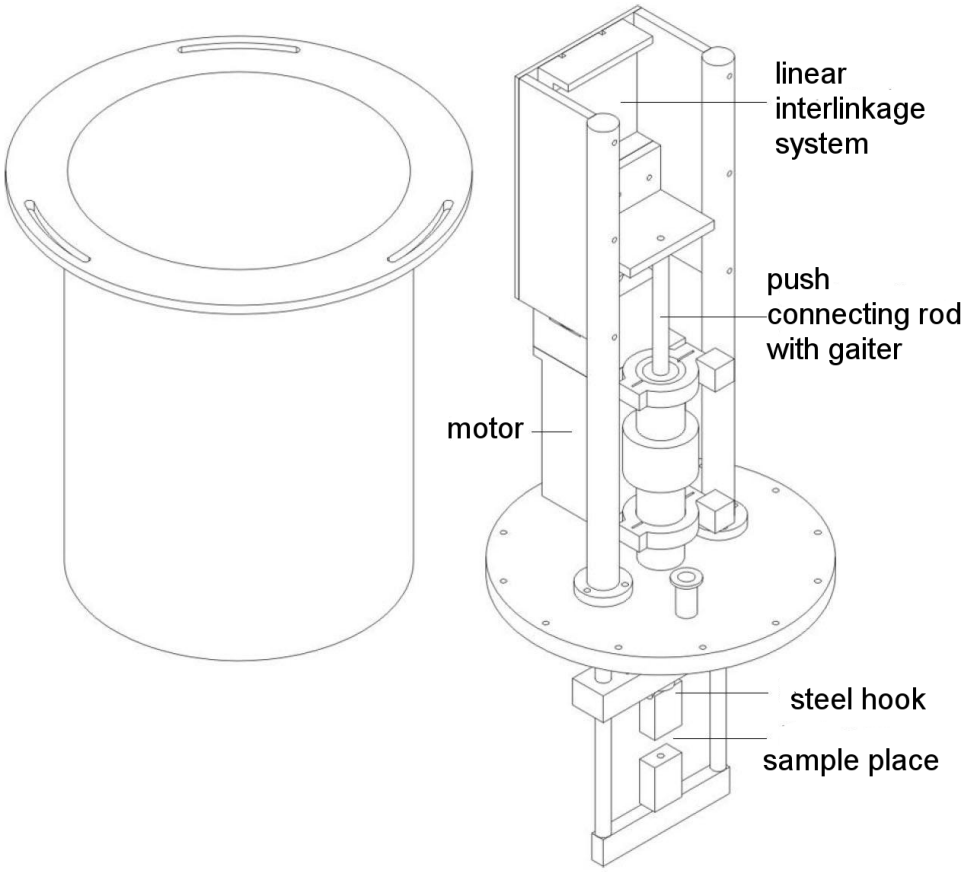

Figure 4.19.: **Sketch of large sample cell** [91]

The sketch of the building structure of this sample cell is shown on the figure 4.19. Its loading engine consists of a (push) connecting rod, which is moved by a linear stage assembled with a servo-motor (manufactured by Hauser EMD). The servo-motor is controlled by its own control unit (of the same manufacturer). For the purpose of hermetic closure, the connecting rod is surrounded by a gaiter. Force is measured by a force sensor, manufactured by Entran.
The acquisition and control of the experiment is done by a special for this purpose developed LabView program through the RS232 interface.

4.4. Sample preparation

Silk gegumming [58] The *Bombyx mori* silk fibres were reeled directly from the cocoons using a specifically designed reeling setup at Oxford University. The cocoons were kept in a water bath during the reeling procedure in order to facilitate the reeling process. The cylindrical reel was specifically designed in order to retrieve the silk bundle without exposing the fibres to mechanical stress.
The sericin coating of the fibres was removed from the silk brins by a standard degumming method. For the degumming process the silk bundle was fixed with cotton threads at several positions (to prevent entanglement). The bundle was immersed in 2l 0.5 %w Na_2CO_3 solution and kept at $70\,^{\circ}C$ for 2 hours (on a hot plate, gentle stirring). Afterwards the bundle was thoroughly washed with deionised water while wearing gloves to remove the Na_2CO_3 and dried on a glass rod overnight.

Single fibre and a small fibre-bundle samples The preparation of the sample for the X-ray scattering experiments was preformed as follows: Single fibres were gently separated from the bundle of degummed fibres and glued on the plastic frame as shown in figures 4.17 and 4.14.

Large bundles For Neutron scattering experiments large sample bundles were used. A long but thin bundle of degummed silk fibres was coiled on a aluminium frame which then was put into the stretching device inside of the sample cell (see figure 4.19).

4.5. *In situ* Scattering Experiments

4.5.1. Synchrotron Scattering

The production of X-ray radiation at synchrotrons is based on the fact, that accelerated charged particles emit photons. Typically one uses light particles such as electrons, accelerated to the velocities closed to the speed of light.
Experiments using conventional X-ray generators (i.e., sealed tubes or rotating anodes) are limited by the available X-ray flux. The greatly increased flux available at synchrotron radiation sources makes it possible to carry out time-resolved in situ experiments e.g. during mechanical tests of specimens.
The response of the nano-structure of bio-materials to mechanical stress thus becomes directly accessible. Furthermore, synchrotron radiation has a very low divergence enables

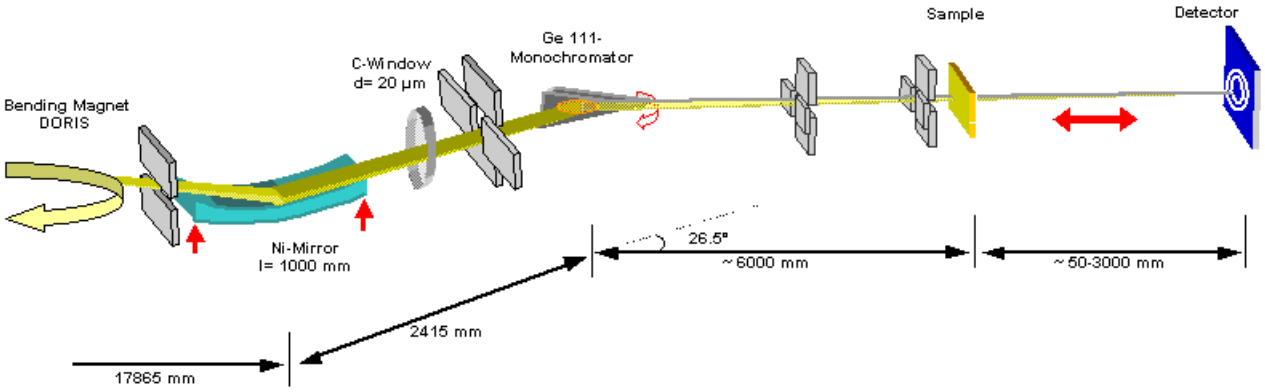

Figure 4.20.: **Layout of the beamline A2, HASYLAB (Hamburg, Germany)** [68]

focusing of X-rays using various optical devices down to micrometre beam size and below. In micro-diffraction experiments, the nano-structure is accessible via the atomic resolution of X-ray diffraction and the micro-structure via a scanning of the sample on the scale of the beam size through the X-ray beam with microscopic position resolution. These parameters on different scales may even be obtained simultaneously in a single experiment.
Below we give a short description of beamlines, where the experiments, reported in this work were done.

Beam line A2 at HASYLAB

Our *in situ* stretching experiments on the silk bundle of the middle size were done on the beamline A2 (HASYLAB, Hamburg, Germany).
A2 [68] is a high flux instrument for a wide and small angle scattering experiments with soft condensed matter materials. It is suitable for time resolved measurements on weakly scattering materials such as polymers. It uses synchrotron of the second generation and sourced by the positron-storage ring DORIS III.
The layout of the A2 beamline is shown on the figure 4.20.
The synchrotron radiation, produced by a deflection magnet, after focusing and passing the monochromator Ge-111, has a fixed energy 8.3 keV, which corresponds to wavelength of about 1.5 Å. The flux at the sample is about 10^9 photons per second. The geometry of the incoming beam can be adjusted using horizontal and vertical apertures. For our experiments a beam of the size 250 × 250 μm was used.
Our stretching device used for these experiments (sample cell HUSTEN, see 4.3.2) has been placed on top of the optical bench and fixed via several translation stages. These stages

allow optimal positioning of the sample relative to the beam.
To store the resulting diffractogramm we used two 2D CCD (charge-coupled device) X-ray detectors. One is the detector manufactured by "Marresearch GmbH", it is offered by the measurement station. Because of high resolution but relatively long acquisition times, it was for statical measurements, where the read-off time was not critical.
The second detector is "Photonic Star (UK) Gemstar 2 HS". It offers a very short readout time of about 300 μs, which leads to a high time resolution during the stretching experiments.

Beam line ID13 at ESRF

Purposes of our micro-diffraction experiments with a single silk fibres were, at least, two fold:

- avoiding the bundle effects (averaging over fibres in the bundle and influence of mechanical interaction between the fibres in the bundle)
- resolving the structural response of the single fibre at the microscopical level through the illumination of the different parts of the sample with a step of about 2-4 μm.

This experiments were curried out using the micro-diffraction facility of the beamline ID13 at ESRF (Grenoble, France).
The beamline ID13 at ESRF (Grenoble, France) has its principal aim to provide small focal spots for diffraction and small-angle X-ray scattering. Additionally to the higher flux, which is common for all synchrotrons of the third generation , this station offers a possibility to focus a beam down to about 0.5 μm. The intensity at the sample is about $2-5\times10^{12}$ photons per second with a divergence about 2.3 mrad. For a better positioning ID13 offers a zoom-microscope pointing parallel to the primary beam. It possesses a $x/y/z$-scanning setup with air bearing rotation and tilt options. The scanning engine can be driven through the software package SPEC, with a server-client interface. This possibility was used to synchronize the stretching experiment with the scanning of the sample i.e. illuminating of the different parts of the sample (see right picture on fig. 4.1). The software we used for a such synchronized scanning is described in section 4.3.1 on page 134. The incident photon energy can be varied in the range from 5 keV up to 17 keV, with the corresponding wavelengths ranging from 2.5-0.73 Å. In all our experiments at ID13 we used the Piezo based sample cell SPLS described in 4.3.1. We used scans of step-wise horizontal (across the sample) and diagonal paths. For our measurements we used a beam size of about 0.5 μm with wavelength 0.96 Å (about 13 keV). To store scattered intensities we used the same Photonic Science CCD detector as in A2 experiments, see subsection 4.5.1, page 141.

4.5.2. Neutron Scattering

Neutron scattering experiments obviously involve the use of large scale facilities as well, i. e., the neutron sources (nuclear reactors or accelerator-based spallation sources). Their *in situ* combination e.g. with mechanical tests is possible by using specialised sample environments and by relying on the high neutron beam stability in combination with negligible beam damage induced by neutrons, making much longer exposition times possible.
Neutron diffraction experiments with wide (WANS) and small (SANS) range of scattering angles give access to the structure of the material at molecular and mesoscopic length scales. Analysing the inelastic (INS) and quasi-elastic neutron scattering spectra it is possible to study the characteristics of molecular dynamics and relaxation processes of material under study. For this purpose the energy range and the resolution of the instruments used have to be in the suitable range. The resolution function limits the visible range of characteristic times values of relaxation processes under study and (together with the accessible energy range) the type of the dynamics accessible with this instrument. To increase the interval of relaxation times one has to use more than one instrument.
The neutron scattering experiments presented in this work were done on several instruments of ILL (Institute of Max von Laue-Pul Langevin) in Grenoble (France), Below we give a short description of these instruments.

Time of flight (TOF) spectrometer IN6

A series of *in situ* stretching measurements were performed on the spectrometer IN6, aimed to study a molecular dynamic response of silk to a load under different humidity. To achieve a reasonable scattered intensity these experiments were done on a large bundle of silk fibres using the `LLC` stretching sample cell (4.3.3).
IN6 is a time-focusing time-of-flight spectrometer provides a facility for quasielastic (QENS) and inelastic (INS) scattering for incident wavelengths in the range of 4 to 6 Å.
The figure 4.21 shows the layout of the IN6. The neutron beam is extracted and focused on the sample with a fixed wavelength, which can be selected from the set: 4.1, 4.6, 5.1 and 5.9 Å. The time focusing is achieved by using a Fermi chopper. To prevent frame-overlap a suppressor chopper is placed before the Fermi chopper and rotates in phase with it at a lower speed. The instruments energy resolution depends on the wavelength and lies in the range of 50 to 170 μeV. The maximum momentum transfer is 2.6 $Å^{-1}$ and the accessible energy range is 3-200 meV. The beam size at the sample is 3 $\times$ 5 cm^2 with a flux of about 8.9 $\times$ $10^4 cm^{-2} s^{-1}$. Scattered neutrons pass through the helium filled flight path and are registering by 337 ^{3}He detectors, placed at a distance of 248 cm from the

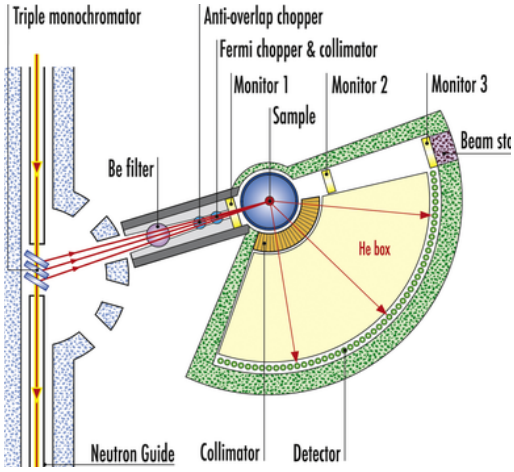

Figure 4.21.: **Instrument Layout of IN6, ILL (Grenoble, France)** [76]

sample. The detectors are on a circular arc with scattering angles ranging from 10° to 115°. The detectors are separated into three horizontal banks with azimuthal angles -15°,0°,15°. Three additional detectors serve as monitors, one of them is in front of the sample and other two are behind the sample. The signal from each of the detectors is subdivided into 1023 time-of-flight channels, which register the number of incoming neutrons per time interval $\Delta = 4.82\mu$s.

Spin-Echo Spectrometer IN11

To test the mesoscopic dynamic of silk material scattering experiments was done on the instrument IN11 (ILL, Grenoble, France). The experiments was done without stretching under several setting of temperature and humidity using sample cells offered by the support of this instrument.

IN11 is an spectrometer aimed to be used to study of slow relaxation phenomena in polymer materials, glasses or magnetic materials. Its principle (fig. 4.22) is based on using the Larmor precession of the neutrons magnetic moment in a magnetic field as an internal clock by the transition of the individual neutrons through two large solenoids placed before and after the sample. The method allows to access the highest possible energy resolution of sub-μeV over a wide wavelength range of incident neutrons. IN11 measures the real part of the intermediate scattering function $I(Q,t)$ (see chapter 3 for definition) directly.
The incident wavelength is 3.8-12 Å with a beam divergence of 15 mrad and diameter of 45 mm. The accessible energy transfer range is [1.3 10^{-5}, 0.15] meV with the range of

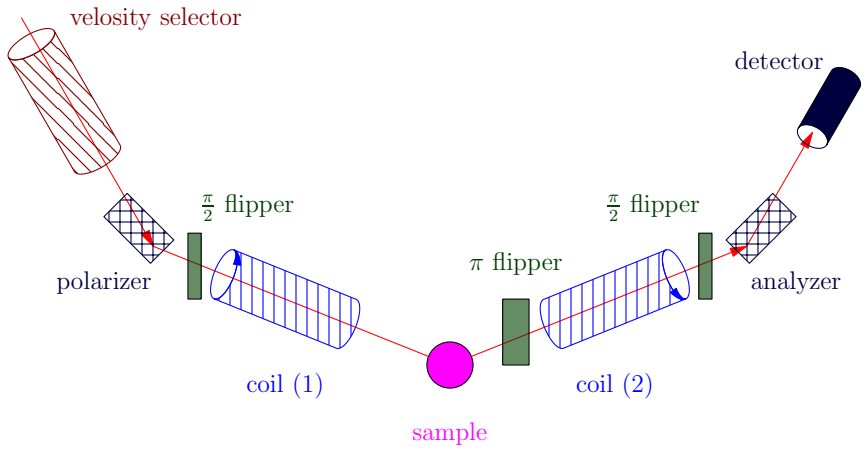

Figure 4.22.: **Sketch of a layout for a spin echo spectrometer basis**

impulse transfer from 0.02 up to 2.7 $Å^{-1}$.

5. Analysis and results

We start this chapter with the description of the procedures of the extraction and reduction of the measured data (section 5.1). Here the processing of the signals from the mechanical measurements and reduction of the X-ray diffraction data are given. Especially, we give the specification of the azimuthal integration procedure and describe the computation of the 002 position and the related strain of silk crystallites. In the section 5.2 the data analysis, modelling and results are presented. The section starts with the description of reduction and analysis of our radiation damage experiments. Using the results of the radiation damage measurements the time protocol of the *in situ* X-ray scattering experiment was chosen. Then, our results about the crystallite modulus and its dependence on humidity are given followed by the use of these results to describe the output of stretching experiments with our combined linear viscoelastic model [93]. Further, we describe the application of the fractional viscoelastic models to the long time stretching experiments. Then, the results for the non-linear models are presented.
The last part of the chapter is devoted to modelling the *in situ* X-ray scattering experiments by our (more detailed) molecular model, where the elongation of crystallites is addressed by the internal rotation of the molecular chains.

5.1. Reduction and Extraction of Data

5.1.1. Mechanical Properties

The mechanical stretching experiments were performed either in the laboratory (AG Müller) as purely mechanical measurements or as *in situ* scattering experiments, performed at large scale facilities (HASYLAB, ESRF, ILL). The used equipment and stretching setups are described in chapter 4. In all our mechanical measurements the controlled parameter was the elongation of the sample (stretching path) recorded together with environmental parameters. The force needed to drive the sample through the given stretching path was measured as a function of stretching and time. The time scales of our interest can be divided into three ranges:

`short time scales: several decades of milliseconds (10 ms - 1 s)`
At these scales the 'glassy response' of the material is visible and in most of the cases can be (at least roughly) obtained by a linear fit of the force to strain relation. The result of such a fit is the so called glassy modulus (see chapter 2 for more details).

`intermediate time scales: from seconds up to some minutes (1 s-10 min)`
Most of our *in situ* X-ray scattering experiments have been performed at this time scale. For pre-stretched material (see 5.2.4) a relaxation phenomenon is visible and can be roughly described in the framework of the viscoelastic theory [35, 93, 168], see chapter 2.

`long time scales: several hours up to a few days (> 1 h)`
Neutron *in situ* scattering experiments are usually performed at this scale. Such experiments allow us to study the dynamics of the system averaged over a long period of time.

The samples were prepared either as single fibres or as a bundle of a few fibres (see page 140).

Conversion of the digitalized signal into physical units The signal can be read from the digitizer card in the form of bits (gains). Each gain is responsible for a level in the analog signal. In the case of the '16 bits-word card' this means that the whole range, accessible to the card input, can be divided into $2^{16} = 65536$ channels (gains). The analog signal has a linear relation to the gain number transmitted from the card. For the purpose of direct conversion from the gains into the physical signal, calibration measurements were performed to get the relation {gain $\longleftrightarrow$ physical value} as a linear function of the gain number. More about calibration measurements can be found in chapter 4. The mechanical values are collected in terms of force 'f' (mN) and elongation or strain 'y' (μm). This was further converted into units, which are convenient for describing material properties [168]:

`stress (GPa)`: is given by the force per cross section area $\sigma = \frac{f}{\texttt{Area}}$
`strain (% or fraction)`: a relative elongation $\epsilon = \frac{\Delta L}{L}$

where: f denotes force (mN), `Area` is the sample's cross section (μm^2), L is the sample length and ΔL the elongation of the sample (μm). Typical values of L were 1-2 mm for the *in situ* X-ray experiments and for a single fibre mechanical measurement. For neutron scattering experiments the length of the sample was in centimeter range.

Shape and components of excitation and response signals Stretching experiments on the bundle of silk fibres were performed using the HUSTEN engine, introduced briefly

in section 4.3.2. The processing of the data measured by the HUSTEN engine is described in [59].

The SLPC (small piezo-loading cell) engine 4.3.1 is used by us for the stretching experiments on single fibres. During all measurements performed with SPLC the engine was used in the loop-back regime, which gives us the necessary stability and linearity of the excitation curves. The elemental motion of this engine is a step- or jump-like movement. On the basis of these jumps many different curve shapes can be assembled by a sequence of successive steps. Fig. 5.1 shows an example of the realisation of a tooth-like curve. For demonstration purposes the height of each single step was chosen larger than usual in our experiments. In the illustration the tooth-like (red) curve is shown, which consists of two parts: upward movements and then downward movements with a velocity $v = 1.5$ μm/s). This curve is realized (blue curve) as a sequence of successive steps, each with the same height of 4 μm and duration 2.67 s.

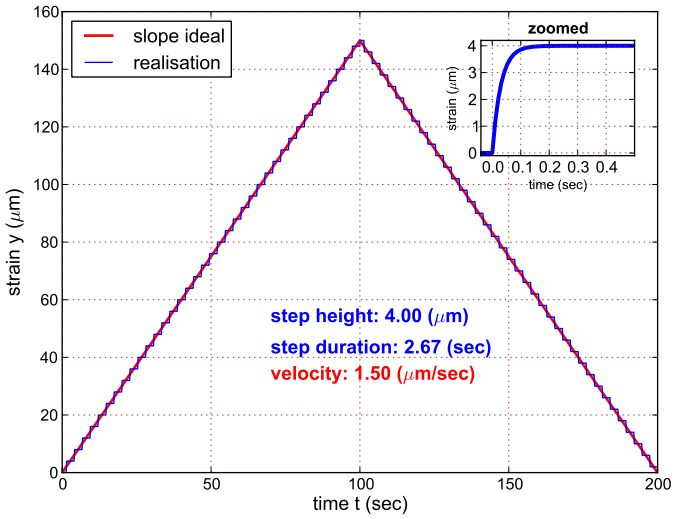

Figure 5.1.: **An example of realisation of a tooth-like curve**
A tooth-like curve, i.e. an upward slope and then a downward slope with velocity v=1.5 (μm/s), realized as a sequence of successive steps. For demonstration purposes the height of each single step (4 μm) is chosen to be larger than in our actual experiments. The inset at the top-right of the figure shows details of the raising part of the step zoomed out near the start point.

The piezo-driven strain signal (in the loop-back regime) can be considered to be a sum of

three essential components:

$$y(t) = y_s(t) + \eta(t) + \Delta y(t) \tag{5.1}$$

where $y_s(t)$ denotes the main part of the signal (strain path), $\eta(t)$ the usual mechanical noise (e.g. vibrations of the surrounding environment) and $\Delta y(t)$ the loop-back operational signal, which is used by the driver electronics to control the strain path. Figure 5.2 (a,c) shows an example of a strain step recorded over a time interval of about 2 s. Here the black curve represents the measured points $y(t)$, the red curve is the main part of the strain signal $y_s(t)$ and the green curve is the contribution from the loop-back component $\Delta y(t)$. It is clearly visible that the last two terms have a smaller amplitude than $y_s(t)$.
We assume the response to $y(t)$ to be a superposition of three terms, as well:

$$f(t) = f_s(t) + \eta_f(t) + \Delta f(t) \tag{5.2}$$

where:
$f(t)$ is the force measured as the response to the excitation $y(t)$ in 5.1 above, in detail: $f_s(t)$ is the response to $y_s(t)$, $\Delta f(t)$ is the response to the operational signal, and $\eta_f(t)$ is the random component due to the environmental noise.
For steps with an amplitude larger than 5 μm we can neglect the last two parts of the signal in the equations (5.1, 5.2). However, for smaller step amplitudes the influence of the noise and operational signal increases and has to be taken into account. In such a case we will smoothen the noise component (re-binning) and remove the operational component, using Fourier transform techniques.

Smoothening (de-noising) procedure and removing of the operational signal.
If we assume that the noise $\eta(y)$ has a random character, then this component can be smoothened using the re-binning procedure. Or, alternatively, applying a discrete wavelet transform, one can remove some number of levels (the fine-grained components) from the detailed spectra of wavelet expansion.
The loop-back operational signal is oscillatory. It possesses a characteristic frequency spectrum which is concentrated around 100 Hz and has a small spreading width. The silk responds to this nearly steady-state excitation with a similar vibration but its characteristic frequency spectrum is concentrated around 50 Hz. Both can be easily removed using a Fourier filtering procedure. (The shift of the response spectrum to the lower frequency is not yet understood, but it seems that silk fibres act as an active filter in the frequency range mentioned above.)

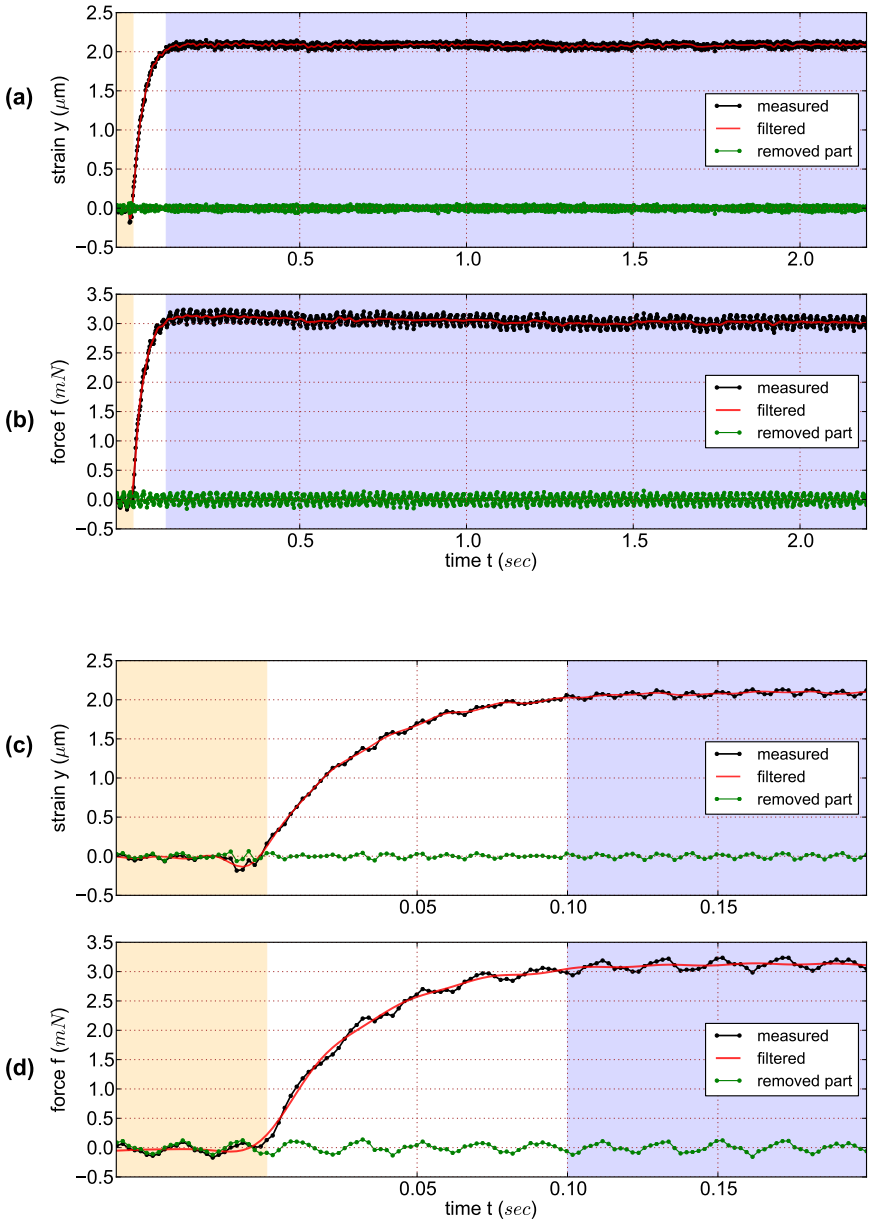

Figure 5.2.: **De-noising and removing of the loop back operational signal** This figure shows the example of the reduction of the smoother part of the signal by the method of subtraction of a narrow frequency band, contained in the Fourier spectrum of the signal. The black line shows measured data, the red line shows the filtered signal and the green one is the removed part of the measured signal, associated with the operational signal Δy. Plots (c,d) give a detailed view, zoomed out at the raising point of the step curve shown at plots (a,b).

Figure 5.2 shows an example of such a de-noising procedure. Sub-figures 5.2 (c,d) represent a zoomed-out view of the same signal (and the response to it) as depicted on the sub-figures (a,b). Plots, denoted by (a,c), show the strain path signal and (b,d) show the force measured as response to the signal shown in (a,c). The red colored curves in 5.2 (a,c) are associated with $y_s(t)$ in the equation (5.1) and in 5.2 (b,c) the red colored curves are associated with $f_s(t)$ in the equation (5.2). They were obtained by applying a filtering procedure to the measured data represented by black curves (y and f).

Analytical description and specification of the strain step For modeling a response function we need to have the excitation signal (strain path) in an analytical form, i.e. as a function of the time.
For experiments at long time scales it is sufficient to approximate the strain step as a Heaviside function $h_0 H(t - t_0)$. The curve can be specified by the step height h_0 and the step starting time (rising point) t_0.
At the scale of 10-1000 milliseconds the step can be approximated by a curve of the following form:

$$y(t) = h_0(1 - A\exp(-\frac{t}{\tau_1}))(1 + B\exp(-\frac{t}{\tau_2})) \tag{5.3}$$

$$= h_0\left(1 - A\exp(-\frac{t}{\tau_1}) + B\exp(-\frac{t}{\tau_2}) - AB\exp(-\frac{t}{\tau_1} - \frac{t}{\tau_2})\right) \tag{5.4}$$

where: $h_0, A, B, \tau_1, \tau_2$ are parameters, which can be adjusted to the measured data. $\{A, B\}$ define the form of the step-like curve and $\{\tau_1,\tau_2\}$ determine the duration of the raising stage. For discussing a viscoelastic response to a signal described by the equation (5.3) we will need the Laplace transform of it. For this purpose the expression (5.3) is slightly modified by an expansion into exponential terms (see 5.4), and we get the Laplace transform as:

$$\hat{y}(s)/h_0 = \frac{1}{s} - \sum_{i=1}^{3} C_i \frac{\tau_i}{1 + \tau_i\, s} \tag{5.5}$$

where: coefficients $\{C_1,C_2,C_3\}$ are defined as $\{A, -B, AB\}$ respectively and $\tau_3 = 1/\tau_1 + 1/\tau_2$.

Determination of the strain offset Initially, before stretching, the sample fibre is bent and a small amount of force is needed to adjust and hold it in the straight state. Figure 5.3 shows a typical plot of force versus stretching path measured on a silk fibre (blue curve). The stretching path is measured with respect to a reference point, at which no force-response of the sample is visible. In the range between the zero strain point and

a point marked by the green point the system exhibits a small deviation from the elastic behaviour (Hooke's law). This is due to the adjustment effects mentioned above. Because the system responds nearly elastic in the range just above the green point, we assume that the ideally straight fibre will start to resist to the elongation starting at the position on the strain path, marked by the red point. This position is associated with the length of the ideally straight fibre.
To describe the amount of elongation one needs to know the position on the stretching path (the strain offset) where the fibre starts to respond if it would not be bent. At this point the fibre is assumed to be aligned but yet not elongated.

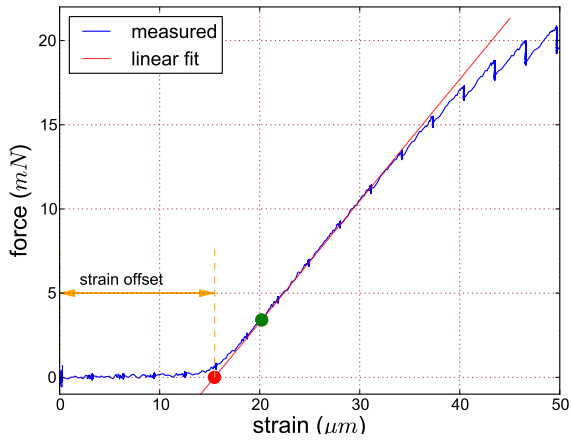

Figure 5.3.: **Strain offset**
The blue curve shows the measured data $f(y)$. The red line represents the linear fit in the "elastic range". The red point is the strain offset (see text). The green point shows approximately where the response of the real fibre coincides with the response of idealized straight one.

The following procedure is used to obtain the value of the strain offset (see fig. 5.3):

1. During a some initial time interval the response of the sample is assumed to be nearly elastic.
2. A linear fit of the measured data is performed in this "elastic region".
3. The intersection of this line with the abscissa determines the value of the strain offset.

In figure 5.3 the red line is an example of such a linear fit. The red point is the position of the strain offset. The green point shows approximately where the response of the real

fibre coincides with the response of the idealized straight one. For smaller elongations the contribution from the process of adjustment is visible.

5.1.2. Initial data reduction for X-ray scattering experiments

The recorded data were processed by standard procedures of the data reduction software 'fit2d' [64] for the spacial, geometry and polarization correction. The distance between the sample and the detector d was defined from the diffraction image of a standard sample, such as Al_2O_3 or Tripalmitin powder, which was measured additionally in each of the experimental setups. The sample-detector distance d is related to the known scattering angle 2θ of a Debye-Scherrer ring and distances r from the location of the ring relative to the beam centre in a recorded diffraction image as:

$$r = d \tan 2\theta.$$

For each experimental configuration the expression above was fitted to a set of Debye-Scherrer rings from the standard powder sample with d as fit parameter. The resulting fits confidence interval was taken as the experimental error in the value of the distance d.

A definition of 'cakes' for the Bragg reflections of interest

In the WAXS experiments we will mostly be interested in the position and shape of the two strongest peaks from silk: the meridional peak (002) and the equatorial peak, containing two reflections (200) and (020). The positions of these reflections contain the information about the size of the unit cell and hence, in the case of stretching experiments, about the relative elongation of the crystallites. Some auxiliary information can be extracted from the position of the 'diagonal' reflection (021). Figure 5.4 shows the position of all these reflections on a diffraction image of silk.

To study the behaviour of the intensity as a function of the momentum transfer Q usually a 1D curve is extracted from a diffraction image. For this purpose one cuts an area containing a reflection of interest from the diffraction image. The boundary of this area are four coordinate lines in the polar coordinate system $\{Q,\phi\}$, centred at the beam centre (see fig. 5.4 for an example of such areas). In the jargon of the most popular program for preprocessing diffraction images 'fit2d' such areas are called 'cakes'. Choosing a sequence of support points along the Q coordinate, one computes the intensity, averaged along the ϕ axis, for each value of Q in the chosen set.

Lattice strain

Bragg's law gives a direct relation between the position of a reflection peak and the d-

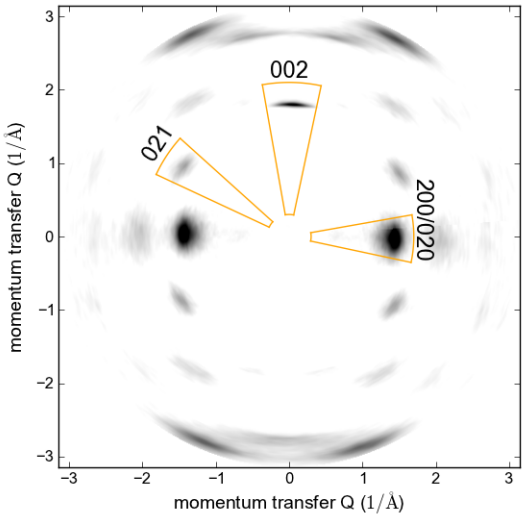

Figure 5.4.: **Definition and nomenclature of the reflections of interest**
A diffraction image of *Bombyx mori* silk measured at ID13 is presented. The regions bounded by the orange lines are the ranges of our interest, containing (1) the meridional peak with indices $hkl = (002)$, (2) the equatorial reflections with indices $hkl = (200, 020)$ and (3) the reflection specified by the indices $hkl = (021)$. Such regions, usually called 'cakes', are specified by the two limiting values of the momentum transfer Q and of the angle ϕ in the diffraction image. The $1D$ curve $I(Q)$ is obtained by averaging over the angle ϕ.

spacing in the direction of this peak. Hence, the amount of the lattice deformation can be read from the diffraction images. The change in the spacing of the crystallite lattice can be observed by plotting the corresponding reflection intensity versus momentum transfer. Figure 5.5 shows scattered intensities of the 002 reflection for several values of applied stress, where the effect is clearly visible. The shown intensities result from the radial integration over the cake area defined in figure 5.4. Measuring scattered intensity as a function of the applied stress allows to estimate the elastic modulus of the crystallites in the fibre as a linear fit of the lattice elongation against the applied stress [93, 107, 158–160, 163]. One of the methods for computing the position of the 002 reflection, which is widely accepted in the literature, consists in computing the distribution centre of the function $I(Q)$ or by fit of the shape of $I(Q)$ by a suitable profile function [93, 158–160]. We used the latter method. The results are presented and discassed in in sec. 5.2.2.

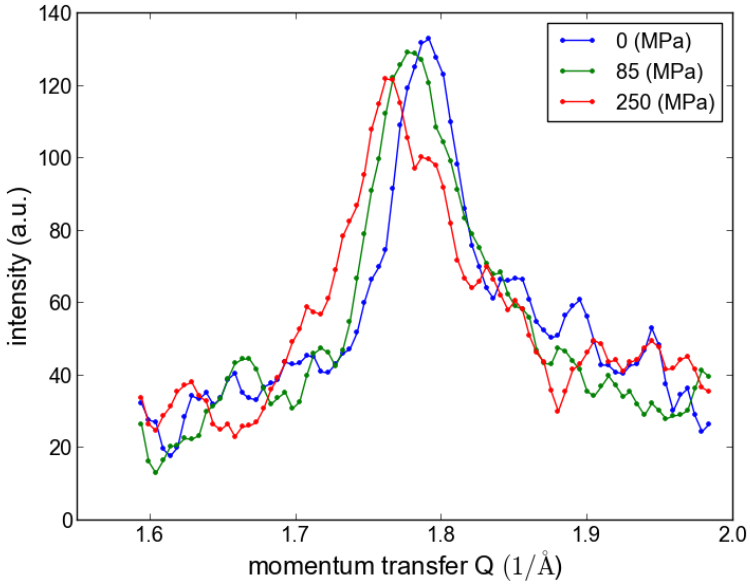

Figure 5.5.: **The shift of the** 002 **reflection with increasing of stress**

5.1.3. Measurements overview

Below an overview of the main measurements of this thesis is given. Table 5.1 lists the measurements performed on large instrument facilities. See section 4.4 for description of these instruments and table 2.1 (on the page 29) for definition of strain excitations. At the instruments ID13 and A2 for each environment/excitation, listed in the table, measurements were performed on several samples (from 3 to 7). In the case of neutron scattering experiments (IN6, IN11) the repeating quote was only 1-2. The results from the additional SAXS measurements on BW4 (DESY, Hamburg) and the dynamical neutron scattering experiments on IN10 (ILL, Grenoble) were used in the current work only indirectly and, hence, are not included in the list of the main measurements.

With the aim of supporting the *in situ* experiments on large instruments and testing our mechanical (viscoelastic) models a large set of the off-line stretching experiments were performed on single fibres in the laboratory of the group of Prof. Dr. Müller at the university of Kiel. These experiments were done at room temperature of about 22-26°C. A rough classification of these off-line measurements is shown in table 5.2.

instrument	type of sample	environment (target)		excitation of strain	initial states
		T (°C)	RH (%)		
ID13	single fibre	25	5,25,43,73,100	ramp/steps	native
	single fibre	25	25,100	ramp	prestretched
A2	bundle of fibres	23	25,43,60,73,100	cyclic tooth/ramp	native
IN6	bundle of fibres	26.5	25,73,100	sequence of ramps	native
IN11	bundle of fibres	26.85	100% H_2O	no excitation	native
	–	26.85	100% D_2O	–	–

Table 5.1.: **Main measurements on large instruments**
For description of strain excitations see table 2.1 on page 29. The columns with environmental parameters show only target-values, they can slightly variate from one sample to the other.

- **relaxation**
  - **excitation:** (single) step
  - **initial sample states:** native and prestretched
  - **time of measurement:** from several minutes to several days
  - **RH (%):** 20-28, 43, 73, 92-100
- **intermediate dynamics**
  - **excitation:** cyclic tooth, ramp
  - **initial sample states:** native, prestretched
  - **rates of strain (μm/s):** 0.25, 0.5, 1.0, 1.5, 2.0, 2.5, 5.0
  - **RH (%):** 20-28, 73, 92-100
- **longtime dynamics**
  - **excitation:** cyclic tooth, implemented by steps
  - **initial sample states:** native
  - **steps height (μm):** 2-5
  - **mean rates of strain (nm/s):** 0.1, 0.18, 0.5, 0.8
  - **RH (%):** 26-31

Table 5.2.: **Classification of the off-line stretching (single fibre) experiments**
The length of each fibre was 1 and 2 mm. The number of experiments performed per RH/excitation type was 3-10. The 'longtime dynamics' experiments was not repeated, i.e. only one experiment were done per each mean velocity shown in the table.

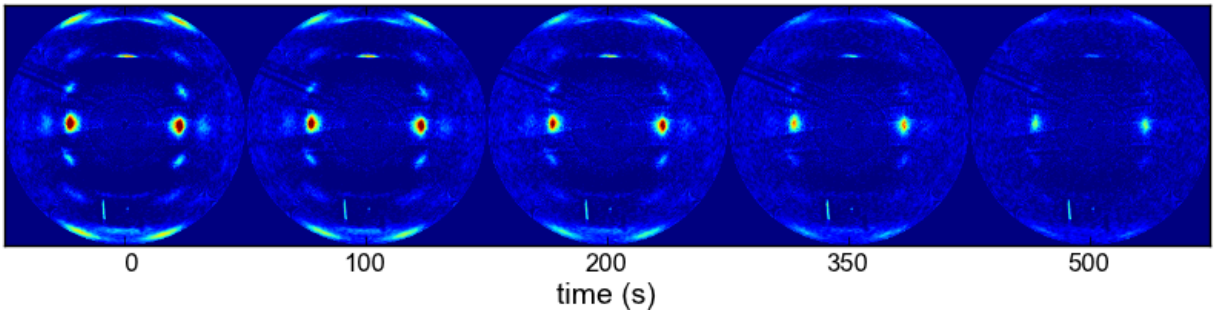

Figure 5.6.: **Evolution of diffraction images in the radiation damage experiment** The figure demonstrates the evolution of the radiation damage of the *Bombyx mori* silk crystallites at the relative humidity of 27% and a temperature of 25° C. The measurements were carried out at the beamline ID13. Compare with fig. 5.7, where 1D curves of the averaged scattered intensities $I(Q)$ are shown for the same set of measurements with different radiation times.

5.2. Modelling and Analysis

5.2.1. Radiation damage of *Bombyx mori* silk crystallites measured on the beamline ID13

Due to the high intensity of the X-ray beam at the beamline ID13 one needs to take into account the effects of radiation damage when preparing experiments with biological materials. Below we show the results of a simple experiment aimed at measuring the life time of a sample of *Bombyx mori* silk under X-ray or radiation. A single fibre of *Bombyx mori* silk was placed in the sample cell and was kept aligned by applying a stress of about 50 MPa. Then the sample was periodically exposed with a period of 2.5 seconds, 2.0 second of exposure time and a pause of 0.5 seconds between the exposures. The diffraction images of these exposures were recorded by the CCD detector, mentioned in the section 4.5.1. The measurements were carried out at ambient temperature, 25° C, and at two different relative humidities, namely 27% and 90%. The effect of the radiation damage is clearly visible in figure 5.6 which shows a sequence of measured diffraction images for several radiation times.

The time- and Q-dependence of the intensity of the (002, 020/200, 021) peaks is shown in figure 5.7 on the page 159. With increasing exposure time the decrease of intensities and broadening of the peaks is observed, while the position of the peaks remains nearly unchanged.

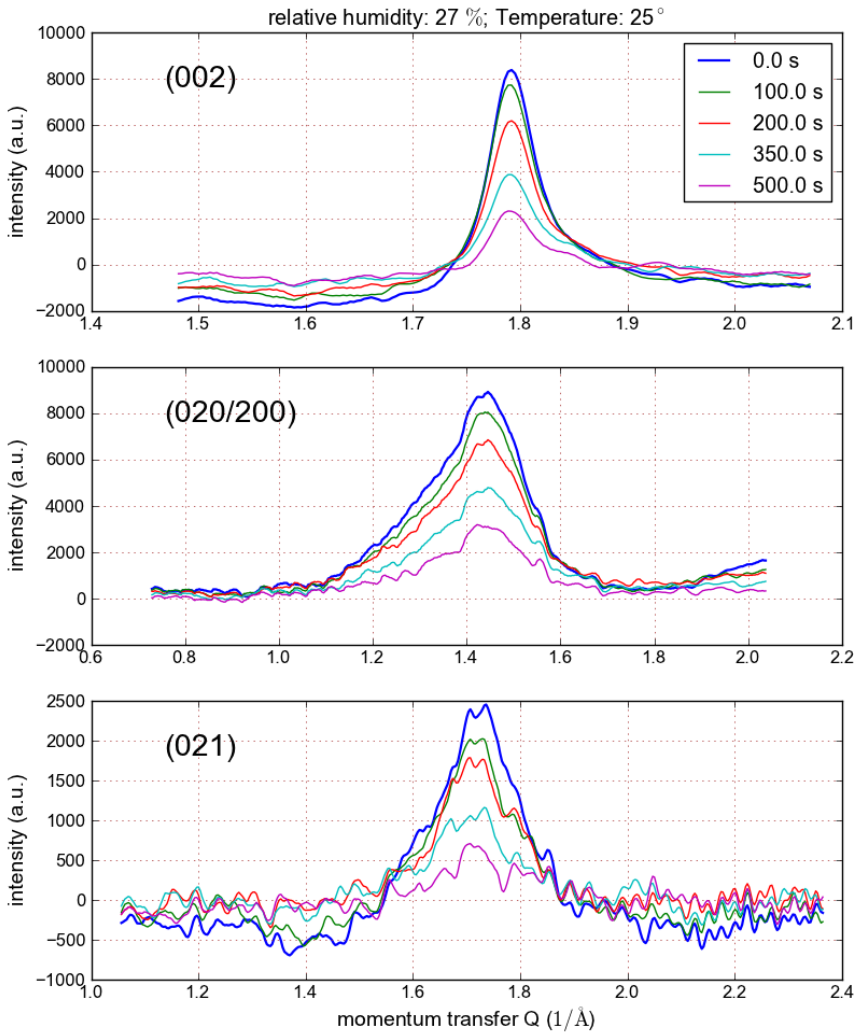

Figure 5.7.: **Evolution of the form of peaks in the radiation damage experiment** The figure shows the intensity curves $I(Q)$ of the peaks $002, 020/200, 021$ measured for several radiation times at ambient relative humidity 27%. The reduction of the intensities and a broadening of the peaks are clearly visible. The corresponding diffraction images are shown in the figure 5.6.

To get a first approximation of the life time of the crystallites under radiation we averaged the scattered intensities over the areas around the peaks of interest in each diffraction image. The averaging areas are sketched in figure 5.8. The resulting curve of the dependence

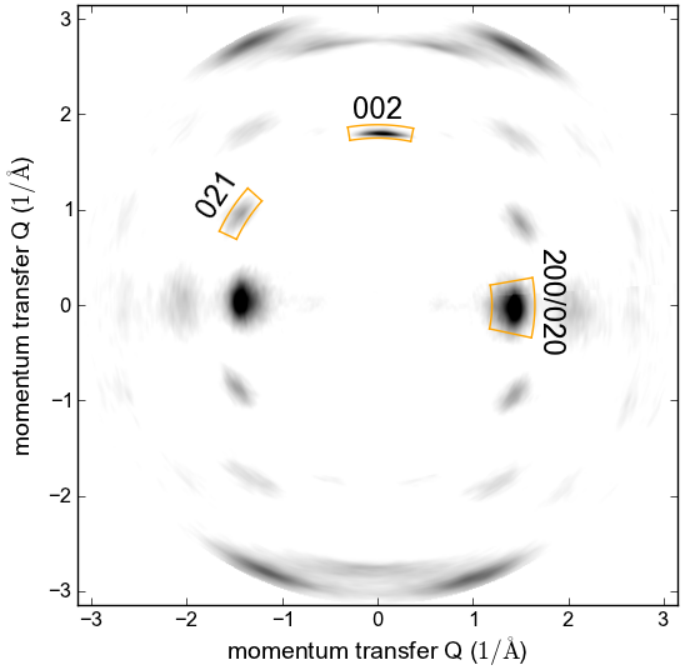

Figure 5.8.: **The areas used for intensity averaging**
The figure sketches the areas in which the intensity is summed to compute the dependence of the averaged peak intensities from the time.

of the averaged intensity from the radiation time is shown in figure 5.9 on page 161. All these curves exhibit nearly the same behaviour:

- Initially, during the time interval of about $50 - 100$ seconds the curves show a small plateau with nearly constant magnitude.
- Then a roughly exponential decay of averaged intensity is observed.

The small jitters of the averaged intensity curves in figure 5.9 are due to the material flow with respect of the beam position. Because of the very small size of the micro beam used, the intensities are very sensitive to the small material flow in/around the beam in the sample. This flow is caused by the response of the sample to the background oscillations and the relaxation process of the initially aligned sample. In the case of the measurements at a relative humidity of 90%, additionally, the response of the material to the change of the environment (from dry to wet) contributes to the flow of the material on a microscopic

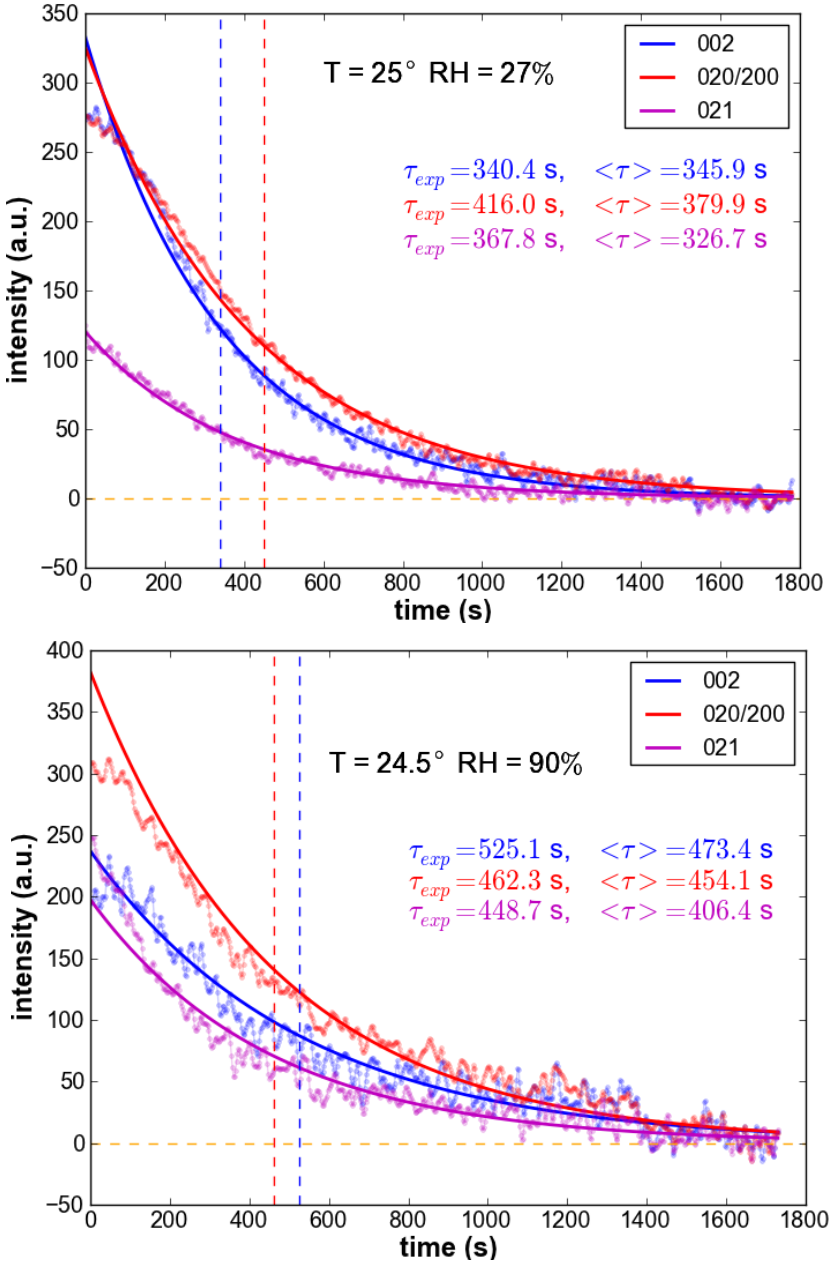

Figure 5.9.: **The evolution of the diffraction patterns**
The figure shows the evolution of the intensity of the 3 peaks of interest of the *Bombyx mori* silk sample under radiation. Measured points points and lines of the fitted decay low are shown (see the text).
The top pane gives the results of measurements at ambient environmental conditions. The bottom pane shows the results of measurements at the relative humidity of 90%.

scale. It was not possible to avoid its influence completely because the characteristic times of this response are of the order of several hours.

The approximate values of the life-time (or the time of decay) of the crystallites were computed (i) by evaluation of the statistical `mean life-time` $< \tau >$ and (ii) by fitting a decay exponent with characteristic (decay) time τ_{exp}.

The statistical mean time of life is evaluated as:

$$< \tau >= \frac{\sum_k (t_k - t_0) I_k}{\sum_j I_j} \tag{5.6}$$

where j, k is the number of the exposure or (equivalently) the diffraction image in the stored sequence, t_j is the time point of the exposure j and I_j the averaged peak intensity at the exposure time t_j. t_0 is the starting point of the exposition sequence.

The usual exponential law is used to fit the averaged scattered intensity of each peak of interest is:

$$I(t) = I_0 \exp\left(-\frac{t}{\tau_{\exp}}\right) \tag{5.7}$$

where τ_{exp} is the decay time and I_0 is the initial intensity.

The two methods give very similar characteristic times, as shown in figure 5.9. From the above results we interpreted the time interval of $300 - 350$ s as the life time of the crystallites.

On the basis of these results we did our choice in the parametrisation of our *in situ* stretching experiments at the beamline ID13 as follows.

For convenience we repeat the main aspects of the experimental setup, described in 4.1. The silk fibre is stretched up to the elongation of 100-200 μm. Then the stretching was stopped to do the measurements on the relaxing sample. The stretching is performed either with constant velocity (stretching rate) of about 1μm/s or as a sequence of small steps. Simultaneously, the sample is periodically exposed and the diffraction image is recorded. Because of the small size of the microbeam of ID13 and the small diameter of the sample fibre we have to scan in the direction perpendicular to the sample-fibre choosing, at least, 5 points. At each of these points we have to record a diffraction image. So, roughly speaking, to expose the sample every 2μm of elongation we need to do about 100 scans performed over a time of about 200 seconds. Additionally, we need 50-100 scans during the relaxation period.

Because of the relative short life time of the sample, we are constrained in the choice of parameters such as the time interval of exposure and the number of the exposure points in a scan, the stretching rate, the length of the elongation of the sample.

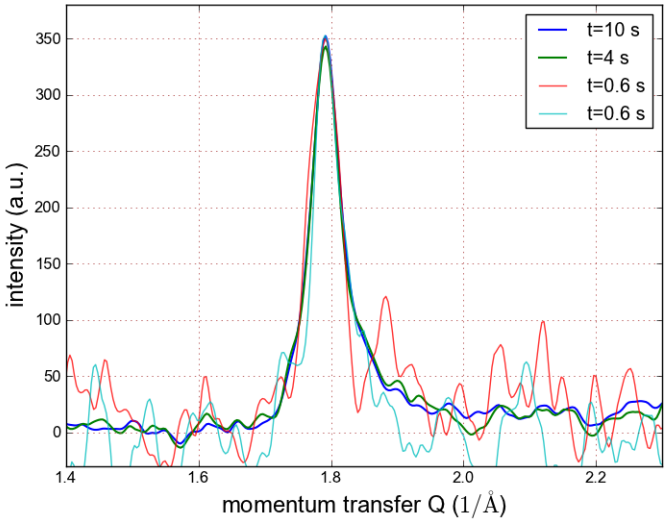

Figure 5.10.: **Averaged intensities of the (002) peak for several exposure times.**

The limitation on the duration of the stretching experiment constrained us either to move with larger velocities or to use shorter elongation intervals.
The exposure was chosen to be about 0.6 s and the duration of the stretching experiment was chosen to be 100-150 s. The short time of exposure is very critical because it leads to very low counting rates and leaves us with the very low signal to noise ratio. Additionally, the signal with count levels below the threshold of the detector sensitivity leads to an artificial (spurious) behaviour. In fig. 5.10 these effects are demonstrated. As example, the sequence of averaged intensities curves $I(Q)$ of the meridional peak (002) for several different times of exposure is chosen. It is visible that for the short exposure time of 0.6 seconds the level of the sensitivity threshold is about of 1/5 of the peak intensity. Under stretching the above ratio will increase due to the spreading of the meridional peak over the Q-scale.

5.2.2. Studying the lattice deformation of the fibroin crystals under tensile load

The silkworm silk *Bombyx mori* was investigated at ambient temperature and several humidity contents. X-ray diffraction experiments were carried out *in situ* during a stretching experiments on a several bundles of silkworm silk and on single fibres. An overview of our measurements which are relevant for this work are given in section 5.1.3 (page 156). The cyclic tooth, ramp and cyclic step strain (for definitions see stimuli catalogue in sec.2.1.4) excitation were used. The strain rates 0.025%/s and 0.1%/s of the tooth excitations were applied. The experiments with bundles were carried out using synchrotron X-ray with beam size 200 μm $\times$200 μm at a beam line $A2$, $HASYLAB$ (Hamburg, Germany) and the experiments with single fibres were performed using a micro-sized beam at a beam line $ID13$, $ESRF$ (Grenoble, France), see sec.4.5.1. The lattice strain of the β-sheet fibroin crystals in the direction of the tensile stress was determined from the shift of the radial position of the 002 reflection [93, 107, 158–160, 163].

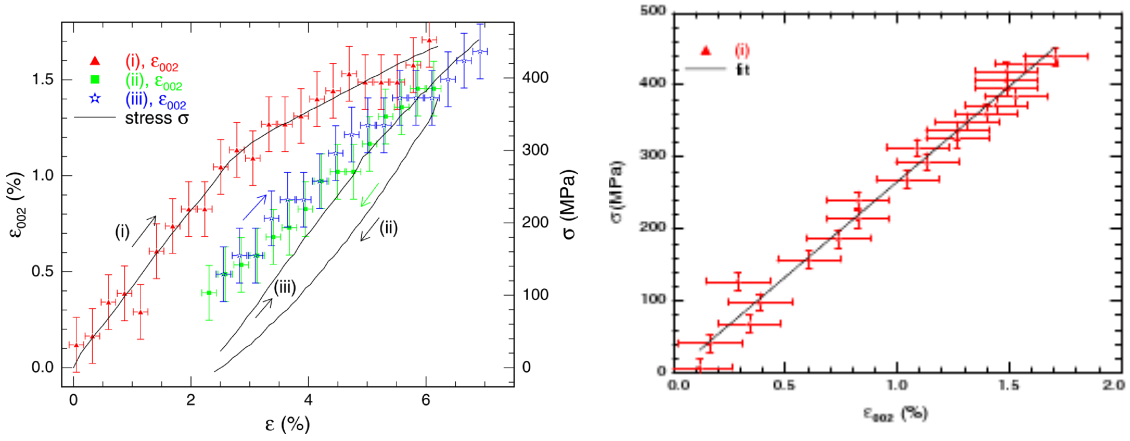

Figure 5.11.: **Strain-Stress curves compared with ϵ_{002} (fibre bundle)**
The left pane shows a typical strain stress curves (solid lines on the right scale) of bundle of a silkworm *Bombyx mori* fibres measured on beam line $A2$ with a cyclic tooth excitation (compare to fig. 5.15). The data of the unstretched fibres are labelled by the numbers (i),(ii) for increasing and decreasing strain, respectively. The data of the pre stretched fibre bundle for increasing strain are marked by the number (iii). The symbols give the crystallite uni-axial strain ϵ_{002} (left scale), as determined from the meridional reflection 002 of the fibre diffraction image.
The right pane shows the linear fit of the stress-strain curve of the fibroin crystallite in silkworm silk. The values of ϵ_{002} are determined from the meridional reflection 002 and the values of σ are averaged measured values over the exposure time interval. The crystallite elastic modulus $G_c = 26.5 \pm 0.8$ GPa is determined from the linear fit.

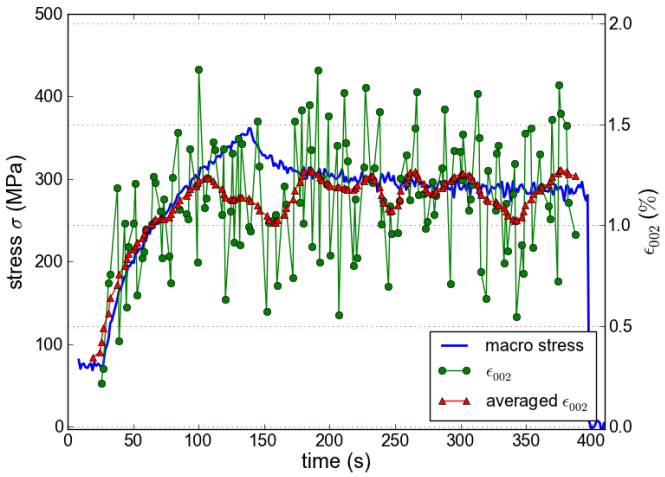

Figure 5.12.: **Stress-response curve compared with ϵ_{002} (single fibre)**
A typical stress-response curve (solid blue line, left scale) of an unstretched single silkworm fibre measured on beam line $ID13$ with a ramp strain excitation. The green symbols give the crystallite uni-axial strain ϵ_{002} (right scale), as determined from the meridional reflection 002 of the fibre diffraction image. The red symbols represent the smoothed version of the curve given by green symbols. The crystallite elastic modulus $G_c = 24.5 \pm 1.4$ GPa is determined from the linear fit of the proportionality coefficient.

The computer-driven tensile testing device $HUSTEN$ (see 4.3.2, page 136) was used in the experiments on silkworm silk bundles at beam line $A2$. The computer-driven tensile testing device $SPLC$ (see 4.3.1,132) were used in the experiments on silkworm silk bundles at beam line $ID13$.

As in the experiments on bundle of fibres (see example in fig. 5.11, left pane) so in the experiments on the single fibres (fig. 5.12) the crystallite strain ϵ_{002}, determined from the 002 reflection, follows (in the mean) the shape of the stress curve. The appropriate scaling factor between the two values can be determined by a linear fit of σ versus ϵ_{002} (see example in fig. 5.11, right pane). There is no deviation from the linear behaviour (in mean) even after the yield point at ϵ_{002} of about of 1%. The corresponding effective crystallite modulus at ambient humidity is $G_c = (26.5 \pm 0.8)$ GPa from the experiments on fibre bundles and $G_c = (24.5 \pm 1.4)$ GPa from the experiments on single fibres. This result is in agreements with previously published data ranging from 16 to 28 GPa [159, 160]. The comparison of the behaviour of the ϵ_{002} values taken from the experiments on fibre bundles and on a single fibres shows that their scatter around the mean curve has larger amplitude for the single fibres than for the bundle. This can be addressed to the low statistic due to the small amount of material in the beam for the experiments of single fibres. In the experiments

with bundles of fibres such effects are smeared out. The elongations ϵ_{002} of the crystallites in the sample are the measure of the internal stress in the surrounding matrix in which they are embedded.

The presence of such variations in the crystallite elongation leads us to assume a wide distribution of the internal stress in the fibre. The mean value of this distribution is the applied macroscopic stress measured by our "sensor".

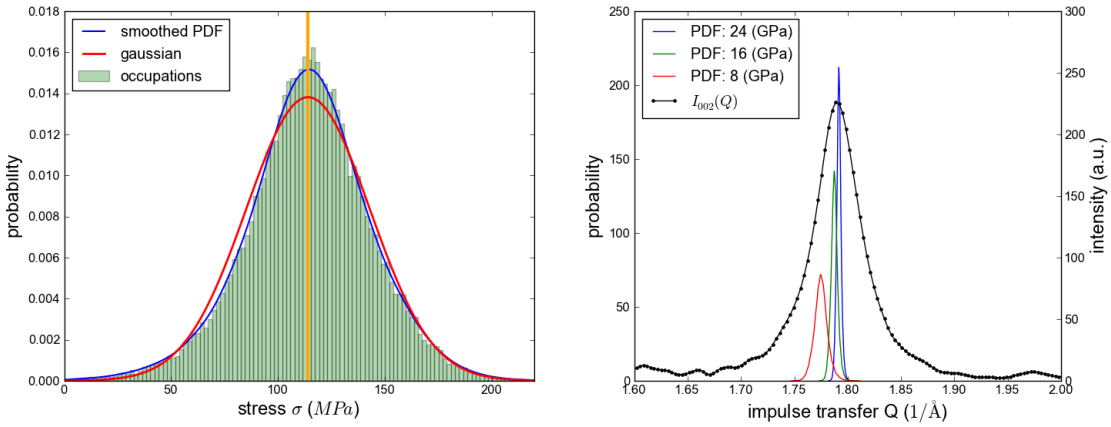

Figure 5.13.: **Relation of the stress deviation to the peak position**
The variation of the macroscopic stress through the measurements at constant strain in a very noisy environment is shown (left pane). The plot shows the probability to find a stress applied to the sample during the measurement time. This is proportional to the length of time interval the system spends under a given stress. The right pane shows the peaks broadening effect of such distribution for three values of the elastic modulus. The comparison of the width of the broadening due to such effects with the width of the measured meridional peak (002) shows that such effects can be neglected.

Another source of the broadening of the distribution in the crystallite elongation is the background vibrations and the variation in the stress due to the stretching through the recording a diffraction image will cause a distribution of the applied stress. Generally, such a distribution leads to a broadening of the masured peaks positions. But, in our case, the width of such distribution is sufficiently small to be ignored. Figure 5.13 shows an example of the macroscopic stress distribution measured in a very noisy environment (left plot) and the effect of the presence of such distribution on the peak position for three different elastic modulii. The largest standard deviation for the stress distribution in our measurements was under the level of about 25 GPa. The variation in the crystallite elongation cause

by such variation is of the magnitude about 0.1% or smaller, which is much smaller then measured variation in ϵ_{002}.

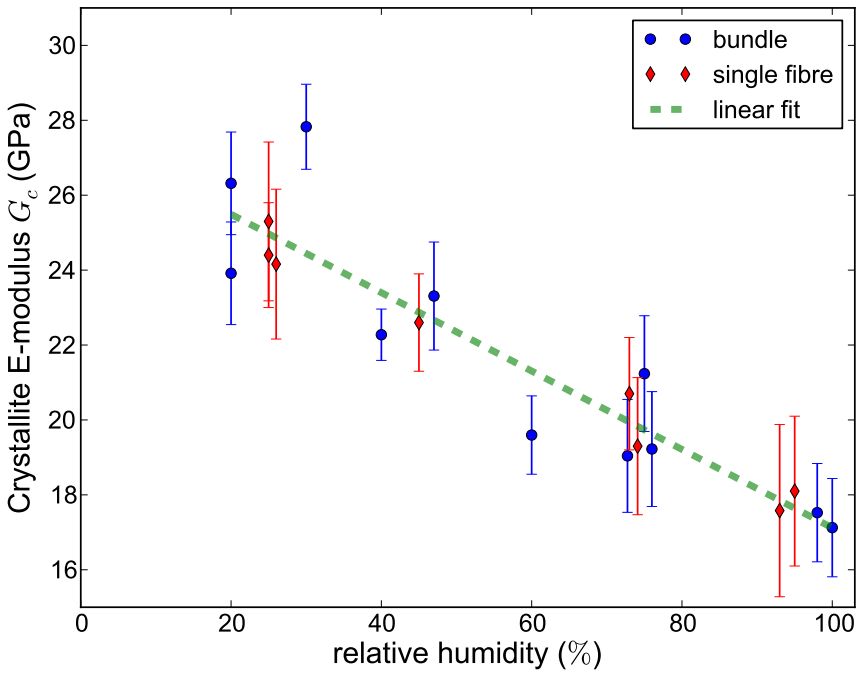

Figure 5.14.: **Silkworm silk crystallites elastic modulus as function of RH** The measured elastic modulus of crystallites in silkworm silk fibres is plotted for several values of the relative humidity (RH)[a]. The blue circles represent the measurements at bundles of silk fibres and the red diamonds represent the measurements at single fibres. The green dashed line is the linear fit, predicting $G_c = 26.8\,\mathrm{GPa}$ in the dry environment (RH of 0%) and $G_c = 17.0\,\mathrm{GPa}$ in the wet environment (RH of 100%). The slope is $10.42 \times 10^{-2}\,(\mathrm{GPa}/\%)$.

[a] An overview of measurements is given in the section 5.1.3 (page 156).

The novel results of our measurements is the dependence of the crystallite modulus from the relative humidity of the environment. The figure 5.14 shows the plot of the values of the crystallite elastic modulus versus relative humidity. The tendency of the crystallite modulus to decrease with increasing of the relative humidity is clearly visible.
But water molecules do not penetrate the crystallites [155] hence the source of this effect must be addressed to the interface effects (changes in the excess energies). Indeed, the crystallites are of the mesoscopic size. For crystallites of such small size the surface and interface effects are very important so the changes in the water contents of the direct environment of the crystallites can cause variation of such properties as elastic modulus

[16, 73, 74].
The mechanical aspects of these experiments and their application to the determination of viscoelastic moduli of the host matrix embedding the crystallites fibres are discussed in the next two sections.

5.2.3. Qualitative discussion of stretching experiments

Figure 5.15 shows a typical example of the behaviour of a single silk fibre stretched with a constant rate of strain. The excitation (strain) is the "cyclic tooth", described on the page 29. The very first cycle was applied to the samples in the virgin (vestal) state (i.e. fully relaxed sample without strain history). The response shows a very large hysteresis with a well-defined yield point and a less defined (spread) secondary yield point (for yield point see sec. 2.3). On successive cycles the sample is prestretched: it is about 5% longer, it shows a smaller hysteresis and the secondary yield point has nearly disappeared. In the case of ambient relative humidity (RH) the response of the prestretched silk shows a simpler response. The form of the responses at the back-path is very similar at each RH and for different states of stretching history. At a relative humidity higher than about 70-80% the response of the fibre seem to be rubber-like. For the ambient RH, on the other hand, the sample shows a reduced rubber-like response, usual for polycrystalline polymeric materials in the transition range, see discussion in the chapter 2.3.
In general we can assume that silk fibres possess at least two states:

unstretched/virgin A thermodynamically stable virgin state, i.e. the state without stretching history.

prestretched A metastable state (or sequence of very similar metastable states). It is the state of the silk fibre after, at least, one stretching cycle. In this state fibres are about 4-6% longer. After any successive stretching the fibre is (mechanically) in a state very similar to the prestretched state.

The appearing of a secondary yield point in stretching experiments with a constant rate of strain leads us to suggest the presence of at least two kinds of dissipative processes [15]. One of them has to be nearly finished after the transition, i.e. in the prestretched state (compare with "chemical model of flow" in chapter 2.3). The viscosity of these phases seems to be a function of stress. This is especially clearly visible from the example shown in fig. 5.16. The figure represents results of a stretching experiment at ambient environmental conditions (T=22°C, RH=24%) and with the following sample geometry: length 2 mm and area about 120 μm^2. In this experiment the 'tooth excitation' is realized by a sequence

of small strain steps with height = 1.42 μm. It is clearly visible that the relaxation time decreased with increasing stress and that the fibre starts to relax after the yield point. Such a behaviour is in agreement with the assumption of the models discussed in chapter 2.3.
The prestretched state has a very low rate of dissipation of the order of decades of hours. At the timescale of the experiment, this state can be considered to be nearly stable. But on longer timescales silk exhibits a tendency to restore its virgin state. In the example shown in the figure 5.16 the magenta line represents measurements done during the stretching with the same strain path as described above. However, the experiment was performed after the sample was brought into contact with water and then relaxed for more than 19 hours. The tendency to restore the virgin state is clearly visible. Note the appearance of the secondary yield point on the magenta curve. It is evident that the sample is much closer to the virgin state than to the prestretched one.

5.2.4. A combination of the linear viscoelastic model with measurements from *in situ* stretching X-ray scattering experiments

Here we present our attempts to extract mechanical properties of silk using a very simple linear viscoelastic model for the analysis of the *in situ* X-ray diffraction experiments. The results discussed below was partially reported in [93]. The description given here must be considered as relatively simplistic, such a simple model cannot give a detailed description of media as complex as silk fibres. The stretching equipment (SPLC) is described in sec. 4.3.1. The figure 5.16 shows an example of such a measurements where force and strain were sampled with the rate of 1000 Hz. The tooth strain excitation was released by a sequential set of steps of the height of 1.42 μm, the mean rate of strain of the tooth is 1%/s. The stress-response function was measured for increasing and decreasing strain on a previously unstretched fibre (blue curve) and then again in a second cycle for the same, thus, prestretched sample (green curve). See sec. 5.2.3 for the discussion about the virgin-prestretched relation.
The numeric values we use in the following discussion are related to the measurements at ambient environmental conditions.

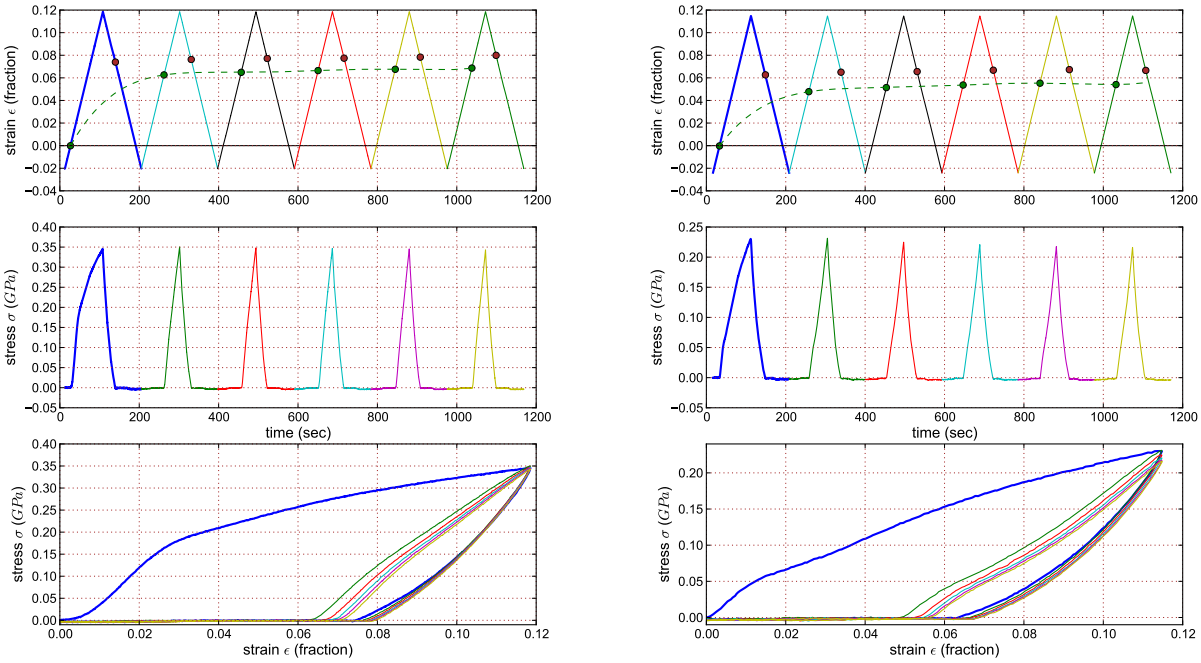

Figure 5.15.: **Stretching experiment with a 'cyclic tooth' stimulus**
The figure shows two stretching experiments with the strain path in the form of a 'cyclic tooth' (see definition on page 29). The left column shows data measured at a relative humidity of 33% and the right column measurements at a relative humidity of 92%. Other parameters where the same for both experiments: the temperature T=26°, the rate of strain $\dot{\epsilon}_0 = 1.4410^{-3}$ (i.e. 1.73 μ m/sec) and the sample geometry: the length about 1.2 mm and cross section 154 μm^2.
The upper plots show the strain path as a function of time, the plots in the middle show the stress-response of the sample and the bottom show the stress-strain behaviour.
On the upper plots the green points show strain values at which the responding stress starts to increase (strain offsets). Brown points show positions where the responding stress has disappeared (on the back-path). The dashed green line is an eye-guide.

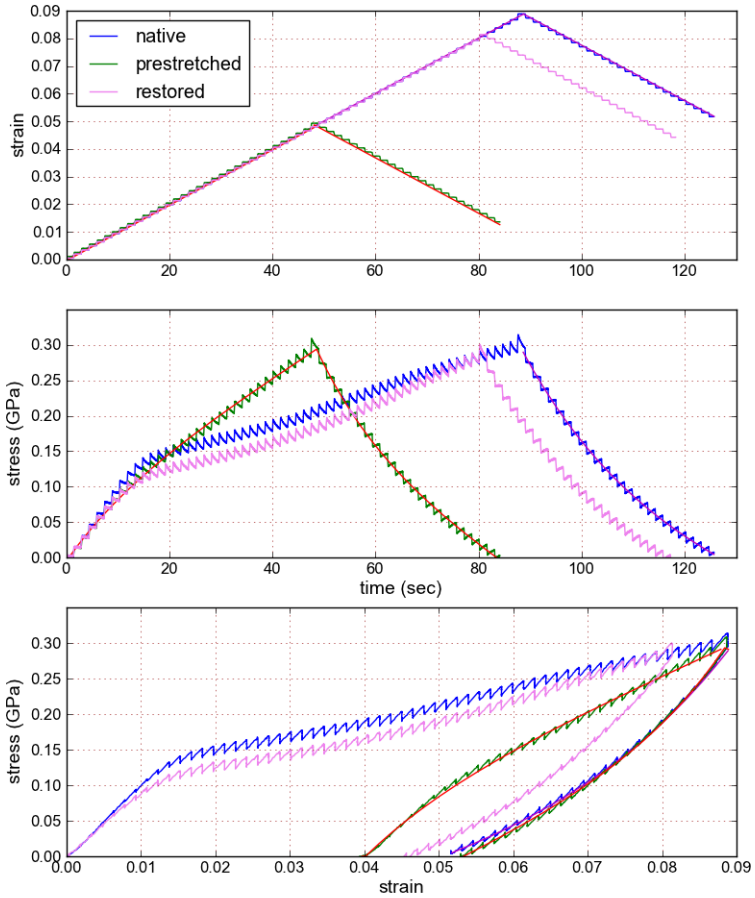

Figure 5.16.: **Experiment with a 'cyclic tooth' realized by successive steps** The figure shows a result of the stretching experiment with a 'cyclic tooth' realized by applying a set of successive steps of strain at ambient environmental conditions. The mean rate of strain is about $\dot{\epsilon}_0 = 1\%/\mathrm{s}$, the height of each step was about 1.42 μm, i.e. 0.07%. The upper plots show the strain path as a function of time, the plots in the middle show the stress-response of the sample and the bottom show the stress-strain behaviour. The blue curve shows data measured at the first 'tooth' excitation, the green one at the second 'tooth'. The magenta coloured line shows the data measured at the same 'tooth' but after the sample was saturated with water and then dried during about 19 hours. On the top plot and plot in the middle, all curves were adjusted (for convenience) to the response starting point offset. On the bottom plot the adjustment to the upper part of the response on the back-path was performed for the blue and green curves and the adjustment to the initial point was done for the blue and magenta curves. The smooth lines (red, magenta) are fits of the 3-component standard solid model.

Viscoelastic model for silk behaviour at moderate relative humidities

At a relative humidity lower than 70% the prestretched sample surprisingly shows a behaviour which allows a very simple phenomenological description in the context of the linear viscoelastic theory. The model is discussed in chapter 4. Its schematic dash-pot

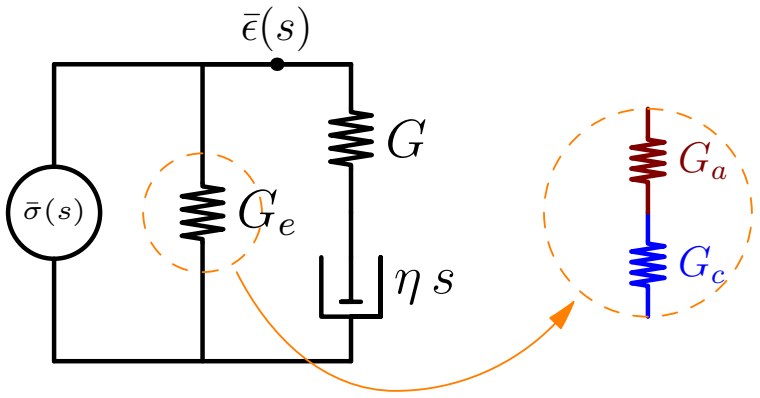

Figure 5.17.: **Dashpot-spring diagram of the three-parameter Maxwell model** Springs G_e, G represent the purely elastic and relaxing moduli, respectively, and η stands for viscosity. Strain is symbolized by ϵ and σ stands for the measured stress. G_e may be split up in elastic contributions G_c and G_a from crystalline and amorphous silk regions, respectively.

diagram is shown in figure 5.17. The model parameters G_e, G, τ are (theoretically) independent of the shape of the strain excitations. The equilibrium modulus G_e defines the purely elastic behaviour (at least at the time scale of the experiment) and is reponsible for the asymptotic behaviour at long times, the relaxing modulus G and viscosity η define the relaxation behaviour. Secondary quantities of the model are the response time $\tau = \eta/G$ and the glassy stretch compliance (modulus) $G_g = G_e + G$. The latter defines the asymptotic behaviour at small times. This value defines the initial modulus of the sample.

The model response to mechanical perturbations

The response to the excitation in the form of a Heaviside step $\epsilon_0 H(t)$ is

$$G(t) \equiv \sigma(t)/\epsilon_0 = G_e + Ge^{-\frac{t}{\tau}} \tag{5.8}$$

The response to the step excitation of our stretching engine (SLPC), which is analytically

modeled by equation (5.3), is given by:

$$\sigma(t) = \epsilon_0 \left(G_e + Ge^{-\frac{t}{\tau}} - \sum_{i=1}^{3} C_i \left(G_e\, e^{-\frac{t}{\tau_i}} + G\, \frac{\tau\, e^{-\frac{t}{\tau_i}} - \tau_i\, e^{-\frac{t}{\tau}}}{\tau - \tau_i} \right) \right) \tag{5.9}$$

where: coefficients $\{C_i,\tau_i\}$ are defined in (5.3).
We define the **generalised viscosity** $\eta(t)$ as the response to the unit slope excitation $\epsilon = \dot{\epsilon_0} t$, with the constant rate of strain $\dot{\epsilon_0} = 1$. Then the generalized viscosity of the model above is described by

$$\eta(t) \equiv \sigma(t)/\dot{\epsilon_0} = G_e t + G\tau \left(1 - e^{-\frac{t}{\tau}}\right) \tag{5.10}$$

In terms of this generalized viscosity function $\eta(t)$ the response described by the model to a non-cyclic tooth excitation takes the following form:

$$\sigma(t) = \dot{\epsilon_0} \begin{cases} \eta(t) & \text{if } t \leqslant t_{turn} \\ \eta(t) - 2\eta(t - t_{turn}) & \text{if } t \in (t_{turn}, 2t_{turn}) \\ \eta(t) - 2\eta(t - t_{turn}) + \eta(t - 2t_{turn}) & \text{if } t \geqslant 2t_{turn} \end{cases} \tag{5.11}$$

Equations (5.8) and (5.11) were fitted to the measured data, with fitting parameters $\{G_e, G; \tau\}$.
The values $G_e, G; \tau$ have to be interpreted as average macroscopic material properties. As the fibroin crystals recover their initial d-spacing immediately after rupture of the fibre, it was observed in the corresponding experiments (where fibres were stretched further), we know that the crystalline phase behaves purely elastic on the time scale of our measurements (see sec 5.1.2). One may thus interpret G_e as the (elastic) property of the crystalline-amorphous composite and $\{G,\tau\}$ as parameters of the relaxation processes occurring only in the amorphous phase and possibly in the boundary region between the crystalline and the amorphous phases.

Probing the lattice deformation of the fibroin crystals under tensile load

In a macroscopic model as that presented here, neither the crystalline nor the amorphous elastic modulus are known a priori or from stretching measurements. The measurements with *in situ* x-ray diffraction provide access to information about crystalline phase separately, as it probes the lattice deformation of the fibroin crystals under tensile load. The protocol of the tensile testing experiment on single fibres and bundles of fibres is described in the sec. 5.2.2 It is very similar to the protocol of single fibres experiment described in this section.

The crystal strain ϵ_{002}, determined from the 002 reflection [159], follows the shape of the stress-strain curve almost exactly. The appropriate proportionality factor between the stress and the crystalline strain ϵ_{002} was determined in a linear fit. At the ambient environmental conditions the corresponding elastic crystal modulus is $G_c = 26.5 \pm 0.8$ GPa (bundle experiments) and $G_c = 24.5 \pm 1.4$ GPa (single fibre experiments) [1]. This is in a good agreement with previously published data [113,159,160]. The linear relation between crystalline strain ϵ_{200} and stress σ provides strong evidence that the stress is uniformly distributed over the fibre cross section. This means, that in the fibre as a whole, the β-sheet crystals, and the amorphous regions carry the same load. This is in agreement with the morphology of silk fibres on the molecular level (see chapter 1): the same chain participates piecewise in the crystalline and the amorphous phases. Hence, the load is distributed over a parallel connected units, with each of these units consists of serially stacked crystalline and amorphous pieces. The constant stress scenario has previously been suggested based on Raman spectroscopic results [161]. It corresponds to a serial arrangement of crystalline and amorphous regions in the composite, known as the Reuss model in polymer physics [150]. The situation is schematically depicted in Fig. 5.17 where the elastic modulus G_e is split into amorphous (G_a) and crystalline (G_c) elastances. It should be noted that those are in parallel to the elements G and η standing for the relaxation processes of the amorphous regions.

For a serial configuration of amorphous and crystalline elastances, the reciprocal value of the equilibrium modulus G_e can be written as $1/G_e = 1/G_a + 1/G_c$. Here the famous combination rule "retardances add in series" applies [168]. G_e and G_c are already known from our experiments, so that at ambient humidity $G_a = 6.3\ (GPa)$ is calculated as the elastic modulus of the amorphous matrix, the value is about 4 times smaller than G_c . Consequently, the amorphous matrix should account for most of the macroscopic fibre strain, which indeed has to be the case as can be seen in combined plots of crystallites strain ϵ_{200} and stress σ as functions of strain ϵ (e.g. see Figures 5.11 and 5.12).

The value of G_a is in striking agreement with the relaxing modulus $G = 6.6\ GPa$ from the viscoelastic model above, thus corroborating our microscopic interpretation of that model. Both G_a and G are mechanical parameters of the same amorphous silk material, describing its purely elastic and its viscoelastic response, respectively. In that picture, the crystals follow Hooke's law as perfect springs. They might thus be used as `built-in` "`sensors`" for stress in the composite material. The curves of $\epsilon_{200}(\epsilon)$ reproduce even generally curved behaviour of the $\sigma(\epsilon)$. For the prestretched states the behaviour of the

[1] see tables 5.2 and 5.1 in section 5.1.3 for a list of our measurements.

crystalline strain ϵ_{200} shows an offset with respect to the curves measured starting from the virgin state. This offset is too large (about 4% for ambient humidity) to be explained by any unexpected changes of the x-ray scattering geometry (e.g., changed sample-to-detector distance). This offset can be addressed to a non-relaxed internal stress in the amorphous regions of prestretched silk fibres.

5.2.5. Relaxation tensile tests and fractional viscoelasticity of silk

At moderate humidity and for a short measured time the data from the relaxation tensile tests on silk fibres in the prestretched state can be well described with the viscoelastic model described above. The equation (5.8) is fitted to the measured data with the same parameter set $\{G_e, G; \tau\}$ as for the stretching experiments with a tooth-like excitation. But to describe measurements over longer time intervals (about hours) one needs extend the model with additional Maxwell elements as shown in figure 5.18. The fit parameters are G_e and a set of G_i, τ_i $(i = 1 \dots N)$ and N is the number of Maxwell elements in the model.

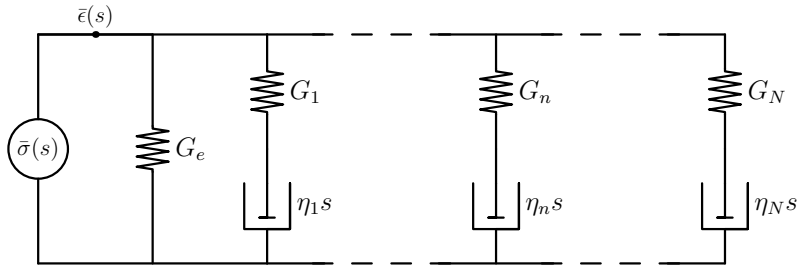

Figure 5.18.: **Generalized Maxwell model of a viscoelastic body**

Because of the large number of the model elements (parameters) it is nearly impossible to guess the suitable initial parameters. Hence we used the popular X-procedure [168] in our fits. This procedure consists of the successive subtraction of the linear fits to the longest time tails of measured data plotted in the log plot. In such a way one successively determines the values of the Maxwell elements starting with the element with longest relaxation time, i.e. the element (G_N, η_N) in the figure. Such fits are not unique and show no systematics in the distribution of the G_i, τ_i values. The variation of the results from sample to sample was to large for a systematic description of the relaxation phenomena, for more details see [75]. The drawbacks of this approach, when applied to a complex materials, is well known [168] and has fundamental nature discussed in the section 2.2.

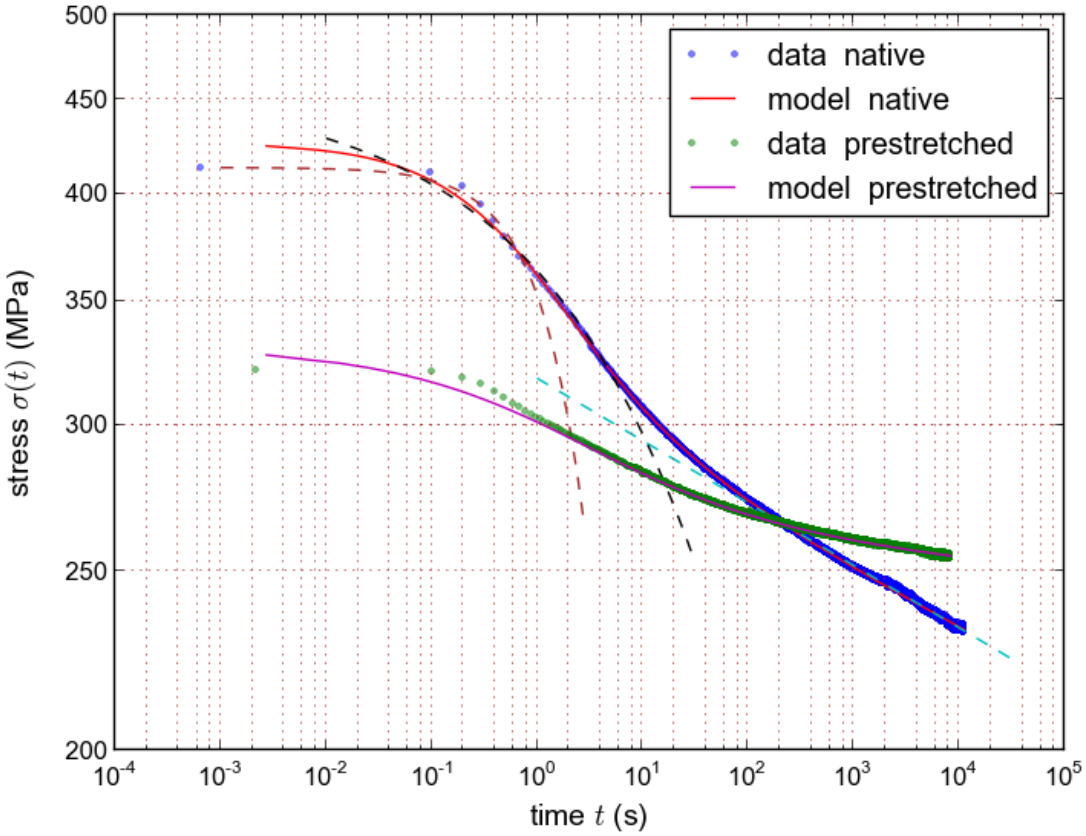

Figure 5.19.: **Relaxation of silk fibre in an ambient enviroment**
The figure shows the log-log plot of the relaxation measurements of silk fibres at environment condition with the temperature 23° C and the relative humidity 27%. The blue/green points represent the measured data and red/magenta lines show the fit of the `Fractional Standard Solid Model` for native and prestretched silk fibres. The light deviation of the model from the measured data in the time range [0,0.5] seconds is mostly caused by the deviation of the excitation strain curve from the idealized Heaviside step-form. The cyan dashed line shows the `inverse power asymptotic` $\sigma(t) \sim 1/t^{\beta}$ and the brown dashed line shows the `exponential decay low`. The black dashed line shows the `stretched exponent approximation` $\sigma(t) \sim \exp\left(-(t/\tau)^{\beta}\right)$. As it was mentioned early (see page 51), the fractional relaxation function interpolates between the stretched exponent (at small t) and power function (at large t) [48].

On the other hand, the fact that long time tails of the relaxation curves behave close to the inverse power of time law leads us to assume the presence of long memory effects as described in the section 2.2. Indeed, the data from the relaxation tensile tests (at RH up to 80%) on the native and prestretched silk can be well described by the Fractional Standard Solid Model introduced in section 2.2 on the page 54, see equations: (2.94-2.95). Due to the small number of the model parameters this approach yields more systematic description of the measured data. The only difficulty of this approach is of the computational nature: there are no standard procedures to compute the special functions participating in the solution and there is no standard approach for numerical inversion of the Laplace transform. Our computation was based on the Block Pulse Function method introduced at the end of section 2.2 (page 55). The results of the analysis of the measured data are following. The fractional exponents q, μ are found to be in the range $[0.4 - 0.65]$ with the difference between them $q - \mu \in [0.0005 - 0.005]$. The characteristic relaxation time τ is found to be in the interval $[1 - 3]$ seconds. The values q and μ are close to the exponent value 1/2 of the fractional approximation to the Rouse model in the limit of the infinite dashpots, see section 2.2.
Figer 5.19 shows an example of the fit of the fractional standard solid model to the data from relaxation tensile experiments with the native silk (upper pane) and the prestretched silk (lower pane). The measurements was done on the same silk fibre. As the strain excitation the idealized Heaviside step function of time was assumed. The fibre shows the characteristic relaxation time and fractional exponents $\tau = 1.11s, q = 0.6068, \mu = 0.576$ in the native state and $\tau = 2.42$ s, $q = 0.434$, $\mu = 0.428$ in the prestretched state. Additionally, to demonstrate the non-Debye character of the relaxation behaviour of silk, the exponential (Debye) relaxation (brown dashed line) and the inverse power low (cyan dashed line) are shown on the figure. Generally, the fractional model gives a good description of the silk relaxation on the long time scales of the order up to 10^6 s or larger.

These results allow very interesting geometrical interpretation based on the correspondence between the statical representation of the silk morphology (e.g. like the Termonia model shown on the figure 5.20) and the dynamical arrangement of the relaxing elements (figure 5.21) due to the fractal description of the viscoelastic body given by Heymans and Bauens in [71]. Firstly we note that with increasing the time scale one needs to take into account the correlation effects on the longer space scale. This means that we need to consider the correlated behaviour of many crystallites and the question is raised how they are (dynamically) interconnected. Let us consider a geometry similar to the Termonia model [166] which describes only the elastic (statical) behaviour of silk. The schematic representation

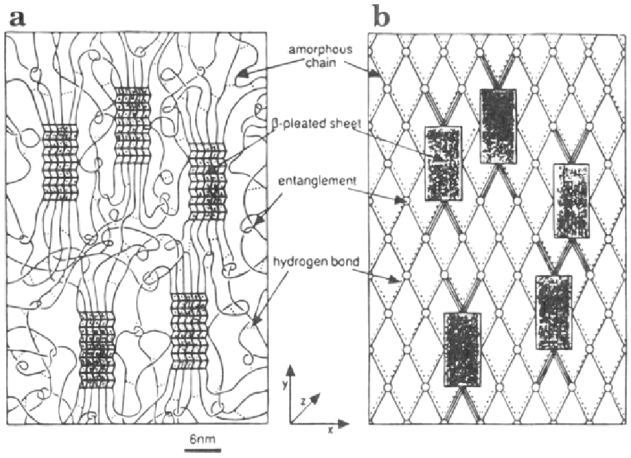

Figure 5.20.: **Termonia model of a spider silk**

Left: Model of the dry dragline.

Right: More schematic representation in which the details of the amorphous chains have been omitted and only end-to-endvectors are shown. Individual hydrogen bonds have been replaced by "overall" bonds (dotted lines) connecting every entanglement to its neighbors. The three- line vectors indicate the high-modulus layer in the amorphous phase. (The figure is reproduced from [166]).

of this model is shown in figure 5.20.

To model the time-dependent viscoelastic behaviour of a such system we can introduce two elemental elements: elastic modulus E and viscosity η and arrange them into a self-similar (fractal) dynamical representation as it was done by Heymans and Bauwens in [71]. Later one can extend this by introducing two elastic moduli: one for the matrix and one for the crystallite parts as in our viscoelstic model described above. The most elementary form of such fractal model is shown on the left pane of figure 5.21. This arrangement describes a self-similar composite modulus X which can be found from the equation on the Laplace/Fourier space:

$$X = \left(\frac{1}{E} + \frac{1}{X}\right)^{-1} + \left(\frac{1}{i\omega\eta} + \frac{1}{X}\right)^{-1} \tag{5.12}$$

where ω is either Laplace variable or Fourier frequency. The result is:

$$X = E\sqrt{i\omega\tau} \tag{5.13}$$

where $\tau = \eta/E$ is the characteristic time of the basic element and is the shortest relaxation time of the model. In the time domain this equation yields a fractional derivative of the

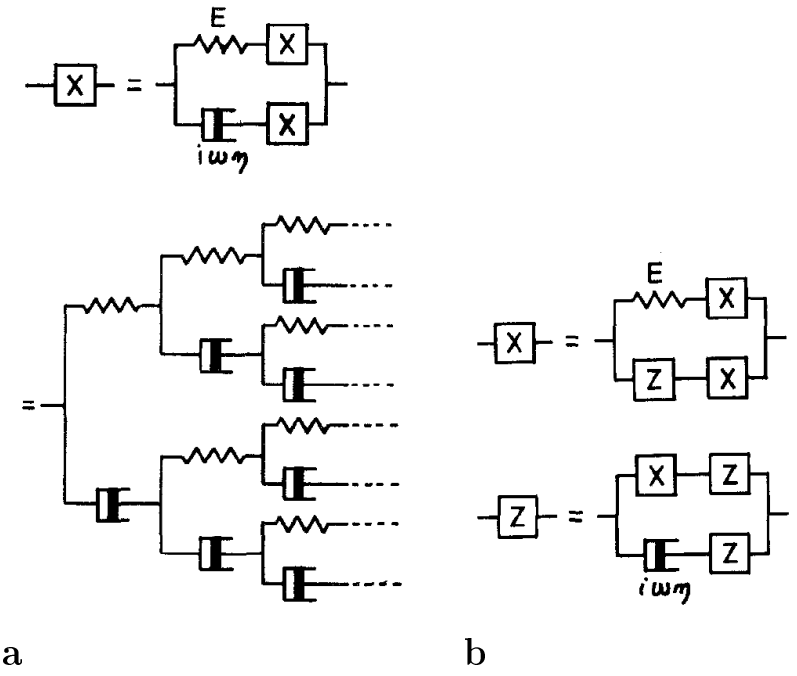

Figure 5.21.: **Self-similar (fractal) model for viscoelastic behaviour**
Left: the most simple fractal model in its compact and expanded forms.
Right: the decomposition of the elements to extend the model shown on the left pane. *eta* is elemental viscosity, ω is frequency variable in the Fourier domain and E denotes the elemental elastic modulus. (The figure is reproduced from [71])

exponent equals to 1/2. In [71] it was shown that the model can be generalised by successive use of the decomposition shown in figure 5.21 on the right pane. Such generalization can yield any desired fractional exponent in from the interval [0,1]. This allow an additional interpretation of our results based on the self-similarity of relaxation processes.

5.2.6. Analysis of the non-linear behaviour

Motivation

Our linear viscoelastic model used in section 5.2.4 (see figure 5.17) is not sufficient to describe the stress-strain relationship of unstretched silk as well as silk at higher humidity (unstretched/prestretched). Particularly: (i) the stretching curves of the native silk show two yield points (see blue lines in figures 5.15 and 5.16) which cannot be described with the linear viscoelastic theory; (ii) the behaviour of silk at high humidity is non-linear both in the prestretched and in the native state and, as such, cannot be simulated by a linear viscoelastic model. From the details of the relaxation processes on the scale of individual steps in the first stretching cycle (see Fig. 5.16) we deduce a rather sharp transition from a purely elastic behaviour up to the yield point to a fast relaxation process (on the plateau) with a typical relaxation time of about 1.0-2.0 s. In [156,166] the plateau has been attributed to hydrogen bond breaking in the amorphous matrix and in [142] to a transition from a glassy to a rubber-like state (sec. 2.3). The resulting flow-like extension of the amorphous protein chains, which causes the yield point, has an activation barrier, which can may be related with a transition to the faster process. What we observe here is the latter, a behaviour similar to that of a highly viscous polymer melt. Such a consideration is in agreement with the assumption of Robertson [151]. He suggests, that under shear stress the structure of the glass phase transits to a melt-like structure. On this condition the yield point appears as a transition to the flow state. This model was further elaborated and proven experimentally for some glassy polymers by Nanzai [115]. The analysis of these phenomena was performed on the basis of Eyring's reaction rate theory, called Transition State Theory (TST) (see 2.3). Presumably, the earliest model of this kind, suggested for polymeric fibre materials is one by Burte and Halsey [14,15]. They show that the existence of such a pre-activated phase will cause the appearance of secondary yield points. In an earlier study of the creep behaviour of silk fibres in terms of thermally activated flow (see description in sec. 2.3, page 70ff), Eyring [63] reported a value of about 100 kJ/mole (25 kcal/mole) for the activation energy and 11 Å for the length of the flow unit. The latter is about three times the size of a single amino-oxide unit. In this context, the amorphous part of silk might well be regarded as a rubber-like exhibiting entropy elasticity [54, 155]. Our findings provide direct evidence for the proposed additional molecular mechanism leading to the pronounced plateau of stress-strain curves of native silk. The association of a mechanism with activated transitions will clarify the recovering transition from the prestretched state to the virgin state, demonstrated by the magenta curve in fig. 5.16. The difference in the response of silk to stretching at ambient and higher RH can be shown

with the help of figure 5.15:

- at higher RH, one needs a smaller force to maintain the same strain as at ambient humidity.
- the appearance of the plateau in the strain-stress curves of perstretched silk shows that the behaviour is rubber-like.
- at higher RH one observes a strain hardening phenomenon, which is not present in the response of the prestretched silk fibres at ambient RH.

The previous considerations for the fibre in a virgin stretching state at ambient conditions are applicable to silk at higher humidity in both stretching states. It seems that the presence of water molecules causes a decrease of activation barriers, promoting the transition processes. Hence the sample shows a reduced resistance to tensile load. Additionally, the increase of the backwards rate can cause partial restoration of the virgin state inside the prestretched state.
Generally, the behaviour of silk fibres is non-linear both in the prestretched and in the virgin states, and, as such, cannot be simulated by a linear viscoelastic model. Of course, there are two exceptions: (i) the behaviour of the prestretched silk at intermediate humidity can be described by a linear viscoelastic model [93], this case is discussed in section 5.2.4; (ii) the long time relaxation behaviour at any RH, described with a fractional linear viscoelastic model in section 5.2.5. In this two exceptional cases the linear description can be considered as a linearisation of a more general non-linear model, needed for uniform description of the behaviour of silk at any humidity in the virgin as well as in the prestretched states. The rest of this section is devoted to an application of a such non-linear model to experimental data.

Experimental evidence for the presence of activation processes

In addition to the above-mentioned facts and observations there are, at least, two experimental evidences supporting the idea that elongation processes in silk are governed by activating processes and can be simulated by the TST theory. The first one is the observation that the yield stress in stretching experiments with a constant rate of strain has a logarithmic dependence from the rate of strain [77] (see more about the yield point in chapter 2 on pp. 77 ff.) An example of such a behaviour of silk fibres is shown in figure 5.22. The other one is the dependence of the glassy elastic modulus from the applied stress. This behaviour can be determined from the experimental stress-strain curve where the shape of the strain excitation was implemented by a step-wise curve. One such experiment is shown in the figure 5.23. The figure shows the response of a silk fibre to a

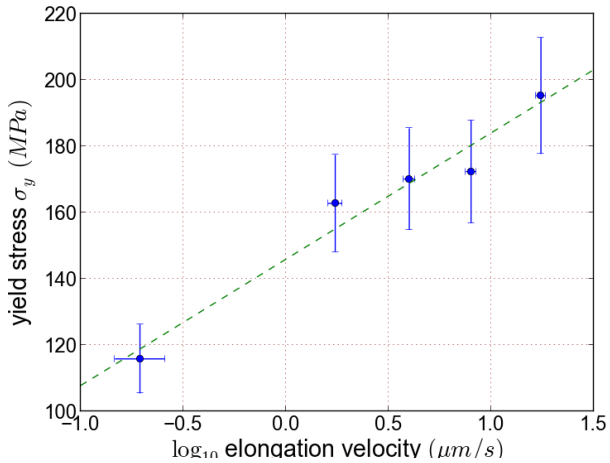

Figure 5.22.: **Stress of yield point for different rates of strain**
Values of the stress at the first yield point for several rates of strain are displayed (T=26° C, RH=33-35%). The stretching experiments were performed at a constant rate of strain. The blue points show the measured values and the green dashed line is a linear fit. The stress at the yield point is a nearly linear function of the logarithm of the rate of strain. This observation is a clear hint towards the processes quantitatively described by the TST theory [77].

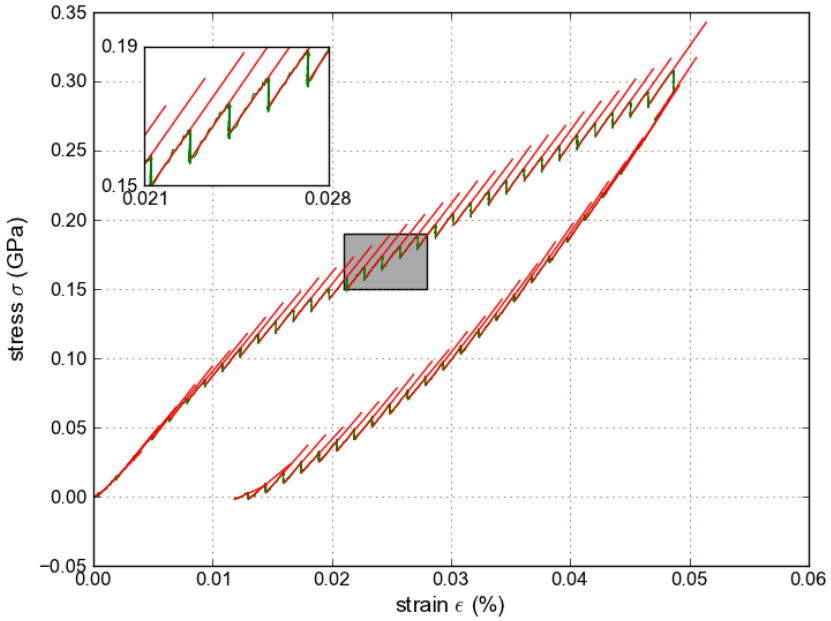

Figure 5.23.: **Determination of the glassy elastic modulus**
The figure shows the response of a prestretched silk fibre (RH = 35%, T=23° C) to a tooth strain excitation, realized as a sequence of small steps. The green curve shows the measured data and the red lines are linear fits. The insert shows details of the fits of the raising part of the steps. Compare with figure 5.24.

tooth strain excitation, realized as a sequence of small steps with a rising time about 50 ms. Due to the high rate of strain on the rising part of each step the response in stress behaves nearly linear. It can be fitted by a linear function $\sigma(\epsilon) = G_g\epsilon + \sigma_0$, separately for each step. Each fit parameters G_g produce an approximation of the modulus of the instantaneous response for the particular step. The sequence of the fitted values of G_g gives us an approximation of the behaviour of the instantaneous (glassy) modulus as a function of stress and/or strain. The green curve shows the measured data; the red lines are linear fits.

The results of this procedure are shown in figure 5.24. The upper pane of the figure shows the response of a silk fibre to a tooth strain excitation realized by a sequence of small steps (compare with fig. 5.16). The middle pane shows the instantaneous (glassy) modulus G_g as a function of time and the bottom pane shows G_g as function of stress. The results are shown for the measurements on a fibre in the three states: virgin (native), prestretched and partially restored (from the prestretched to the virgin state).

The virgin state of the fibre is drawn in blue, the pre-stretched fibre in green and the partially relaxed to the virgin state fibre in magenta colour. The magenta coloured region marks the stress range of the yield point. The sharp raising part of the $G_g(\sigma)$ on the bottom pane is due to the alignment of the micro-fibrils caused by the applied stress. The rest of the curve exhibits a variation of G_g with two hysteresis crossings at the yield point. Note that this part of the curve lies in the range from 10 to 14 GPa with a mean value of about 12 GPa. This coincides with the value of the initial glassy modulus given by our linear viscoelastic model. The dependence of the glassy modulus as well as a hysteresis behaviour leads us to assume non-linear viscoelastic laws of the Eyring type.

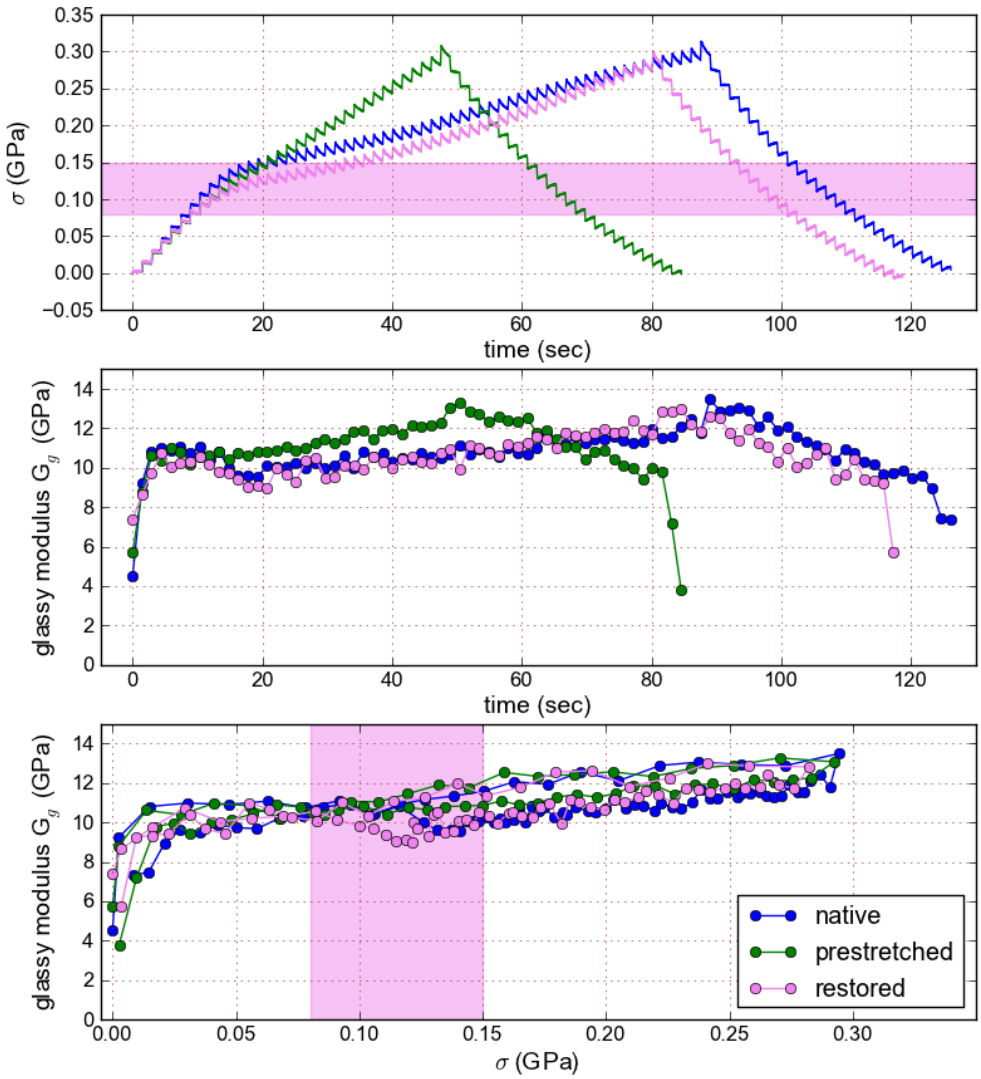

Figure 5.24.: **Glassy elastic modulus as a function of time and stress**
Upper pane: response of a silk fibre to a tooth strain excitation realized by a sequence of small steps (compare with fig. 5.16). Middle pane: instantaneous (glassy) modulus G_g as a function of time. Bottom pane: G_g as a function of stress. Regions in magenta mark the stress range around the yield point. The experiment was performed at RH = 35%, T=23° C.

Application to measured data

Below, we will show the results of the application of models based on the non-linear viscoelasticity which is governed by activation processes. The detailed description of these models is given in 2.3. For convenience, we will start with a short summary of the model adapted for the fit of the measured data.

Model and specifications

The non-linear models we use here are based on the Transition State Theory and can be considered as a generalization of the linear viscoelastic models (see chapter 2.3 and e.g. [33,146,147,167]). This approach adopts the idea that a deformation of the amorphous component of silk consists of thermally activated processes involving the motion of nano-sized molecular subsystems called molecular units. Hence, new dash-pot elements have to be introduced. They are governed by non-linear laws of thermally activated processes. Molecular movements underlying the deformation of a material can be classified either as slipping or as folding processes. The slipping processes can be well-described by the Eyring-Tobolsky models [146, 147].
Here we will describe the material behaviour based on the folding-type transformations. It is given in terms of the population dynamics of molecular units undergoing transitions between a few states, each characterised by a specific length and elasticity. The transition from one state to another is described in analogy with the kinetics of chemical reactions (see e.g. [23]), where reaction rates are given by TST. These units are assumed to be serially connected and, hence, the macroscopic elongation is defined by the above-mentioned population of states with different elongation of the molecular units. A natural representation of such models is similar to the Maxwell Unit of the linear viscoelastic theory. The pane (b) in the figure 5.25 presents a general scheme of such models, while the pane (a) shows more detailed representation of the two-state model. If there are only two elongation states accessible for the molecular units (but there may be more than one energy level per elongation), then the elongation of the dashpot element ϵ_1 is given by:

$$\epsilon_1 = \epsilon_\infty \frac{x_B(\sigma) - x_B^{eq}}{1 + \epsilon_\infty x_B^{eq}} = \epsilon_0 \left(x_B(\sigma) - x_B^{eq} \right) \tag{5.14}$$

where $\epsilon_\infty = (L_B - L_A)/L_A$ is the relative elongation of the molecular unit due to the transition from a state with the shorter length L_A to the state with a longer length L_B ($L_B > L_A$); x_B^{eq} is the equilibrium population (fraction) of the molecular units in the states

with larger length L_B. The proportionality coefficient ϵ_0 introduced above is:

$$\epsilon_0 = \frac{\epsilon_\infty}{1 + \epsilon_\infty x_B^{eq}}$$

The composed elastic moduli is calculated as follows:

$$G_e(x_B) = \left(\frac{1}{G_c} + \frac{1 - x_B}{G'_A} + \frac{x_B}{G'_B} \right)^{-1} = \left(\frac{1 - x_B}{G_A} + \frac{x_B}{G_B} \right)^{-1} \tag{5.15}$$

where G_c is the elastic modulus of the crystalline region of silk fibre, G'_A, G'_B are elastic moduli of the molecular units in their short and elongated states, respectively. For convenience, in the second expression in (5.15) we did incorporate the elastic modulus of the crystalline regions into the moduli G_A, G_B of the short and long states, respectively.
The external stress σ relates to the strain of the fibre ϵ and the strain of the dashtop ϵ_1 as:

$$\sigma = G_e(x_B) \left(\epsilon - \epsilon_1(x_B, \sigma) \right) \tag{5.16}$$

Equation (5.16) together with (5.14) and equations of population dynamics (see below) define the viscoelastic behaviour of the material under study.
For the two-state model, the population dynamics is defined by the master (Fokker-Planck) equation obeying to the law of the probability conservation:

$$\begin{cases} \dot{x}_B = -k_{BA} x_B + k_{AB} x_A \\ x_A + x_B = 1 \end{cases} \tag{5.17}$$

and for the 3-state model by the set of equations:

$$\begin{cases} \dot{x}_B = -\left(k_{BA} + k_{BC}\right) x_B + x_A k_{AB} + x_C k_{CB} \\ \dot{x}_C = -\left(k_{CA} + k_{CB}\right) x_C + x_A k_{AC} + x_B k_{BC} \\ x_A + x_B + x_C = 1 \end{cases} \tag{5.18}$$

The last expressions in (5.17, 5.18) are probability conservation laws. The symbol x_α denotes the population (fraction) of the state α and $k_{\alpha\beta}$ denotes the rate coefficient for transitions $\alpha \to \beta$. The latter are transitions between 2 states separated by barriers. they can be functions of an externally applied stress.
In the 3-state model only the rate coefficients k_{AC} and k_{CA} are independent of the external stress, because their lengths are equal (see fig. 5.26).
Usually, a (free energy) barrier separating two states can be given in two representations, sketched as blue and brown symbols in figure 5.26(a). The first representation defines a

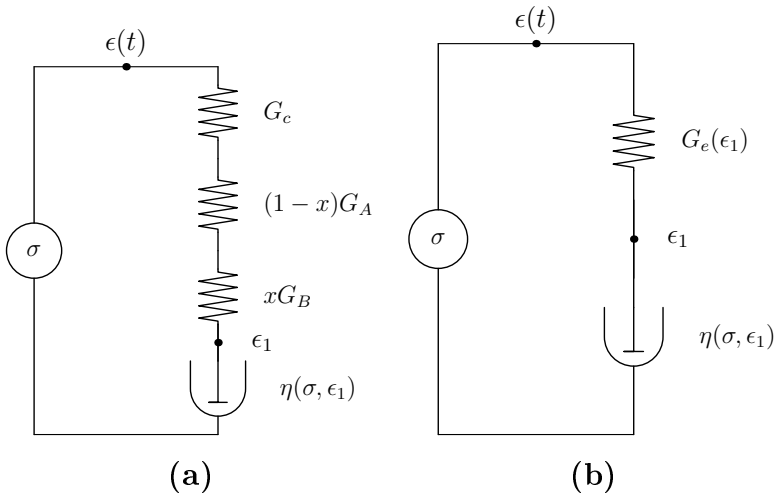

Figure 5.25.: **Viscoelastic schema for n-state model**
The figure shows a schematic representation of the viscoelastic system modelled with a molecular species possessing two elongation states A,B. (a) shows the detailed representation of the 2-state model and (b) the generalized representation with the composed elastic element G_e. G_A and G_B are elastic moduli of the species A and B, respectively. G_c denotes the elastic modulus of the crystalline phase. The element $\eta(\epsilon_1,\sigma)$ denotes the generalized viscosity governed by activation processes. Symbolically, it represents a relation between the stress σ and the rate of strain $\dot{\epsilon}_1$. This relation is implicitly defined by the master equation of the population dynamics.

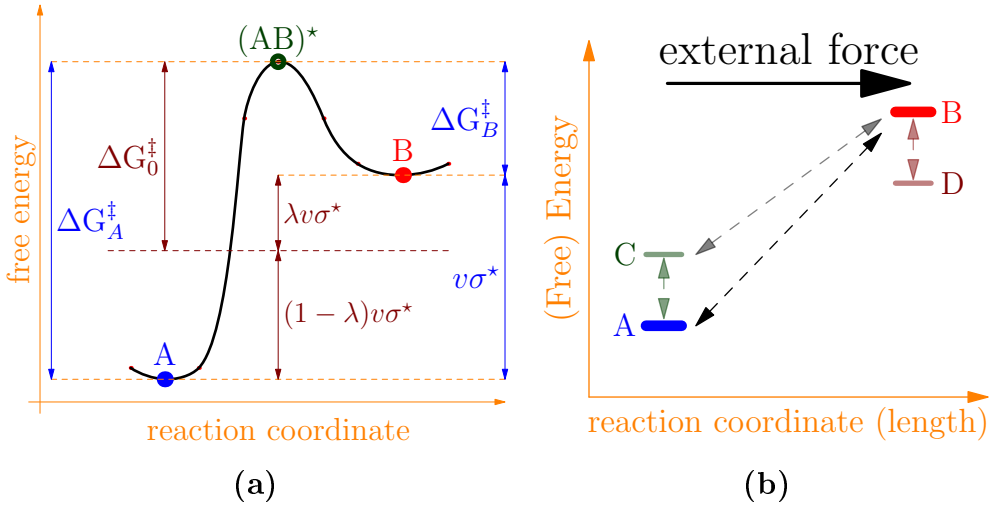

Figure 5.26.: **Energy landscapes**
(a) a sketch illustrating two states separated by an energy barrier. (b) shows a landscape for the three and four-states viscoelastic models. The states A and C are characterized by the same length L_A while B and D have the length L_B. The arrows indicate possible transitions in the system.

potential barrier through its heights $\Delta G_A^\ddagger$ and $\Delta G_B^\ddagger$, activation volume v and a symmetry parameter λ. In this notation the rate constants for the transition $A \leftrightarrow B$ take the form:

$$k_{AB} = \frac{k_B T}{h} e^{-\frac{\Delta G_A^\ddagger - (1-\lambda)v\sigma}{k_B T}}; \qquad k_{BA} = \frac{k_B T}{h} e^{-\frac{\Delta G_B^\ddagger + \lambda v\sigma}{k_B T}} = k_{AB} e^{v\frac{\sigma-\sigma^\star}{k_B T}} \tag{5.19}$$

where k_B, h, T denotes Boltzmann, Plank constants and temperature, respectively; σ is an external stress and $v\sigma^\star = \Delta G_A^\ddagger - \Delta G_B^\ddagger$ is the averaged work, needed for the $A \to B$ transition. The 'internal stress' $\sigma^\star$ equals to the amount of the external stress needed to make the energy levels of the states A and B equal. The symmetry parameter λ is variable in the interval $\lambda \in (0,1)$, close to 1.

The second representation is more intuitive and can be called 'internal stress' representation. In this representation a potential barrier is defined by its mean height $\Delta G_0^\ddagger$, internal stress σ, activation volume v and symmetry parameter λ. In the 'internal stress' notation the rate constants for the transition $A \leftrightarrow B$ take the form:

$$k_{AB} = \frac{k_B T}{h} e^{-\frac{G_0 + (1-\lambda)v(\sigma^\star - \sigma)}{k_B T}}; \qquad k_{BA} = \frac{k_B T}{h} e^{-\frac{G_0 - \lambda v(\sigma^\star - \sigma)}{k_B T}} = k_{AB} e^{v\frac{\sigma-\sigma^\star}{k_B T}} \tag{5.20}$$

The transformation between these two representation is given by:

$$\Delta G_0^\ddagger = \lambda \Delta G_A^\ddagger + (1-\lambda)\Delta G_B^\ddagger; \qquad v\sigma^\star = \lambda \Delta G_A^\ddagger - (1-\lambda)\Delta G_B^\ddagger \tag{5.21}$$

$$\Delta G_A^\ddagger = \Delta G_0^\ddagger + (1-\lambda)v\sigma^\star; \qquad \Delta G_B^\ddagger = \Delta G_0^\ddagger - \lambda v\sigma^\star \tag{5.22}$$

Application of the 2- and 3-state models

Generally, the 2-state model allows a sufficiently good description of the behaviour of the prestretched silk fibres at any humidity. But it is not sufficient for a quantitative simulation of the native fibres, at least at high humidity. Two examples are given in figure 5.27. The pane (a) shows data measured at a RH of about 28% and (b) at a RH of about 93%. The yellow lines show fits of the data from the stretching experiments with native silk and the red line with prestretched fibres. The fit parameters were: elastic moduli G_A and G_B of the molecular units in the state A and B, respectively; the average potential height $\Delta G_0^\ddagger$, the internal stress $\sigma^\star$, the activation volume v and the symmetry parameter λ. The values of the parameters for the example above are given in the following table:

RH (%)/sample state	G_A/G_B(GPa)	$\Delta G_0^\ddagger$(kJ/mole)	$\sigma^\star$(MPa)	v (Å^3)	λ	ϵ_∞
28/native	12.52/5.78	87.6	97	80.0	0.91	0.184
93/native	3.3/18.30	85.9	126	82.7	0.94	0.172
28/prestretched	11/6	84.7	139	80	0.91	0.049
93/prestretched	3.1/8.24	81.3	-113	48.0	0.88	0.221

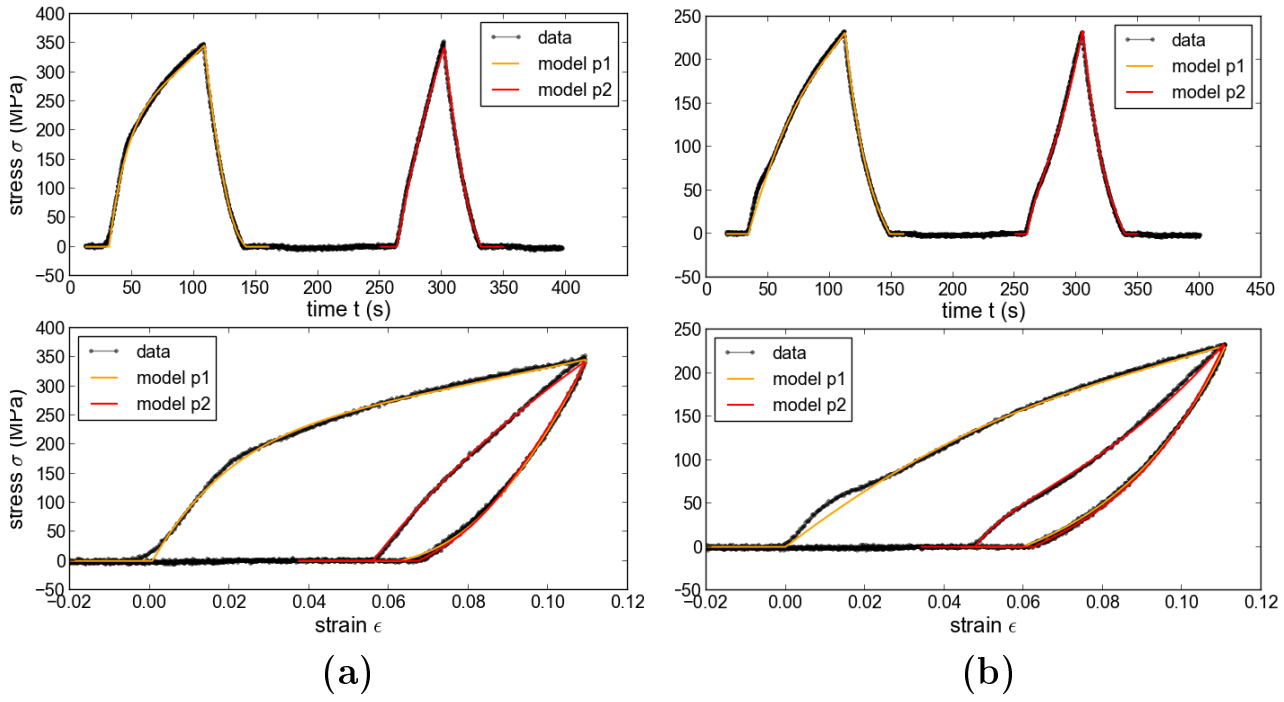

Figure 5.27.: **Fit with the 2-state model**

The figure shows fits of the 2-state model to the data from the stretching experiments with a cyclic tooth excitation in strain. The shown experiments were performed with native and prestretched silk at two humidities: (a) RH=28% and (b) RH=93%. The yellow line shows the results of the fit to the first tooth cycle and the red line shows the fit to the second cycle. It is clear that the model can describe the stretching of native silk (first cycle) rather qualitatively. On the other hand, prestretched silk (successive cycle) is described sufficiently well even on a quantitative level.

Additionally, for the prestretched fibres the initial (latent) strain was fitted, with the following results: 0.056 for the RH=28% and 0.048 for RH=93%.

The 3-state model provides and improved description of the behaviour of native silk. Especially, it can reproduce the first and the second yield regions of the stretching curve. An example of the fits of the model to the experimental data is shown in figure 5.28. The parameters of the model are: elastic moduli of the short states $G_A = G_C$ and long state G_B; the parameters of the barriers responsible for the transition $A \leftrightarrow B$ and $C \leftrightarrow B$; the energy difference $\Delta G_{AC} \equiv \Delta G^{\ddagger}_{AC} - \Delta G^{\ddagger}_{CA}$ for the barrier of the $A \leftrightarrow C$ transition and the relative elongation of the single molecular unit ϵ_∞. The parameter set for the AB and

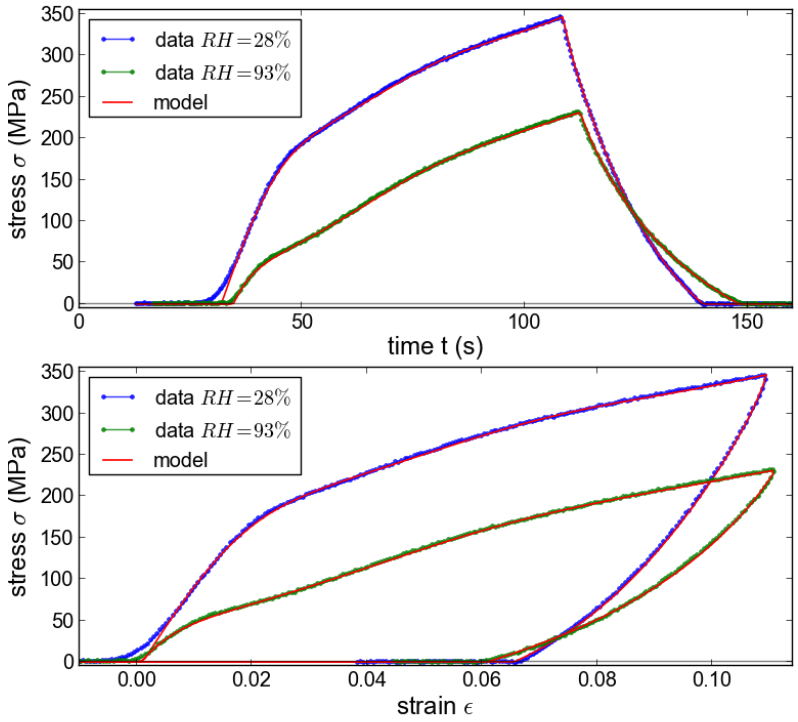

Figure 5.28.: **Fit the 3-state model**

The figure shows fits of the 3-state model to stretching experiment on the native silk. A cyclic tooth excitation in strain was used. The measured data sets are the same as on the figure 5.27.

CB barriers are given in the 'internal stress' representation, i.e. $\Delta G_0^{\ddagger}$ - mean height of the barrier, $\sigma^{\star}$ - the internal stress, v - activation volume and λ - symmetry parameter. Because the contribution from the$A \leftrightarrow C$ transition is negligible, on the time scale of the present experiments, the mean barrier height for the barrier AC was fixed at $\Delta G_0^{\ddagger}$=200 (kJ/mol). The value of the height difference ΔG_{AC} was defined by the energy conservation law, i.e. $\Delta\Delta G_{AC}^{\ddagger} = v\,(\sigma_{AB}^{\star} - \sigma_{CB}^{\star})$. Additionally, we have forced the activation volumes for the AB and BC barriers to be equal.

In the table below: the energy values $\Delta G_0^{\ddagger}$ and $\Delta\Delta G_{AC}^{\ddagger}$ are given in (kJ/mol) the internal stress $\sigma^{\star}$ in (MPa) and the activation volume v in Å^3.

RH	G_A/G_B	barrier AB				barrier CB				barrier AC	ϵ_∞
%	(GPa)	$\Delta G_0^{\ddagger}$	$\sigma^{\star}$	v	λ	$\Delta G_0^{\ddagger}$	$\sigma^{\star}$	v	λ	$\Delta\Delta G_{AC}^{\ddagger}$	
28%	11.7/9.6	89.8	121	93.6	0.24	86.3	48.8	93.6	0.2	4.12	0.116
93%	11.9/5.7	88.15	4.2	71.21	0.36	84.95	-90.3	71.21	0.05	4.05	0.243

Taking the crystallites' Yang modulus from the scattering experiments, i.e. about 25 (GPa) for the RH=28% and 18 (GPa) for the RH=93%, (see pp. 164- 168 and 173- 175) one can compute moduli of the molecular units from the amorphous regions using the equation (5.15). For the native silk at RH=28% the results are: about 8 (GPa) for the elastic modulus of our molecular units in the short states A,C and about 6-7 (GPa) for the long state B. And, for prestretched silk at RH=28% the results are: 7 and 5 (GPa) for the short and long states, respectively. The latter is in agreement with the results for the application of our linear viscoelastic model for the similar data set discussed on page 173ff. It is surprisingly that in the 3-state model the elastic modulus for the short states A and C is varied so little with the change of the relative humidity while the long state B exhibits a large variation (up to 55% relative to its initial value) when the RH is changed from RH=25% to about 95%. In this interval of RH the change in the middle heights of the barriers AB and BC is about 2-4% while the internal stress changes dramatically with increasing humidity. It seems that with increasing RH the energy level of the B state approaches the level of the A state and at RH=90% it is lower than the level of the C state. Similarly, the potential barrier separating the C and B states loses its symmetry with increasing of RH while the symmetry parameter of the barrier separating A and B states remains to be nearly unchanged. Generally, the results show that the molecular units change their size and configuration with variation of the water contents in the fibres. The activation volume is varying about 95 to 70 Å^3, while the molecular relative elongation ϵ_∞ is varying from 0.1 to 0.25 in the above-mentioned range of RH. If we assume that the area of our molecular units is of the order of the area of the peptide-plane (i.e. about of 8-10 Å^2) we get the values of about 10 Å and 8 Å for typical elongation of these units at the RH of 28% and 93%, respectively. Note, that the value 10 Å is very close to the length (11 Å) of the 'flow units' reported by Eyring [63][2]. The elongations from above implies that the length of the molecular units is equal to 86 Å at the RH=28% and to 33 Å at RH=93%. This clearly shows the general tendency: with increase of the relative humidity the molecular mobility increases (the height of barriers decreases) and the average size of the molecular units participating in the elongation movements decreases (humidity induced contraction effect).

[2] He reported the value 100 kJ/mole for the height of the barrier which is a bit larger (by about 10 %) then our values but has the same order.

Conclusion about the application of our viscoelastic models

For silk fibres we clearly succeeded in separating the mechanical properties of it's crystalline and it's amorphous phase. their interplay has been shown as well. A link between the macroscopic viscoelastic behaviour and the mechanisms at the molecular length scale has been established. The β-sheet crystals do not only act as nodes or dragging beds in a disordered molecular network [166], but they are elastically deformed themselves and thus contribute to the extensibility of silk.
The linear model, discussed above, is purely rheological and does not require any geometrical information (or assumptions) on the distribution of crystalline and amorphous phases, which an analysis in the framework of composite mechanics would do [135]. The model fully accounts for the semi-crystalline morphology of silk and can explain the mechanical properties of prestretched spider dragline silk, as we confirmed in a fit to measured data from [142]. It provides a first feeling for values of mechanical parameters of pure amorphous phase and allows further elaborations to include larger interval of relative humidity and temperature.
We did show that for long time scales silk fibres exhibit rather non-Debey relaxation which can be well described by a fractional viscoelastic theory 2.2. Such a behaviour points to a presence of long-memory effects. More precise, this means that the memory of excitations is not lost instantaneously (as in the case of the Debye relaxation) but rather propagates in time through the interactions between elemental relaxation events. In this description the response is governed by a derivatives of fractional order $[0.4 - 0.65]$. The non integer exponent of the derivatives participating in the constitutive equation of the silk response on the long time scales can be addressed to the dynamical self similarity of the composite relaxation process. On the other hand such a behaviour is not in contradiction with a picture where the relaxation is going through a successive sequence of thermally activated elemental processes (trapping) [38]. Using non-linear models based on the TST theory we showed that much of the viscoelastic behaviour of silk fibres stems from the molecular mechanisms, which are based on activation processes. The analysis of the data with this type of models not only allows to estimate the elastic moduli and relaxation times but also gives access to averaged qualities on the molecular level. Our results are in accord with the Eyring results from the analysis of the creep behaviour of silk, based on the same molecular mechanism. The increase of the molecular mobility within silk with increasing RH is clarified through the reducing the activation barriers. At least qualitatively, the non-linear models allow to describe, all our observation related to the mechanical response of silk at the intermediate time scales for both stretching states and in the whole RH range.

5.2.7. Molecular model of fibroin crystallites deformation in silk fibres based on standard peptide unit and geometrical constrains.

Motivation

In the diffraction experiments on bio-composite materials the scattered intensity and the profile of the diffraction peaks are not only defined by the structure, but also by the geometrical form of crystallites (or its distribution) and the orientation probability distribution of the crystallites in the sample [126]. Alone, taking into account the rotational effect geometrically (without introducing the crystallites shape and structure factors) leads to a qualitatively better description of the measured diffraction data (see [124]). The effect of the anisotropic orientation distribution has been recently studied on spider silk [169], by simulation methods (Monte Carlo) accompanied by diffraction experiments. The "comparison analysis" performed by the authors (the measured data were not directly fitted) allowed to extract the geometrical and statistical parameters of the samples. Especially, it was proven that inter-crystallite effects are negligible and, therefore, the measured data were analysed in terms of single-crystallite scattering.
Additionally, the effect of strain (or strain distribution) has to be taken into account by *in situ* diffraction experiments. The elongation of the fibre along its axis causes stress acting on the crystallites and leads to their deformation. The response of a crystallite to an applied stress can be twofold [113, 120]: (i) The extension can occur by (a) bond stretching and/or by (b) bond angles bending (affine deformation). In this case stronger binding forces lead to a response with a relatively large value of the elastic modulus (about 200-250 GPa). (ii) The extension is the result of internal rotations, e.g. a change in dihedral angles [3] with weaker potentials. The second type usually is related to a smaller elastic modulus (about 10-45 GPa) [120]. The elastic modulus of silk crystallites, reported in the literature (see e.g. [113, 120, 160]), is in the range of 13 to 28 (GPa). These considerations invite us to study the effects of non-affine deformations of the crystalline regions of the silk fibres.
The presence of an orientation distribution not only affects the shape of the diffraction peaks but also their position. This can be studied best with the strongest diffraction peak - the 002 reflection. A variation in the orientation distribution will cause a change in its mean position which can be misinterpreted as stretching. The effect of the orientation was studied by other methods in [120, 126].

[3] the definition of dihedral angles is given 5.2.7 on the page 206 and in ch.1, pages 9-10

This motivated us to incorporate the following effects into our fit model: (i) an elongation by the internal rotation, (ii) an anisotropic distribution in the crystallite orientations with a finite width and favoured orientation along the fibre axis.

Model setup

The following facts are known from the literature:

- The main part of the diffraction patterns is due to the nano-crystallites. In the literature a mean size of a crystallite of about 3nm × 5nm × 8nm is reported. With the size of the unit cell about $(a,b,c) = (9.4, 9.5, 6.98)$ (Å) [106, 163] we have approximately (3,5,10) numbers of unit cells (lattice numbers) in the (a, b, c) directions, respectively.

- The crystallite structure is assumed to possess the monoclinic space group $\boldsymbol{P}2_1(\boldsymbol{C}_2^2)$ [106, 163].

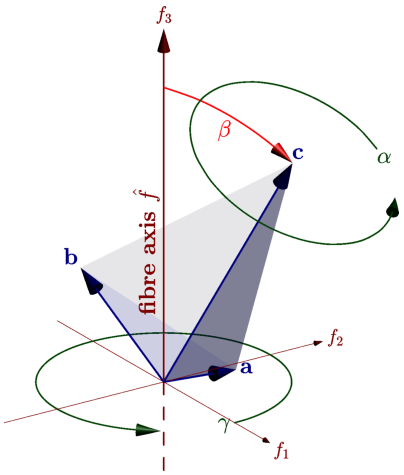

Figure 5.29.: **The parameters of a crystallite orientation.**
The parametrisation of the orientation of the crystallite with respect to the fibre frame is shown. $\{f_1,f_2,f_3\}$ – is a fibre coordinates frame, $\{\mathbf{a},\mathbf{b},\mathbf{c}\}$ – represents the coordinate system of a crystallite. The assumed distribution possesses an anisotropy only over the β angle between the $\hat{c}$-axis of the crystallites and the fibre axis $\hat{f} \equiv \vec{f}_3$, shown as a red arc-arrow. The two green arc-arrows represent rotations with an isotropic probability distribution.

Our model is based on the following assumptions:

- As is usually done, the whole sample (fibre) is considered as a macroscopic ensemble consisting of two kinds of regions: (i) an amorphous matrix enclosing (ii) crystalline

regions. The latter consist of a large number of small crystallites, which themselves can be considered as a statistical ensemble. We are interested in the average scattering intensity over the distribution of the crystallite orientation in this ensemble.

- The form of crystallites is assumed to be simple brick-like build up by L,M,N unit cells in the directions x,y,z. The size of a unit cell is characterized by three spatial lattice constants (a,b,c) in these directions. The scattering function of a single crystallite is a product of two components: the form factor and the structure factor. The former is independent of the internal structure of a unit cell and describes only the effects of the crystallites shape. The latter depends on the unit cell structure.

- The brick-like crystallite shape provides the simple form factor known as Laue intensity, defined as follows:

$$I_L(\vec{q}) = I_L(\vec{q}; L,M,N) = \prod_{i=1}^{3} \left| \frac{\sin \frac{N_i \vec{q} \cdot \vec{d}_i}{2}}{\sin \frac{\vec{q} \cdot \vec{d}_i}{2}} \right|^2 \tag{5.23}$$

  where: $\vec{q}$ is the momentum transfer, $d_i \in (a,b,c)$ denotes the size of the unit cell in the direction $i \in \{x,y,z\}$ and $(N_x, N_y, N_z) = (L,M,N)$, respectively.

- The unit cell is composed of 4 peptide chains. Each chain consists of two peptide units described by the simple rigid peptide planar model first proposed by Pauling et.al. [22], with spatial parameters recently updated by [30, 31]. The size of the unit cell and the positions of the atoms are governed by the symmetry of the unit cell, the geometry of peptide planes and dihedral (torsion) angles of peptide chains (see [30, 31, 66, 89, 145]). Knowing the positions of the atoms allows us to write the structure factor as

$$S(\vec{q}) \quad = \quad \left| \sum_j f_j(Q) \mathrm{e}^{\mathrm{i}\vec{q} \cdot \vec{r}_j} \right|^2 \tag{5.24}$$

  where: Q is the modulus of the vector of momentum transfer, $\vec{r}_j$ position vector of the atom labelled by j, $f_j(Q)$ denotes the atoms form factor. A detailed description of the unit cell is given later, see pages 201 - 218.

- On the basis of the measured data we assume the distribution of crystallite orientations to have a cylindrical symmetry and to be anisotropic only in the angle between the fibre axis and the crystallite c-axis. In the parametrisation with Euler angles

$\hat{\Omega}$ = (α,β,γ) (see fig. 5.29) the orientation probability distribution function (**OPDF**) then has the following form:

$$\boldsymbol{\rho}(\hat{\Omega}) = \frac{1}{4\pi^2}\rho(\beta) \tag{5.25}$$

So, the OPDF does not depend on the two angular degrees of freedom (α, γ), represented by arc-like arrows coloured green in the figure 5.29. It is only a function of a single variable, the azimuthal (latitude) angle β, represented by the red arc-like arrow.

- We will adopt two further simplifications:
  - We will assign the same (mean) value of stress applied to each crystallite in the ensemble.
  - As a first approximation, we consider the situation where all crystallites have the same size. This can be easily generalized without any change in our procedure. Indeed, for a given distribution function $\Psi(L,M,N)$, describing the probability to find a crystallite with the (L,M,N) lattice numbers, we only have to replace the shape function I_L defined in (5.23) by the new one, defined as:

$$\bar{I}_L(\vec{q}) = \sum_{L,M,N} \Psi(L,M,N)\, I_L(\vec{q};\, L,M,N) \tag{5.26}$$

Based on the above assumptions the scattering intensity from a single crystallite in the ensemble is a product of two factors: the form factor I_L represented by the Laue shape-function and a structure factor $S(\vec{Q})$:

$$I_c(\vec{q},\hat{\Omega}) = I_L(\vec{q},\hat{\Omega})\, S(\vec{q},\Omega) \tag{5.27}$$

where: $\hat{\Omega}$ described the orientation of a crystallite and can be expressed by the Euler angles. This contributes to the total intensity with an amplitude proportional to the probability $\boldsymbol{\rho}(\hat{\Omega})$ of finding a crystallite with the orientation $\hat{\Omega}$. The intensity I_c mainly depends on the three cosines of angles between the vector of momentum transfer and the coordinate vectors of the unit cell $\{\vec{q}\cdot\vec{a}, \vec{q}\cdot\vec{b}, \vec{q}\cdot\vec{c}\}$ and of the geometrical form (size) of the crystallite together with its structure.
The total measured intensity is the ensemble average of the single crystallite scattering function I_c in (5.27), the average taken over all the orientation states $\hat{\Omega}$ of a crystallites weighted with OPDF $\boldsymbol{\rho}(\hat{\Omega})$:

$$I(\vec{Q}) = \int \boldsymbol{\rho}(\hat{\Omega}) I_c(\vec{Q},\hat{\Omega}) d\Omega \tag{5.28}$$

$$= \frac{1}{4\pi^2}\int_0^{\pi} \sin(\beta)\,\rho(\beta)\,d\beta \int_0^{2\pi}\int_0^{2\pi} d\gamma\, d\alpha\, I_c(\vec{q},\hat{\Omega}) \tag{5.29}$$

The integration is over the whole space of rotational states of a crystallite. In the second line the independence of the OPDF from the longitude angles α and γ is shown explicitly. The (co)latitude angle can be specified through the relation $\cos(\beta) = \hat{c} \cdot \hat{f}$, where $\hat{f}$ [4] denotes the unit vector along the fibre axis $\vec{f}_3$, see fig. 5.29.
In the next section we will describe the computation of $I(\vec{Q})$ and outline a suitable numerical procedure.

Averaged Intensity

Assuming the OPDF function $\rho(\Omega)$ to be sufficiently "good", i.e. smooth and differentiable we have a situation where all the functions under the integrals in (5.28, 5.29,) of the previous section are periodic, smooth and infinitely (many) times differentiable with respect to their angular variables $\hat{\Omega} = (\alpha, \beta, \gamma)$. This means that a polynomial series expansion will have a rapid convergence. Mostly it will be spectral or, at least, geometrical convergence. This leads us to use the spectral methods in the computation of the averaged intensity $I(\vec{q})$ introduced above in eq. (5.28). Below we show the evaluation of this averaging in terms of the spherical harmonics Fourier transform (see e.g. [10, 27]).
The main idea is the following: the integrand in (5.28) consists of two functions $\rho_3(\hat{\Omega})$ and $I_c(\vec{q}, \hat{\Omega})$ which can be expanded into a series of orthogonal functions separately. The value of the integral is then obtained by summing the (weighted) product of expansion coefficients. For the geometry under consideration the most suitable choice is the set of spherical harmonics $\{Y_{lm}\}$ and the set of Legendre polynomials $\{P_l\}$ as functional bases, see [1, 10] for details. The index sets are $(l = 0,1,2\ldots, m = -l, -l+1,..,l)$ and $(l = 0,1,2,\ldots)$, respectively.
The spectral approach allows us to do separate evaluations of the participating functions with predescribed tolerance, each on its own characteristic scale. This will reduce the number of computations and allows to separate the domains of fitting parameters, e.g., we can fit the parameters of the OPDF without recomputing the shape factor and structure factor.
The computation of the total intensity (5.28, 5.29) is done in two steps. (i) Firstly, using the independence of the OPDF from the parameter γ we evaluate the integration over this variable. The result is the intensity from a crystallite averaged over rotations about its c-axis, which has a cylindrical symmetry. Its depends only on the dot product $\hat{c} \cdot \hat{q}$. (ii) Then the averaging over all orientations $\hat{c} = (\gamma, \beta)$ of the c-axis is done using spectral

[4] in the following we will intensive use the notation $\hat{X}$ meaning the direction of a vector $\vec{X}$ which has not to be confused with $\hat{X}$ denoting an operator X.

methods. The orientation of the fibre $\hat{f}$ is assumed to be fixed.

Let us introduce the intensity from a single crystallite averaged over all rotations about its c-axis as

$$\bar{I}_c(\vec{q}\cdot\hat{c}) = \bar{I}_c(Q,\hat{q}\cdot\hat{c}) \equiv \frac{1}{2\pi}\int_0^{2\pi} I_c(\vec{q},\hat{\Omega})\,d\alpha = \frac{1}{2\pi}\int_0^{2\pi} I_L(\vec{q},\hat{\Omega})\;S(\vec{q},\Omega)\,d\alpha \tag{5.30}$$

where we used the convention:

$$\vec{q} = \hat{q}Q \tag{5.31}$$

The application of direct numerical quadratures for the evaluation of (5.30) can fail or will take a lot of processor time. The difficulty is due to the fact that the integrand is a product of two differently scaled functions: one of them is $S(\vec{Q},\Omega)$ which is a slowly varying function, nevertheless its numerical evaluation requires a lot of processor time; the other is the shape-factor $I_c(\vec{q},\Omega)$ which can be computed relatively fast, but it varies very rapidly (as it is fine scaled) and possesses sharp peaks requiring a dense integration/approximation grid. There is a more suitable approach, which is very similar to the Clenshaw-Curtis quadrature [20, 45]: the integral is easily computed applying the adaptive fast discrete Fourier (cosine) transform to each of these functions separately and, then, computing the value of this integral as their scalar product in the Fourier space. In other words, the value of integral is the sum of the product of the Fourier expansion coefficients of the two participating functions. This approach allows to reduce the computing time and, additionally, to control the errors without repeated evaluation of the integrand functions. The computation error can be estimated from the values of few last expansion coefficients and/or from the iterative evolution of the value of the first coefficient (for the error estimation in adaptive procedures see e.g. [143]).

With $\bar{I}_c(Q,\hat{q}\cdot\hat{c})$ from (5.30) the equation (5.28) can be reduced to:

$$I(\vec{Q}) = \frac{1}{2\pi}\int_0^{2\pi} d\gamma \int_0^{\pi} \sin(\beta)\,\bar{I}_c(Q,\hat{c}\cdot\hat{q})\,\rho(\hat{c}\cdot\hat{f})\,d\beta \tag{5.32}$$

$\bar{I}_c(Q,\hat{c}\cdot\hat{q})$, the result of the integration in (5.30), is a function of only two variables: the absolute value of momentum transfer Q and the angle between $\hat{q}$ and $\hat{c}$. Hence, for fixed Q, we can expand it into a series of Legendre polynomials of the variable $\hat{c}\cdot\hat{q}$:

$$I_c(Q,\hat{c}\cdot\hat{q}) \;=\; \sum_{l=0}^{\infty} A_l(Q)P_l(\hat{c}\cdot\hat{q}) \tag{5.33}$$

The expansion coefficients $A_l(Q)$ are defined as:

$$A_l(Q) \equiv \frac{2l+1}{2} \int_{-1}^{1} I_c(Q,x) P_l(x) dx \tag{5.34}$$

In our procedure we compute values of $A_l(Q)$ through the Chebyshev interpolation of $I_c(Q, \hat{c} \cdot \hat{q})$ followed by the conversion of the Chebyshev interpolation coefficients into the coefficients of the Legendre series expansion (see algorithm 473 [136]).
Using the addition theorem (see e.g. [1, 10]) for Legendre Polynomials we separate the variables as

$$I_c(Q,\hat{c} \cdot \hat{q}) = \sum_{l=0}^{\infty} A_l(Q) \frac{4\pi}{2l+1} \sum_{m=-l}^{l} Y_{lm}(\hat{q}) Y^{\star}_{lm}(\hat{c}) \tag{5.35}$$

We can proceed similarly with the OPDF $\rho(\beta)$:

$$\rho(\beta) = \sum_{l} \rho_l P_l(\hat{c} \cdot \hat{f}) = \sum_{l} \rho_l \frac{4\pi}{2l+1} \sum_{m=-l}^{l} Y_{lm}(\hat{c}) Y^{\star}_{lm}(\hat{f}) \tag{5.36}$$

where the expansion coefficients are defined in the same manner as A_l in (5.34) and $\cos(\beta) = \hat{c} \cdot \hat{f}$.
The equations (5.32, 5.33, 5.36) offer a possibility to integrate the product $I_c(Q,\hat{c} \cdot \hat{q}) \rho(\hat{c} \cdot \hat{f})$ over all orientations of $\hat{c}$ which we parametrized by the angles γ, β.
Using the orthogonality of the spherical harmonics we arrive at

$$I(\vec{q}) = \sum_{l} \frac{2}{2l+1} A_l(Q) \rho_l P_l(\hat{q} \cdot \hat{f}) \tag{5.37}$$

The equation (5.37) describes the intensity of the whole crystalline ensemble as a function of the expansion coefficients of the OPDF, the modulus of the momentum transfer Q and the angle between the orientation $\hat{f}$ of the fibre axis and the orientation $\hat{q}$ of the vector of the momentum transfer $\vec{q}$.
If the orientation of the fibre, the function of single crystallite intensity and the OPDF are given, then the total intensity is a function of the vector $\vec{q}$, only.
Additionally, there is an implicit dependence on the unit cell parameters (in the structure factor $S(\vec{q})$) and the parametrisation of the shape function $I_L(\vec{q})$ (in our case it is the numbers (L,M,N) of the Laue shape function). All the parameters can be adjusted by fitting the model to the measured diffraction data.
So knowing the OPDF, the structure factor and the shape function one can compute point wise the whole diffraction image using equation 5.37 for suitable parametrisation of the vector $\vec{q}$, e.g. in terms of the usual scattering angles (θ, ϕ). To compute the intensity in a

sector of the diffraction image with $\phi \in [\phi_1, \phi_2]$ for some given values of $\phi 1, \phi 2$, one needs to integrate the intensity in equation 5.37 over the variable ϕ as:

$$\begin{aligned} I(Q) \equiv I(\theta) &= \int_{\phi_1}^{\phi_2} I(\vec{q}) d\phi \\ &= \sum_l \frac{2}{2l+1} A_l(Q) \rho_l \int_{\phi_1}^{\phi_2} P_l(\hat{q} \cdot \hat{f}) d\phi \end{aligned} \tag{5.38}$$

Below, to put all said above together, we sketch an algorithm for the evaluation of the intensity $I(\vec{Q})$ (5.37) of an ensemble of crystallites with any isotropic orientation distribution:

- **Input:**

  $\{V_\theta, V_\phi\}$ an array of the polar coordinates of the $\vec{q}$ at which the values of the intensity is requiested.

  OPDF(β) the function to evaluate OPDF at angles β

  S($\vec{q}$) the function to evaluate the unit cell structure

  IL($\vec{q}$) the function of crystallite shape factor (Laue intensity function)

  tol the tolerance for the errors of computations

- **Output:** An array of values of ensemble averaged intensity $I(\vec{q})$, defined by eq.(5.29).

---

1. compute expansion coefficients ρ_l of OPDF as in eq.(5.36). The truncation number if defined by the given tolerance **tol**.
2. for each θ in V_θ:
   a) compute expansion coeficients $A_l(Q)$ using equations (5.30, 5.35).
   b) for each ϕ in V_ϕ: compute values of intensity $I(\theta,\phi)$ as in eq. (5.37)
3. return: array of the values I(θ,ϕ) for $\theta \in A_\theta$ and $\phi \in A_\phi$

Modeling the silk structure factor.

The main target of this subsection is the setup of the computation model for the structure factor needed to evaluate the intensity in equation (5.37). The computation of the structure factor takes into account only the atom form factors of the heavy atoms CNO in the periodical structure of the $-(Ala-Glu)_n-$ amino-sequences which is approbed simulation model of the silk β-sheet crystalites [41,160]. The model will be constructed on the basis of the rigid peptide planes together with the crystallite unit cell symmetry combined with the molecular symmetry of the participating chains and the intuitively clear mirror symmetry of the projection of the H-bonds on the ab-plane of the unit cell. The model contains of 6 parameters to adjust positions of the 36 heavy atoms in the unit cell coordinate system. So it is possible to fit the diffraction intensity computed by the model to the measured data.

In what follows we firstly specify the set-up for geometrical computation. Then we describe the spatial structure of peptide helices and β-sheets and outline the procedure for an evaluation of the X-ray scattering function for the α-helix and the structure factor for the β-sheet crystallites.

Idealized geometry of the peptide helix

Since the work of Pauling [132,133] the modelling of proteins was based on the assumption that the peptide backbone has a certain ideal geometry independent of the chemical environmental context, see figure 5.30. The rigid geometry model assumes fixed bond lengths and angles, leaving torsion angles as the only variables needed to define the structure. The idealized (averaged) values for the geometry of the peptide plane (backbone) have varied a little over the decades, the most frequently used values are shown in figure 5.30. Such models assume a nearly flat structure of the amid group, i.e. the value of torsion angle Ω (around the C-N axis) is about 180°. Therefore, the degrees of freedom in the backbone conformation are the two dihedral angles Φ and Ψ per residue (sketched in figure 5.31). These angles define for each atom C^α the rotation of the left and right peptide planes about the $N-C_\alpha$ and $C_\alpha-C$ bonds, respectively [173] (more on dihedral angles see page 206).

In the following we will parametrize the two simplest standard structures (α-helix and β-sheet) in terms of the dihedral angles. For β-sheets this will allow us to relate the dihedral angles with the crystallographic unit cell parameters used to fit the experimental data from the X-ray scattering experiments. We will follow the route introduced in [145] and elaborated in [66] relating the protein secondary structure with the Ramachandran

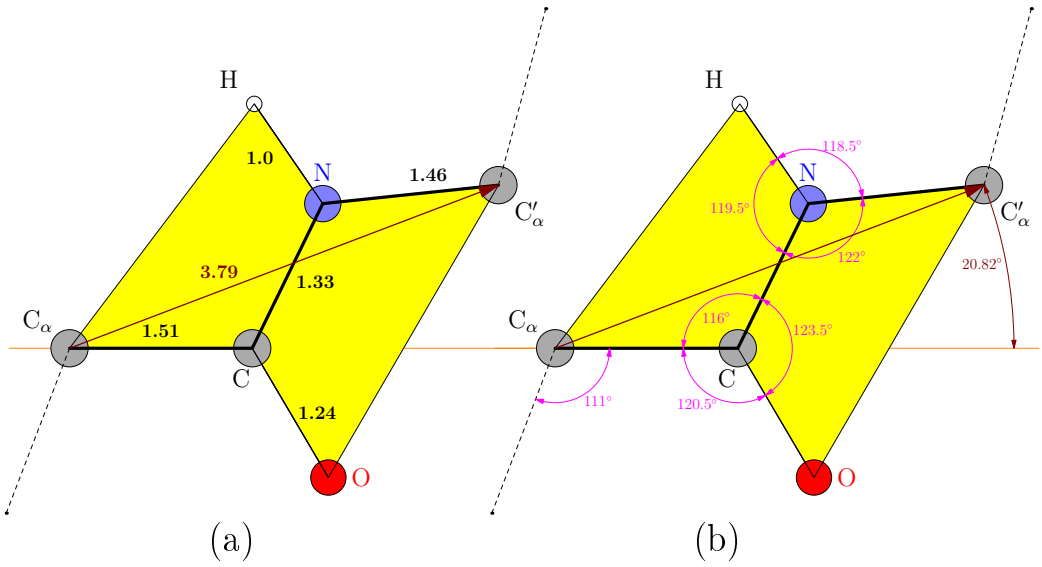

Figure 5.30.: **Geometry of an averaged peptide plane [30, 31].**
The left pane (a) shows the bond-lengths and the right pane (b) shows the bond-angles of the 'standard peptide' unit.

torsion angles. In [145] Quine uses the theory of the screw motion to describe standard motifs in the protein secondary structure, where the positioning of the protein backbone (peptide plane) is described in terms of local helix parameters (the rotation axis and angle; translation along the rotation axis), which he relates to the torsion angles.
The simplest regular helical structure of a protein chain can be considered as built from the copies of an initial peptide plane P_0 by sequentially application of an Euclidean isomeric transformation $\hat{\mathcal{S}}$ as

$$(1 + \hat{\mathcal{S}} + \hat{\mathcal{S}}^2 + \hat{\mathcal{S}}^3 \ldots)P_0 \tag{5.39}$$

with $\hat{\mathcal{S}}$ consists of a rotation followed by a translation, i.e. $\hat{\mathcal{S}} = \hat{\mathcal{T}}_{\vec{v}}\hat{\mathcal{R}}^{\hat{u}}(\theta) := \{\hat{\mathcal{R}}^{\hat{u}}(\theta)|\vec{v}\}$. $\hat{\mathcal{T}}_{\vec{v}}$ denotes the translation-operation over the vector $\vec{v}$. $\hat{\mathcal{R}}^{\hat{u}}(\theta)$ denotes the operation of the

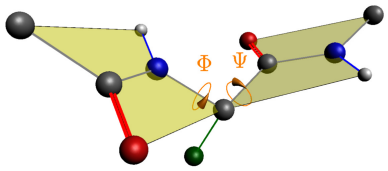

Figure 5.31.: **Sketch showing the torsion angles Ψ,Φ**
Rem: on the all of our 2D and pseudo-3D sketches we represent each atom type by its usual in the literature colour: H - white, C - grey, N - blue, O - red. Only the first atom of residuals will be an exception. We usually represent them by the green colour.

rotation by the angle θ around the axis $\vec{u}$ through the origin.

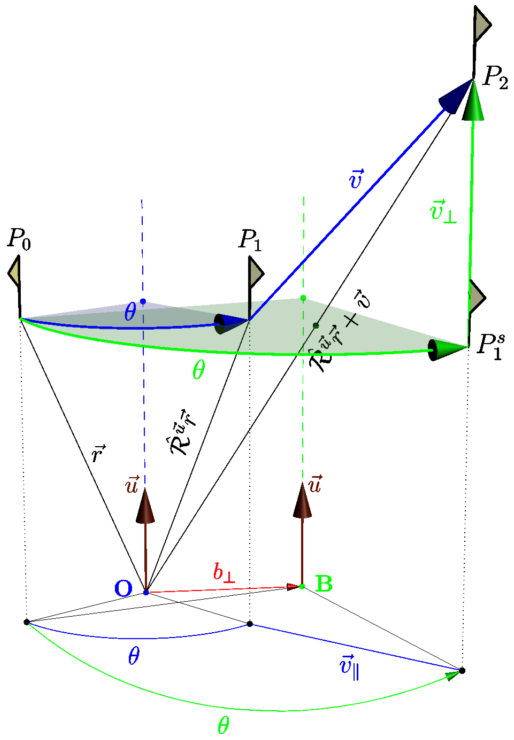

Figure 5.32.: **Equivalence of rotation-translation $\hat{\mathcal{S}}$ to screw displacement.** The figure shows traces of two displacements of a body placed at a point $\vec{r}$. The body is represented by a triangular flag. One displacement is the rigid body displacement consisting of the rotation around the axis $\hat{u}$ through the origin **O** and the translation by a vector $\vec{v}$: $P_0 \to P_1 \to P_2$. The trace of this transformation is displayed by the thick blue arrows: the arc-arrow θ represents the rotation and the straight arrow $\vec{v}$ represents a translation. The projection of this path onto the plane perpendicular to the rotation axis is shown by the thin blue lines. The other displacement is the equivalent screw transformation $P_0 \to P_1^s \to P_2$ consisting of the rotation around the axis $\hat{u}$ through the point $\mathbf{B} = \mathbf{O} + \vec{b}_\perp$ and the translation by the vector $\vec{v}_\parallel$, which is the component of $\vec{v}$ parallel to the rotation axis. This movement is represented by the thick green arrows and its projection onto the plane perpendicular to $\vec{u}$ is represented by the thin green lines. Both movements equally transform the point P_0 at $\vec{r}$ to the point P_2 at the $\hat{\mathcal{R}}^{\hat{u}}(\theta)\vec{r} + \vec{v}$.

Due to the Chasles theorem ([70,89,145]) we can describe any rigid body displacement as a screw motion, see demonstration sketch in figure 5.32. A `screw motion` consists of two successive operations: a rotation around some fixed point **B** and a translation parallel to the rotation (screw) axis. The parametrisation of the screw displacement consists of the (rotation) screw axis (specified by the unit vector $\hat{u}$ and the point **B**), the rotation angle θ and the length of the translation t.

The relations between the translation-rotation (specified by $\hat{u}, \theta, \vec{v}$) parameters and those

of screw motion equivalent to it (specified by $\{\vec{b}, \hat{u}, \theta, t\}$) are [70]:

$$\begin{aligned} \vec{b}_\perp &= \frac{1}{2}\left(\vec{v}_\perp + \hat{u} \times \vec{v}\ \cot(\frac{\theta}{2})\right) \\ t &= |v_\parallel| = \vec{v} \cdot \hat{u} \\ \vec{v}_\perp &= \vec{v} - \hat{u}\, t \end{aligned} \tag{5.40}$$

where the symbol $\perp$ denotes the component perpendicular to the rotation axis and $b_\perp$ is the shortest vector from the origin to the screw axis.
That means that equation (5.39) describes a simple helix with the axis parallel to the rotation axis through the point $\vec{b}$. The (non integer) number of peptide planes (or residues) per turn is π/θ, the rise per residue $t = \vec{v} \cdot \hat{u}$ and the pitch of the helix is $p = n\, t$. All these parameter are functions of the dihedral angles Φ, Ψ. So we can find these values from the known dihedral angles or, expressed differently, knowing the parameters of the helix one can compute the values of the dihedral angles. In a β-sheet crystallite structure the protein chains build the degenerated helix with 2-residuals per turn and $\theta = \pi$, so the length of the folding period along the peptide chain specifies the values of both dihedral angles. The known dihedral angles and the crystallographic symmetry of the unit cell of the β-sheet crystallite will completely specify the structure factor of the unit cell.

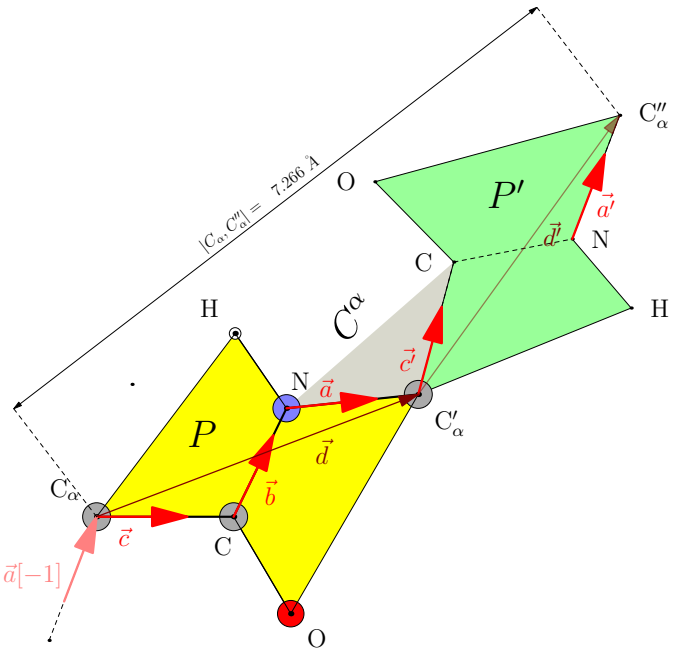

Figure 5.33.: **Peptide local frames**

The figure visualize the definitions of the planes of the types P and C^α (5.42 - 5.45) on the example of a maximally extended double-segment of a protein chain with a peptide units (planes) geometry shown in the figure 5.30. The unit vectors $\vec{c}, \vec{a}$ define the peptide plane frame P, coloured yellow. Similarly, the unit vectors $\vec{c}', \vec{a}'$ define the (second) peptide plane frame P', coloured green. The unit vectors $\vec{a}, \vec{c}'$ define the residual frame C^α. The vector $\vec{d} \equiv \overrightarrow{C_\alpha C'_\alpha}$ is called the virtual bond of the peptide plane P.

Local frames. To describe the parameters of $\hat{\mathcal{S}}$ (eq. 5.39) in terms of dihedral angles two kinds of local frames are introduced. The first one describes the peptide plane and the second the residual. Let us define two unit vectors in the peptide plane as shown in figure 5.33. The figure shows a double segment of a chain built from N-terminus to C-terminus. The unit vector in the direction $C_\alpha C$ is denoted as $\hat{c}$ and the unit vector pointing in the direction NC'_α is denoted as $\hat{a}$.
$\vec{d}$ is defined as 'virtual bond' of the peptide plane equal to the vector $\overrightarrow{C_\alpha C'_\alpha}$ (see figures 5.30 and 5.33):

$$\vec{d} \equiv \overrightarrow{C_\alpha C'_\alpha} \;=\; \hat{c}|C_\alpha C| + \hat{b}|CN| + \hat{a}|NC'_\alpha| \tag{5.41}$$

- **Peptide plane frame P:**
  The orthonormal coordinate system is defined as a triple:

$$\{e_1, e_2, e_3\}_P = \{\hat{c},\ \hat{n} \times \hat{c},\ \hat{n}\}, \tag{5.42}$$

where the normal vector $\hat{n}$ is defined as

$$\hat{n} = \frac{\hat{c} \times \hat{a}}{\|\hat{c} \times \hat{a}\|}. \tag{5.43}$$

- **Residual frame C^α:**
  The orthonormal coordinate system is defined as a triple:

$$\{e_1, e_2, e_3\}_{C^\alpha} = \{\hat{a},\ \hat{n}_c \times \hat{a},\ \hat{n}_c\}, \tag{5.44}$$

  where the normal $\hat{n}_c$ is defined as

$$\hat{n}_c = \frac{\hat{a} \times \hat{c}'}{\|\hat{a} \times \hat{c}'\|}. \tag{5.45}$$

Dihedral angles Φ, Ψ. [5]

For sequence of three unit vectors $\hat{u}_1, \hat{u}_2, \hat{u}_3$ (see figure 5.34) one can define a dihedral angle as the rotation angle from the plane $\hat{u}_1 \times \hat{u}_2$ into the plane $\hat{u}_2 \times \hat{u}_3$ in a counter-clockwise sense. Its numerical value is defined as argument of the complex number Z, i.e.:

$$\begin{aligned} \theta &\equiv Tor(\hat{u}_1, \hat{u}_2, \hat{u}_3) &&= Arg(Z) \\ Z &= -\hat{u}_1 \cdot \hat{u}_3 + (\hat{u}_1 \cdot \hat{u}_2)(\hat{u}_2 \cdot \hat{u}_3) + \mathbf{i}\ \hat{u}_1 \cdot (\hat{u}_2 \times \hat{u}_3) \end{aligned} \tag{5.46}$$

where $Tor(\ldots)$ denotes a function of torsion angle of it arguments and $Arg(Z)$ is the argument of a complex number Z, i.e. $Arg(Z) = \ln(Z/|Z|)$. The derivation of (5.46) is given in appendix A.1.

In the recommendation of the IUPAC-IUB Commission on Biochemical Nomenclature (CBN) [18] the torsion (dihedral) angle for a system of four atoms {A,B,C,D} (see figure 5.35) is defined as the angle between the plane $\vec{u}_1 \times \vec{u}_2$ containing (A,B,C) and the plane $\vec{u}_2 \times \vec{u}_3$ containing (B,C,D). Equivalently, in the projection of the system onto a plane normal to the B-C bond, the angle between the projection of A-B and the projection of C-D is called the `torsion angle` of A and D about the bond B-C. In the configuration where the projections of A-B and C-D are coincide the torsion angle is defined to be zero. With the setup above the protein dihedral (Ramachandran) angles are defined as follows [145]:

$$\begin{aligned} \Phi &= \phi + 180^\circ &&= Tor(\hat{c}, \hat{a}, \hat{c}') + 180^\circ \\ \Psi &= \psi &&= Tor(\hat{a}, \hat{c}', \hat{a}') \end{aligned} \tag{5.47}$$

[5] the other equivalent terms are the torsion angles or internal rotation angles

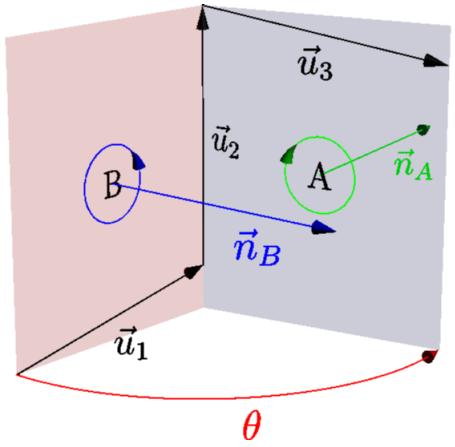

Figure 5.34.: **Dihedral angle of three non-collinear vectors**
the figure shows a dihedral angle as defined of a three unit non-collinear vectors $\vec{u}_1, \vec{u}_2, \vec{u}_3$. A, B are planes spanned by the pairs $(\vec{u}_1, \vec{u}_2)$ and $(\vec{u}_2, \vec{u}_3)$, respectively. $\vec{n}_A, \vec{n}_B$ are normals to these planes. The dihedral angle $Tor(\vec{u}_1, \vec{u}_2, \vec{u}_3) = \theta$ is defined as angle of counter-clockwise rotation from $\vec{n}_B$ to $\vec{n}_A$ around the axis $\vec{u}_2$.

There are tree planes participating in the definition of these dihedral angles: two adjusted (successive) peptide planes (the P frames) and one residual plane (the C^α frame). The peptide planes are spanned by the vectors $\{\hat{c}, \hat{a}\}$ and $\{\hat{c}', \hat{a}'\}$. The C^α plane is spanned by the $\{\hat{a}, \hat{c}'\}$ vectors, compare figures 5.33 and 5.31.

The relation between regular helix parameters and Φ,Ψ-angles

As mentioned above the transition from a peptide plane to the next can be described as a rotation and a successive translation along the virtual bond vector $\vec{d}$.
For convenience we introduce the following abbreviations:

$$\begin{aligned} \xi &:= \widehat{ca} \\ \chi_0 &:= \widehat{NC_\alpha C} \\ \chi^+ &:= \chi_0 + \xi =: \chi \\ \chi^- &:= \chi_0 - \xi \end{aligned} \tag{5.48}$$

where $\xi = \widehat{ca}$ denotes the angle between unit vectors $\hat{c}$ and $\hat{a}$, χ denotes the angle $\widehat{NC_\alpha C}$, i.e. the angle between $\hat{a}$ and $\hat{c}'$. Then the rotation from a peptide plane to the next in a regular helix structure can be described as [145]:

$$\hat{\mathcal{R}}^{\hat{u}}(\theta) = \hat{\mathcal{R}}^{\hat{a}}(\phi)\, \hat{\mathcal{R}}^{\hat{n}}(\chi^+)\, \hat{\mathcal{R}}^{\hat{c}}(\psi) \tag{5.49}$$

where ϕ, ψ - are torsion angles defined in (5.47). This equation relates two dihedral angles with the rotation angle and axis of the screw motion from peptide plane to the next. The

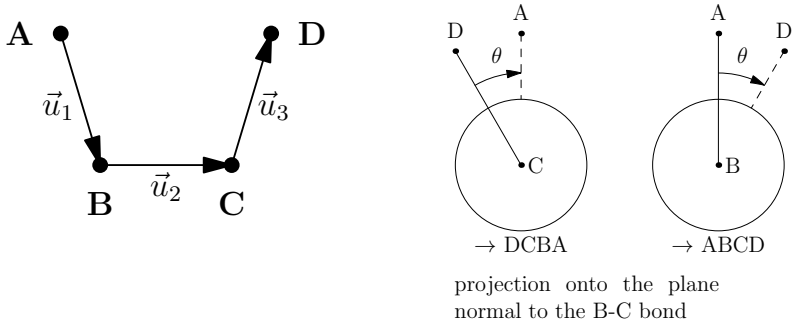

Figure 5.35.: **Newman projection illustrating the sign of torsion angles**
The left pane shows the zero-configuration of a set of four atom, used in the definition of the torsion angle. The right panes shows a projections onto a plane normal to the BC bond together with the `measuring` direction of the torsion angle. For each of the views (DCBA and ABCD) on the right pane, a right-handed turn of the bond to the from atom about the central bond gives a positive value of torsion angle.

computation can be done in terms of rotation matrices, spherical trigonometry, quaternions or more common (and a lot easier) in terms of geometric (or Clifford) algebra (see e.g. [70]). The author used the latter. The computation is shown in the appendix A.1 on the page 255. The resulting rotation is defined as rotation around the axis $\hat{u}$ by the angle θ and is specified by the following relations:

$$\begin{aligned} u_0 := \cos\frac{\theta}{2} &= \cos\frac{\phi}{2}\cos\frac{\psi}{2}\cos\frac{\chi^+}{2} - \sin\frac{\phi}{2}\sin\frac{\psi}{2}\cos\frac{\chi^-}{2} \\ \vec{u} := \hat{u}\sin\frac{\theta}{2} &= \hat{e}_1\left(\cos\frac{\phi}{2}\sin\frac{\psi}{2}\cos\frac{\chi^+}{2} + \sin\frac{\phi}{2}\cos\frac{\psi}{2}\cos\frac{\chi^-}{2}\right) \\ &\quad + \hat{e}_2\left(\cos\frac{\phi}{2}\sin\frac{\psi}{2}\sin\frac{\chi^+}{2} - \sin\frac{\phi}{2}\cos\frac{\psi}{2}\sin\frac{\chi^-}{2}\right) \\ &\quad + \hat{e}_3\left(\cos\frac{\phi}{2}\cos\frac{\psi}{2}\sin\frac{\chi^+}{2} + \sin\frac{\phi}{2}\sin\frac{\psi}{2}\sin\frac{\chi^-}{2}\right) \end{aligned} \tag{5.50}$$

Here $\{\hat{e}_1, \hat{e}_2, \hat{e}_3\}_P$ is the triple of coordinate vectors in the P frame specified in (5.42). The angles between the screw axis and the vectors $\vec{d}, \hat{c}, \hat{n}$ can be obtained from scalar products:

$$\vec{d}\cdot\hat{u} = \frac{\vec{d}\cdot\vec{u}}{\sqrt{1-u_0^2}} \geqslant 0 \tag{5.51}$$

$$\hat{c}\cdot\hat{u} = \frac{\hat{c}\cdot\vec{u}}{\sqrt{1-u_0^2}} \tag{5.52}$$

$$\hat{n}\cdot\hat{u} = \frac{\hat{n}\cdot\vec{u}}{\sqrt{1-u_0^2}} \tag{5.53}$$

Spherical coordinates (α, β) of the rotation axis can be computed as:

$$\begin{array}{rcccl} \alpha & = & \arccos(\hat{n}\cdot\hat{u}) & = & \arccos\frac{1}{|\vec{u}|}(\hat{n}\cdot\vec{u}) \\ \beta & = & \arg(\hat{c}\cdot\hat{u} + i\,\hat{e_2}\cdot\hat{u}) & = & \arg\frac{\vec{u}}{|\vec{u}|}\cdot(\hat{e}_1 + \mathrm{i}\,\hat{e}_2) \\ |\vec{u}| & = & \sqrt{1-\cos(\frac{\theta}{2})} & & \end{array} \tag{5.54}$$

where α and β are azimuthal and polar angles of the screw axis $\hat{u}$, respectively; $\vec{u}$ and θ are given by the relations (5.50).

The coordinates of the first residual carbon atom C_β For given directions $\hat{a}$ and $\hat{c}'$ and values of the A = N-C_α-C_β, B = C-C_α-C_β and C = C_β-C_α-N angles we can write the unit vector $\hat{r}$ of the direction C_α-C_β as $\hat{r} = x\hat{a} + y\hat{c}' + z\hat{n}$, (x,y) is the solution of:

$$\begin{pmatrix}\cos A \\ \cos B\end{pmatrix} = \begin{pmatrix}1 & \cos C \\ \cos C & 1\end{pmatrix}\begin{pmatrix}x \\ y\end{pmatrix} \tag{5.55}$$

i.e.

$$\begin{pmatrix}x \\ y\end{pmatrix} = \begin{pmatrix}\cos A - \cos B\cos C \\ \cos B - \cos A\cos C\end{pmatrix}\frac{1}{\sin^2 C} \tag{5.56}$$

and the third coordinate $z = \sqrt{1-|x\hat{a}+y\hat{c}'|^2} = \sqrt{1-x^2-y^2-2xy\cos(C)}$.

Model for β-sheet crystallite The simplest approximation to the amino acid sequence of molecular chains in the silks crystallite region is commonly assumed to be of the type $(-Glu-Ala-)_n$ [106,163,164] which is arranged into the pleated-sheet conformation [132]. The unit cell possesses at least $P2_1$ symmetry and is filled with 4 (sub-) chains, each consisting of two peptide planes. These four chains are subdivided into two pairs, each pair forms a sheet structure by hydrogen bonding (OH-bonds). Two chin segments participating in the same sheet are independent with respect to the cell symmetry group and the two sheets participating in a unit cell are related through the two-fold screw symmetry. The commonly assumed model for the silk structure of sheets is an anti-parallel *beta*-sheet structure, where the orientation of the molecular chains in a sheet are alternating between up and down [106]. There are two possible variation of this model structure: polar and anti-polar [164]. The difference is only in the arrangement of the residues. In the `polar anti-parallel structure`: all the methyl groups of alanine residues are on the one side of the sheet. While, in the `anti-polar anti-parallel structure`: the alanine residues are alternately placed on the both sides of a sheet. In the first case two neighbour molecules in a sheet are related through the two fold rotation symmetry in the plane of the β-sheet,

while in the second only the peptide units (planes) posses this symmetry. In the most of our examples we will show only the first variation of the model structure.
Let $\{\hat{u}_a, \hat{u}_b, \hat{u}_c\}$ be the basis of the unit cell with dimensions $\{a,b,c\}$. The basis vectors of the cell are perpendicular to each other. The c-axis is directed parallel to the fibre axis, the a-axis is in the β-sheet plane and the b-axis is orthogonal to the β-sheet plane.
The structure of the chains in the silk β-sheet can be seen as repetitive helices with 2 peptide units per turn. We assume the same geometry of the standard peptide plane describing the Ala and Glu units. Hence, the screw symmetry of the molecular back-bone is the same as of the unit cell. Only the position of residuals will deviate from this screw symmetry.

Geometrical constraints and reduction of the free parameters of the unit cell. There is a series of geometrical constraints to the structure of a chain inside of the unit cell:

1. to be compatible with the crystal-symmetry the screw-rotation (from a peptide plane to the next plane) has to be a half turn rotation $\theta = 180°$. The rotation axis $\hat{u}$ of this displacement has to be parallel to the c-axis of the unit cell.

2. the virtual bonds of two successive planes and the c-vector of unit cell build a triangle, so that $c = 2\,(\vec{d} \cdot \hat{u}_c)$.

3. in the β-sheet plane (i.e. $\hat{u}_c \times \hat{u}_a$ plane) all the C-O $\cdots$ H-N bonds between neighbour chains have to be nearly linear and have approximately equal projections onto the β-plane. Or, alternativelly, the projections onto the $\hat{u}_a \times \hat{u}_b$ plane of the two OH-bonds one coples two bottom peptide units and other the two top peptide units of the two neighbor chains in the β-sheet are mirror symmetric with respect to the plane parallel to $\hat{u}_c \times \hat{u}_a$ contening the molecular screw axes. Additionally, at the ambient conditions the O$\cdots$N distance has to be about 2.8 Å.

The constraints 1. and 2. mean that the length c is a function of the torsion angles Φ,Ψ through the relations for rotation angle θ and its axis $\hat{u}$ in equations (5.50):

$$\begin{aligned} \cos(\tfrac{\theta}{2}) &= 0 \\ 2\,\vec{d} \cdot \hat{u} &= c \end{aligned} \tag{5.57}$$

The value of c (or equivalently the Φ,Ψ values) completely specifies the relative configuration of the chains in the unit cell and the only remaining degree of freedom is the rigid

rotation of the chain as a whole about it's screw axis. Together with the equations (5.40) these conditions define the coordinates of the intersection of the molecular screw axis with the peptide plane and the screw translation vector as:

$$\begin{aligned} \vec{b}_{\perp} &= \tfrac{1}{2}\left(\vec{d} - (\vec{d}\cdot\hat{u})\hat{u}\right) \\ \vec{v}_{||} &= (\vec{d}\cdot\hat{u})\hat{u} \end{aligned} \tag{5.58}$$

The point $b_{\perp}$ is a molecular screw centre and it will coincide with the unit-cell origin if we rotate the plane so that the molecular screw axis will coincide with the z-axis of the crystallite.
The third condition allows to approximate the angle of the rotation of the whole chain around the c-axis with respect to the unit-cell axis and the unit cell spacial parameter 'a'. Mathematically, the geometrical part of the constraints from above can be formulated as

$$\begin{aligned} \hat{\sigma}_c &= \hat{u} \\ \hat{\sigma}_a &= \frac{\hat{h}_{\perp} + \hat{o}_{\perp}}{|\hat{h}_{\perp} + \hat{o}_{\perp}|} \\ \hat{\sigma}_b &= \frac{\hat{\sigma}_c \times \hat{\sigma}_a}{|\hat{\sigma}_c \times \hat{\sigma}_a|} \end{aligned} \tag{5.59}$$

where: $\hat{h}_{\perp}, \hat{o}_{\perp}$ denote the normalized components of the $\vec{NH}$ and $\vec{CO}$ bond-vectors, respectively, orthogonal to $\hat{u}$. The vectors $\hat{\sigma}_a, \hat{\sigma}_b, \hat{\sigma}_c$ are the unit vectors of the crystallite unit cell. These expressions can be used to relate the basis of the local peptide frame to the basis of the crystallite unit cell, e.g. the rotation matrix from the local frame into the frame of the unit cell can be expressed as $R_{i,j} = \hat{\sigma}_i \cdot \hat{e}_j$. This rotation is described by the Euler angles $(-\alpha, -\beta, -\gamma)$, where α, β are the spherical coordinates of the screw axis $\hat{u}$ defined by eq. (5.54) and γ is the angle between the orthogonal to $\hat{u}$ component of the $C_{\alpha} \rightarrow C$ bond and the σ_a above.
This allows us to calculate the orientation of the peptide plane in the unit cell for a given length c or, equivalently, for a given value of torsion angle Φ (or Ψ) and finally to define the atomic positions in crystallite unit cell, as will be described in the next paragraph.
Below, we give a short listing of the steps needed to construct a double peptide unit from the initial one and relate it with the unit cell coordinate system, assuming the value of the dihedral angle Φ is given (see figure 5.36 visualizing the discussed transformations):

- On the basis of the configuration of the initial peptide plane compute the vectors $\hat{a}, \hat{c}$.
- Compute the value of the second dihedral angle Ψ as function of the given angle Φ.

- Compute the screw displacement in the local coordinat system of the initial peptide plane and apply it to the initial peptide unit.
- Compute the vectors $\hat{a}\prime, \hat{c}\prime$ for the second peptide plane.
- Compute the coordinates of the residual atom (C_β or H).
- Using the constraints for the H-bonds, compute the rotation matrix. Now we know the coordinates of the atoms in the chain relative to the coordinate system of the unit cell and we can apply the other symmetry operations to fill the unit cell with the other 3 chains (this will be discassed in the next section).

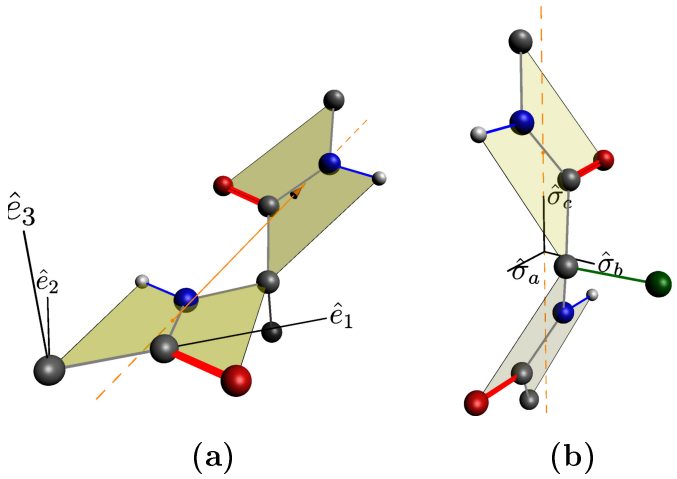

Figure 5.36.: **A chain segment consisting of two planes in the loacal and crystallite frames**

The figure shows a pair of peptide planes related through the molecular screw displacement described in the text. The values of dihedral angle are $\Phi = -141°, \Psi = -138.328°$. The orange dashed line represents the rotation axis of the molecular screw movement from a peptide plane into the next and the orange arrow represents the translation vector of this screw displacement. (a) The view in the local frame $(\hat{e}_1, \hat{e}_2, \hat{e}_3)$ of coordinate system connected with the first peptide plane, laying in the xy-plane. The second plane is obtained from the first one applying the srew operation, which rotation is given by (5.50) and translation vector is the "virtual bond" defined by (5.41). (b) The view of the same chain rotated into the frame of unit-cell coordinates $(\hat{\sigma}_a, \hat{\sigma}_b, \hat{\sigma}_c)$. The $\hat{\sigma}_a$-asis coinsids with the crystallite a-direction, $\hat{\sigma}_c$ is directed along the fibre axis. The rotation matrix is defined as $R_{i,j} = \hat{\sigma}_i \cdot \hat{e}_j$, where $\hat{\sigma}_i$ are computed as in (5.59). The rotation is choosen to satisfy the geometrical constraints discussed on the page 210.

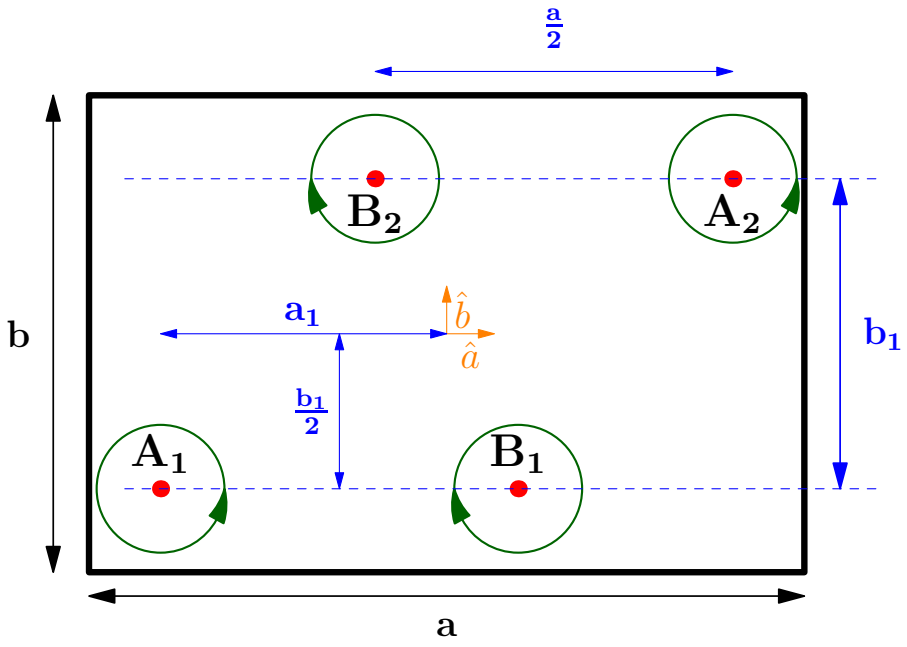

Figure 5.37.: **Positions of the peptide chains in the unit cell**
The figure shows a sketch of the positioning of the peptide planes in the unit cell together with chain-labelling convention used. This is the top view to the unit cell. The red points represent the positions of the molecular screw axis. a,b represent the size of the unit cell, a_1,$\frac{b}{2}_1$ is the coordinates of the lower-left chains centre. The distance between the chains in the β-sheet is $\frac{a}{2}$, b_1 is the "first" distance and $b - b_1$ is the "second" distnace between the β-sheets.

The structure factor

The unit cell of the β-sheet crystallites possesses three symmetry operations: the screw displacement $\hat{S}$ due to the crystallographic symmetry $P2_1$, the 180° rotation $\hat{R}_2$ around the axis parallel to $\hat{e}_b$ and local (molecular) screw displacement $\hat{S}_{mol}$ due to the symmetry between peptide planes in the chains, as discussed previously. The `last two are not symmetries of the space group`, but they follow from the structure of the β-sheets and the structure of the molecular chain [106, 163, 164].

Due to these symmetries each atom type from the standard peptide plane will appear 8 times, participating in the 4 peptide units, in the unit cell. And each residual atom has at least 4 symmetry induced equivalent atoms in the unit cell. Figure 5.39 demonstrate this situation schematically.

Using the operations above we can generate 8 positions of the set of symmetric atoms in the unit cell as

$$\vec{r}_i = \hat{P}_i \vec{r}, \qquad \vec{r} = (x,y,z) \tag{5.60}$$

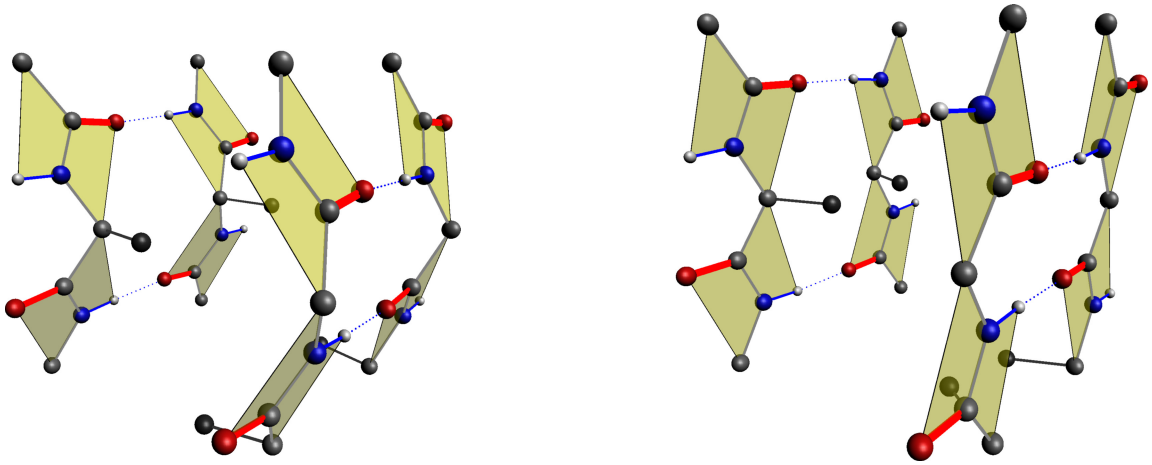

(a) **(b)**

Figure 5.38.: **Peptide planes in a unit-cell**
Figure shows a four peptide chains segments '$Ala-Gly$' filling a unit cell of the β-sheet crystallite for two configurations: (a) the non-stretched configuration with $\Phi = -141^{\circ}$, lattice parameters (a,b,c) = $9.48, 9.5, 6.98$ Å, (b) the completely stretched (flat) configuration with $\Phi = -180^{\circ}$, lattice parameters (a,b,c) = $9.24, 9.5, 7.29$ Å. Only Ala residual is shown, but without hydrogen components.

where $\vec{r}$ denotes coordinate-vectors of the initial position of an atom in the chain placed `in the bottom left corner` of the unit cell.

For a given atom in the peptide plane the vector $\vec{r}$ is a function of the initially given values of the dihedral angle Φ the size parameters of the cell a, b and coordinates of the molecular screw axis of the first chain A_1 (see figure 5.37). The transfomation from the local frame into the unit cell frame defining this dependence is described in the previous section.

The operators $\hat{P}_i$ relating $\vec{r}$ with the coordinate vector of an atom in the i plane are defined as follows:

$$\begin{array}{lllllll} \hat{P}_1 & = & \hat{I}d, & \hat{P}_2 & = & \hat{S}_{mol}\hat{P}_1 & A_1 - chain \\ \hat{P}_3 & = & \hat{S}\hat{P}_1, & \hat{P}_4 & = & (\hat{T}_c^{-1})\hat{S}\hat{P}_2 & A_2 - chain \\ \hat{P}_5 & = & \hat{R}_2\hat{P}_1, & \hat{P}_6 & = & \hat{R}_2\hat{P}_2 & B_1 - chain \\ \hat{P}_7 & = & (\hat{T}_c^{-1})\hat{S}\hat{P}_5, & \hat{P}_8 & = & \hat{S}\hat{P}_6 & B_2 - chain \end{array} \tag{5.61}$$

where the operation T_c is the translation by the vector $c\hat{e}_c$. In the 3rd column the labels of the chains, containing the planes in the two first columns, are listed.

For convenience, we give below the actual form of this operators in the representation in

the homogeneous 4D space (see e.g. [5]):

$$P_1 = \begin{pmatrix} 1&0&0&0\\0&1&0&0\\0&0&1&0\\0&0&0&1 \end{pmatrix}, \quad P_2 = \begin{pmatrix} -1&0&0&-\frac{1}{2}a\\0&-1&0&-b_1\\0&0&1&\frac{1}{2}c\\0&0&0&1 \end{pmatrix}, \quad P_3 = \begin{pmatrix} -1&0&0&0\\0&-1&0&0\\0&0&1&\frac{1}{2}c\\0&0&0&1 \end{pmatrix}, \quad P_4 = \begin{pmatrix} 1&0&0&\frac{1}{2}a\\0&1&0&b_1\\0&0&1&0\\0&0&0&1 \end{pmatrix},$$
$$P_5 = \begin{pmatrix} -1&0&0&0\\0&1&0&0\\0&0&-1&0\\0&0&0&1 \end{pmatrix}, \quad P_6 = \begin{pmatrix} 1&0&0&\frac{1}{2}a\\0&-1&0&-b_1\\0&0&-1&-\frac{1}{2}c\\0&0&0&1 \end{pmatrix}, \quad P_7 = \begin{pmatrix} 1&0&0&0\\0&-1&0&0\\0&0&-1&-\frac{1}{2}c\\0&0&0&1 \end{pmatrix}, \quad P_8 = \begin{pmatrix} -1&0&0&-\frac{1}{2}a\\0&1&0&b_1\\0&0&-1&0\\0&0&0&1 \end{pmatrix}, \tag{5.62}$$

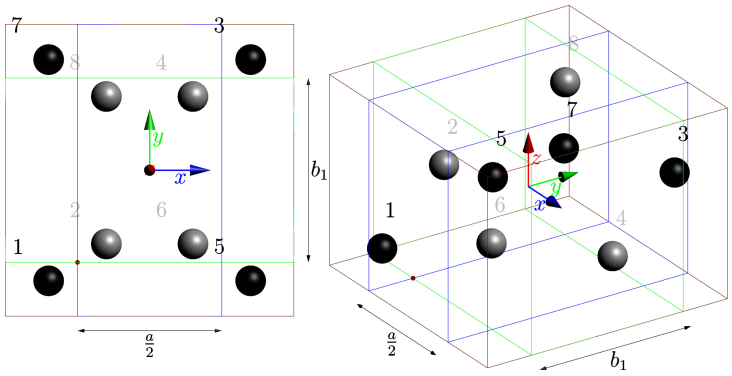

(a) Top View **(b) 3D Perspective View**

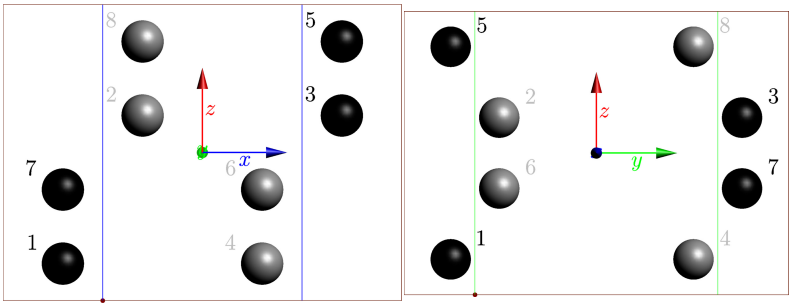

(c) Front View **(d) Side View**

Figure 5.39.: **The symmetry of the atoms inside the unit cell**
The figure shows the symmetry displacements of an atom starting at the position labelled by 1. The enumeration labels are corresponding to the order of the application of the symmetry operators described in text. The black and grey balls are connected by the local (molecular) screw symmetry inside the chains. The atom positions (1,2) relate to the (5,6) by a 180° rotation around the $\hat{e}_b$ axis due to the β-turns inside the β-sheet plane. The axes of the molecular screw displacement are going throw the intersections of the green and blue lines and are parallel to the $\hat{e}_c$ axis.

The result of (5.60-5.62) is the following set of 8 positions of atoms of the same kind:

$$\begin{array}{lcllcll} \vec{r}_1 & = & (x,y,z) & \vec{r}_2 & = & \left(-x-\frac{1}{2}a,\ -b_1-y, z+\frac{1}{2}c\right) & A_1-chain \\ \vec{r}_3 & = & \left(-x,\ -y, z+\frac{1}{2}c\right) & \vec{r}_4 & = & \left(x+\frac{1}{2}a, b_1+y, z\right) & A_2-chain \\ \vec{r}_5 & = & (-x,y,\ -z) & \vec{r}_6 & = & \left(x+\frac{1}{2}a,\ -b_1-y,\ -z-\frac{1}{2}c\right) & B_1-chain \\ \vec{r}_7 & = & \left(x,\ -y,\ -z-\frac{1}{2}c\right) & \vec{r}_8 & = & \left(-x-\frac{1}{2}a, b_1+y,\ -z\right) & B_2-chain \end{array} \tag{5.63}$$

For simplicity, the last two equation are given for the case where $a_1 = a/4$, the generalization can be easily done by corresponding shifting of the molecular chains along the a-axis.

Computation the structure factor of the unit cell. For a given parameter of the standard peptide plane our model of the structure factor has the following minimal set of free parameters:

- dihedral angle Φ,
- the length of the unit cell vector $\vec{b}$,
- the parameters (a_1, b_1) defining the position of the chain A_1 in the unit cell. Where b_1 means the distance between the β-sheets inside a unit cell and $b-b_1$ is the distance between the β-sheets of two neighbours unit cells.
- The length of the OH bonds, which can be a function of the environmental conditions. Alternatively, one can use the length of the unit cell vector $\vec{a}$ as a parameter of the model.

The computation of the atomic positions inside the unit cell is going over the following steps:

Input: (i) The set of free parameters from the list above. (ii) The parameters of the standard peptide plane (e.g. as defined in [30,31])

Output: An array with the atomic positions inside the unit cell

---

1. compute the relative atomic positions of the standard peptide plane from given parameters.

2. evaluate the second dihedral angle Ψ and coordinates of the molecular screw axis $\vec{u}$ using the equations (5.50) and the condition that the angle of the screw rotation $\theta = \pi$. The length of the c coordinate vector of the unit cell is evaluated according to eq. (5.57).

3. compute the coordinates of the chain centre and the translation vector of the screw using eq.(5.58). At this step we are knowing the parameters of the molecular screw transformation from the first plane to the next $\hat{S}_{mol}$.

4. compute the value of the length of the unit cell basis vector a and the coordinates of the directions of the unit cell basis vectors in the local frame P as described by the equation (5.59) and taking in to account the 3rd constraint.

5. compute the position of the residual atom C_β with eq. (5.56).

6. make transformation to the frame of the unit cell and translate the chains (molecular) centre in to the position with coordinates $(-a_1, -b_1/2, 0)$. This is the position of the lower-left chain A_1. At this step we are know the atomic coordinates of the lower plane of the chain A_1.

7. evaluate the positions of the atoms in the other planes using the symmetry operations of the molecule $\hat{S}_{mol}$ and of the unit cell (5.60, 5.61 or 5.62) or, equivalently, using eq. (5.63).

Knowing the atomic positions and the atomic form factors $f_\mu(q)$, the structure factor is readily computed as:

$$\left| \sum_\mu f_\mu(|\vec{q}|) e^{i\vec{q}\cdot\vec{r}_\mu} \right|^2$$

where $\vec{r}_\mu$ is the position vector of the atom labelled as μ and f_μ is its form factor.

Variation of the model parameters and their effect. In this section we show effects on the scattering caused by the variation few selected model parameters.

Variation of the dihedral angles Φ. The dihedral angle Φ defines the length of the (c, a) lattice constants and, hence, is responsible for the stretching-compression of the crystallites along the c-axis. For each Φ the configuration of the unit-cell changes so that the length of the H bonds remains nearly constant and the OHN angle takes its value closest to the 180° (means 0° departure from linearity). In our naive model this corresponds to the minimal energy of H-bonds in the unit cell, i.e. a minimal deviation from the linearity for a chosen NO distance (about 2.8 Åfor ambient environment). In the figure 5.40 the left pane shows the dependence of the lattice constants c and a from the dihedral angle Φ. The right pane shows the deviation of the OHN configuration from a linear one. Figure 5.41 demonstrates the effect on the scattered intensity of the 'equator' peak ($hkl = 020/200$) on the left pane and the 'meridian' peak ($hkl = 002$) on the right pane. The movement of the 'meridian' peak mimics the behaviour of the lattice constant c (the red curve in the figure 5.40), but the changes of the lattice constant a is nearly invisible in the stretching range of the silk, the corresponding values of Φ are $|\Phi| \geqslant 142°$. So, the model describes a small Poison effect between relating the c and a constants but it will be very difficult to observe in the *in situ* X-ray scattering experiment. On the other hand the length of the b lattice constant is the main factor specifying the position of the 'equator' peak but it remains free in our model and is defined mostly by the minima of the Van der Waals interaction. In our study the length of the b is a free fit parameter.

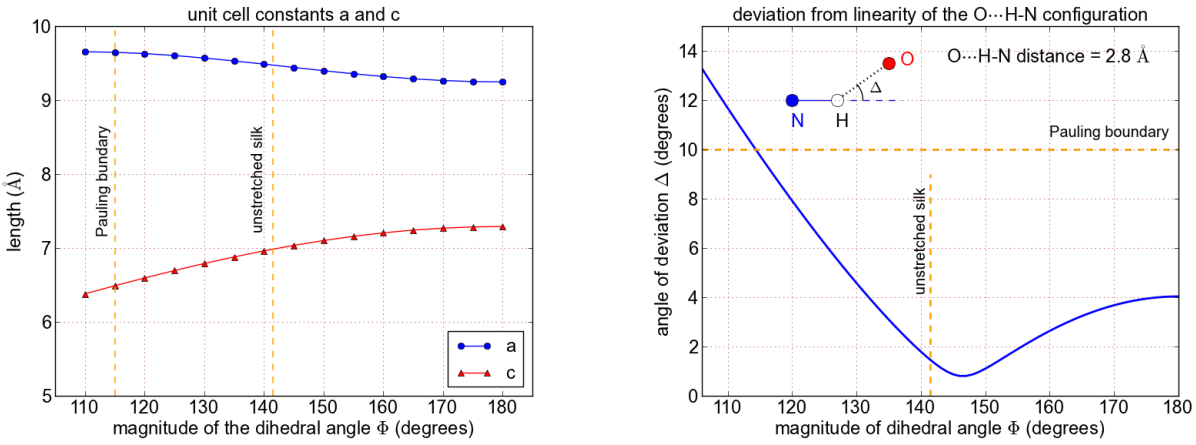

Figure 5.40.: **Unit cell geometry as a function of the dihedral angle Φ**
The figure shows the variation of the unit cell constants (on the left pane) and the angle Δ, describing, the departure from the linearity of the $O\cdots H-N$ configuration (on the right pane) as a functions of the dihedral angle Φ. For convenience we show the absolute value of Φ on the abscissa (Φ is negative). The insertion on the top of the right pane sketches the definition of the angle Δ used as measure of the deviation from the linearity of the H-bonds in the β unit cell.
The values of the internal cell constants was chosen to be: $a_1 = 3.0$ Å, $b_1 = 4.2$ Å, see fig. 5.37 for geometry of the unit cell. The other fixed parameters of the model are: $b = 8.5$ Å, L,M,N = (7,9,32), fibre orientation 7.98° and the Gaussian as OPDF with the variance (width) 17° and the mean (offset) 0°.

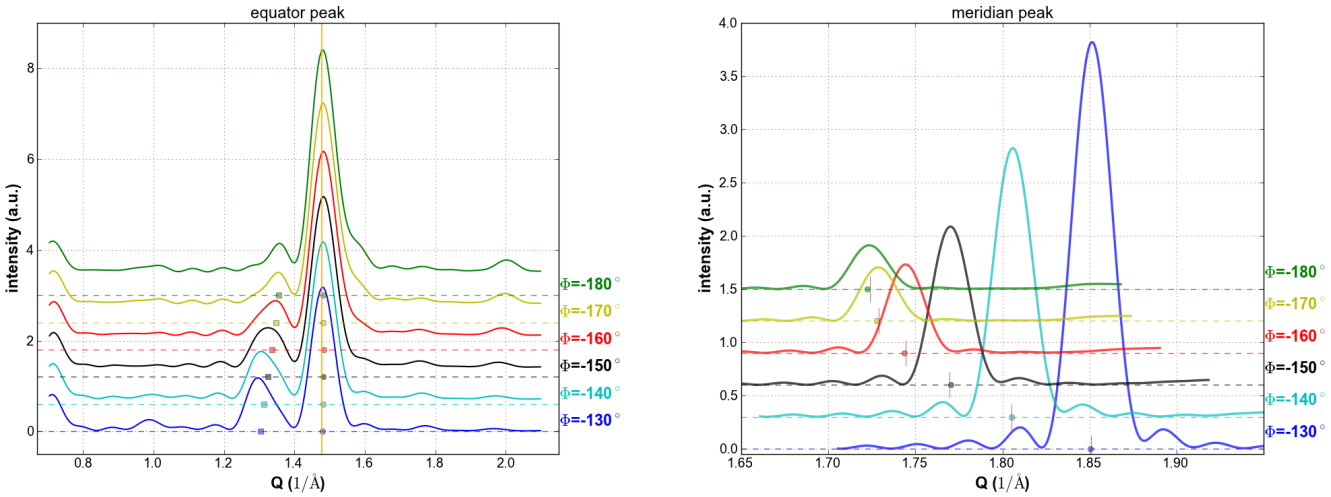

Figure 5.41.: **Integrated intensity as function of the dihedral angle Φ**
The figure shows plots of the integrated intensities for several values of the dihedral angle Φ. The equator peak is shown on the left side and the equator peak ($hkl = 002$) on the right side. The integration was done over the interval $90 \pm 5^\circ$ for the 002 peak and of $\pm 20^\circ$ for the equator peak of the azimuthal scattering angle ϕ. The fixed model parameters were chosen as in fig. 5.40. The dashed lines shows zero-levels for each curve and dots (squires) on these lines are positions of the peak maxima. The orange line on the left pane shows the theoretical position ($4\pi/a$) of the 020 reflection. The short brown lines on the right pane shows the position ($4\pi/c(\Phi)$) of the 002 reflection.

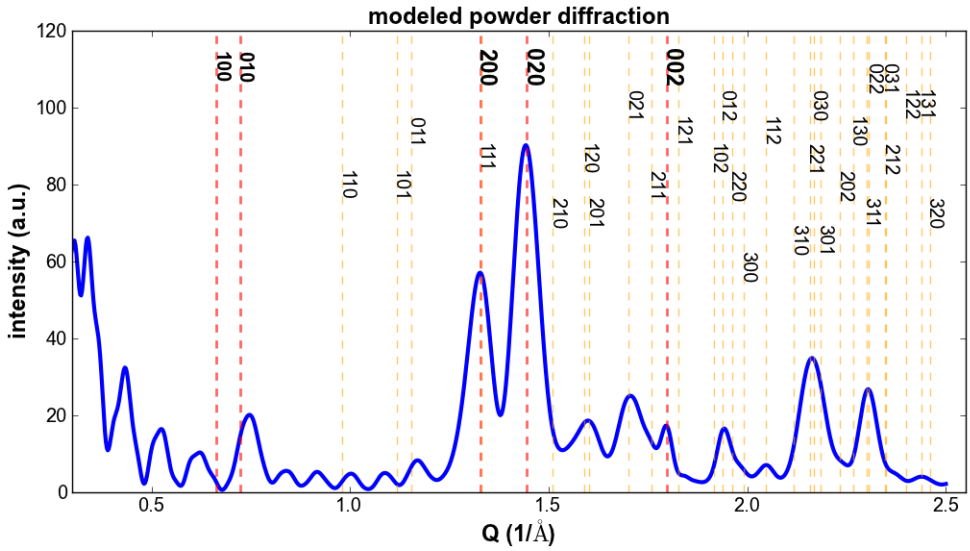

Figure 5.42.: **Computed powder diffraction**
The figure shows the powder diffraction image computed with the model configured as: $(L,M,N) = (7,9,28)$, $\Phi = -142.0°$, $b = 8.7$ Å, $b_1 = 5.0$ Å, $a_1 = 2.3674$ Å. The geometrical minimization yields: $a = 9.47$ Å, $c = 6.99$ Å and $\Psi = 139.385°$, H bond depature from linarity is 1.347°. The dashed lines shows the location of the reflections and are labeled with corresponding hkl indexes.

The OPDF For convenience we show on the figure 5.42 an example of the computed powder diffractorgramm together with the location of the reflections and their hkl indexes. The easiest visible effect of the anisotropic orientation distribution of the crystallites in the fibre is demonstrated in the figure 5.43. The figure shows three diffraction images computed for the same model parameters with the exception of the width of the OPDF. It is ready visible that with increasing the width of the distribution the peaks spreading out in the both (radial and azimuthal) directions. Additionally, the 002 peak is loosing intensity. This means that the width of the OPDF can be directly estimated from the measured diffraction image. Additionally, the bottom peak of the 002 reflection is appearing with the widening of the OPDF. As it can be concluded from the comparision of the figures 5.43(a,b) and 5.44(a,b) the shift of the mean value of the OPDF yields a similar effect but with additional deformation of the reflections equi-level contours. In the last case the spreading effect is caused by the splitting of the each reflex into the two peaks, this is visible in the second row (b,d) of the figure 5.44.

Another effect of the OPDF is the drift of the 002 with the broadening and/or shifting the mean of the OPDF. Figure 5.45 illustrates this phenomenon on the example of the integrated scattering intensity curve for 'meridional' 002 and 'equatorial' 020/200 peaks.

This effect is a simple consequence of the scattering geometry as it is demonstrated by the sketch in the figure 5.46 and can be formulated as follows. The peak maxima of 002 reflection appears for vector of impulse transfer $\vec{q}$ which projection on the crystallite $\hat{c}$ axis satisfies the interference (Bragg) condition $4\pi/c$. The optimally oriented crystallite is when the Bragg condition above is satisfied by the $q = 4\pi/c$. For the crystallites rotated away from the optimal orientation this condition is yields by a larger q.

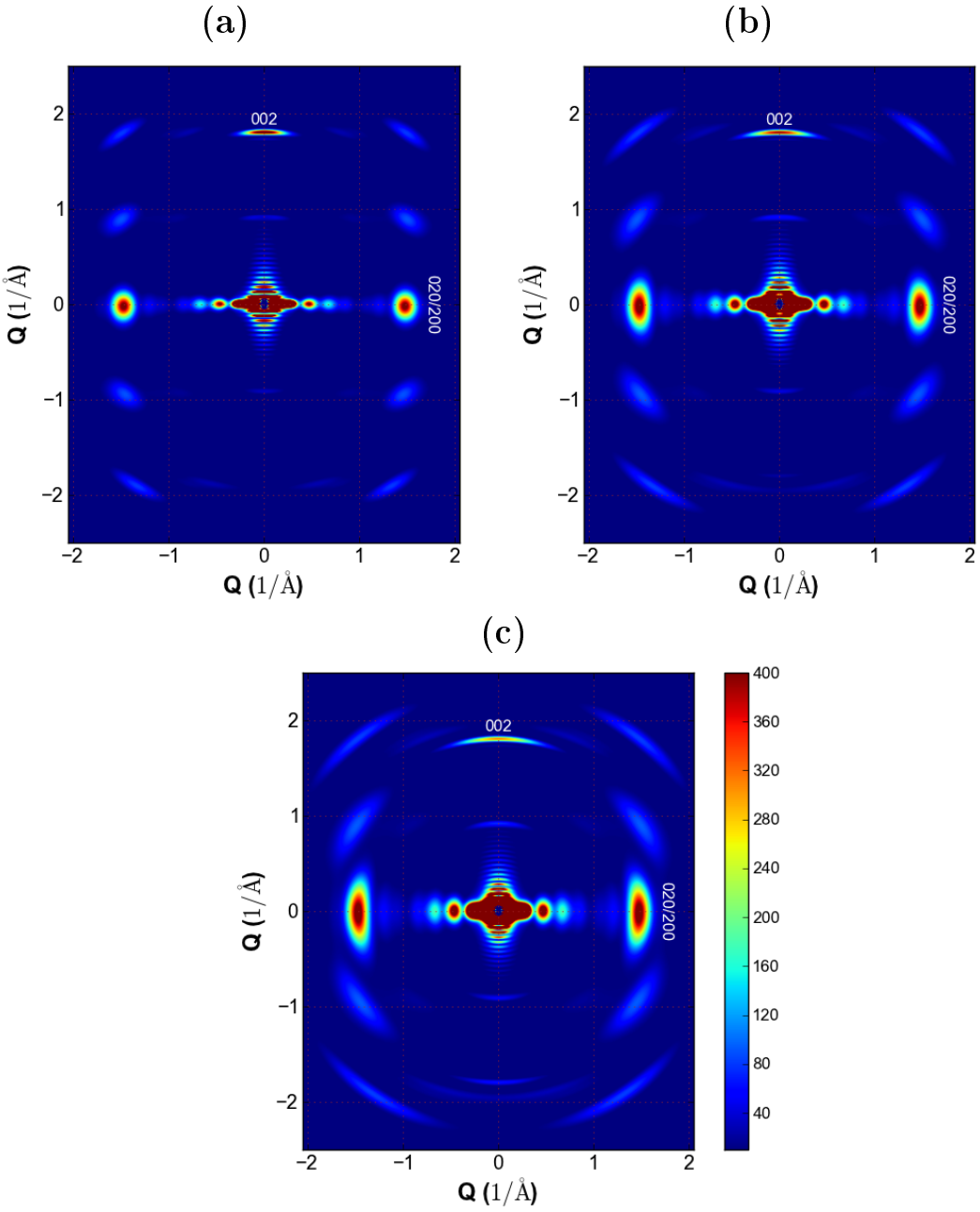

Figure 5.43.: **Computed diffraction image for several widths of OPDF with mean equal** $0°$**.**

The figure shows three diffraction images computed for the model with the same parameters with exception one – the width of the OPDF. Which is chosen to be (a) $\sigma = 7°$, (b) $\sigma = 12°$ and (c) $\sigma = 17°$. The computation is done for a tilted fibre (about $8°$).

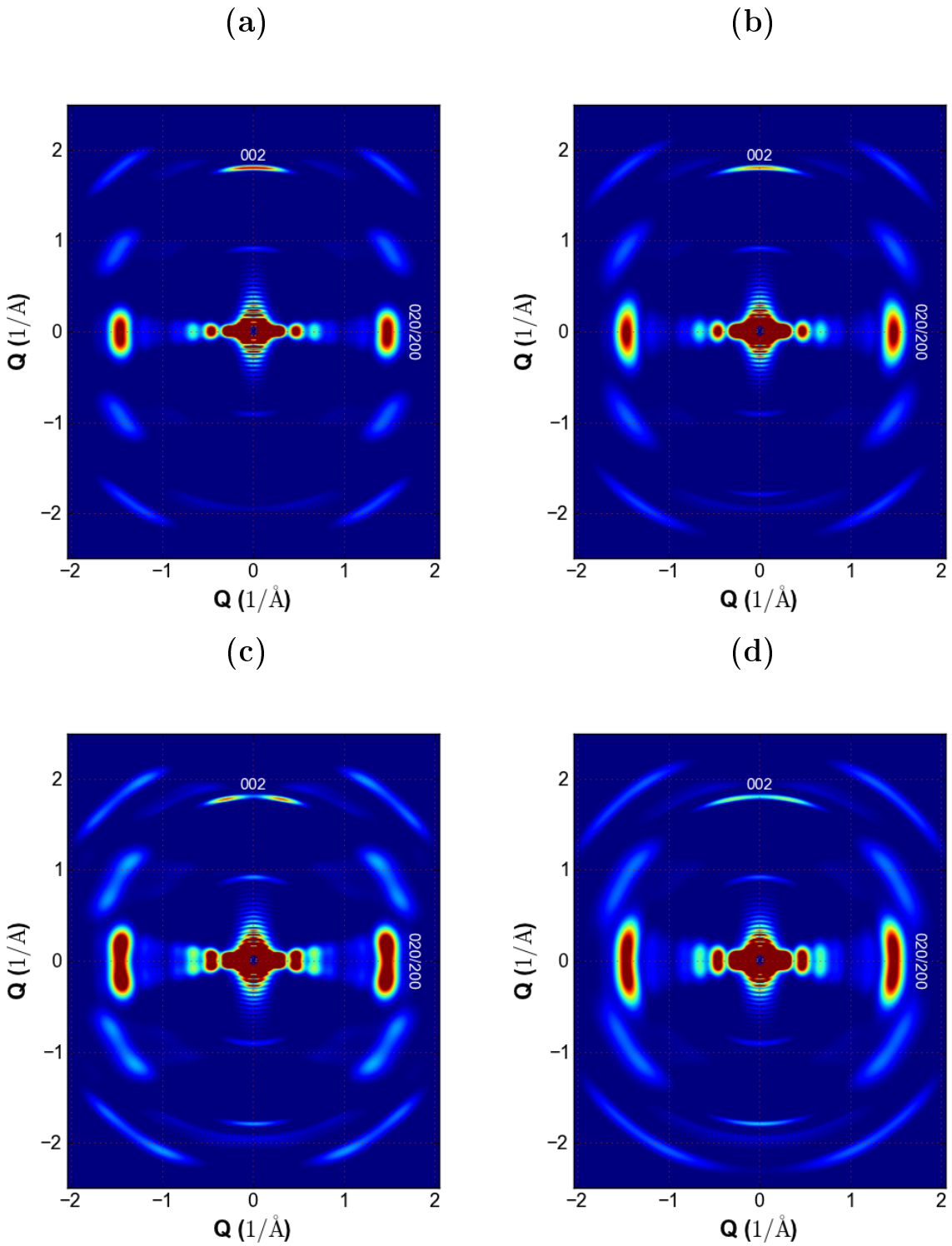

Figure 5.44.: **Computed diffraction image for two width of OPDF with mean equal** $5°$**.**

The figure shows three diffraction images computed for the model with the same parameters with exception two – the width and mean of the OPDF. Which is chosen to be (a) $\sigma = 7°$ and mean $5°$, (b) $\sigma = 12°$ and mean $5°$, (c) $\sigma = 7°$ and mean $10°$, (d) $\sigma = 12°$ and mean $10°$. The colour scale is the same as in figure 5.43. The computation is done for a tilted fibre (about $8°$).

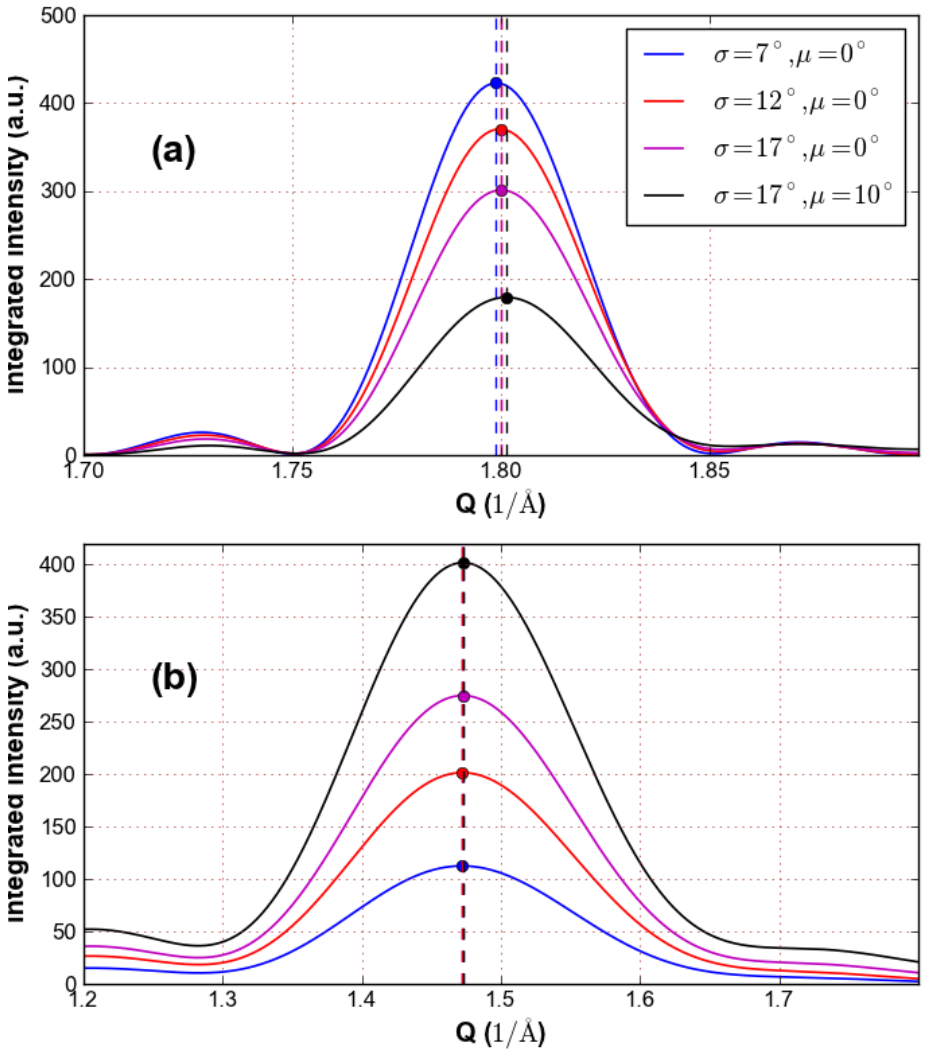

Figure 5.45.: **The drift of the** 002 **with the broadening of the OPDF**
The figure shows the integrated intensity of the **(a)** 002 reflex and **(b)** 020/200 reflex for several values of the width (σ) and mean (μ) of the OPDF. The location of the maxima is pointed by the dashed line of the same colour as the curve. The drift of the position of the maxima is clearly visible for the 002 reflex. All this curve are cake-integration of the of the corresponding computed diffraction images from the figures 5.43 and 5.44.

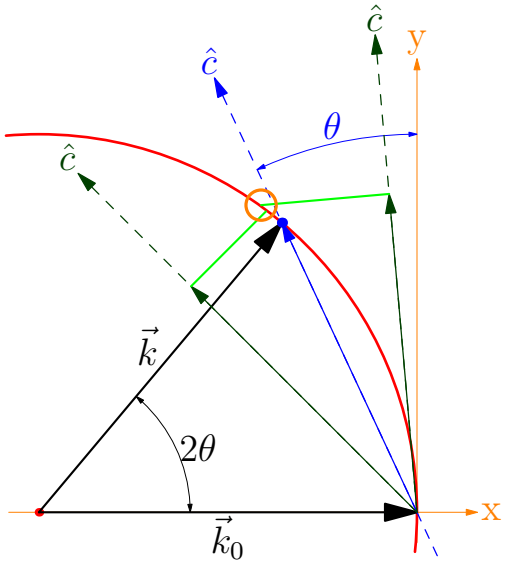

Figure 5.46.: **The geometry of the effect of drifting of the** 002 **reflex**
The figure illustrates the effect of enlarging of the value of the scattering impulse transfer vector due to the rotation of the crystallite away from the optimal orientation. The large red circle represents the Ewald sphere, the black arrow labelled as $\vec{k}_0$ represents the impulse of the incident beam. The black arrow $\vec{k}$ represents the impulse of the scattered beam by the optimal oriented crystallites, i.e. the orientation where the Bragg condition ($|\vec{k}-\vec{k}_0| = 4\pi/c$) is satisfied. The dashed arrows are the directions of the c-axis of crystallites: optimal oriented is represented by the blue arrow and rotated away from the optimal orientation are represented by the dark-green dashed arrows. The solid dark-green and blue arrows represented crystallites Bragg vectors ($4\pi\hat{c}/c$). It is evident that the scattering condition for the dark-green arrows are satisfied for the vectors $\vec{q}$ larger than for the blue arrow. On the figure this is marked by the small orange circle.

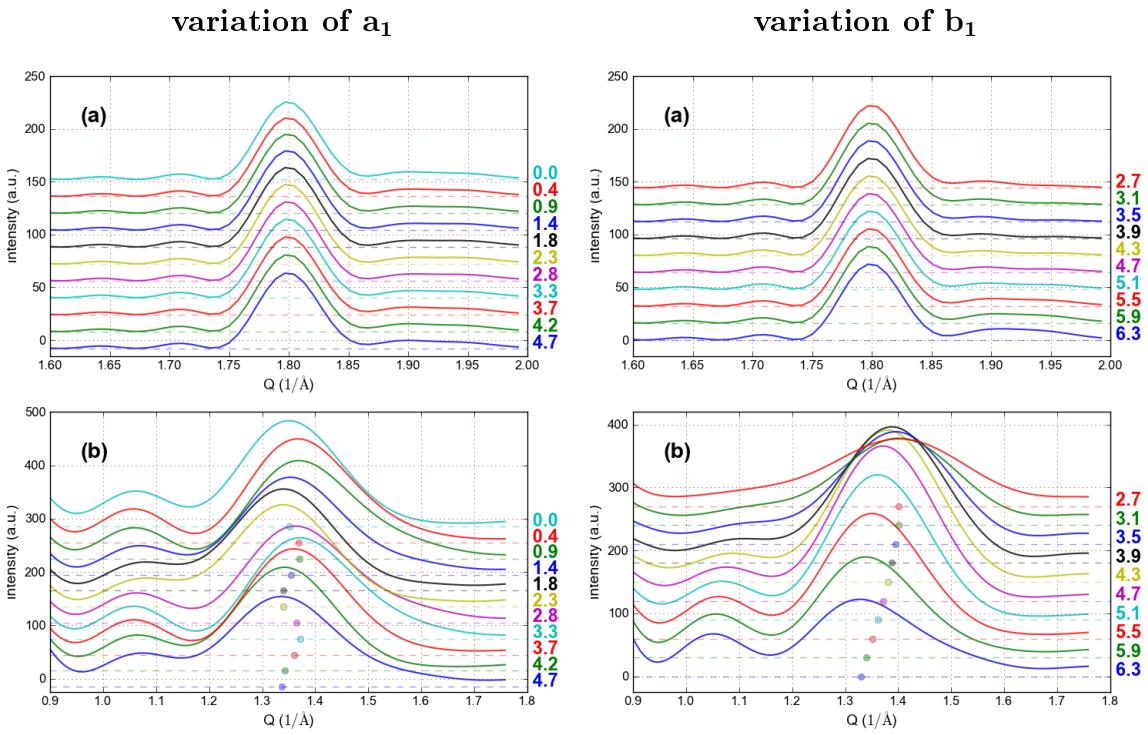

Figure 5.47.: **The effect of the variation of internal parameters** a_1,b_1
The figure shows the scattering intensities of the meridional 002 (a) and equatorial 020/200 (b) reflexes computed for several values of the a_1 (the left pane) and b_1 (the right) pane with other parameters of the model holding fixed. The values of the varying parameter are shown on the right of the corresponding plot in the color the corresponding curve. The colored points on the plots for equator peak plots (b) on the left and right panes represented the location of the peak maxima for the curve of the same colour.
The fixed parameters are: fibre tilt angle $\theta_f = 8.0581°$ (optimal tilt); circular Gaussian as OPDF with $\sigma = 17°$, $\mu = 0°$; $\Phi = -142°$ and $\Psi = 139.39°$; a,b,c = $(9.47, 9.0, 6.99)$ Å. Additionally we choose $b_1 = 5.5$ Åfor the variation of a_1 and $a_1 = 0$ Åfor the variation of b_1.

The variation of the internal unit cell spacing parameters a_1,b_1 The internal parameters of the unit cell a_1, b_1 (see fig. 5.37) influence the configuration of atom position in the $a - b$ projection without change the size of the unit cell. Hence the affected the interference in these directions. The figure 5.47 shows an example of such effects on the meridional 002 and 020/200 reflexes. As it clearly visible the variation of this parameters affected mostly the form and position of the equatorial peaks.

5.2.8. Application of the model from section 5.2.7 to a measured data

To apply our model to real data from *in situ* X-ray scattering experiments the following is assumed:

- The shape of the orientation distribution density function (OPDF) of crystallites in a silk fibre is taken to be of Gaussian shape:

$$\rho(\theta) = A \exp\left(-\frac{(\theta-\theta_0)^2}{2\sigma_\theta^2}\right) \tag{5.64}$$

  where $\theta \ \mathbf{mod}\, 2\pi$ is the angle of the crystallite's orientation, θ_0 describes the angular offset[6], σ_θ is the width of the angular distribution and A is the normalization factor.
- The signal is assumed to result from scattering events from an ensemble of crystallites with different size.
- For the stretched (and hence, relaxing) fibre we will follow a stress ensemble hypothesis, i.e. we assume that there is a distribution of stress (along the fibre axis) over crystallites. Generally speaking, an increase of strain cause a relaxation processes in the fibre which in turn leads to a broadening of the stress distribution. This is especially true, when the protocol includes a continuous variation of strain.

Thus, for the description of the scattering intensity of relaxed fibres we will apply the ensemble model, defined as:

$$I_{ens}(\vec{Q}) = \sum_{L,M,N} A_{L,M,N} I(\vec{Q},\{L,M,N\}) \tag{5.65}$$

where $\{L,M,N\}$ denotes the number of unit cells in the directions $\vec{a},\vec{b},\vec{c}$, respectively. $I(Q,\{L,M,N\})$ is the scattered intensity averaged over the OPDF of individual crystallites of the size L,M,N. The intensity is a function of the model parameters described in the previous sections[7]. The above-mentioned parameters have to be fitted with non-linear minimization procedures. The weights $A_{L,M,N}$ are adjusted by a linear least squares fit at each call of the intensity function $I_{ens}(Q)$.
Figure 5.48 shows an example of a simultaneous fit of this ensemble model to the reflections (002), (020/200) of the relaxed fibre (with no stress applied). Here, for demonstration

[6] This parameter will be initially assumed to be zero. Generally, it is responsible for the shape of the reflexion and slightly correlated with the width of the distribution σ_θ

[7] for motivation and models setup see pages 193ff, for the algorithmic description of the averaging over the OPDF and the calculation of the structure factor see pages 200 and 217

purposes the size distribution is chosen to be broader than usual: $N \in [3-33]$ and L,$M \in 2-12$. The results of such fits show that only scattering intensities from the $N \in [14-20]$ (mean value about 18) and L,$M \in [3-8]$ (mean value about 5-7) contribute. Scattering from very small crystallites, i.e. $N \in [2-8]$ and L,$M \in [1-3]$, only adds to the background and can be neglected in further analysis. Thus, the resulting size of silk crystallites is about $100-150$ Å in the fibre-direction and about $50-80$ Å perpendicular to it. The resulting width σ_θ was about $7-10°$ and the size of the unit cell about $\{a,b,c\} = \{8.5, 9.6, 6.99\}$ Åwith a corresponding dihedral angle Φ of about 145°.

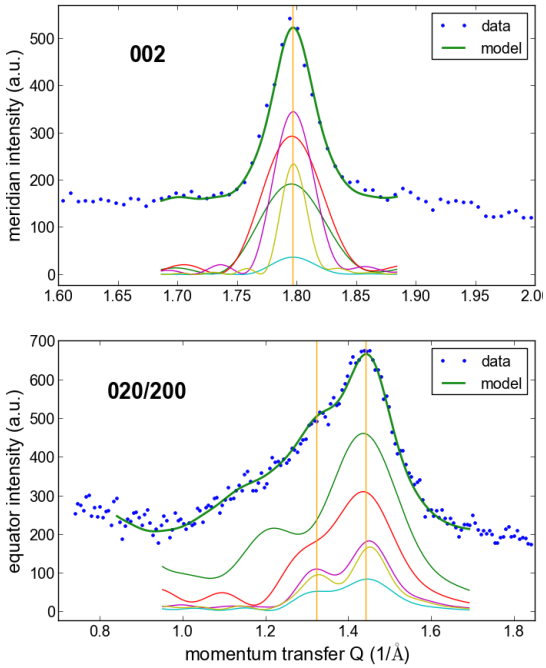

Figure 5.48.: **Fit of the size-ensemble model to two reflections of relaxed silk** The blue points represent the measured data and the thick red line represents the fit. The lines at the bottom of plots show the main contributors from a set of crystallites distributed over sizes $\{L,M,N\}$, with L,$M \in [2-12]$ and $N \in [3-33]$. For convenience, their amplitudes were magnified by factor 3. For the purpose of clarity, some of the lines as well as the background lines are not shown. The colour of lines corresponds to the size of the crystallites, expressed by L,M,N, as: green - [2,4,13], red - [4,5,14], cyan - [5,6,20], magenta - [5,7,21], yellow - [5,8,33].

In the following we will apply the model to the definition of the elastic modulus of the silk crystallites from the *in situ* X-ray scattering experiments. At each value of the external stress σ the scattered intensity curves of the 002-peak is fitted with our model and so the peak position and, hence, the lattice d-spacing in the $\hat{c}$ direction will be determined. Thus,

as a result of this procedure the values of the crystallite elongation ϵ_{002} as a function of the applied stress σ are obtained. Then, the crystallite modulus is defined from the linear fit $\sigma \sim \epsilon_{002}$. The proportionality coefficient is the required elastic modulus G_c. Before we go further, we have to note, that there is a pronounced effect of the peak broadening as the applied stress is increased. This effect is illustrated in figure 5.49, where two 002-reflections corresponding to a two different stress values (5 and 235 MPa) are shown (blue points). In our model such a broadening is mostly due to (i) a reduction the crystallite size (breaking of crystallites) or (ii) a broadening of the strain distribution over the crystallites. The latter is more realistic, it can be caused by relaxation processes in the amorphous host matrix. The first hypothesis assumes the reducing of the crystallite size, e.g. due to breaking of the crystallites. But the width (and shape) of the 002-peak recovers after removing the stress and, even so, after the fibre breakage. Hence the crystallites cannot be destroyed by the applied force.

This leads us to favour the second hypothesis, which assumes that, at each value of the applied stress σ there is a (time and location dependent) variation of the internal stress exerted by the crystallites in the fibre. Because the shape of the strain distribution is unknown, we will use a statistical approach, where the mean elongation of crystallites is defined as follows:

- Instead of adjusting the value of the dihedral angle Φ (which is responsible for the crystallite elongation) by the non-linear model fit, the scattered intensities will be calculated for a representative set $\{\Phi_k\}$ of the dihedral angles.
- Then weighting coefficients A_k, describing a degree of the contribution from each member k of the above-mentioned set, are defined by a linear least-squires fit to the data points.
- When the values of the coefficients A_k are determined, they can be used to estimate the mean value of the dihedral angle.

This means that equation (5.65) has to be modified as[8]:

$$\left\langle I(\vec{Q}) \right\rangle_{\Phi} = \sum_{\Phi_k} \sum_{L,M,N} A^k_{L,M,N} I_k(\vec{Q},\{L,M,N\}) \tag{5.66}$$

where $\left\langle I(\vec{Q}) \right\rangle_{\Phi}$ denotes the scattered intensity, averaged over the distribution of the dihedral angles; $A^k_{L,M,N}$ are the weighting coefficients to be fitted. k is an index running over the set of the values $\{\Phi_k\}$. The meaning of the function $I_k(\vec{Q},\{L,M,N\})$ and other

[8] do not confuse coefficients $A^k_{L,M,N}$ with A_k.

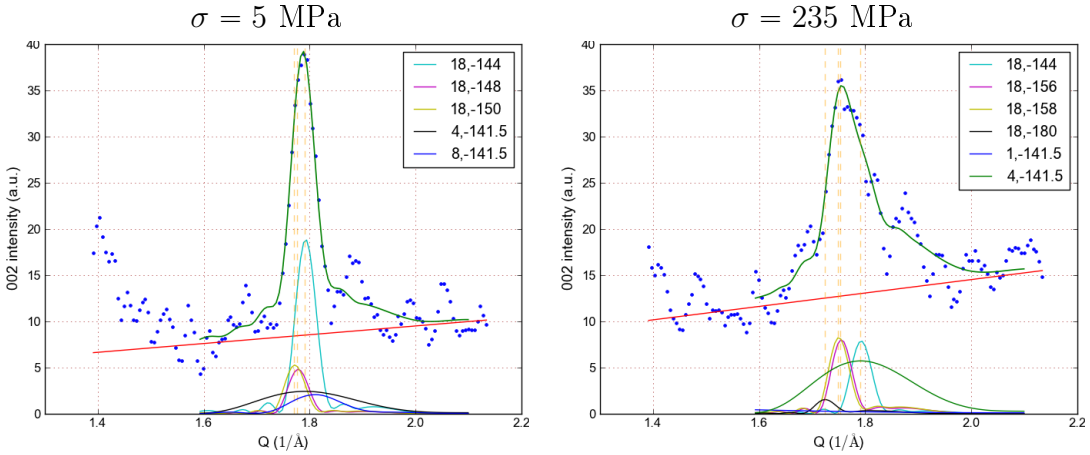

Figure 5.49.: **Stress ensemble fit of the** 002**-peak**
002-reflections of a single silk fibre for two values of stress are shown. To account for the possible crystallite breakage and the distribution in the stress inside the fibre the data are simulated as an ensemble of differently stressed crystallites of different size. The blue points represent the measured data, the background is given by the straight red line and the green line represents the fit. The lines at the bottom of the plots show the main contributors which are documented in the plot legends by the number of the unit cells in the $\hat{c}$ direction and the value of the dihedral angle Φ (degrees) which is responsible for the elongation state of a single crystallite. The yellow (vertical) dashed lines mark the position of the maxima of the main contributors.

parameters is the same as in the equation (5.65). The weights A_k, measuring the contribution from a specific value of Φ_k to the intensity, as well as a probability $P(\Phi_k)$ to find a crystallite with the elongation corresponding to Φ_k are defined as follows:

$$A_k = \sum_{L,M,N} A^k_{L,M,N} \tag{5.67}$$

$$P(\Phi_k) = \frac{A_k}{\sum_k A_k} \tag{5.68}$$

The values introduced above are functions of the applied stress σ. For each value of σ the mean value of Φ and, hence, the mean elongation of the crystallites is defined as an average value:

$$\langle \Phi \rangle = \sum_k P(\Phi_k)\, \Phi_k \tag{5.69}$$

The elongation of the crystallites corresponding to this mean value of the dihedral angle is the desired mean elongation.

Figure 5.49 shows two examples for the above-described fit procedure and figure 5.50 the resulting relation of stress to the crystallite's elongation ϵ_{002} from which the elastic modulus

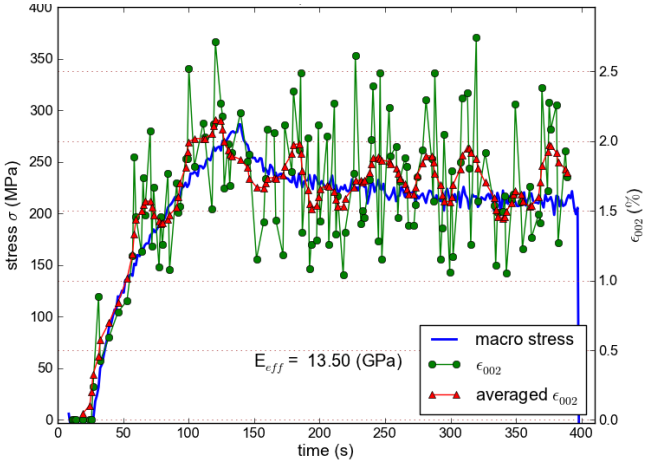

Figure 5.50.: **Stress-response curve compared with ϵ_{002}**
The solid blue line shows a typical stress-response curve of a single silk fibre (left scale). The green symbols give the crystalline uni-axial strain ϵ_{002} (right scale), as determined from the meridional 002-reflection. The red symbols represent the smoothened version of the curve given by green symbols. The effective crystallite elastic modulus $G_c = 13.5 \pm 1.8$ GPa is determined from the linear fit of the proportionality coefficient.

can be determined. The most interesting result of this analysis concerns the fact that the determined moduli are about 1.5 times smaller that the values resulting from the usual procedure, described on the pages 164ff. For the intermediate RH = 23% (RH for the example shown in figure 5.50) the elastic modulus resulting from our model is 13.5 GPa while the usual approach gives 24.5 GPa. Such a reduction of the elastic moduli is due to the dependency of the scattered intensity of an individual crystallite from the state of its elongation. Indeed, the amplitude of the scattering intensity decreases with increasing of elongation. This effect is illustrated in figure 5.41. The source of this behaviour is the variation in the interference caused by an internal rotation of the protein chains in the crystallite during the elongation. As consequence, the 002 reflecton intensity scattered from the individual crystallite decreases with the increase of elongation. In our statistical approach the abovementioned effect results in the larger values of weights A_k for elongated crystallites in comparison with the models, where intensities are independent from the state of elongation.

It is interesting to note, that molecular simulations, which are based on dispersion forces, predict values of the elastic modulus from 13 GPa to 16 GPa [113,159,160][9], which are very close to our finding. A further study is desirable with the aim to resolve this discrepancy between the results from the usual approach and our model.

[9] in [113] the value 10 GPa is reported.

6. Discussion

Here we discuss the experimental and theoretical results presented above in the framework of a new general model of the mechanical properties of silk. We introduce additional results from complementary experiments and put them into perspective.

6.1. The general characterisation of the mechanical properties of silk

A short recapitulation of the relevant morphology of silk is given, followed by the general characteristics of the mechanical response of silk. This is done in relation with our measurements and their theoretical description. The latter will be discussed in the following sections.

Morphology and structure

Generally, silk is a composite, hierarchically structured material with a nested, interleaved structure. On the mesoscopic level silk consists of polycrystalline regions embedded in a (more or less) amorphous polymer (peptide) matrix.

At the molecular level the main building block of silk fibres is the polypeptide chain composed of two sub-chains: fibroin-H and fibroin-L. The first sub-chain has an almost periodic pattern $(-Ala-Glu-)_n$ (see the whole code in the figure 1.7) and participates in the crystalline regions of silk. The other sub-chain, with a less ordered code (see fig. 1.6), participates in the amorphous matrix. The backbone structure of these chains is described by the repetition of the so-called peptide plane, amino-acid unit $H_2N-C_\alpha-HCO_2$. These units are joined by peptide bonds between the carboxyl and amino groups of adjacent amino acid residues[1]. We described the morphology of silk in more detail in chapter 1. We adapt a widely used approximation to our purpose. There, the only degree of freedom of a peptide chain is the set of dihedral angles between the peptide units (called Φ and Ψ)[2]. The

[1] see figures: fig 1.2 on page 8, fig 5.30 on page 202 and fig 5.33 on page 205.

[2] see e.g. figures: fig. 1.4 on page 10 and fig. 5.31 on page 202.

third dihedral angle (called Ω) together with the length and angles of the covalent bonds remains unchanged in all conformations the chain takes in variable chemical and physical environments (see e.g. [22, 31, 134]). This allows us to introduce the so-called "Standard Peptide Plane Model" of the peptide unit above with the well-defined parametrisation [31] taken from a large amount of existing experimental data [3].
The crystalline parts of silk consist of small β-sheet crystallites with a characteristic size of about 10 nm. As the name suggests, they are constructed by stacks of parallel β-sheets consisting of parallel polypeptide sub-chains connected laterally by hydrogen bonds. The planes are held together by Van der Waals forces. One of the vectors, spanning the unit cell, ($\vec{c}$) is along the aligned molecular sub-chains. The β-sheets are parallel to the plane, defined by the vectors $\hat{a}$ and $\hat{c}$. They are stacked along the direction $\hat{b}$.
We will refer to these facts and notations later.

General characteristics of the mechanical behaviour of silk

The study of the molecular dynamics of silk by our group using *in situ* neutron scattering experiments shows that silk is an elastomer. Its response to an external force has an entropic character [155]. As an elastomer it responds to applied loads by time dependent, strongly dissipative processes. Its viscoelastic behaviour results mainly from slippage[4] between groups of long polypeptide chains and rotations around joints between the (more or less) rigid chain monomers, i.e. amino-acid units. The slippage is mostly responsible for the mechanical behaviour of silk on the long-time scales (order of hours or days) and the internal rotation is manifested mainly at moderately long time scales (order of seconds and minutes). For a more detailed discussion the reader is referred to chapter 2 (pp. 60 ff, 66 ff). All our viscoelastic models applied and/or constructed in this work are built on the basis of the above-mentioned observations and obey the laws of non-equilibrium thermodynamics.
Here we give a short summary of the general characteristics of the silk's behaviour on moderate time scales with the help of the response to a strain excitation in the cyclic tooth form (for definition see our stimuli catalogue on the page 29). Additionally, a discussion is given on page 168. Figure 6.1 sketches the characteristic properties of the silk behaviour in such experiments. The olive curve shows the behaviour of the native sample, i.e. sample without previous stretching history. Through the raising part of the stretching curve the response exhibits two yield regions with softening and hardening regimes. The first stretching forces the sample to transit from the native (stable) state to the, so-called, pre-

[3] see detailed discussion on pages 201ff.
[4] translation of a chain or a group of chains relative the other along their main axis.

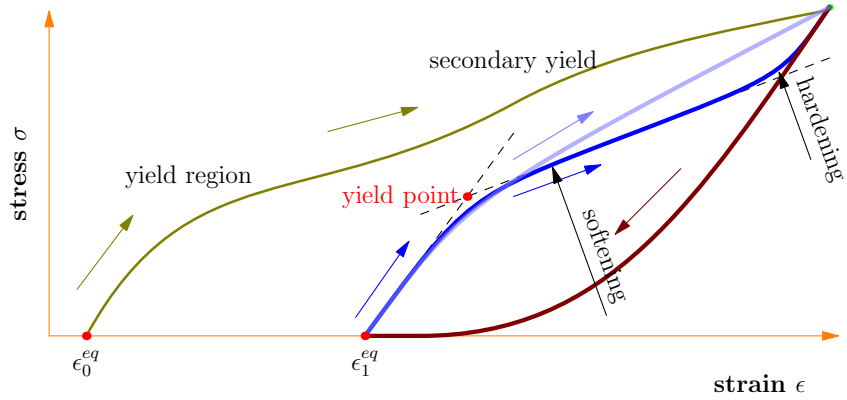

Figure 6.1.: **Sketch of the silks response to a tooth excitation of strain** The olive curve represents the stretching of silk starting from the native state (no stretching history). The blue and light blue curves show the typical response of the pre-stretched silk in a wet and dry environment, respectively. The brown curve represents the back path, common to all stretching states. Arrows show the direction of the strain change: elongation or contraction. $\epsilon_0^{eq} - \epsilon_1^{eq}$ is the relative elongation of the sample through the transition from the native to the pre-stretched state. Compare with figures 5.15 and 5.16.

stretched state. The latter is metastable by its nature but the characteristic time of its dissipation processes is much longer than the time of the measurement. The behaviour of the sample on the back path is represented by the brown curve and is approximately the same for all stretching states of the sample. At the point ϵ_1^{eq} the sample is (effectively) at rest and, obviously, it is longer than in the native state, marked by the (red) point ϵ_0^{eq}. The response to the raising part of the second cycle of the tooth is represented by blue curves. Their characteristics are strongly dependent on the humidity and the rate of strain. For silk at low and moderate relative humidity (up to about 70%) it is less curved (bent) than in the case of high relative humidity. Surprisingly, the behaviour of pre-stretched silk at moderate humidity allows a very simple description in terms of the linear viscoelastic theory [93]. However, the behaviour of native silk (at any humidities) and pre-stretched silk (at high humidity) are strongly non-linear and show regimes with both a softening and hardening behaviour. Without external force pre-stretched silk shows a tendency to restore its native state (see discussion on pages 168 ff, and figure 5.16). Later, in this chapter (section 6.3), we will discuss this, as well as the ansatz for the phenomenological modelling of the silk behaviour at all humidities, and the transition from the native to the pre-stretched state in more detail. It is well known that silk is very strong at moderately

long time scales: there its response is comparable to that of steel. However, a very weak force applied over a long time interval suffice to break it. This demonstrates very well that stretched silk has no well defined statical/equilibrium state. Another demonstration of the non statical nature of the mechanical response of silk is shown in figure 6.2. There, the response of the silk fibre to a tooth strain excitation with a very small rate of strain, is presented. The mean elongation velocity is 0.18 nm/s. Step 95 was held much longer than the other and the silk sample relaxes over a time interval of about two days.

A more convenient way to study the long-time behaviour is by relaxation experiments. Our measurements show that on large time scales the silk relaxation approaches an asymptotic with an inverse power law $\approx 1/t^{\nu}$. This leads us to assume that the behaviour on such long time scales is mostly due to the slicing/slipping movement of the large part of the molecular chains and that it is realized by processes with memory (non-Debye relaxation). A very good description within the linear fractional viscoelastic theory (section 2.2), is possible. Our application of this theory to the long-time relaxation experiments on silk fibres is discussed in the chapter 5 on page 175 ff.

The dissipative molecular dynamics of silk can be measured by neutron quasi-elastic scattering (QENS). It can be well-described in terms of the fractional theory of the anomalous diffusion. Similar to the linear fractional viscoelastics it is formulated in terms of fractional calculus, which is based on the notion of the fractional derivative (integration) operator. We will return to these experiments in section 6.3.

With the aim to get more detailed information the above-mentioned experiments and theoretical models have to be combined with information on the molecular structure as it can be obtained by X-ray scattering. This approach allows to estimate the elastic moduli of the silk crystallites and also to get a first feeling of the characteristics of the amorphous part of the silk structure, such as its elastic moduli and relaxation times (see chapter 5: pp 173 ff and pp 169 ff) [93].

For the purpose of gaining more information from the measured X-ray diffraction images we developed a new, detailed molecular model and computation procedures for the X-ray scattering intensity from the polycrystalline regions of the stretched silk fibres 5.2.7. A short overview of our approach is given in section 6.2.

Below, we describe three characteristic time scales, which we observe in our stretching experiments:

- short time scales: measurement in milliseconds up to one second. Here the glassy response is visible or by large amplitude of strain the forced folding can be observed.
- moderate time scale: characterized by time intervals from seconds to several minutes. Here classical dynamics and viscoelasticity are the main components of the silk

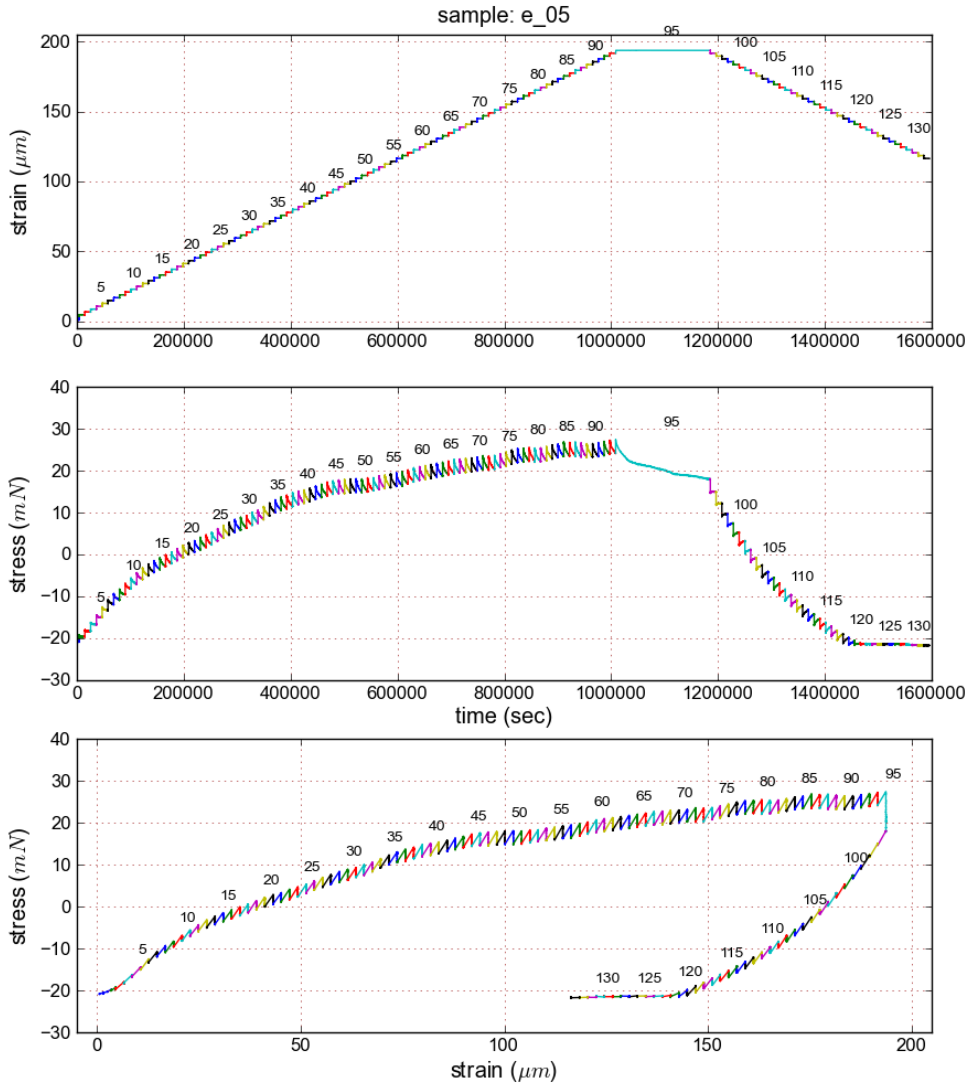

Figure 6.2.: **Response to a very slow (tooth) elongation**
The figure shows the response of a native *Bombyx mori* silk fibre of 1 mm length to a very slow tooth excitation (the average rate of strain is about 0.18 nm/s). The tooth was realized by small steps, each of 2.5μm height and duration of 3 hours. The numbers along the curve show the enumeration of the steps. Step 95 was much longer, 55 hours (more than 2 days). Through the whole duration of the step 95 the sample fibre continues to reduce its resistance to the applied strain. Generally, the shape of the response curve is very similar to the form observed in experiments with moderate strain rates (about some μm/s), i.e. 3-4 order of magnitude faster. The force curve shows two yield regions and the usual form of the curve on the back path. Compare with figures 5.15 and 5.16.

behaviour and the fractional processes are only at their beginning. The viscoelastic behaviour can be modeled either by purely linear viscoelastic models or by using the non-linear dynamical models originating in the Eyring rate theory[5] (see sec. 2.3). On this time scales we assume that the protein folding processes (based on the internal molecular rotation and sliding) are dominant.

- long time scale: characteristic time intervals of hours to several days. Here the fractional character of the silk viscoelastic behaviour becomes visible. On this time scale a dominance of the large scale slipping of the (unfolded) molecular chains can be assumed.

6.2. Crystallite structure of a stretched silk fibre.

Neutron and X-ray scattering experiments belong to the best-suited methods for studing the internal properties of matter on the molecular level. Most of the knowledge about the structure and dynamics of condensed matter stems from such scattering experiments. In our *in situ* scattering experiment we have studied the structure and dynamics of stretched silk fibres as a function of the applied strain. In wide-angle X-ray scattering (diffraction) experiments our main effort was to study the behaviour of the silk crystallites under stress. To this end the specification of the elastic properties of the crystallites offers a possibility to use them as embedded force sensors. This gives us an access to informations about the local stress (distribution) in the silk fibres at a given strain which further allows a more detailed study of the mechanical properties of the amorphous component of the silk fibres.

Lattice strain and the elastic modulus of crystallites.

Here we review the procedure for extracting information about the lattice deformation under applied stress from the X-ray diffraction images. In spite of a lack of justification it is the most frequently used procedure [93, 107, 158–160, 163]. More details are given in sec. 5.2.2 and in the sec. 5.1 on page 154.

An application of external stress to a silk fibre causes a lattice deformation of the β-sheet crystallites embedded in the fibre's amorphous matrix. Due to the direct relation[6] between the position of a reflection peak and the d-spacing in the direction of this peak, the amount of the lattice deformation can be read from the diffraction images. The change in the

[5] Transition State Theory

[6] i.e. Bragg law

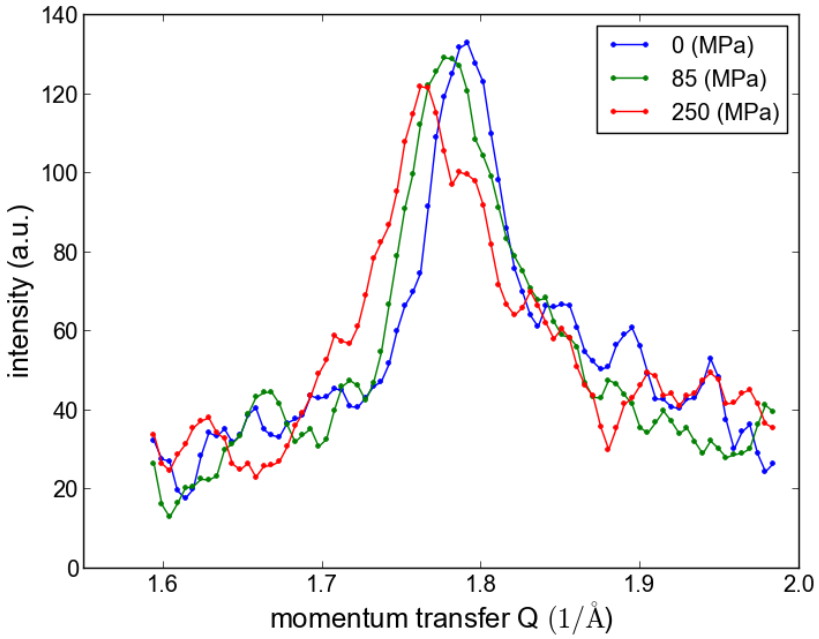

Figure 6.3.: **The shift of the** 002 **reflection with increasing of stress**
Reproduction of the figure 5.5.

spacing of the crystallite lattice can be observed by plotting the corresponding reflection intensity versus momentum transfer. Figure 6.3 shows scattered intensities of the 002 reflection for several values of applied stress, where the effect is clearly visible. Measuring scattered intensity as a function of the applied stress allows to estimate the elastic modulus of the crystallites in the fibre as a linear fit of the lattice elongation against the applied stress. One of the methods for computing the position of the 002 reflection, which is widely accepted in the literature, consists in computing the distribution centre of the function $I(Q)$ or by fit of the shape of $I(Q)$ by a suitable profile function [93, 158–160]. Such an approach can be done under the assumption that either (i) all crystallites in the fibre are under the same stress (very sharp distribution of stress) or (ii) one needs to assume a distribution of the stress/strain over the crystallites ensemble with a finite width. The former assumption is not a very physical one. The latter assumption implies that the scattered intensity from differently elongated crystallites equally contributes to the measured diffraction image.

In such a way we obtained a crystallite modulus of 25 GPa which is consistent with values reported in the literature. On the other hand, it is in contradiction with modules of about 10 GPa resulting from molecular simulations [113]. Some attention was paid to this

contradiction by adapting the theory to the experimental results (see e.g. [159, 160]).
It was observed that stretching (along the fibre axis) of the silk fibres causes a well-observable elongation of its crystallites along their scroll axis $\hat{c}$ but the spacing in the directions normal to $\hat{c}$ remains nearly unchanged, which implies, that the Poisson effect is very small. This behaviour has to be compared with the recently observed behaviour of silk crystallites under (isotropic) high external pressure [94]: pressure-induced changes of the spacing along the $\hat{c}$ axis were much smaller than in the directions normal to it.
The value of the elastic modulus of silk crystallites also depends on the relative humidity (see discussion in 5.2.2 on the page 164). I.e. the elastic modulus decreases with increasing humidity. Because the water cannot enter into the crystallites the softening of the crystallites can be attributed to interface effects. Indeed, the surface/interface effects play a very important role for mesoscopic particles [73, 74].

Further refinement.

To get more information from X-ray diffraction images one needs a suitable parametrization of the form and structure factors of the crystallites in the strained fibre. Additionally, one needs a parametrization of the distribution of the orientations of crystallites, their size/form (or its distribution) and the distribution over the lattice strain in the ensemble of the crystallites in the fibre at a given amount of applied stress. At a given value of applied stress/strain the X-ray scattering intensity, as measured in an experiment, is the average of the intensity scattered from a single crystallite over all possible crystallite orientation, sizes and deformations.
For the further refinement of our data from the *in situ* scattering experiments we developed a new computation model which is based on geometrical minimization and the above-mentioned averaging procedure. The detailed description of the model and its first applications to experimental data is given in the chapter 5 on the pages 193-227. The form of the crystallites is assumed to be brick-like. Hence, the Laue function was taken as a crystallite form factor. The computation of the structure factor for a given elongation of a crystallite in the direction of the c-axis is based on the assumption that the process of the deformation of the lattice is realized by an internal rotations of the molecular chains in the unit cell. Hence, the crystallographic symmetry and configuration of the covalent bonds in the unit cell remain unchanged. The crystallographic symmetry of the silk crystallites is taken from the early studies (see e.g. [107, 163]). The above-mentioned internal molecular rotations are viewed as rotations of the peptide planes connected to each other. The latter are assumed to be rigid, so their planar atomic configuration is known *a priori*. It was

taken from the International Tables for Crystallography, **F** [31].
For every given elongation the optimal rotation is computed using a geometrical minimization under following constrains: the crystallographic symmetry and given elongation. The procedure minimizes the deviation of the H-bonds from their optimal geometrical configuration. After the minimization all atomic position in the unit cell are known, and the structure factor and, hence, also the scattered intensity from a single crystallite can be computed. The computation is based on the Pauling Rules for the peptide planes in the β-structure. The procedure of the averaging over the rotational distribution was heavily optimized using spectral functional methods and algorithms, so the computation of the 512×512 pixels diffraction image for an ensemble of the crystallites of a given size can be done on a desk PC in 5 - 15 minutes.
The model can be used either for simultaneous fitting of a characteristic set of reflections or to fit a complete diffraction image. Free parameters of such fits are the unit cell constants, parameters specifying the distributions over crystallite orientations, size and strain. This information can be further used in the analysis of the macroscopic data of stretching experiments. Additionally, after inclusion of the intermolecular interactions, it can be used as a basis for molecular simulations. In any case, it would be very interesting to compare the results of the model with results of truly molecular simulations.
The model presented above is based on well-established results about geometry and configuration rules for the secondary conformations of peptide chains (particularly for β-sheets) obtained from a large amount of experimental data. No assumption about intermolecular interaction potentials or dynamical properties of the studied system is made. Hence, it can be classified as a computation procedure rather than as a simulation model. The only *ad hoc* assumptions which have to be made concern the specific shape of the orientation- and size distributions.
The model predicts that by stretching along $\hat{c}$ the variation of the spacing in the $\hat{a}$ direction is very small, nearly invisible. This prediction is verified by our measurements. There, the spacing along the $\hat{b}$ axis is a free fit parameter of the model. The other prediction is the dependence of the amplitude and shape of the scattered intensity from the elongation of a crystallite along the $\hat{c}$ axis. This causes a decrease of the value of the elastic modulus resulting from the fits of the model to our data from *in situ* X-ray scattering experiments. A value of about $10-12$ GPa was found, which is about 1.5 times smaller than the modulus obtained from the usual procedure, that is without accounting for the intensity variation. This resolves the contradiction between the measured and simulated values mentioned in the previous subsection. This observation needs to be further studied before it can be considered as finally established.

6.3. Modelling the mechanical properties

The mechanics at moderate time scales

In spite of the complexity of both the structure and the molecular dynamics of silk the (macroscopic) mechanical behaviour of pre-stretched silk fibres can be well-described in terms of the linear viscoelastic theory. This is true for ambient relative humidity (up to about 70%) and for moderate time scales. Under these conditions the measured mechanical response curves can be described with the so-called 'Standard Solid Model' which is the simplest model of a solid body in the framework of the linear viscoelasticity. The relevant aspects of the theory are given in the chapter 2 (pages 19– 39). Our application of the linear viscoelastic theory to the measured data is described in chapter 5 (pages 169 ff). There, to take the semi-crystalline morphology of silk into account, we extend the Standard Solid Model: (i) a separate spring element is included to describe the behaviour of the crystallite and (ii) we re-interpret the dash-pots as frictional dissipation of energy, resulting not only from the amorphous parts of silk, but also from the interface of the crystalline and amorphous regions. This allows us to separate the mechanical properties of crystalline and amorphous phases but also to show their interplay. Using the value of the elastic modulus of crystallites, known from the *in situ* X-ray diffraction experiments, we were in a position to estimate the viscoelastic characteristics of the amorphous matrix.
The model described above failed to describe the behaviour of native silk (at any humidity) and of native/pre-stretched silk at humidities greater than 70%. As symbolically sketched in figure 6.1, the response of silk fibres in a wet environment (represented by the blue curve) and the response of native silk at any humidity (olive curve) exhibit a non-linear behaviour. Hence, if we want a single description of native and pre-stretched silk in a wider range of humidity we are forced to abandon the linearity. The detailed description of our non-linear models together with their motivation is given in the chapter 2 (pages 60 ff) and the results of their application to the behaviour of silk is given in the chapter 5 (pages 180 ff). Here we only give a short summary of our approach.

The foundation of our approach is the Transition State Theory (TST), whose application to viscoelastic phenomena can be considered as a generalisation of the linear viscoelastic theory (see e.g. [33, 146, 147, 167]). It adapts the idea that a deformation of the amorphous component of silk consists of thermally activated processes involving the motion of molecular units[7] (segments of peptide chains) over potential barriers. Hence, new dash-pot elements have to be introduced. They are governed by non-linear laws of thermally ac-

[7] molecular units: do not confuse them with peptide planes mentioned in section 6.1.

tivated processes. Again, molecular movements underlying the deformation of a material can be divided into slipping and folding processes. The slipping processes can be well described by the Eyring-Tobolsky models [146, 147].

Motivated by recent developments regarding protein folding (see the discussion on pages 66 ff) we picked up some old ideas published by Burte and Halsey [14, 15]. They describe viscoelastic deformations in terms of the population dynamic of molecular units undergoing transitions between a few states, each possessing its own length and elasticity. This corresponds to the stochastic modelling of the protein folding given by R. Zwanzig in [186]. The transition from one state to another is described in analogy to the kinetics of chemical reactions (see e.g. [23]), where reaction rates are given by TST. The macroscopic elongation is then defined by the above-mentioned population of states with different elongation of molecular units. This defines the laws for the non-linear dash-pot element, which have to be incorporated into the viscoelastic model to simulate this type of behaviour of the material under study.

We must note here that molecular units, as mentioned above, must be understood in a very averaged sense. Their elongation states should not be taken as separate discrete entities, but rather as an average over a large spectrum of similar states. The main assumption concerns a well defined boundary separating ranges of different degrees of elongation and energy. The conditions of applicability of such few-state kinetics are similar to the two-state kinetics suggested in [186] for describing protein folding.

Generally speaking, such few-state models of elongation replace a large group of folding processes by an averaged one. This elongation process follows a simple scheme, accounting for (at least) three main aspects: (1) an elongation of a material is accompanied by a large number of spatial transformations on the mesoscopic level; (2) the underlying mechanisms are thermally activated processes; (3) an elongation is not endless, i.e. there must be a limiting boundary. Stepping over the latter causes a much stronger response and/or breaking of some molecular chains.

For the purpose of clarity we describe two models in more details:

`Two-state model`: The simplest form of such models is the two-state model, where the amorphous part is considered as consisting of molecular units of the same type. They can occupy two elongation states, say A and B; A denotes the compact (short) state and B denotes the elongated state. The elongation, corresponding to the $A \leftrightarrow B$ transition, is proportional to the population x_B of the species in the state B. This behaviour of the material is simulated in terms of a Maxwell unit with a non-linear dash-pot part and a spring. The spring represents of the contributions from the elasticity of the states A, B and from the crystalline regions. The behaviour of the dash-pot is governed by the rules

of the transitions $A \leftrightarrow B$. Hence, it is a function of stress and population x_B.
This simple model allows surprisingly good descriptions of the mechanical response of the pre-stretched silk fibres over the whole range of humidity!

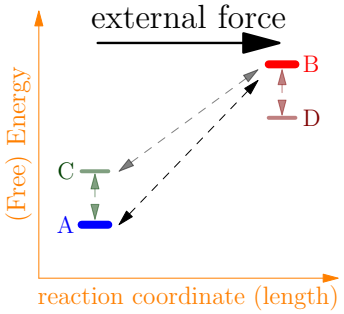

`Three-state model`: To describe the behaviour of silk in the native stretching state we require an additional state, say C, which can be characterized as pre-molten or pre-activated. The molecular units in this state have the same length as in the state A, but the energy level of state C must be higher than that of the state A. The scheme is sketched in the figure on the left-side, where state D is reserved for later use. This new state (C) can be thought of as describing the molecular units in a conformation as compact as in the state A but with some H bonds broken. The barriers separating the state C from the states A and B have to be chosen to provide reaction rates $A \leftrightarrow C$ which are much smaller than that of the processes $A \leftrightarrow B$ and $C \leftrightarrow B$. On the other hand the rates of the reaction $C \leftrightarrow B$ must be larger than that of the reaction $A \leftrightarrow B$. Note, that the $A \leftrightarrow C$ transition is independent of the external stress, because it exhibits no elongation.
This model accounts for: (1) the notion of the native and pre-stretched sample states, (2) the appearance of the secondary yield point (in the stretching path from the native state) and (3) the transition from the native state to the pre-stretched state and back. As in the two-state model the elongation of the dash-pot is controlled by the population of the elongated state B. The principle of the model can be demonstrated with the following simplified scheme:

- The native state is characterized by the equilibrium population of states A, B and C (without external perturbation). By stretching of the sample starting from this state the most frequent transition is $C \rightarrow B$, which is responsible for the appearance of the first yield point.
- When the population of the state C is exhausted, the transition $A \rightarrow B$ will dominate and is responsible for the second yield point.
- Through the back path (e.g. as represented by the brown line in the figure 6.1 on the page 235) the most frequent transition is $B \leftarrow C$. At the end of the back path the state C will be overpopulated. This causes a two-fold effect: (a) the sample in the pre-stretched state is longer than it was in the native state, (b) by the successive stretching the kinetics will be dominated by $C \leftrightarrow B$ transition, hence the behaviour will be very similar to that of the two-state model describing the behaviour of the pre-stretched sample.

- If the pre-stretched sample is left at rest, then the slow redistribution processes will take place driving the system to the equilibrium distribution, i.e. the sample returns to the native state.

At least qualitatively, the three-state model describes all our observations related to the mechanical response of silk in its both stretching states and this in the whole range of humidities.
Indeed, fits of measured data with the three-state model give a very good quantitative description for the stretching curve of the native silk (represented by the olive line in figure 6.1) as well as for the back path (represented by the brown line). Examples are shown in figures 5.27 and 5.28. However, the calculated length of the pre-stretched sample (point ϵ_1^{eq}) resulting from the model is much shorter than measured. Hence, the model failed to describe the successive stretching in one pass and we cannot give a quantitative description of the native $\leftrightarrow$ pre-stretched transitions. This drawback can be overcame by further extension of the model, introducing a separate dash-pot describing the dissipation due to the sliding (which will cause the irreversible elongation) and/or taking into account the interaction of the molecular units with their environment as well as mutual interaction. The latter can be realized by introduction of the third (post-molten) state D with only the $D \leftrightarrow B$ transition allowed (for this state). The state D can be thought to account for a molecular alignment, caused by the mutual interaction or interaction with the surrounding of the elongated molecular units (state B). This results in a state D with the length close to that of B state but with a lower energy level. The behaviour of the resulting four-state model will be close to the observation and this resolves the above problem.

Mechanical response on long-time scales.

In our study we encountered a deviation of the relaxation behaviour of silk at long-time scales from the classical (Debye) relaxation. Non-Debye relaxation implies the presence of memory effects. Formally, the underlying dynamics looses its Markovian character and the constitutive equations governing the behaviour of the material, become integro-differential. Fortunately, silk is a member of a large class of materials whose long-time viscoelastic behaviour can be described in terms of the fractional viscoelastic theory. This theory is an extension of the classical viscoelastic theory introducing a new viscoelastic element (fractional dash-pot) relating stress and strain by means of fractional order derivative.
The notion of the operation of a fractional derivative exists since the times of Leibniz. Nowadays there is a fully established theory of the calculus of the differential and integral operators of fractional order (see e.g. [87, 105]). In the last few decades it was used to

establish new models in many fields of physics, such as viscoelasticity, heat conduction, anomalous diffusion, chaos etc., see e.g. [7,86,109]. In spite of the fact that the operations of integration and differentiation of fractional order have no well established geometrical interpretation, the notion of fractional operations arose quite naturally in the study of the dynamics of systems with self-similar composition of random processes, like diffusion and polymer dynamics [6, 52, 109, 112, 119].

We introduce the relevant theoretical aspects in chapter 2 section 2.2. Our application to the data from our long-time relaxation experiments is described in chapter 5 (pages 175 ff). The fits of the model of the Fractional Standard Solid type results in the fractional exponents laying in the range $[0.4 - 0.6]$. This can be compared with the value 0.5 for the Rouse model, used to describe a long linear polymer chain. The Rouse model is a particular example of models describing self-similar arrangement of interrelated processes. We discuss this interpretation on pages 178 ff.

There is no well-established theoretical description unifying the non-linear aspects of the short range behaviour with the fractional linear response on the long-time scales. The separate description of the behaviour on the different time scales is possible because of the short/moderate time scales the processes of fractional behaviour are not yet established. Hence the processes, responsible for the non-linear behaviour, are dominating. But, in the long time measurements one deals with a situation where all short time (non-linear) processes are nearly completed and the fractional viscoelasticity dominates the behaviour of the material.

6.4. Fractional self diffusion as measured with QENS.

To access the dynamics of silk at the molecular level, *in situ* neutron scattering experiments were done on time-of-flight spectrometer IN6 at the ILL. For additional measurements the backscattering instrument IN10 and the spin echo spectrometer IN11 were used. In this study we apply quasielastic (QENS) and low-energy inelastic (INS) neutron spectroscopy using the H atoms (dominant incoherent scatter) as a spectroscopic probe to further understand the internal behaviour of the silk fibres. The incoherent neutron scattering spectroscopy accesses both temporal and spatial molecular correlations through the Van Hove autocorrelation function $W(\vec{r},t)$. The measured quantity is the intensity which is closely related to the scattering function $S(Q,\omega)$ or (in the case of IN11) the intermediate scattering function $I(\vec{Q},t)$; both are obtained by Fourier transform from from $W(\vec{r},t)$ [8]. (here $\hbar\omega$ means energy transfer, $\hbar$ is the Plank constant and $\vec{Q}$ denotes the scattering vector).

For biomaterials the technique is sensitive to the single-particle autocorrelation of the H atoms visible by the incoherent scattering.

We used an experimental setup combining *in situ* tensile tests and hydration with cold neutron time-of-flight spectroscopy on aligned bundles of silk fibres. The supplementary recording of the neutron backscattering and spin-echo spectra was done on the unstretched silk samples using an *ex situ* humidisation. The results were reported in [154] where the QENS part of spectra was analysed in terms of the combination of the classical constrained and unconstrained jump and constrained continuous diffusion models. The analysis demonstrated that the classical diffusion models, where the $I(Q,t)$ dissipates exponentially, are insufficient to describe the dissipation processes in the sample. The resulting model can describe the QENS data only in a small subregion of the accessible range of energies and momentum transfers. The description of QENS spectra, fitted in this way, was of rather qualitative character, but nevertheless provides strong evidence for the presence of a sub-diffusional dynamics.

Here we show that the fractional diffusion model [109] can be successfully used to describe the collective intercorrelated internal dynamics of the humid silk proteins as is seen through the Van Hove's autocorrelation function. A similar approach to proteins in solution was given in [88].

This model describes a sub-diffusion type of motion, sometimes called a fractal time random walk, where the characteristic waiting time can diverge while the characteristic spatial length remains finite. The correlation function obeys the equation

$$\frac{\partial}{\partial t}W(\vec{r},t) = {}_0D_t^{1-\alpha}\frac{1}{\tau_0^\alpha}\nabla^2 W(\vec{r},t) \tag{6.1}$$

or, equivalently

$${}_0D_t^{\alpha}W(\vec{r},t) - \frac{t^{-\alpha}}{\Gamma(1-\alpha)}W_0(\vec{r}) = \frac{1}{\tau_0^\alpha}\nabla^2 W(\vec{r},t) \tag{6.2}$$

where symbol ${}_0D_t^\alpha$ represents the Riemann-Liouville fractional differentiation operator of the order (power) $\alpha \in (0,1]$; for more details see section 2.2. τ_0^α is the inverse of the generalized diffusion constant and is defined by the spatial σ_c and time τ_c characteristic scales as

$$\frac{1}{\tau_0^\alpha} = \frac{\sigma_c^2}{\tau_c^\alpha}$$

and is measured in units of $[s^\alpha/\text{Å}^2]$. The initial value $W_0(\vec{r})$ dissipates with the inverse power law $\sim t^{-\alpha}$. In the limit $\alpha \to 1$ the above equations reduce to the Fick's law describing the classical diffusion process [8]. In the literature it was recognized that the the replacement of the time derivative in the diffusion equation by a fractional operator

accounts for memory effects which are reported for many complex systems (see references in [109]). The spatial Fourier transform of eq. (6.2) results in the following equation for the intermediate scattering function $I(\vec{Q},t)$:

$$ {}_0D_t^{\alpha} I(Q,t) - \frac{t^{-\alpha}}{\Gamma(1-\alpha)} = -\frac{Q^2}{\tau_0^{\alpha}} I(Q,t). \tag{6.3} $$

It is the fractional relaxation equation described in section 2.2 on page 49. The solution of 6.3 is given by the Mittag-Leffler function:

$$ I(Q,t) = I_0(Q) E_{\alpha}(-|t/\tau|^{\alpha}) \tag{6.4} $$

so the single modes of 6.2 decay in accordance with the Mittag-Leffler patterns with characteristic time:

$$ \tau^{\alpha} = \tau_0^{\alpha}/Q^2. $$

The behaviour of the intermediate scattering function $I(Q,t)$ and the corresponding scattering function $S(Q,\omega)$ are shown in figure 6.4. From the figure it is seen that by decreasing the parameter α the dissipation of the initial state initially increases but then slows down at longer times, as represented by the flatter tails of the curves. This causes a broadening of the wings by the $S(Q,\omega)$ with a simultaneously sharping of the curve in the middle range close to zero.

Effectively, the discussed model requires only two parameters: τ_0 and α ! The two model parameters must be compared with 11 parameters needed to describe the same data in terms of classical diffusion [154]. Figure 6.5 shows an example of the application of the fractional diffusion model to the measured scattering function $S(Q,\omega)$ for several Q. The figure shows the data measured with unstretched humid silk and fitted by the above model with $\alpha = 0.508$ and $\tau_0 = 341\ ps/\text{Å}^2$ (both with confidence interval of about 6%). The longer tails of $I(Q,t)$ were observed by us as about nano-second relaxations in the spectra additionally measured on the spin-echo spectrometer IN11.

The success of the model leads us to assume that the movement of single molecules and chains in humid silk occurs in strongly correlated fashion: many transport processes are strongly interconnected and their mutualy influence causes memory effects. We assume that it is this unifying collective character of the dynamics which allows us to describe the dissipative behaviour of such a complex system by a model with only a few parameters.

The author cannot resist the temptation to compare the results concerning the long-time relaxation experiments and the current simulation of the QENS spectra by the fractional diffusion dynamics. In case of silk both show the presence of memory effects: one – on the time scale of several hours/days and on the molecular time scales from picoseconds to

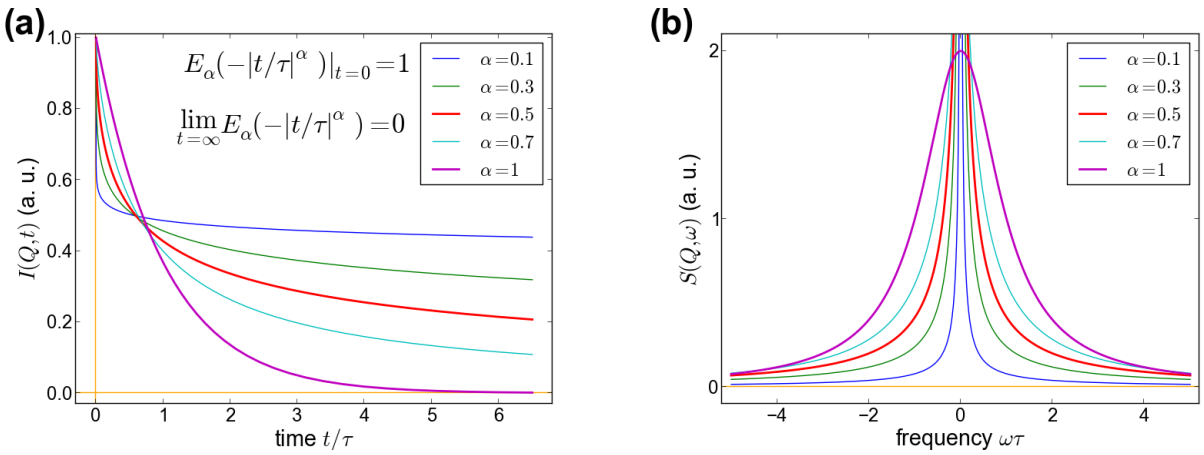

Figure 6.4.: **Fractional subdiffusion**

The figure shows (a) the intermediate scattering function $I(Q,t)$ and (b) the incoherent scattering function $S(Q,\omega)$ for several values of the fractional power α. The line in magenta shows the case $\alpha = 1$ corresponding to the usual diffusion (Fick's law). The red line shows the behaviour for $\alpha = 1/2$, which is close to our finding for silk.

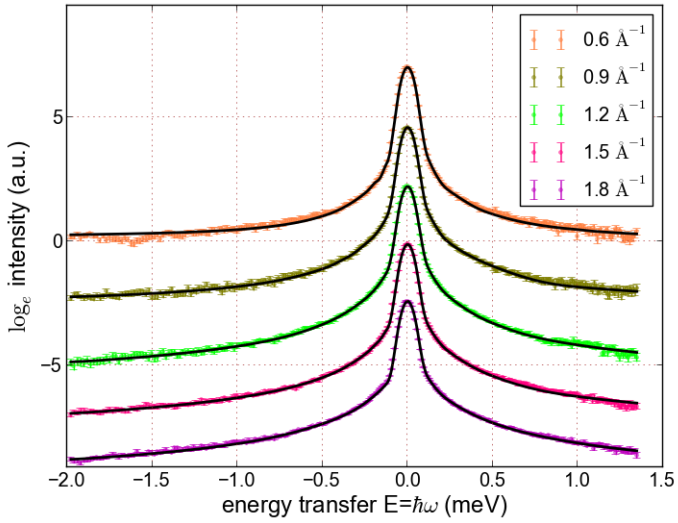

Figure 6.5.: **QENS spectra of unstretched silk**

The quasi-elastic scattering function shown for several values of the momentum transfer. Black lines show the fractional sub diffusion model fitted to the measured data.

nanoseconds the other. Both experiments are based on measurements over relatively long periods of time: 6-30 hours of the data recording in the case of neutron scattering and several hours to days in the case of the relaxation experiments. In the both cases the resulting order (power) of the fractional differentiation operators, accounting for the memory effects, was close to 1/2. This value occurs in two famous model of fractional dynamics. The first one is the Rouse model, describing the relaxation dynamics of long/infinite polymer chains in solution. The other is a model system of dynamical processes simulated with dash-pots and springs interconnected by a simple fractal structure. It seems that memory effects propagate from the molecular to the macroscopic level and find their manifestation also in the long time relaxation experiments.

7. Conclusions and outlook

The focus of this thesis was on the mechanical properties of *Bombyx mori* silk. The goal is to learn about the response of this material to an external (mechanical) perturbation. This is done by monitoring changes of the microscopic structure in the crystalline regions. In parallel, molecular dynamics of the amorphous phase are studied. In order to achieve this goal *in situ* scattering experiments were performed: synchrotron X-ray radiation and cold neutrons were used as probes of the structure and dynamics, respectively. Extensive use of instruments at large scale facilities has been made. Because the mechanical behaviour of silk exhibits a pronounced time-dependent nature much attention was devoted to the temporal evolution of the phenomena under study. In order to get better access to the evolution of the mechanical properties of silk, in our stretching experiments, we covered several time intervals, ranging from fractions of a second up to several days. Another very important parameter which influences the properties of silk is the water content of the surrounding atmosphere. In order to take this influence into account we performed all our experiments at controlled environmental conditions. The theoretical analysis of our experimental data results in a set of interrelated viscoelastic, structural and dynamical models. They allow mimic of silk behaviour in a wide range of applied forces and elongations. Furthermore, they help to clarify (i) the basic principles on which the viscoelastic behaviour of silk is based as well as (ii) the geometrical/structural aspects of the elongation of the β-sheet crystallites in silk. All computational aspects of our models are presented in this thesis in the form of highly optimized [1] algorithms and implemented in software packages, e.g. computing of non-linear responses, Mittag-Leffler functions, solving fractional equations, geometrical optimizations and multi-dimensional rotational averaging. They are ready for use in further studies of silk. – Some results of this study already have been reported [93] and additional publications are in preparation.

For our *in situ* experiments on single fibres a highly specialized stretching sample cell was designed and built. It has a high sampling rate and allows sufficient resolution in the mon-

[1] Due to the requirement to fit our models to a large amount of measured data, much work and time was spent to optimize their computation. As a result, some of our routines were about 1000 time faster than their initial direct implementation.

itoring and driving of the stretching process under controlled environmental conditions. A software package has been designed and implemented which controls all the hardware integrated in the sample cell. Its server-client architecture allows a remote access to the stretching process. The software allows to communicate with a software of large facility instruments to drive a scattering experiment synchronously with a chosen stretching protocol.

We found that silk fibres can either be in a stable or metastable viscoelastic states (see e.g. pages 234, 168 or [93]). The first state, that of silk fibres without any stretching history, is called virgin or native. The other one, called the pre-stretched state occurs when an external force is applied. Obviously, the viscoelastic behaviour of silk in the native state deviates from that in the pre-stretched state. An interesting fact is the existence of a back transition pre-stretched→native extending over long times.

The measured mechanical behaviour of silk is successfully described by models based on the Transition State Theory (TST). There, the elongation of the sample is related to a large number of thermally activated processes. The model describes all measured data (in a wide range of humidities) at moderate time scales. It clarifies the non-linear character of the stretching curves and, for the first time, the nature of the transition native↔pre-stretched. An activation energy of these processes of the order of $100\frac{\mathrm{kJ}}{\mathrm{mol}}$ has been determined. This quantity is a decreasing function of the humidity; hence water acts as a plasticizer: it increases the molecular mobility within silk[2].

The analysis of our *in situ* scattering experiments shows that the β-sheet crystallites in silk exhibit a purely elastic behaviour. This finding justifies the use of crystallites as force sensors embedded in the amorphous phase of silk, as we have done. In spite of the fact that water molecules do not penetrate the crystallites we observe a decrease of the crystallites' elastic modulus with the increase of the water content in the surrounding atmosphere. We address this effect on interface phenomena. Since neither the modulus of the crystallites nor of the amorphous phase of silk is known *a priori* or directly measurable by stretching experiments, we have combined stretching tests with the X-ray scattering technique in a viscoelastic modelling. In this way we got access to elastic moduli of both, crystalline and amorphous regions; as well as to the relaxation properties of the amorphous phase.

Further progress has been achieved in the understanding and description of the elongation of β-sheet crystallites within silk. Our detailed model describes the atomic configuration in the crystallites as a function of the elongation ϵ_c. This allows for a calculation of the structure factor $S(\vec{Q};\epsilon_c)$. Assuming adequate distributions of the parameters of crystallites

[2] This is in accord with our finding from neutron scattering experiments [154].

in the ensemble (e.g. orientation) the averaged diffraction image can be computed and fitted to an experimentally recorded one. Our model clarifies the mechanism of the elongation of crystallites and explains why the observed Poisson effect is very small. No assumptions about potentials need to be made; thus, it would be very interesting to compare predictions of this model with results of potential-based computer simulations.

Important results were also obtained concerning the long-time relaxation experiments as well as Quasielastic Neutron Scattering (QENS) experiments. Both deal with the long-time behaviour but each on its own scale: macroscopic and molecular, respectively. Both show the presence of memory effects in the underlying dynamics, manifesting themselves in an anomalous relaxation/diffusion behaviour. Both allow descriptions in terms of the fractional linear dynamics. In both cases, the order (power) of the fractional differential operator, which appears in the dynamical laws of the underlying phenomena, is close to 1/2. Such a value usually arises in studies of long chain polymers with a self-similar organisation of the dynamical sub-processes. The applicability of the fractional theory to the dynamics and viscoelasticity of silk was previously not considered in the literature. It opens a wide perspective for better understanding the mechanical behaviour of silk.

In this work a link between the macroscopic viscoelastic behaviour and the mechanism at the molecular length scales has been established. With our experimental techniques and analyses we could separate the mechanical properties of the crystalline region of silk from those of the amorphous part, as well as show their interplay.

Outlook: The amount of open questions and possibilities in further studies of silk *'is legion*[3]; here we will point out only few of them. The usefulness of very detailed, wide-ranged phase diagrams of silk with respect to environmental conditions (temperature, humidity, pH-values etc.) would be enormous. Our models can be used here as classification tools. Stress and strain ensembles in a stretched silk fibre could be accessed by *in situ* X-ray scattering experiments with sub-μm beams. The quantities measured in such experiments are distributions in crystallite size, orientation and stress as a functions of the location inside a fibre. In spite of the success of our mechanical models they have an averaged (mean field) nature and do not allow a detailed description of silk at the mesoscopic scale. Such an extended description would be possible in terms of a mesoscopic non-equilibrium thermodynamics (e.g. [148]). An experimental foundation of this could consist in combination of *in situ* measurements: small angle scattering, diffraction with a sub-μm sized X-rays beam and cold neutron scattering at several energy resolutions.

[3]Gospel of Luke, 8.30

A. Appendix

A.1. Appendix to the chapter 5

Computation of the rotation defined in the equation (5.49). In the frame of the Geometric (Clifford) Algebra over the $3D$ Euclidean vector space a rotation of an angle θ about an axis $\hat{q}$ is described by the rotor (see e.g. [70])

$$\mathbf{R}_{\vec{q}}(\theta) = \exp\left(\mathrm{i}\,\hat{q}\,\frac{\theta}{2}\right). \tag{A.1}$$

Where 'i' denotes the unit pseudo-scalar in the $3D$ space. This can be separated into scalar and bi-vector parts:

$$\mathbf{R}_{\vec{q}}(\theta) = q_0 + \mathrm{i}\,\vec{q} = \; q_0 + \mathrm{i}\,\hat{q}\; q = \cos\frac{\theta}{2} \; + \; \mathrm{i}\,\hat{q}\sin\frac{\theta}{2}, \tag{A.2}$$

where $q_0 = \cos(\theta/2)$ is the scalar part of the rotor and $\mathrm{i}\,\vec{q} = \mathrm{i}\,\hat{q}\sin(\theta/2)$ is its the bi-vector part. $\hat{q}$ is the unit vector in the direction of the rotation axis.
The rotation of an object X from the algebra is described as

$$X' = \mathbf{R}_{\vec{q}}(\theta)^{\dagger} X \mathbf{R}_{\vec{q}}(\theta)$$

The rotation defined by equation (5.49) is represented by the rotor:

$$\mathbf{R}_{\vec{u}}(\theta) \;=\; u_0 + \mathrm{i}\,\vec{u} \;=\; e^{\mathrm{i}\hat{c}\psi/2}\, e^{\mathrm{i}\hat{n}\chi/2}\, e^{\mathrm{i}\hat{a}\phi/2} \tag{A.3}$$

which can be computed in two steps.
First, the product of the first two term in (A.3) gives:

$$Q = q_0 + \mathrm{i}\vec{q} \;=\; (c_0 + \mathrm{i}\vec{c})\,(n_0 + \mathrm{i}\vec{n}) \tag{A.4}$$

the scalar and vector parts of Q reads:

$$\begin{aligned} q_0 \;&=\; c_0 n_0 - \vec{a}\cdot\vec{n} \;=\; c_0 n_0 \\ \vec{q} \;&=\; c_0\vec{n} + n_0\vec{c} + i\,\vec{c}\wedge\vec{n} \;=\; c_0\vec{n} + n_0\vec{c} - \vec{c}\times\vec{n} \;=\; c_0\vec{n} + n_0\vec{c} - cn\hat{e}_2 \end{aligned} \tag{A.5}$$

where '$\cdot$' denotes the inner-product (scalar-product), '$\times$' - usual vector cross-product and '$\wedge$' is the Grassmann's exterior (wedge) product.
Second, the triple product will be

$$\mathbf{R}_{\vec{u}}(\theta) \;=\; u_0 + i\,\vec{u} \;=\; Q\,e^{i\hat{a}\phi/2} \;=\; (q_0 + \mathrm{i}\,\vec{q})\,(a_0 + \mathrm{i}\,\vec{a}) \tag{A.6}$$

Then the separation into the scalar and bi-vector component reads:

$$\begin{aligned} u_0 &= q_0 a_0 - \vec{q}\cdot\vec{a} \\ \vec{u} &= q_0\vec{a} + a_0\vec{q} + i\,\vec{q}\wedge\vec{a} \end{aligned} \tag{A.7}$$

Combining equations (A.5, A.7) and rearranging the terms gives:

$$\begin{aligned} u_0 &= c_0\,n_0\,a_0 - n_0\;\vec{a}\cdot\vec{c} + \vec{n}\cdot(\vec{a}\times\vec{c}) \\ \vec{u} &= c_0 n_0\,\vec{a} + a_0 n_0\,\vec{c} + (a_0 c_0 + \vec{a}\cdot\vec{c})\,\vec{n} \\ &\quad +\mathrm{i}\,(a_0\,\vec{c}\wedge\vec{n} + c_0\,\vec{n}\wedge\vec{a} + n_0\,\vec{c}\wedge\vec{a}) \end{aligned} \tag{A.8}$$

This further simplifies to

$$u_0 = (a_0 n_0 c_0) - (a n_0 c)\cos\xi - (anc)\sin\xi \tag{A.9}$$

$$\begin{aligned} \vec{u} &= \hat{c}\,(a_0 c n_0 + a c_0(n_0\cos\xi + n\sin\xi)) \\ &\quad \hat{a}\,(a c_0 n_0 + a_0 c(n_0\cos\xi + n\sin\xi)) \\ &\quad \hat{n}\,(a_0 c_0 n - a c(n_0\sin\xi - n\cos\xi)) \end{aligned} \tag{A.10}$$

$$\begin{aligned} &= \hat{e}_1\,(a_0 c n_0 + a c_0(n_0\cos\xi + n\sin\xi)) \\ &\quad \hat{e}_2\,(a_0 c n + a c_0(n_0\sin\xi - n\cos\xi)) \\ &\quad \hat{e}_3\,(a_0 c_0 n - a c(n_0\sin\xi - n\cos\xi)) \end{aligned} \tag{A.11}$$

where we did use the naming convention introduced in (A.2). The bi-vector component is expanded into components of the triple $\{\vec{c},\vec{a},\vec{n}\}$ in (A.10) and of the basis $\{\hat{e}_1,\hat{e}_2,\hat{e}_3\}$ of the peptide plane P in (A.11). Substitution $n_0 = \cos\frac{\chi^+}{2}, n = \sin\frac{\chi^+}{2}$ give us:

$$u_0 = a_0 c_0\;\cos\frac{\chi^+}{2} - a c\;\cos\frac{\chi^-}{2} \tag{A.12}$$

$$\vec{u} = \hat{e}_1\left(a_0 c\;\cos\frac{\chi^+}{2} + a c_0\;\cos\frac{\chi^-}{2}\right) \tag{A.13}$$

$$\hat{e}_2\left(a_0 c\;\sin\frac{\chi^+}{2} - a c_0\;\sin\frac{\chi^-}{2}\right) \tag{A.14}$$

$$\hat{e}_3\left(a_0 c_0\;\sin\frac{\chi^+}{2} + a c\;\sin\frac{\chi^-}{2}\right)$$

Derivation of the equation (5.46) for the value of the torsion angle. We identify the two oriented planes shown in figure 5.34 with the two unit bi-vectors ($\hat{A} = \hat{u}_2 \wedge \hat{u}_3 = \mathrm{i}_3\hat{n}_1$ and $\hat{B} = \hat{u}_1 \wedge \hat{u}_2 = \mathrm{i}_3\hat{n}_2$), where i_3 is the 3D Euclidean pseudo-scalar $\mathrm{i}_3 \equiv \hat{e}_1\hat{e}_2\hat{e}_3$. The dihedral angle θ can be specified through the relation: $-\hat{B}\hat{A} = e^{\mathrm{i}_3\hat{u}_2\theta}$ [70]. Then

$$e^{\mathrm{i}_3\hat{u}\theta} = -(\hat{u}_2 \wedge \hat{u}_3)(\hat{u}_2 \wedge \hat{u}_3) = \hat{u}_1 \cdot (\hat{u}_2 \wedge \hat{u}_3) \cdot \hat{u}_3 + \hat{A} \times \hat{B}$$

can be expanded into

$$\hat{u}_1 \cdot (\hat{u}_2 \wedge \hat{u}_3) \cdot \hat{u}_3 = (\hat{u}_1 \cdot \hat{u}_2\hat{u}_3 - \hat{u}_1 \cdot \hat{u}_3\hat{u}_2) \cdot \hat{u}_2$$

$$-\hat{B} \times \hat{A} = \hat{n}_2 \wedge \hat{n}_1 = \mathrm{i}_3\hat{u}_1 \cdot (\hat{u}_2 \times \hat{u}_1)$$

which results in the relations (5.46), if we consider the plane $\mathrm{i}_3\hat{u}_2$ as complex plane $\mathbb{C}$.

List of Figures

List of Tables

Bibliography

[1] M. Abramowitz and I. A. Stegun. *Handbook of mathematical functions.* Dover Publications,inc., New York, 1964.

[2] Jens Als-Nielsen and Des McMorrow. *Elements of Modern X-Ray Physics.* John Wiley & sons, Ltd, 2001.

[3] Gregory H Altman, Frank Diaz, Caroline Jakuba, Tara Calabro, Rebecca L Horan, Jingsong Chen, Helen Lu, John Richmond, and David L Kaplan. Silk-based biomaterials. *Biomaterials*, 24(3):401–416, 2003.

[4] M. Angst, T. Brückel, Richter D., and Zorn R., editors. *Scattering Methods for Condensed Matter Research*, volume 33. Schriften des Forschungszentrum Jülich, 2012.

[5] H. Arnold. Transformation in craystallography. In Theo Hahn, editor, *International tables for crystallography: space-group symmetry*, volume IV of *International tables for crystallography*, chapter 5, pages 69–81. D. Riedel Publishing, Dortrecht:Holland/Boston:U.S.A., 1983.

[6] R. L. Bagley. A theoretical Basis for the Application of Fractional Calculus to Viscoelasticity. *J. Rheol.*, 27(3):201–210, 1983.

[7] D. Baleanu et al. Newtonian law with memory. *Nonlinear Dyn.*, 60:81–86, 2010.

[8] M Bée. *Quasielastic neutron scattering.* Adam Hilger, Briston and Philadelphia, 1988.

[9] B. Bernstein and A. Shokooh. The Stress Clock Function in Viscoelasticity. *Journal of Rheology*, 24(2):189–211, 1980.

[10] L. C. Biedenharn and J.D. Louck. *Angular Momentum in Quantum Physics: Theory and Application.* Cambrige University Press, 1985.

[11] M. A. Biot. Theory of Stress-Strain Relations in Anisotropic Viscoelasticity and Relaxation Phenomena. *Journal of Applied Physics*, 25(11):1385–1391, 1954.

[12] M. A. Biot. Thermoelasticity and Irreversible Thermodynamics. *Journal of Applied Physics*, 27(3):240–253, 1956.

[13] S. Blügel. Scattering Theory: Born Series. In *43rd IFF Spring School "Scattering Methods for Condensed Matter Research: Towards Novel Applications at Future Sources*, 2009.

[14] Harris Burte and George Halsey. A new theory of non-linear viscous elasticity. *Textile Research Journal*, XVII(9):465, 1947.

[15] Harris Burte, George Halsey, and J. H. Dillon. A new concept of the mechanical behavior of Fibers. *Textile Research Journal*, XVIII(8):449, 1947.

[16] Carlos Bustamante, Jan Liphardt, and Felix Ritort. The Nonequilibrium Thermodynamics of Small Systems. *Physics Today*, pages 43–48, July 2005.

[17] Yang Cao and Bochu Wang. Biodegradation of Silk Biomaterials. *Int J Mol Sci*, 10(4):1514–1524, 2009.

[18] CBN. Abbreviations and symbols for description of conformation of polypeptide chains; rules approved 1974. Technical report, IUPAC-IUB, London, Butter Worths, 1974.

[19] C. F. Chen and Y. T. Tsay. Walsh Operational Matrces for Fractional Calculus and Their Application to Distributed Sytem. *Journal of The Franklin Institute*, 303(3), March 1977.

[20] C.W. Clenshaw and A.R. Curtis. A method for numerical integration on an automatic computer. *Numerische Mathematik*, 2(1):197–205, 1960.

[21] comedi. The Control and Measurement Device Interface, COMEDI., jan 2008. `http://www.comedi.org`.

[22] Robert B. Corey and Linus Pauling. Fundamental Dimensions of Polypeptide Chains. *Proc. R. Soc. Lond.*, B 11 141(902):10–20, March 1953.

[23] Kondepudi D. *Introduction to Modern Thermodynamics*. John Willey and Sons, Ltd, 2008.

[24] Kaplan D.L., W. Adams, B. Farmer, and C. Viney, editors. *Silk polymers: material science and biotechnology*, volume 54 of *ACS Symposium Series*, 1994.

[25] Kaplan DL, Mello CM, S Arcidiacono, S Fossey, K Senecal, and W Mulle. Protein based materials. In McGrath K. and Kaplan D.L., editors, , pages 103–131. Birkhauser, Boston, 1999.

[26] G. Doetsch. *Einfürung in Theory and Anwendung der Laplace-Transformation.* Birkhauser, Basel und Stuttgard, second edition, 1970.

[27] J.R. Driscoll and D.M. Hely. Computing Fourier Transorms and Convolutions on the 2-Spheres. *Adv. App. Math.*, 15:202–250, 1994.

[28] A. D. Drozdov and B. Israel. Fractional differential models in finite viscoelasticity. *Acta Mechanica*, 124:155–180, 1997.

[29] Basil A. Dunell and George Halsey. Thixotropic Viscoelastic Systems. *Textile Research Journal*, 18:178–186, 1948.

[30] R A Engh and R Huber. Accurate bond and angle parameters for X-ray protein structure refinement. *Acta Crystallographica Section A*, 47(4):392–400, Jul 1991.

[31] R. A. Engh and R. Huber. Structure quality and target parameters. In M. G. Rossmann and E. Arnold, editors, *International Tables for Crystallography Volume F: Crystallography of biological macromolecules*, pages 382–392. Springer, 2006.

[32] Henry Eyring. The Activated Complex in Chemical Reactions. *J. Chem. Phys.*, 3:107–115, 1934.

[33] Henry Eyring. Viscosity, Plasticity, and Diffusion as Examples of Absolute Reaction Rates. *J. Chem. Phys.*, 4:283, 1936.

[34] Henry Eyring, S. H. Lin, and S. M. Lin. *Basic chemical kinetics.* New York, [United States] : John Wiley and Sons, 1980.

[35] J D Ferry. *Viscoelastic Properties of Polymers.* Wiley, New York, 1961.

[36] J. D. Ferry, R. F. Landel, and M. L. Williams. Extensions of the Rouse Theory of Viscoelastic Properties to Undiluted Linear Polymers. *J. Appl. Phys.*, 26(4):359–362, 1955.

[37] A V Finkelstein and O V Galzitskay. Physics of protein foldin. *Physics of Life Review*, 1(1):23–5, 2004.

[38] A. Fischer, K. H. Hoffmann, and J C. Schön. Competitive trapping in coplex state spaces. *Journal of Physics A: Math. Theor.*, 44:075101, 2011.

[39] Henry E Fischer, Adrian C Barnes, and Philip S Salmon. Neutron and x-ray diffraction studies of liquids and glasses. *Reports on Progress in Physics*, 69:233–299, 2006.

[40] Cheryl Wong Po Foo and David L Kaplan. Genetic engineering of fibrous proteins: spider dragline silk and collagen. *Advanced Drug Delivery Reviews*, 54(8):1131–1143, 2002. Engineered Protein Polymers for Drug Delivery and Biomedical Applications.

[41] Stephen A. Fossey, George Némethy, Kenneth D. Gibson, and Harold A. Scheraga. Conformational energy studies of β-sheets of model silk fibroin peptides. I. Sheets of poly(Ala-Gly) chains. *Biopolymers*, 31(13):1529–1541, 1991.

[42] Ch Friedrech. Relaxation and retardation functions of the Maxwell model with fractional derivatives. *Rheol. Acta*, 30:151–158, 1991.

[43] Evance M. G. and Polanyi M. Some applications of the transition state method to the calculation of reaction velocities, especially in solution. *Transactions of the Faraday society*, 31:875–894, 1935.

[44] Andrew Gemant. A Method of Analyzing Experimental Results Obtained from Elasto-Viscous Bodies. *Physics*, 7:311, 1936.

[45] W. Morven Gentleman. Implementing Clenshaw-Curtis quadrature, 1 methodology and experience. *Commun. ACM*, 15:337–342, May 1972.

[46] Stefano Gianni, Nicholas R. Guydosh, Faaizah Khan, Teresa D. Caldas, Ugo Mayor, George W. N. White, Mari L. DeMarco, Valerie Daggett, and Alan R. Fersht. Unifying features in protein-folding mechanisms. *Proc. Natl. Acad. Sci.*, 100(23):13286–13291, 2003.

[47] Stefano Gianni, Nicholas R. Guydosh, Faaizah Khan, Teresa D. Caldas, Ugo Mayor, George W. N. White, Mari L. DeMarco, Valerie Daggett, and Alan R. Fersht. Unifying features in protein-folding mechanisms. *Proceedings of the National Academy of Sciences*, 100(23):13286–13291, 2003.

[48] W. G. Glöckle and T.F. Nonnenmacher. Fractional integral operators and Fox functions in the theory of viscoelasticity. *Macromolecules*, 24:6426–6434, 1991.

[49] W. G. Glöckle and T.F. Nonnenmacher. Fox function representation of non-Debye relaxation processes. *J. Stat. Phys.*, 71:741–757, 1993.

[50] W. G. Glöckle and T.F. Nonnenmacher. A fractional relaxation equations for proteine dynamics. In *Fractals in biology and medicine*. Birkhauser, 1994.

[51] W. G. Glöckle and T.F. Nonnenmacher. Fractional relaxation and the time-temperature superposition principle. *Rheol. Acta*, 33:337–342, 1994.

[52] W.G. Glöckle and T.F. Nonnenmacher. A fractional calculus approach to self-similar protein dynamics. *Biophysical Journal*, 68(1):46–53, 1995.

[53] John M Gosline, M Edwin DeMont, and Mark W Denny. The structure and properties of spider silk. *Endeavour*, 10(1):37–43, 1986.

[54] John M Gosline, Mark W Denny, and M Edwin DeMont. Spider silk as rubber. *Nature*, 309:551–552, 1984.

[55] PA Guerette CS Ortlepp JM Gosline and KN Savage. The mechanical design of spider silks: from fibroin sequence to mechanical function. *Journal of Experimental Biology*, 202:3295–3303, 1999.

[56] I. Gradstain and I. Rishik. *Tabels of series, products and integrals.* Verlag MIR, Moskau, 1981.

[57] Thomas G. W. Graham and Robert B. Best. Force-Induced Change in Protein Unfolding Mechanism: Discrete or Continuous Switch? *The Journal of Physical Chemistry B*, 115(6):1546–1561, 2011.

[58] Imke Greving. Silk degumming. Privat communication, 2012.

[59] Ingo Grotkop. *Influence of Water on the Mechanical Properties of Wood Investigated Using X-Ray and Neutron Scattering.* PhD thesis, university, Kiel, 2006.

[60] A. Guinier. *X-ray diffraction in crystalls, imperfect crystalls, and amorphous boodies.* Dover Publications,inc., 1994.

[61] Sung-Won Ha, Hanna S Gracz, Alan E Tonelli, and Samuel M Hudson. Structural Study of Irregular Amino Acid Sequences in the Heavy Chain of Bombyx mori Silk Fibroin. *Biomacromolecules*, 6(5):2563–2569, 2005. doi: 10.1021/bm050294m.

[62] Osnat Hakimi, David P Knight, Fritz Vollrath, and Pankaj Vadgama. Spider and mulberry silkworm silks as compatible biomaterials. *Composites: Part B*, 38:324–337, 2007.

[63] George Halsey, Howard J. White, and Henry Eyring. Mechanical Properties of Textiles, I. *Textile Research Journal*, 15(9):295–311, 1945.

[64] Andy Hammersley. *Reference Manual*, 2004. Available online at `http://www.esrf.eu/computing/scientific/FIT2D`; visited on January 8th 2013.

[65] Peter Hänggi, Peter Talkner, and Michal Borkovec. Reaction-rate theory: fifty years after Kramers. *Rev. Mod. Phys.*, 62(2):251–341, Apr 1990.

[66] Robert M. Hanson, Daniel Kohler, and Steven G. Braun. Quaternion-based definition of protein secondary structure straightness and its relationship to Ramachadran angles. *Proteins*, 79:2172–2180, 2011.

[67] T. T. Hartley and C. F. Lorenzo. A solution to the Fundamental Linear Fractional Order Differential Equation. Technical Report 208693, NASA/TP-1998-208693, dec 1998.

[68] A2, HASYLAB. `http://hasylab.desy.de/facilities/doris_iii/beamlines/a2`.

[69] HEIDENHAIN. Measurement and Control Technology for Demanding Positioning Tasks. `http://www.heidenhain.com/`.

[70] D. Hestenes. *New foundation for classical mechanics*. Kluwer, Dordrecht/Boston/London, Dordrecht/Boston/London, second edition, 1999.

[71] Nicole Heymans and J. C. Bauwens. Fractal rheological models and fractional differential equations for viscoelastic behavior. *Rheologica Acta*, 33:210–219, 1994.

[72] R. Hilfer and H. J. Seybold. Computation of the generalized Mittag-Leffer function and its inverse in the complex plane. *Integral Transforms and Special Functions*, Vol. 17(9):637–652, sept. 2006.

[73] T. L. Hill. *Thermodynamics of small system*. Dover: New York, 1994.

[74] Terrell L. Hill. Thermodynamics of Small Systems. *The Journal of Chemical Physics*, 36(12):3182–3197, 1962.

[75] A. Hoffmann. Messung der viskoelastischen Eigenschaften biologicher Fasermaterialien. Master's thesis, Universitet Kiel, 2008.

[76] ILL. Instruments and groups of Institut Laue-Langevin, Grenoble, France. http://www.ill.eu/instruments-support/instruments-groups:.

[77] Ward I.M. and Sweeney J. *An Introduction to the Mechanical Properties of Solid Polymers*. John Wiley & sons inc, 2004.

[78] S Inoue, K Tanaka, F Arisaka, S Kimura, K Ohtomo, and S Mizuno. Silk fibroin of Bombyx mori is secreted, assembling a high molecular mass elementary unit consisting of H-chain, L-chain, and P25, with a 6:6:1 molar ratio. *J Biol Chem.*, 51(275):40517–28, 22 2000.

[79] Satoshi Inoue, Kazunori Tanaka, Hiromitsu Tanaka, Kohei Ohtomo, Toshio Kanda, Morikazu Imamura, Guo-Xing Quan, Katsura Kojima, Tetsuro Yamashita, Tasuku Nakajima, Hideharu Taira, Toshiki Tamura, and Shigeki Mizuno. Assembly of the silk fibroin elementary unit in endoplasmic reticulum and a role of L-chain for protection of α1,2-mannose residues in N-linked oligosaccharide chains of fibrohexamerin/P25. *European Journal of Biochemistry*, 271(2):356–366, 2004.

[80] IUCr's. International Tables for Crystallography. `http://it.iucr.org/`, 2012. Accessed: 12/12/2012.

[81] Ylva Ivarsson, Carlo Travaglini-Allocatelli, Maurizio Brunori, and Stefano Gianni. Mechanisms of protein folding. *European Biophysics Journal*, 37:721–728, 2008. 10.1007/s00249-007-0256-x.

[82] Piezosystem jena GmbH, may 2005. `http://www.piezojena.com`.

[83] Zhihua Jiang and Walter Schaufelberger. *Block Pulse Functions and Their Applications in Control Systems*, volume 179 of *Lecture Notes in Control and Information Sciences*. Springer Berlin / Heidelberg, 1992. 10.1007/BFb0009170.

[84] Hyoung-Joon Jin and David L Kaplan. Mechanism of silk processing in insects and spiders. *Nature*, 424:1057–1061, 2003.

[85] Hiroshi Kawakami, Hiroshi Yamanaka, and Yukuo Nanzai. Thermally stimulated recovery of plastic strain in crosslinked and uncrosslinked epoxy/amine systems. *Polymer*, 46(25):11806–11813, 2005.

[86] Li Kexue and Peng Jigen. Laplace transform and fractional differential equations. *Applied Mathematics Letters*, 24(12):2019–2023, 2011.

[87] A. A. Kilbas, H.M. Srivastava, and J.J. Trujillo. *Theory and Applications of Fractional Differential Equations*, volume 204 of *North-Holland Mathematics Studies*. North-Holland Mathematics Studies, 2006.

[88] G. R. Kneller. Fractional Brownian dynamics in proteins. *Journal of Chemical Physics*, 121(20), 2004.

[89] G. R. Kneller and P. Calligari. Efficient characterization of proteine secondary structure in terms of screw moitions. *Acta. Cryst.*, D62:302–311, 2006.

[90] Wiebke Knoll. Neutronenstreuexperimente an Seidenfasern. Master's thesis, university, Kiel, 2009.

[91] Klaas Kölln. *Morphologie und mechanische Eigenschaften von Zellulosefasern Untersuchungen mit Röntgen- und Neutronenstreuung.* PhD thesis, university, Kiel, 2004.

[92] H. A. Kramers. Brownian motion in a field of force and the diffusion model of chemical reactions. *Physica*, 7(4):284–304, 1940.

[93] Igor Krasnov, Imke Diddens, Nadine Hauptmann, Gesa Helms, Malte Ogurreck, Tilo Seydel, Sergio S. Funari, and Martin Müller. Mechanical properties of Silk: Interplay of Deformation on Macroscopic and Molecular Length Scales. *Phys. Rev. Lett.*, 100(048104), February 2008.

[94] C. Krywka et al. X-ray Diffraction on *Bombyx mori* Silk under high pressure. private communication.

[95] Anthoula Lazaris, Steven Arcidiacono, Yue Huang, Jiang-Feng Zhou, Franois Duguay, Nathalie Chretien, Elizabeth A Welsh, Jason W Soares, and Costas N Karatzas. Spider Silk Fibers Spun from Soluble Recombinant Silk Produced in Mammalian Cells. *Science*, 295(5554):472–476, 2002.

[96] Schiffer L.I. *Quantum Mechanics*. New York: McGraw-Hill, 1955.

[97] Yuanlu Li and Ning Sun. Numerical solution of fractional differential equations using the generalized block pulse operational matrix. *Computers and Mathematics with Applications*, 62:1046–1054, 2011.

[98] David K. Lide. `http://www.d-r-h.de/hilfstabellen/klima_def_luftfeuchte.html`.

[99] H. J. Lipkin. Physics of Debye-Waller Factors. *eprint arXiv:cond-mat/0405023*, May 2004.

[100] H.J. Lipkin. *Quantum Mechanics: New approaches to selected topics*. Dover Books on Physics Series. Dover Publications, 2007.

[101] J Magoshi, Y Magoshi, and S Nakamura. Crystallization, liquid-crystal, and fiber formation of silk fibroin. *Applied polymer symposia*, 41:187–204, 1985.

[102] J Magoshi, Y Magoshi, and S Nakamura. Physical-properties and structure of silk .10. the mechanism of fiber formation from liquid silk of silkworm bombyx-mori. *Polymer Communications*, 26(10):309–311, 1985.

[103] J Magoshi, Y Magoshi, and S Nakamura. Physical-properties and structure of silk .9. liquid-crystal formation of silk fibroin. *Polymer Communications*, 26(2):60–61, 1985.

[104] J Magoshi and S Nakamura. Physical-properties and structure of silk .8. effect of casting temperature on conformation of wild silk fibroin films. *Journal of polymer science part b-polymer physics*, 23(1):227–229, 1985.

[105] Francesco Mainardi. *Fractional calculus and waves in linear viscoelasticity: An Introduction to Mathematical Models*. Imperial College Press, 2010.

[106] RE Marsh, RB Corey, and Pauling. An investigation of the structure of silk fibroin. *Biochimica et Biophysica Acta*, 16:1–34, 1955. Enter text here.

[107] RE Marsh, RB Corey, and L Pauling. The Crystal Structure of Silk Fibroin. *Acta Crystallographica*, 8(1):62, 1955.

[108] F. C. Meral, T. J. Royston, and R. Magin. Fractional calculus in viscoelasticity: An experimental study. *Commun Nonlinear Sci Numer Simulat*, 15:939–945, 2010.

[109] R. Metzler and J. Klafter. The random walk's guide to anomalous diffusion: a fractional dynamics approach. *Physics Reports*, 339:1–77, 2000.

[110] K. S. Miller and B. Ross. *An introduction to the frcational calculus and fractional differential equations*. John Wiley & sons inc, New York, 1993.

[111] P. H. Mott, A. S. Argon, and U. W. Suter. Atomistic modelling of plastic deformation of glassy polymers. *Philosophical Magazine A*, 67:931–978, 1993.

[112] Heymans N. and Bauwens J.-C. Frctal rheological models and fractional differential equations for viscoelastic behaviour. *Rheol. Acta*, 33:210–219, 1994.

[113] K. Nakamae, T. Nishino, and H. Ohkubo. Elastic modulus of the crystalline regions of silk fibroin. *Polymer*, 30(7):1243–1246, 1988.

[114] Yukuo Nanzai. Nonlinear Rheology in Glassy Polymers. *Journal of the Society of Rheology , Japan*, 33(5):223–237, 2005.

[115] Yukuo Nanzai. Nonlinear Rheology in Glassy Polymers. *Journal of the Society of Rheology , Japan*, 33(5):223–237, 2005.

[116] K. L. Ngai. Evidence of universal behaviour of condensed matter at low frequences/long times. In T. V. Ramakrishnan and R. M. Lakshmi, editors, *Non-Debay relaxation in condensed matter*, pages 78–94. Singapore, 1987.

[117] NI. National Instruments Corporation. `http://www.ni.com/`.

[118] R R Nigmatullin. On the Theory of Relaxation for Systems with ldquoRemnantrdquo Memory. *physica status solidi (b)*, 124(1):389–393, 1984.

[119] R R Nigmatullin. The realization of the generalized transfer equation in a medium with fractal geometry. *physica status solidi (b)*, 133(1):425–430, 1986.

[120] Takashi Nishino, Katsuhiko Nakamae, and Y. Takahashi. Elastic modulus of the crystalline regions of Tussah silk. *Polymer*, 33:1328, 1992.

[121] Bengt Nölting, Neema Salimi, and Ulrich Guth. Protein folding forces. *Journal of Theoretical Biology*, 251(2):331–347, 2008.

[122] T.F. Nonnenmacher and W. G. Glöckle. A fractional model for mechanical stress relaxation. *Phil. Mag. Lett.*, 64:89–93, 1991.

[123] P.G. Nutting. A new general law of deformation. *J. Franklin Inst.*, 191:679–685, 1921.

[124] Malte Ogureck. Formal description of microbrils in wood. Master's thesis, Strukturforschung an Werkstoffen Institut für Experimentelle und Angewandte Physik der Christian-Albrechts-Universität zu Kiel, 2007.

[125] L. Onsager. Reciprocal Relations in Irreversible Processes. *Phys. Rev.*, 37:405–426, 1931.

[126] O. Paris and M. Müller. Scanning X-ray microdifraction of complex materials: Diffraction geometry consideratins. *Nucl. Instr. and Meth. in Phys. Res.*, B 200:390–396, 2003.

[127] R. B. Parlin, R. J. Marcus, and H. Eyring. Irreversible thermodynamics and rate theory. *Proceedings of the National Academy of Sciences*, 41(11):900–907, 1955.

[128] L Pauling and RB Corey. Atomic coordinates and structure factors for 2 helical configurations of polypeptide chains. *Proceedings of the national academy of sciences of the United States of America*, 37(5):235–240, 1951.

[129] L Pauling and RB Corey. Configuration of Polypeptide Chains. *Nature*, 168(4274):550–551, 1951.

[130] L Pauling and RB Corey. Configurations of polypeptide chains with favored orientations around single bonds - 2 new pleated sheets. *Proceedings of the National Academy of Sciences of the USA*, 37(11):729–740, 1951.

[131] L Pauling and RB Corey. The pleated sheet, a new layer configuration of polypeptide chains. *Proceedings of the national academy of sciences of the USA*, 37(5):251–256, 1951.

[132] L Pauling, RB Corey, and HR Branson. The Structure Of Proteins - 2 Hydrogen-Bonded Helical Configurations Of The Polypeptide Chain. *Proc. Natl. Acad. Sci. USA*, 37(4):205–211, 1951.

[133] Linus Pauling and Robert B. Corey. Two hydrogen-bonded spiral configurations of the polypeptide chain. *J. Am. Chem. Soc.*, 72(11):5349–5349, 1950.

[134] Linus Pauling and Robert B. Corey. Stable Configurations of Polypeptide Chains. *Proc. R. Soc. Lond. B*, 141(902):21–33, March 1953.

[135] J Pérez-Rigueiro, C Viney, J Llorca, and M Elices. Mechanical properties of silkworm silk in liquid media. *Polymer*, 41(23):8433–8439, 2000.

[136] Robert Piessens. Computation of Legendre Series Coefficients [C6]. *Comm. ACM*, 17(1):25, 1974.

[137] I. Podlubny. The Laplace Transform Method for Linear Differential Equations of the Fractional Order. In *eprint arXiv:funct-an/9710005*, page 10005, October 1997.

[138] I. Podlubny, T. Skovranek, and B.M. Vinagre Jara. Matrix approach to discretization of fractional derivatives and to solution of fractional differential equations and their systems. In *Emerging Technologies Factory Automation, 2009. ETFA 2009. IEEE Conference on*, pages 1–6, sept. 2009.

[139] Igor Podlubny and Kennet V. Thimann. Fractional Differential Equations: An Introduction to Fractional Derivatives, Fractional Differential Equations, to Methods of Their Solution and Some of Their Applications. In *Mathematics in Science and Engineering*, volume 198, pages xv–xxiv, 1–340. Elsevier B.V., 1998.

[140] Eli Pollak and Peter Talkner. Reaction rate theory: What it was, where is it today, and where is it going? *Chaos: An Interdisciplinary Journal of Nonlinear Science*, 15(2):026116, 2005.

[141] D. Porter, F. Vollrath, and Z. Shao. Predicting the mechanical properties of spider silk as a model nanostructured polymer. *The European Physical Journal E*, 16:199–206, 2005.

[142] D. Porter, F. Vollrath, and Z. Shao. Predicting the mechanical properties of spider silk as a model nanostructured polymer. *The European Physical Journal E: Soft Matter and Biological Physics*, 16:199–206, 2005. 10.1140/epje/e2005-00021-2.

[143] W. H. Press, S. A. Teukolsky, W. T. Vetterling, and B. P. Flannery. *Numerical Recipes in C Numerical Recipes in C, Second Edition*. Cambrige University Press, 1992.

[144] J.M.S. Prewitt. Object Enhancement and Extraction. In B.S. Lipkin and A. Rosenfeld, editors, *Picture Processing and Psychohistories*. Academic Press, 1970.

[145] J. R. Quine. Helix parameters and proteine structure using quaternions. *J Mol Struct*, 460:53–66, 1999.

[146] Taikyue Ree and Henry Eyring. Theory of Non-Newtonian Flow. I. Solid Plastic System. *Journal of Applied Physics*, 26(7):793–800, 1955.

[147] Taikyue Ree and Henry Eyring. Theory of Non-Newtonian Flow. II. Solution System of High Polymers. *Journal of Applied Physics*, 26(7):800–809, 1955.

[148] D Reguera, J M Rubi, and J M G Vilar. The Mesoscopic Dynamics of Thermodynamic Systems. *The Journal of Physical Chemistry B*, 109(46):21502–21515, 10 2005. doi: 10.1021/jp052904i.

[149] M. Reiner. The Deborah Number. *Physics Today*, page 62, 1964.

[150] A. Reuss. Berechnung der Fließgrenze von Mischkristallen auf Grund der Plastizitätsbedingung für Einkristalle . *ZAMM - Journal of Applied Mathematics and Mechanics / Zeitschrift für Angewandte Mathematik und Mechanik*, 9(1):49–58, 1929.

[151] Richard E. Robertson. Theory for the Plasticity of Glassy Polymers. *The Journal of Chemical Physics*, 44(10):3950–3956, 1966.

[152] P.E. Rouse. A Theory of the Linear Viscoelastic Properties of Dilute Solutions of Coiling Polymers. *J. Chem. Phys.*, 21:1272, 1953.

[153] Sensirion. Datasheet, jun 2009. `http://www.sensirion.com`.

[154] Tilo Seydel, Wiebke Knoll, Imke Greving, Cedric Dicko, Michael M. Koza, Igor Krasnov, and Martin Müller. Increased molecular modbility in humid silk fibers under tensile stress. *Physical Review*, E **27**(83):016104, 2011.

[155] Tilo Seydel, Klaas Kölln, Igor Krasnov, Imke Diddens, Nadine Hauptmann, Gesa Helms, Malte Ogurreck, Shin-Gyu Kang, Michael M. Koza, and Martin Müller. Silkworm Silk under Tensile Strain Investigated by Synchrotron X-ray Diffraction and Neutron Spectroscopy. *Macromolecules*, 40(4):1035–1042, 2007.

[156] Zhengzhong Shao and Fritz Vollrath. The effect of solvents on the contraction and mechanical properties of spider silk. *Polymer*, 40(7):1799–1806, 1999.

[157] Zhengzhong Shao and Fritz Vollrath. Surprising strength of silkworm silk. *Nature*, 418(6899):741, 2002.

[158] Yu Shen, Michael A Johnson, and David C Martin. Microstructural Characterization of *Bombyx mori Silk Fibers*. *Macromolecules*, 31(25):8857–8864, 1998.

[159] A. Sinsawat, Y. Pthanarat, Y. Magoshi, R Pachter, and R K Eby. X-ray diffraction and computational studies of the modulus of silk (Bombyx mori). *Polimer*, 43(4):1323–1330, 2002.

[160] A Sinsawat, S Putthanarat, Y Magoshi, R Pachter, and R K Eby. The crystal modulus of silk (*Bombyx mori*). *Polymer*, 44(3):909–910, 2003.

[161] Jutarat Sirichaisit, Victoria L. Brookes, Robert J. Young, and Fritz Vollrath. Analysis of Structure/Property Relationships in Silkworm (Bombyx mori) and Spider Dragline (Nephila edulis) Silks Using Raman Spectroscopy. *Biomacromolecules*, 4(2):387–394, 2003.

[162] Gordon Leslie Squires. *Introduction to the theory of thermal neutron scattering*. Cambrige University Press, 2012.

[163] Y Takahashi, M Gehoh, and K Yuzuriha. Structure refinement and diffuse streak scattering of silk (Bombyx mori). *International Journal of Biological Macromolecules*, 24(2-3):127–138, MAR-APR 1999. 2nd International Symposium on Silk, Charlottesville, Virginia, Jun, 1998.

[164] Y. Takahashi, M. Gehon, and K. Yuzuriha. Crystall Structure of Silk (*Bombyx mori*). *J. Plym. Sci. B: Polym. Phys.*, 29:889–891, 1991.

[165] Kazunori Tanaka, Satoshi Inoue, and Shigeki Mizuno. Hydrophobic interaction of P25, containing Asn-linked oligosaccharide chains, with the H-L complex of silk fibroin produced by Bombyx mori. *Insect Biochemistry and Molecular Biology*, 29(3):269–276, 1999.

[166] Yves Termonia. Molecular Modeling of Spider Silk Elasticity. *Macromolecules*, 27(25):7378–7381, 1994.

[167] Arthur Tobolsky and Henry Eyring. Mechanical properties of polymers. *J. Chem. Phys.*, 11:125, 1943.

[168] N W Tschoegl. *The Phenomenological Theory of Linear Viscoelastic Behavior*. Springer-Verlag, 1989.

[169] S. Ulrich, A. Glišović, T. Salditt, and A. Zippelius. Diffraction from the β-sheet crystallites in spider silk. *Eur. Phys. J.*, E **27**:229–242, 2008.

[170] Léon Van Hove. Correlations in Space and Time and Born Approximation Scattering in Systems of Interacting Particles. *Phys. Rev.*, 95:249–262, Jul 1954.

[171] T. Vehoff, A. Glišović, H. Schollmeyer, A. Zippelius, and T. Salditt. Mechanical Properties of Spider Dragline Silk: Humidity, Hysteresis, and Relaxation. *Biophysical Journal*, 93(12):4425–4432, 2007.

[172] E. Gamma R. Helm R. Johnson J. Vlissides. *Design Patterns, Elements of Reusable Object-Oriented Software*. Addison-Wesley, 1995.

[173] Donald Voet and Judith G. Voet. *Biochemistry*. John Wiley & sons, inc., New York, second edition, 1995.

[174] Fritz Vollrath. Biology of spider silk. *International Journal of Biological Macromolecules*, 24(2-3):81–88, 1999.

[175] Fritz Vollrath. Strength and structure of spiders' silks. *Reviews in Molecular Biotechnology*, 74(2):67–83, 2000.

[176] Fritz Vollrath and David P Knight. Liquid crystalline spinning of spider silk. *Nature*, 410:541–548, 2001.

[177] J. L Walsh. A Closed Set of Normal Orthogonal Functions. *Amer. J. Math.*, 45:2–24, 1923.

[178] B. Warren. *X-ray Diffraction*. Addison-Wesley, 1969.

[179] Wikipedia. Amino Acid, 2010. [Online; accessed 22-July-2010].

[180] P Jeanene Willcox, Samuel P Gido, Wayne Muller, and David L Kaplan. Evidence of a Cholesteric Liquid Crystalline Phase in Natural Silk Spinning Processes. *Macromolecules*, 29(15):5106–5110, 1996. doi: 10.1021/ma960588n.

[181] Stefan Winkler and David L Kaplan. Molecular biology of spider silk. *Reviews in Molecular Biotechnology*, 74(2):85–93, 2000.

[182] W. F. K. Wynne-Jones and Henry Eyring. The Absolute Rate of Reactions in Condensed Phases. *J. Chem. Phys.*, 3:492, 1935.

[183] Extensible Markup Language (XML) 1.0. `http://www.w3.org/TR/REC-xml/`, 2008.

[184] Ain't Markup Language (YAML). `http://www.yaml.org`, 2010.

[185] Cong-Zhao Zhou, Fabrice Confalonieri, Nadine Medina, Yvan Zivanovic, Catherine Esnault, Tie Yang, Michel Jacquet, Joel Janin, Michel Duguet, Roland Perasso, and Zhen-Gang Li. Fine organization of Bombyx mori fibroin heavy chain gene. *Nucl. Acids Res.*, 28(12):2413–2419, 2000.

[186] Robert Zwanzig. Two-state models of protein folding kinetics. *Proc. Natl. Acad. Sci.*, 94:148–150, 1997.

Erklärung

Hiermit versichere ich an Eides Statt, dass die vorliegende Dissertation – abgesehen von der Beratung durch meine wissenschaftliche Betreuer und den angegebenen Quellen – nach dem Inhalt und Form meine eigene Arbeit ist. Sie hat bisher weder ganz noch zum Teil an einer anderen Stelle im Rahmen eines Prüfungsverfahrens vorgelegen. In folgenden Publikationen sind einzelne Teile diese Arbeit enthalten:

- Mechanical properties of Silk: Interplay of Deformation on Macroscopic and Molecular Length Scales, I. Krasnov, I. Diddens, N. Hauptmann, G. Helms, M. Ogurreck, T. Seydel, S. S. Funari, and M. Müller. *Phys. Rev. Lett.*, 100(048104), 2008.

Diese Arbeit ist unter Einhaltung der Regeln guter wissenschaftlicher Praxis der Deutschen Forschungsgemeinschaft entstanden.

Kiel, 27.08.2013

_____

(Igor Krasnov)

Danksagung

Mein erster Dank geht an Prof. Dr. Martin Müller für die freundliche Aufnahme in seine Arbeitsgruppe und die Möglichkeit dieses interessante Thema zu bearbeiten. Ich danke auch für die hoch kompetente und stätige Betreuung der vorliegenden Arbeit. Die Fähigkeit eine demokratische und zugleich kreative Atmosphäre in der Arbeitsgruppe stets aufrecht zu erhalten, hat mich immer beeindruckt.

Prof. Dr. Werner Press gilt meine besondere Dankbarkeit! Sein Beitrag war so groß, daß ich nicht in der Lage bin es in Worte zu fassen!

Monika Seeger danke ich für ihre stets freundliche Unterstützung in Verwaltungs und Bürokratiefragen. Ihre lückenlose Kompetenz hat mich immer zum Staunen gebracht.

Für die hoch professionelle Unterstützung in Themen der Elektronik und Computer Technologie möchte ich Arnd Seeger danken. Zudem danke ich Matthias Greve für seine Unterstützung im technischen Bereich und für die Mitentwicklung der technischen Geräte. Des weiteren danke ich Florian Kunze für die Zusammenarbeit, besonders für die Verwaltung des immer größer werdenden Satzes an experimentellen Rohdaten.

Bei Dr. Christina Krywka und Dr. Anja Glisovic möchte ich mich für das Korrekturlesen bedanken. Die daraus entstandenen Anregungen waren mir stets hilfreich und willkommen. Außerdem möchte ich meinen Dank an Anja Glisovic betonen für ihre hoch effektive Hilfe beim letzten Schliff und der Reformulierung einiger wichtiger und schwieriger Paragraphen der Arbeit.

Für die moralische Unterstützung und ihre Beratung in der Kunst der englischen Formulierung, die sehr hilfreich waren, danke ich Bridget Murphy.

Für die technische Unterstützung der Messungen möchte ich den Betreuerteams von den Instrumenten A2 (Desy, Hamburg), id13 (ESRF, Grenoble), IN6, IN10, IN11 (ILL, Grenoble) danken. Insbesondere gilt das für Tilo Seydel, Manfred Burghammer und Peter Fouquet. Außerdem bin ich Tilo Seydel für die inspirierenden Diskussionen und die Zusammenarbeit bei den Themen der Neutronenstreuung zu Dank verpflichtet.

Meiner Freundin Martina Vogten möchte ich an dieser Stelle auch ganz besonders danken. Vielen Dank für deine Hilfe bei der Gestaltung der Arbeit, deiner Geduld, Motivation und deiner Unterstützung auch in schwierigen Zeiten.